

RICE UNIVERSITY

**Trapping and Evaporation of ^{87}Sr and ^{88}Sr
Mixtures**

by

Pascal Gerry Mickelson

A THESIS SUBMITTED
IN PARTIAL FULFILLMENT OF THE
REQUIREMENTS FOR THE DEGREE

Doctor of Philosophy

APPROVED, THESIS COMMITTEE:

Thomas C. Killian, Chair
Associate Professor of Physics and
Astronomy

Randall G. Hulet
Fayez Sarofim Professor of Physics of
Physics

Daniel M. Mittleman
Professor of Electrical and Computer
Engineering

HOUSTON, TEXAS

APRIL 2010

ABSTRACT

Trapping and Evaporation of ^{87}Sr and ^{88}Sr Mixtures

by

Pascal Gerry Mickelson

This thesis describes trapping and evaporative cooling of ultracold ^{87}Sr and ^{88}Sr mixtures in an optical dipole trap to produce the first Bose-Einstein condensate (BEC) of ^{88}Sr . Furthermore, this work presents thermalization studies that characterize the scattering properties of these ultracold strontium samples. Such ultracold atomic gases have become an important area of research because of their potential for improving optical frequency standards and for realizing quantum computation using neutral atoms. A BEC of ^{88}Sr is particularly interesting because the small value of its background s-wave scattering length may enable the use of optical Feshbach resonances to create two-dimensional solitons. However, the small scattering length for ^{88}Sr also hinders efficient evaporative cooling in the optical dipole trap, a necessary step to producing a BEC. Experiments with other ultracold gases have successfully overcome this hurdle by mixing in a second atomic species which, by introducing stronger

interactions with the weakly interacting species, enables evaporation to colder temperatures via sympathetic cooling. For this work, we use ^{87}Sr to sympathetically cool ^{88}Sr during forced evaporation to quantum degeneracy.

Previous experiments in the Killian Lab characterized ^{88}Sr in detail. Here, I emphasize the new or improved aspects that have allowed trapping and cooling of the mixtures of ^{87}Sr and ^{88}Sr : trapping of ^{87}Sr by itself, spectroscopic measurements of all the stable strontium isotopes to guide the trapping of isotopic mixtures, imaging of both ^{87}Sr and ^{88}Sr , and the various trade-offs necessary to simultaneously trap ^{87}Sr and ^{88}Sr . Finally, I discuss how the thermalization studies of the scattering properties of the isotopes guide the forced evaporation of mixed isotope samples. These efforts result in the production of the BEC of ^{88}Sr , but they also point the way to future studies of fermionic quantum degeneracy in ^{87}Sr and to the rich physics of mixed species ultracold atomic systems.

Acknowledgments

I would not have reached this point without the aid and support of many people. Many thanks to my advisor, Tom Killian, for his invaluable feedback, patience, and support. To the other members of my committee, Randy Hulet and Dan Mittleman, for their time and welcome advice. To my high school physics teacher, Michael Hughes, for romanticizing the perils of experimental physics and encouraging me to pursue science. To Natali Martinez de Escobar for our shared eight year journey through graduate school. To Sarah Nagel, Mi Yan, and Brian DeSalvo for their hard work and companionship during long experimental runs. To all of the other members of the Killian Lab for their advice and good humor. To my friends in disparate places who kept wondering why Texas was a good idea. To my family for their constant love and support despite the distance. And most of all, to Loren for her love, tolerance, and patience as I finished this process: may that I be all of those for you when it is your turn.

Finally, thanks again to Brian DeSalvo for his reminder of my promise to use the interrobang (‽) as punctuation somewhere other than in the acknowledgments: happy hunting!

Contents

Abstract	ii
Acknowledgments	iv
List of Illustrations	vii
List of Tables	x
1 Introduction and Background	1
1.1 Introduction	1
1.2 Quantum Degeneracy and Alkaline Earth Metal Atoms	2
1.3 Comparison of Trapping of ^{87}Sr and ^{88}Sr	7
2 Experimental Methods	13
2.1 461 nm Lasers and Magnetic Trapping	13
2.1.1 Control of the Blue Laser Frequencies	14
2.1.2 Procedure for Trapping Mixtures of ^{87}Sr and ^{88}Sr	23
2.2 Narrow Line MOT Operation for ^{87}Sr and ^{88}Sr	29
2.2.1 Red MOT Cooling of ^{87}Sr	30
2.3 Optical Dipole Trap	40
2.3.1 Principles of Operation	40
2.3.2 Characterization of the Optical Dipole Trap	46
2.4 Imaging Systematics	56
2.4.1 Imaging of Single Isotopes	56
2.4.2 Imaging of Mixtures	67
3 Repumping and Spectroscopic Measurements Using the $(5s5p)^3\text{P}_2 - (5s4d)^3\text{D}_2$ Transition	77
3.1 Overview	77
3.2 Repumping of Atoms Using the $(5s5p)^3\text{P}_2 - (5s4d)^3\text{D}_2$ Transition	78
3.3 Spectroscopy of ^{84}Sr , ^{86}Sr , ^{87}Sr , and ^{88}Sr	86
3.4 Experimental Considerations for Trapping Mixtures	94
4 Unforced Evaporation in the Optical Dipole Trap	97
4.1 Spin-Polarization of ^{87}Sr	97
4.1.1 Evidence for Spin-Polarization	98
4.1.2 Modeling Unforced Evaporation of ^{87}Sr	110
4.2 Mixtures of ^{87}Sr and ^{88}Sr	116

5	Production of BEC by Forced Evaporation of Mixtures of ^{87}Sr and ^{88}Sr	122
5.1	Forced Evaporation Trajectory	122
5.2	Evidence for Bose-Einstein Condensation	129
6	Conclusion	136
A	Calculation of Optical Trap Light Shifts and Scattering Rates	138
B	Effective Cross Section for Imaging	160
B.1	Deriving the Peak Absorption Cross Section	160
B.1.1	Cross Section for ^{88}Sr	160
B.1.2	Decay Rates From Excited States	162
B.1.3	Relating Excitation and Decay Rates to Laser Parameters	163
B.1.4	Rate Equations for ^{87}Sr Ground State Levels	165
B.1.5	Effective Absorption Cross Section for ^{87}Sr	168
B.2	Model Implementation in Mathematica	169
C	OPO Laser	175
C.1	OPO Beam Intensity	175
C.2	Wavemeter Calibration	177
D	Zeeman Splitting of Lineshapes	179
D.1	Energies of the $^3\text{P}_2$ and $^3\text{D}_2$ States	179
D.2	Transition Energies Between the $^3\text{P}_2$ and $^3\text{D}_2$ States	181

Illustrations

1.1	Selected energy levels for strontium	8
1.2	Laser beams for atom trapping and cooling	9
1.3	Isotope shifts for the 461 nm transition	10
1.4	Isotope shifts for the 689 nm transition	11
2.1	Saturation absorption spectroscopy	15
2.2	Zeeman splitting of the $(5s^2)^1S_0 - (5s5p)^1P_1$ transition for ^{88}Sr	16
2.3	Generation of 461 nm light and derivative frequencies	18
2.4	Number of atoms imaged as a function of image beam frequency	21
2.5	$(5s^2)^1S_0 - (5s5p)^1P_1$ and $(5s^2)^1S_0 - (5s5p)^3P_1$ hyperfine structure for ^{87}Sr	22
2.6	Number of ^{88}Sr atoms as a function of time held in the magnetic trap	25
2.7	Study of repumping efficiency in magnetic trap	26
2.8	Number of ^{87}Sr atoms as a function of magnetic trap loading time	27
2.9	Experimental timing for mixed species trapping	29
2.10	One-dimensional MOT cooling	32
2.11	Breakdown of MOT Cooling	33
2.12	Magnetic sub-levels of the hyperfine states of ^{87}Sr	34
2.13	Generation of 689 nm light and derivative frequencies	37
2.14	Settings for Dual 689 nm MOT	38
2.15	Cartoon of the dipole trap induced light shifts	42
2.16	Calculated light shifts for strontium	44
2.17	Calculated scattering rates for strontium	45
2.18	Optical dipole trap cartoon	47
2.19	Generation of optical dipole trap beam	48
2.20	Absorption image of red MOT-to-optical trap transfer	50
2.21	Lifetime of atoms in the optical dipole trap	52
2.22	Parametric excitation measurement of optical dipole trap frequencies	54
2.23	Population dynamics for unpolarized population during application of image beam	60
2.24	Population dynamics for polarized population during application of image beam	61
2.25	Magnetic sub-levels states of ^{87}Sr	63

2.26	Ratio of effective absorption cross section to peak absorption cross section	65
2.27	Experimental timing for dual imaging	69
2.28	Dual isotope imaging	71
2.29	Contamination of mixed isotope images	73
2.30	Experimental timing for blowing away ^{87}Sr atoms in mixtures	74
2.31	Effect of blowing away ^{87}Sr atoms	75
3.1	Selected energy levels and transitions for repumping experiments	79
3.2	Experimental timing for blue MOT operation with no magnetic trapping	81
3.3	Blue MOT atom number as a function of loading time	82
3.4	Spectroscopy of the $(5s5p)^3\text{P}_2 - (5s4d)^3\text{D}_2$ transition for all stable strontium isotopes	87
3.5	Spectroscopy of the $(5s5p)^3\text{P}_2 - (5s4d)^3\text{D}_2$ transition for ^{84}Sr , ^{86}Sr , and ^{88}Sr	88
3.6	Line shapes of ^{88}Sr spectra	89
3.7	Zeeman splitting for ^{88}Sr	90
3.8	King plot showing isotope shifts for the $(5s5p)^3\text{P}_2 - (5s4d)^3\text{D}_2$ transition	93
3.9	Number of ^{87}Sr and ^{88}Sr atoms as a function of repumping laser frequency	95
4.1	$(5s^2)^1\text{S}_0 - (5s5p)^3\text{P}_1$ hyperfine structure for ^{87}Sr	99
4.2	Magnetic sub-levels of the hyperfine states of ^{87}Sr	100
4.3	Splitting of magnetic sub-levels under an applied magnetic field	100
4.4	Spectroscopy of spin-polarized and unpolarized ^{87}Sr	102
4.5	Number of ^{87}Sr atoms as a function of pump beam time	104
4.6	Number of ^{87}Sr atoms as a function of pump beam intensity	106
4.7	Persistence of spin-polarization of a sample held in the optical dipole trap	107
4.8	Unforced evaporation of spin-polarized and unpolarized ^{87}Sr samples	109
4.9	Calculation of effective scattering length of spin-polarized ^{87}Sr	112
4.10	Unforced evaporation of ^{84}Sr	114
4.11	Unforced evaporation of a mixture of ^{87}Sr and ^{88}Sr	117
4.12	Collision cross section as a function of temperature	118
4.13	Rate of elastic collisions as a function of temperature	121
5.1	Forced evaporation cartoon	123
5.2	Forced evaporation trajectory	124
5.3	Trap depths during forced evaporation trajectory	126
5.4	Atom number and temperature evolution during forced evaporation	128
5.5	Absorption images showing emergence of a BEC	130

5.6	Fit of nearly degenerate samples with Bose-Einstein distribution . . .	132
5.7	Extraction of temperature from samples with bimodal distribution . .	133
B.1	Decay paths from excited state levels.	163
C.1	Intensity measurement of 3 μm laser	176
C.2	Wavemeter calibration using absorption spectroscopy	178

Tables

1.1	Scattering length values from two-photon spectroscopy [41] for all the stable isotopes of strontium. The cross species scattering lengths for ^{88}Sr with ^{86}Sr and ^{87}Sr are shown as they have the most promising values for effective sympathetic cooling of ^{88}Sr	5
2.1	Trap frequencies from parametric excitation measurement.	55
2.2	Result of calculating absorption cross sections for ^{88}Sr . Only three configurations have non-zero values of the absorption cross section. These correspond to linearly, right circularly, and left circularly polarized light, respectively.	58
3.1	Isotope shifts and uncertainties of the $(5s5p)^3P_2-(5s4d)^3D_2$ transition at $\lambda=3012$ nm in strontium.	92
4.1	Scattering lengths, extracted from a model of collisional dynamics [79], for unpolarized ^{87}Sr , spin-polarized ^{87}Sr , and ^{84}Sr . All isotopes in this study are loaded by themselves in the optical dipole trap. I list values of the scattering length obtained from two-photon photoassociation spectroscopy [41] for comparison. The rough agreement of the ^{84}Sr scattering length with the value from 2-photon photoassociation spectroscopy (PAS) supports the accuracy of the model, so the fact that the observed scattering lengths of ^{87}Sr are much smaller than the 2-photon PAS scattering lengths suggests that the samples have a high degree of spin-polarization.	115
B.1	Result of calculating absorption cross sections for ^{88}Sr . Only three configurations have non-zero values of the absorption cross section. These correspond to linearly, right circularly, and left circularly polarized light, respectively.	162
C.1	Measurements of the size of the 3 μm laser beam.	177

Chapter 1

Introduction and Background

1.1 Introduction

This work presents trapping of mixtures of ^{87}Sr and ^{88}Sr in an optical dipole trap and the evaporation of these mixtures to produce a Bose-Einstein condensate (BEC) of ^{88}Sr . Unforced evaporation of these samples reveals the scattering properties of the mixtures, showing that mixing ^{87}Sr with ^{88}Sr allows for more efficient evaporation of the latter isotope via sympathetic cooling. As in many other experiments that achieve quantum degeneracy, sympathetic cooling is the key to producing the BEC of ^{88}Sr .

The structure of this thesis is as follows. The remainder of this chapter recounts the development of the techniques used to produce quantum degenerate gases, in general, motivates the study of strontium, more specifically, and provides a brief overview of the differences between trapping and cooling ^{87}Sr and ^{88}Sr . Then, in Chapter 2, I detail the methods used to load mixtures of ^{87}Sr and ^{88}Sr together into an optical dipole trap. Chapter 3 describes spectroscopy and repumping on the $(5s5p)^3\text{P}_2 - (5s4d)3\text{D}_2$ transition for all the stable isotopes of strontium. These studies are important because they inform the trapping of ^{87}Sr and ^{88}Sr . Next, the results of

unforced evaporation experiments with ^{87}Sr and ^{88}Sr , alone and mixed, are discussed in Chapter 4. Finally, in Chapter 5, I present the evidence showing the production of a BEC of ^{88}Sr . The results in Chapter 3 were published in [1], and the work of Chapters 4 and 5 is in [2]. The latter article has been submitted to Physical Review A.

1.2 Quantum Degeneracy and Alkaline Earth Metal Atoms

Trapping and cooling of neutral atoms has opened up a wide range of experiments over the past two decades. In particular, the production of the first Bose-Einstein condensates in 1995 [3–5] opened a new sub-field of experimental atomic physics. The initial focus on bosons expanded to include quantum degeneracy of fermions [6] and boson-fermion mixtures [7].

Even so, many neutral atom species are still difficult to trap because trapping techniques are not universally applicable. Laser light at the necessary frequency may not be available or an atomic species may possess scattering properties that make it difficult to trap and evaporatively cool by itself. For example, an atom species which interacts weakly or not at all cannot be brought to quantum degeneracy because such experiments rely on elastic collisions between atoms for efficient evaporation [8]. To overcome this limitation, many experiments use sympathetic cooling, first demonstrated in rubidium [9], where a weakly interacting species is mixed with a more strongly interacting one. The inter-species scattering length of the mixture

is reasonably large, so inter-species elastic collisions can cool the weakly interacting species to quantum degeneracy.

Multiple species systems were first investigated with multiple isotopes of one species (rubidium) [10] and then with different species (potassium and sodium) [11]. A few years later, sympathetic cooling was used to produce two-component, quantum degenerate rubidium [9], where each component was in a different internal spin state. The first Fermi degenerate gas [6] similarly used potassium in two different Zeeman sub-levels to overcome Pauli blocking of collisions between spin-polarized atoms. Even mixtures of quantum degenerate fermions and bosons were produced in 2001 (lithium) [7], using the boson to sympathetically cool the fermion whose collision rate is affected by Pauli blocking. This selection of experiments make it clear that sympathetic cooling has been broadly applied to the trapping of multiple species, thus increasing the selection of atoms for which quantum degeneracy can be produced.

Almost all of these pioneering experiments were conducted with alkali metal atoms, which have a single electron in the outer shell. While these continue to be fruitful systems of study, alkaline earth metal atoms are also appealing subjects of study. Like the alkali metal atoms, the alkaline earth metal atoms have easily accessible transitions in the visible wavelength regime. However, a filled outer shell of electrons means that they lack hyperfine structure in the ground state, simplifying theoretical treatments of these atoms [12] and reducing energy level shifts due to external fields. Alkaline earth metal atoms also possess narrow optical resonances, resulting

from dipole-forbidden transitions between singlet and triplet states, that make them excellent for optical frequency standards [13].

The existence of these narrow resonances has also driven interest in producing quantum degeneracy of alkaline earth metal atoms. Narrow-line magneto-optical trap (MOT) cooling to the photon recoil temperature, first demonstrated in strontium [14], suggested that alkaline earth metal atoms could be one avenue to all-optical production of BECs [15, 16]. Furthermore, recent work proposes using alkaline earth metal atoms for quantum computing applications [17–19] and analog quantum simulators of many-body systems [20, 21] because the lack of ground state hyperfine structure allows longer coherence times (as with the ground state hyperfine levels of alkali metal atoms) and isolates quantum states from magnetic fields (unlike the alkali metal atoms).

Though the earliest work with narrow-line cooled alkaline earth metal atoms was in strontium [14], calcium [22, 23], radium [24], and ytterbium [25], which has alkaline-earth-like electronic structure, have also been trapped using narrow line MOTs. Quantum degeneracy has now been produced in ytterbium [26, 27] and calcium [28]. Nevertheless, strontium remains an active area of study both experimentally [14, 29–32] and theoretically [33, 34] partly because optical clock techniques are the most advanced for this atom [13, 35]. Furthermore, its intercombination line of 7.5 kHz is neither too narrow (0.4 kHz in calcium) or too broad (132 kHz in ytterbium), enabling efficient cooling in the narrow-line MOT. Finally, larger quantum degenerate

samples ($\sim 400,000$) are possible with strontium [36, 37] than with ytterbium (5,000; [26, 27]) and calcium (20,000; [28]).

The most abundant stable isotopes of strontium, ^{88}Sr (82.6%), ^{87}Sr (7.0%), and ^{86}Sr (9.9%), have long been studied for many of these reasons, but efforts to produce quantum degeneracy of strontium [15, 16, 31, 38] were hindered by lack of knowledge of the scattering properties of the strontium isotopes. Photoassociation experiments [30, 39–41] and Fourier-transform spectroscopy [42] that measured the s-wave scattering lengths of the different isotopes (Table 1.1) helped fill in the missing knowledge of the scattering properties of strontium and explained the limited phase space density obtained in earlier experimental results. For instance, the small scattering length of

Table 1.1 : Scattering length values from two-photon spectroscopy [41] for all the stable isotopes of strontium. The cross species scattering lengths for ^{88}Sr with ^{86}Sr and ^{87}Sr are shown as they have the most promising values for effective sympathetic cooling of ^{88}Sr .

Isotope Pair	Scattering Length [a_0]
88–88	-1.4(6)
87–87	96.2(1)
86–86	823(24)
84–84	122.7(3)
88–87	55.0(2)
88–86	97.4(1)

^{88}Sr means that it evaporates very inefficiently, which likely frustrated earlier efforts to attain quantum degeneracy. Conversely, despite the large, positive scattering length of ^{86}Sr , it was shown that its high three-body recombination rate contributed to high

losses [38]. Eventually ^{84}Sr , in spite of its extremely low natural abundance, became the first strontium isotope to be Bose-condensed [36, 37], partly because of its optimal, positive scattering length.

The same property that makes a BEC of ^{88}Sr technically challenging to produce, the small s-wave scattering length, makes it appealing for other applications. For instance, the combination of this weak interaction and the lack of ground state orbital, spin, and nuclear angular momentum leaves the atom unaffected by electric and magnetic fields, making it a good candidate for interferometers that rely on long coherence times [43]. This weak interaction also benefits optical frequency standards using ^{88}Sr [44]. Finally, the small background scattering length of ^{88}Sr suggests its use to demonstrate low-loss optical Feshbach resonances [33, 45].

This thesis discusses the steps taken to overcome the technical hurdles to production of a BEC of ^{88}Sr . Reaching into the diverse toolbox which atomic physicists have developed over the past decade, we exploit mixed species trapping and sympathetic cooling to increase the phase space density of ^{88}Sr past the limits of previous attempts. We choose to introduce ^{87}Sr into the trap instead of ^{86}Sr because the high rate of three-body recombination in ^{86}Sr considerably shortens sample lifetimes. Furthermore, the ^{88}Sr – ^{87}Sr elastic collision cross section (Table 1.1) is still favorable for efficient evaporative cooling. Unlike most experiments that use sympathetic cooling, we use the fermionic ^{87}Sr as the coolant atom instead of a boson. These efforts culminate in the successful production of quantum degenerate ^{88}Sr .

1.3 Comparison of Trapping of ^{87}Sr and ^{88}Sr

Broadly speaking, the trapping and cooling of ^{87}Sr atoms is similar to that of ^{88}Sr . Initially, strontium atoms are captured from a Zeeman-slowed atomic beam [46, 47] by a magneto-optical trap (MOT) [48] operating on the 461 nm, $(5s^2)^1\text{S}_0 - (5s5p)^1\text{P}_1$ transition (figs. 1.1 and 1.2). The 461 nm transition is not a true two-level system, and one in 10^5 atoms will decay to the $(5s5p)^3\text{P}_2$ state via the $(5s4d)^1\text{D}_2$ state [49]. Atoms in the $(5s5p)^3\text{P}_2$ state are magnetically trappable in the quadrupole magnetic field of the MOT [50], allowing accumulation of atoms in that state for up to the 22 s lifetime of the magnetic trap. After 25×10^6 ^{87}Sr atoms have been trapped, application of a laser operating on the $(5s5p)^3\text{P}_2 - (5s4d)^3\text{D}_2$ transition enables $(5s5p)^3\text{P}_2$ atoms to return to the ground state to be re-captured. Atoms at this stage are typically a few mK warm. Subsequent transfer to a second-stage MOT operating on the 689 nm $(5s^2)^1\text{S}_0 - (5s5p)^3\text{P}_1$ transition further cools atoms to about 1 μK . These ultracold atoms are then loaded into an optical dipole trap, operating at 1064 nm, where most of the studies in this thesis are conducted.

Differences in trapping ^{87}Sr and ^{88}Sr arise for two primary reasons. The first is the shift in the resonance frequencies of all the ^{87}Sr transitions relative to ^{88}Sr (the isotope shift). Figures 1.3 and 1.4 show these isotope shifts for the $(5s^2)^1\text{S}_0 - (5s5p)^1\text{P}_1$ and $(5s^2)^1\text{S}_0 - (5s5p)^3\text{P}_1$ transitions respectively. For the 461 nm transition, the three hyperfine levels of ^{87}Sr (due to the nuclear spin of $I = 9/2$) are red-detuned (lower in frequency) from the ^{88}Sr resonance by about 75 MHz. For the 689 nm

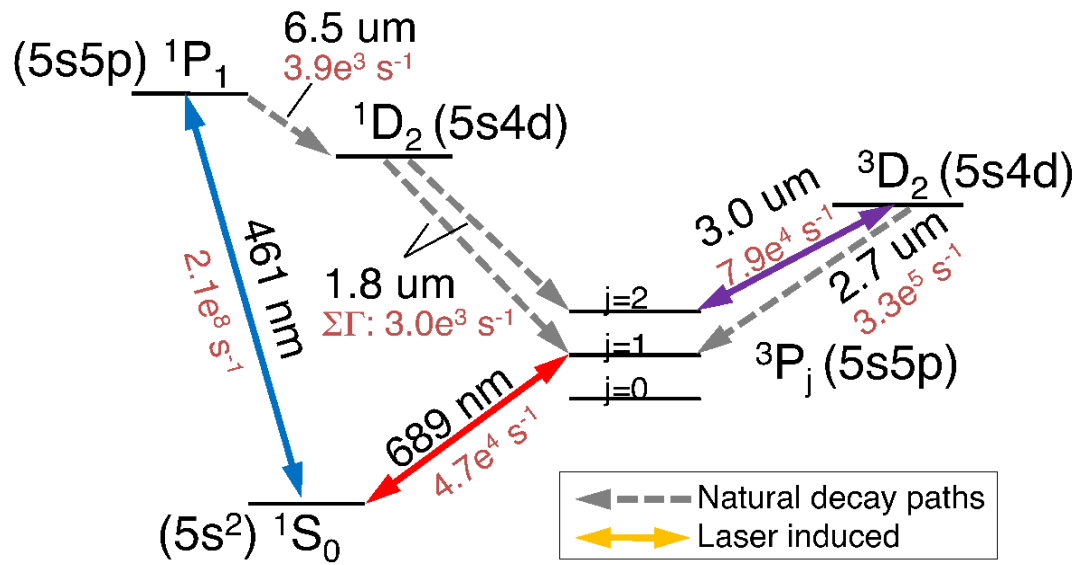


Figure 1.1 : Selected energy levels and transitions for strontium. Solid (colored) arrows represent laser-stimulated transitions while dashed (gray) arrows represent decay paths. Transition wavelengths (nm) and decay rates (s^{-1}) are indicated as well.

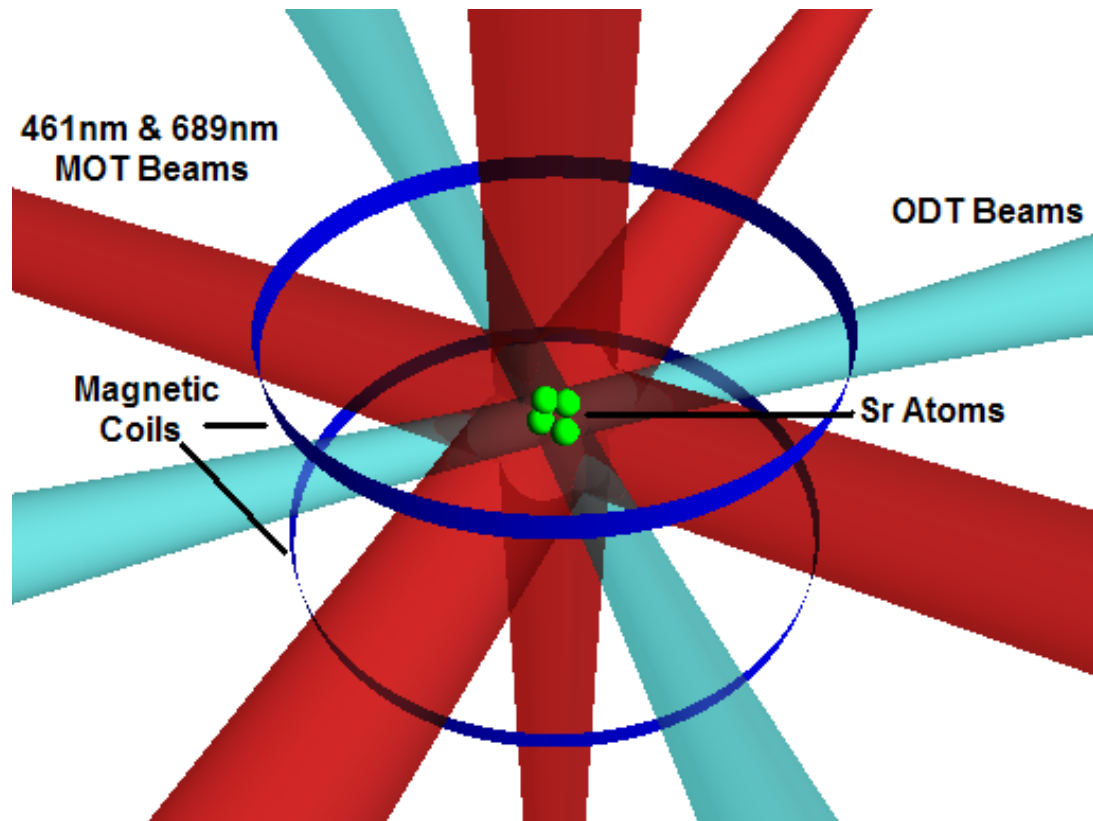


Figure 1.2 : Schematic of the laser beams involved in trapping and cooling strontium atoms. Beams operating on the 461 nm $(5s^2)^1S_0 - (5s5p)^1P_1$ transition initially capture atoms at a few mK in temperature. Magnet coils generate a quadrupole magnetic trap that creates a conservative potential in which to accumulate atoms. After transfer from the magnetic trap to a second-stage MOT operating on the 689 nm $(5s^2)^1S_0 - (5s5p)^1P_1$ transition, atoms have a temperature of about $1 \mu\text{K}$. Finally, atoms are transferred into an crossed beam optical dipole trap, formed by a 1064 nm laser, where forced evaporation can produce very dense and cold samples of strontium.

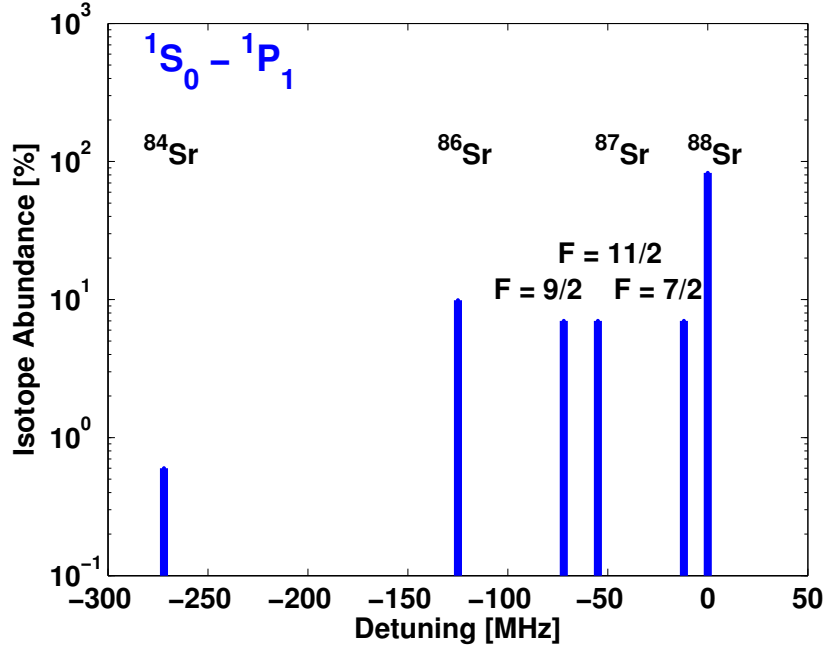


Figure 1.3 : Isotope shifts for the 461 nm transition. The ^{87}Sr isotope shift (levels labeled by the F numbers) is small enough that the same laser that traps ^{88}Sr can be used, with moderate frequency shifts, for trapping and cooling. The ability to store atoms in a quadrupole magnetic trap allows us to first trap ^{88}Sr , then ^{87}Sr .

transition, the shift is even greater at up to 1350 MHz detuned. Because efficient cooling and trapping rely on the production of resonant coherent light, we need to either change the wavelength of the ^{88}Sr lasers or use separate lasers to attain the necessary frequencies for trapping ^{87}Sr . For the 461 nm transition, we change the wavelength, and for the 689 nm transition, we have separate lasers for each isotope. Storing atoms in the magnetic trap is what enables us to use the same 461 nm light for both isotopes; there is no equivalent for trapping in the second-stage 689 nm MOT.

The second reason that trapping ^{87}Sr differs from trapping ^{88}Sr is that ^{87}Sr has

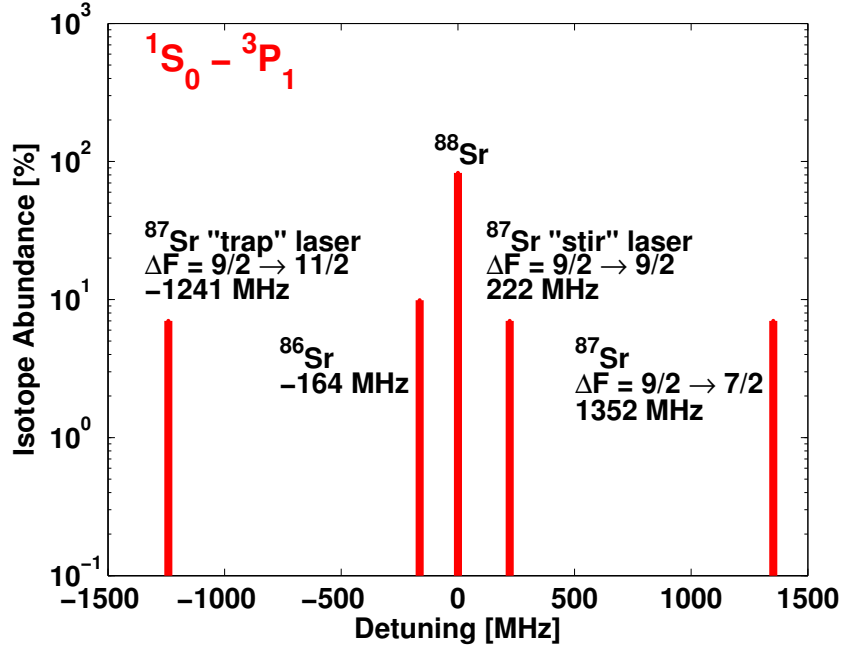


Figure 1.4 : Isotope shifts for the 689 nm transition. Because both ^{87}Sr and ^{88}Sr must be trapped simultaneously in the red MOT, separate lasers are required for each isotope.

nuclear spin, $I = 9/2$. The magnetic level structure that results from having non-zero nuclear spin means that more energy levels exist in each state for ^{87}Sr than for ^{88}Sr . If ^{87}Sr atoms are distributed evenly between all the magnetic sub-levels in the ground state, then the number of atoms in any one state is reduced. Because a low number of ^{87}Sr atoms limits the kinds of experiments we can do, trapping ^{87}Sr requires extra loading time and some different techniques than we use for ^{88}Sr in order to produce dense enough samples.

Successfully overcoming these obstacles ultimately results in mixtures of ^{87}Sr and ^{88}Sr in the optical dipole trap, where sympathetic cooling and efficient evaporation

can take place.

Chapter 2

Experimental Methods

This chapter details the experimental techniques used to trap and cool mixtures of ^{87}Sr and ^{88}Sr . I mostly focus on the details of trapping ^{87}Sr because ^{88}Sr has been discussed extensively in other Killian-lab publications [1, 30, 39, 41, 50, 51]. However, I also describe the technical compromises necessary to produce mixtures of ^{87}Sr and ^{88}Sr in the optical dipole trap.

The first parts of this chapter follow the overview of trapping and cooling given at the end of Chapter 1. I begin by discussing the lasers operating on the 461 nm transition and then explain the loading of both isotopes into the magnetic trap. A section on red MOT operation describes the lasers used to trap ^{87}Sr and the procedures used to trap isotopic mixtures. Then, I present the loading and characterization of the optical dipole trap. I finish by exploring the systematics of imaging samples that contain both ^{87}Sr and ^{88}Sr .

2.1 461 nm Lasers and Magnetic Trapping

This section focuses on how we switch the blue laser frequencies and the experimental sequence in which the magnetic trap is loaded with both ^{87}Sr and ^{88}Sr .

2.1.1 Control of the Blue Laser Frequencies

To account for the isotope shift of ^{87}Sr from ^{88}Sr for all the blue beams, we change the frequency that these beams are referenced to. Our reference frequency is obtained from Doppler-free saturation absorption spectroscopy which locks the frequency of the blue light to the 461 nm atomic transition for ^{88}Sr . Then, we change the frequency of the laser light by Zeeman shifting the energy levels of atoms in the reference vapor cell.

Saturated absorption spectroscopy (Fig. 2.1) is a technique that uses counter-propagating and overlapping laser beams to reduce Doppler broadening of an absorption profile [52]. The first beam (the “pump”) depletes one velocity class of atoms in a vapor cell so that the absorption profile of a second overlapped probe beam (P2) has a hole (called the “Lamb dip”). If both the pump and probe beams are at the same frequency, then the Lamb dip appears at the peak of the absorption profile with a width that can be as narrow as the natural linewidth of the transition. By subtracting the absorption profile of P1 from the absorption profile of P2, the Lamb dip is the only remaining feature. The narrowed line provides a precise way to lock a laser to the transition frequency because the error signal that is generated has a zero crossing point. The zero crossing is a convenient way of monitoring the frequency because, if the frequency moves either positively or negatively, a small correction can be applied to the current controller of the source laser to keep the laser locked to the frequency of the transition. It is also possible to generate an error signal from a Doppler-broadened

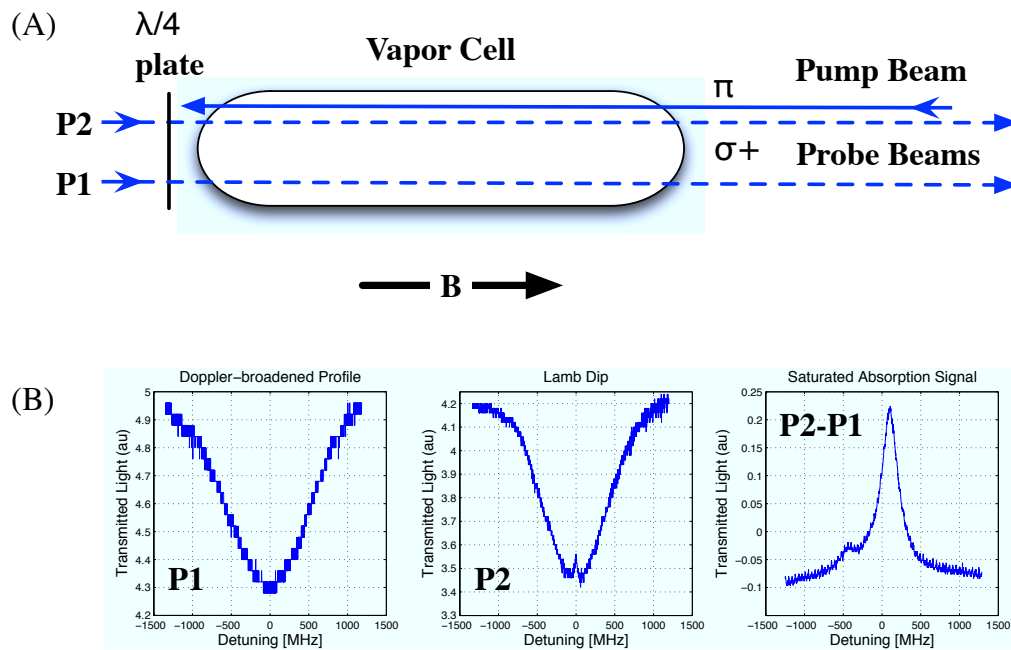


Figure 2.1 : Diagram of Doppler-free saturation absorption spectroscopy with an applied magnetic field. (A) The pump beam depletes one velocity class of atoms so that a Lamb dip is observed in the spectrum of the probe beam (P2) with which the pump beam is overlapped. P1 obtains a spectrum for atoms whose velocity profile is unaffected by the pump beam. (B) Sample spectra from saturation absorption spectroscopy. The Doppler-broadened profile from P1 is subtracted from the Lamb dip profile from P2 to obtain the saturated absorption signal (P2-P1). An error signal can be generated from the saturated absorption signal which allows us to lock our blue lasers to the frequency of the atoms.

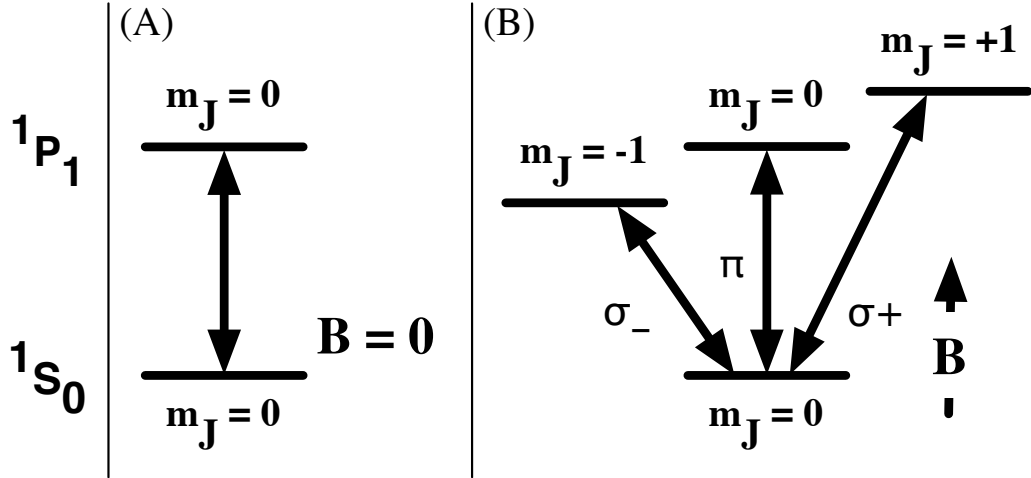


Figure 2.2 : Energy level splitting of ^{88}Sr with an applied magnetic field. For saturated absorption spectroscopy, we are able to take advantage of the Zeeman splitting to drive transitions to the different m_J states because we use differently polarized light for the pump and probe beams. The atom population seen by the probe beam (P2) is saturated by the pump laser which drives atoms from the ground state level. Meanwhile, the probe beams are both right circularly polarized and instead drive transitions to the $m_J = 1$ level. The spectrum of the probe beam (P2) which is overlapped with the pump beam contains the Lamb dip while the spectrum of the other probe beam (P1) provides the Doppler profile without the Lamb dip.

spectrum, but since an absorption line can only be split by roughly a factor of the signal-to-noise ratio of the measurement, achieving a lock good to better than 1 MHz requires very high signal-to-noise ratios.

We can shift the energy levels of the atoms in the saturated absorption vapor cell by applying a strong magnetic field (Fig. 2.2). If we use circularly polarized light for the spectroscopy, we can offset the frequency of our blue lasers while still locking the laser to the Lamb dip. In our set-up, both the pump and probe beams begin linearly polarized. Before entering the chamber, the two probe beams (P1 and

P2) pass through a $\lambda/4$ plate and become circularly polarized. The right circularly polarized component of the pump beam saturates the $m_J = 0 \rightarrow m_J = 1$ transition so that the ground state velocity distribution has a hole (The linearly polarized light also saturates the $m_J = 0 \rightarrow m_J = -1$ transition when it is on resonance with this transition, but this has a small effect which we neglect). Meanwhile, the other probe beam (P1) interacts with an atom population that is unaffected by the pump beam, resulting in a spectrum without the Lamb dip. Taking the difference of the spectra from the two probe beams yields the Lamb dip for the $m_J = 0 \rightarrow m_J = 1$ transition. Because the frequency of the $m_J = 1$ Lamb dip varies with magnetic field, a laser locked to this transition will change frequency proportionally to the applied magnetic field. The frequency tuning range for our saturated absorption cell is about 80 MHz and is limited by the maximum current we can apply. The frequency offset can be changed on a time scale of a few milliseconds, limited by the bandwidth of the servo lock. Finally, a computer-controlled voltage (V_{DAC}) sets the magnetic field, which changes the frequency with a conversion of 8.4 MHz/V [53].

The frequencies of all the blue beams used in the experiment (Fig. 2.3) are derived from a laser whose frequency is determined via the saturation absorption spectroscopy scheme outlined above. Acousto-optic modulators offset the frequency additional amounts for different uses of 461 nm light in the experiment. The base frequency of blue laser light (f_L) is determined by the frequencies of the shift AOM (δ_{shift}) and the amount that the energy levels of the atoms are Zeeman shifted in the

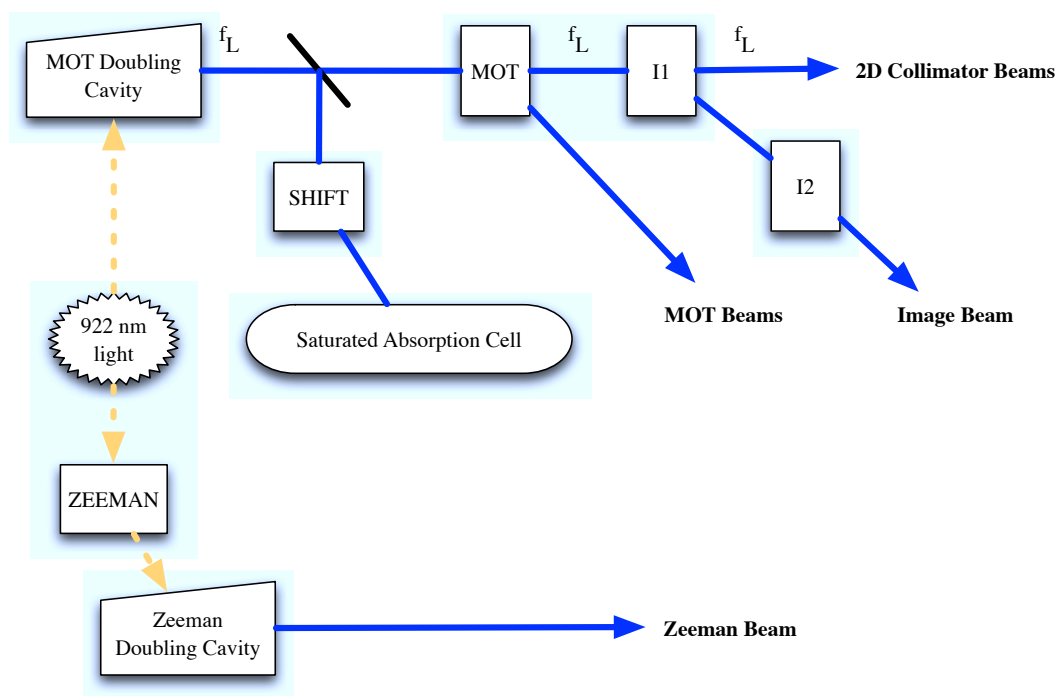


Figure 2.3 : Schematic showing the generation of 461 nm light, and its frequency offset, for trapping and imaging of strontium isotopes. Bold labels indicate light that shines directly on the atoms and rectangles indicate acousto-optic modulators (AOMs). As discussed in the text, the AOMs offset the frequency of the blue laser light (f_L) for different applications in the experiment.

saturation absorption cell (δ_{satabs}). We express f_L as

$$f_L = f_{atoms} + \delta_{shift} + \delta_{satabs}, \quad (2.1)$$

where f_{atoms} is the resonance frequency of ^{88}Sr (f_{88}) that we lock to. For imaging, two additional AOMs (I1 and I2) shift the frequency, so

$$f_{image} = f_L + \delta_{I1} + \delta_{I2}. \quad (2.2)$$

Similarly, one additional AOM sets the frequency of the blue MOT beams:

$$f_{MOT} = f_L + \delta_{MOT}. \quad (2.3)$$

For the Zeeman slower beam, the AOM is placed before the doubling cavity, resulting in

$$f_{zeeman} = f_L + 2\delta_{zeeman}. \quad (2.4)$$

Finally, the two-dimensional collimator has a frequency equal to that of the laser ($f_{2D} = f_L$). The usual operating frequencies for these AOMs are $\delta_{I1} = 76$ MHz, $\delta_{I2} = -52$ MHz, $\delta_{MOT} = -36$ MHz, $\delta_{zeeman} = -253$ MHz, and $\delta_{shift} = -56.0$ MHz.

The frequency shift of the error signal resulting from changing the magnetic field applied to the saturation absorption cell (δ_{satabs}) sets the reference frequency for each experiment. For example, when we trap ^{88}Sr by itself ($f_{atoms} = f_{88}$), we image on-resonance with the atoms ($f_{image} = f_{88}$) to maximize the amount of absorption. To find the frequency of maximum absorption, we independently scan the magnetic field to move the frequency for imaging (Fig. 2.4). For the ^{88}Sr experiments, the

magnetic field is the same for both trapping and imaging. Plugging Eq. 2.1 into Eq. 2.2 and using the above values for the AOM frequencies yields $\delta_{satabs} = 32$ MHz. Consequently, we find that the blue MOT beams are red-detuned 59 MHz ($\approx 2\Gamma$) from resonance, the Zeeman slower beam is red-detuned by ~ 530 MHz, and the 2D collimator beam is red-detuned by only 24 MHz ($< \Gamma$) from resonance.

Trapping ^{87}Sr requires detuning the blue lasers an amount equal to the isotope shift for the 461 nm transition, about 50 MHz [54] from the ^{88}Sr resonance. We optimize δ_{satabs} by varying the magnetic field applied to the saturation absorption cell and observing the number of atoms trapped (Fig. 2.4). This data, for ^{87}Sr , is of atoms trapped in the red MOT. Because absorption depends on the wavelength of the imaging light, the maximum atom number occurs when the imaging light is on-resonance with a transition. The ^{87}Sr peak at about $\delta_{satabs} = -30$ MHz is detuned about 60 MHz from the ^{88}Sr resonance, roughly consistent with the known frequency offset of the $F9/2 \rightarrow F = 11/2$ transition (Fig. 2.5). Additionally, this transition has the largest absorption cross section, so we expect it to have the larger signal. Because we use this detuning ($\delta_{satabs} = -30$ MHz, $V_{DAC} = -3.6$ V) for all of our experiments with ^{87}Sr , the typical laser detunings for ^{87}Sr are each relative to the $(5s^2)^1S_0 - (5s5p)^1P_1$ transition into the $F = 11/2$ state. Likewise, a detuning of $\delta_{satabs} = 30$ MHz and voltage of $V_{DAC} = 3.6$ V is typical for experiments involving ^{88}Sr .

There are several experimental situations where we dynamically jump from one

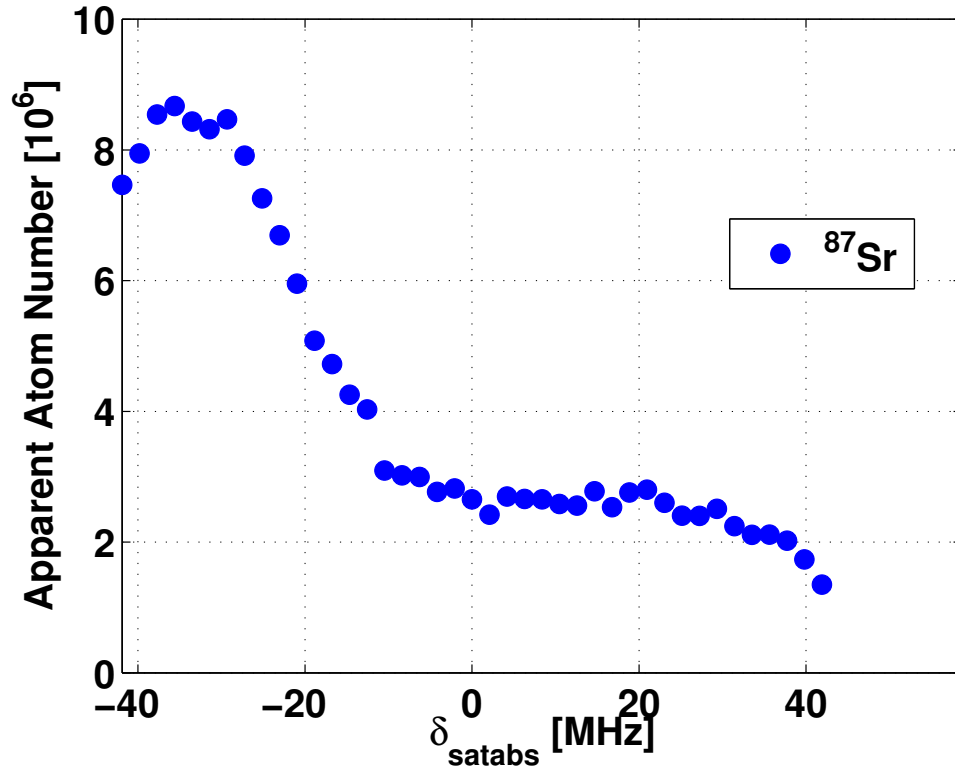


Figure 2.4 : Optimization of the image beam frequency for ^{87}Sr , showing the full tuning range of the saturation absorption cell (δ_{satabs}). A computer-controlled voltage controls the frequency at a rate of 8.4 MHz/V. The number of atoms imaged varies with the frequency of the image beam because the absorption cross section is wavelength-dependent. The maximum cross section should occur on-resonance with transitions from the ground state to excited state. We believe that the peak near $\delta_{satabs} = -30$ MHz is the $F = 11/2$ hyperfine level of the $(5s5p)^1P_1$ state for ^{87}Sr which is approximately 55 MHz detuned from the ^{88}Sr resonance (Fig. 2.5).

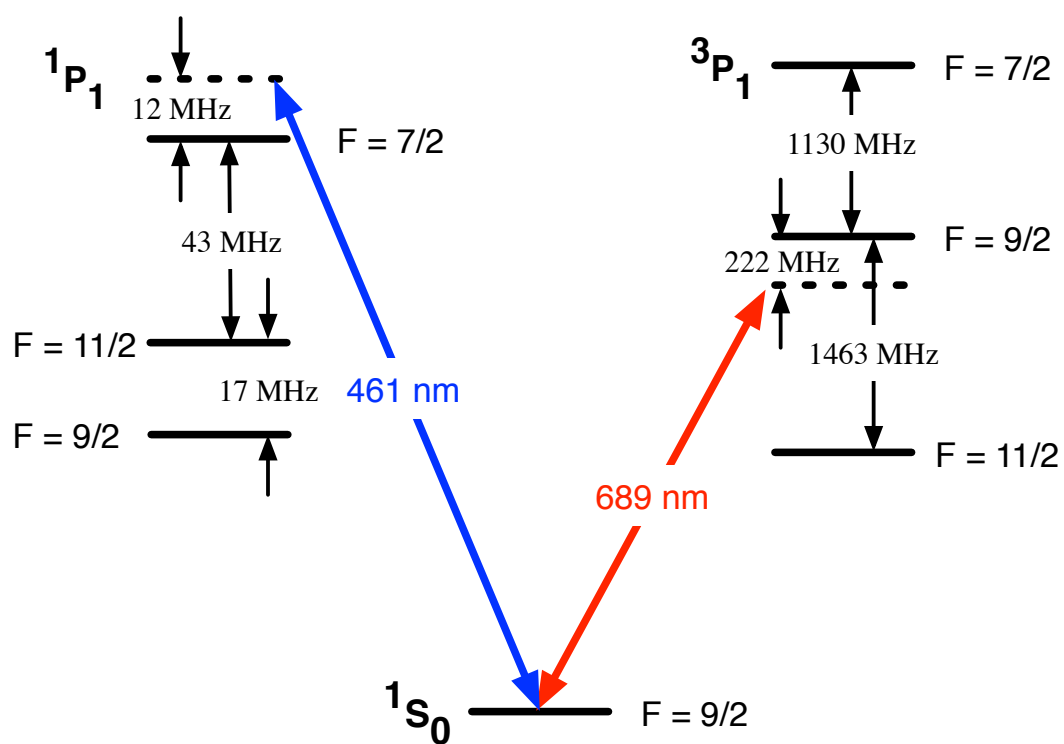


Figure 2.5 : Hyperfine level structure of ^{87}Sr for the 461 nm and 689 nm transitions with detunings from their respective ^{88}Sr counterparts.

value of δ_{satabs} to another. Most importantly for the mixed isotope experiments discussed in this thesis, we change the value of δ_{satabs} so that the blue laser frequencies are first optimized for ^{88}Sr trapping and then for ^{87}Sr trapping. Also, there is no a priori reason that we could not shift the blue frequencies far enough to trap the other stable strontium isotopes (^{84}Sr and ^{86}Sr). Practical limitations to shifting that far are the 80 MHz range of δ_{satabs} , constrained by the current supply used to generate the saturation absorption magnetic field, and possible mode hops in the source laser if the frequency lock were to jump too far. Finally, we also shift δ_{satabs} to optimize imaging of one isotope in a mixture. Section 2.4 discusses some of the issues that arise when imaging mixtures.

2.1.2 Procedure for Trapping Mixtures of ^{87}Sr and ^{88}Sr

Because the blue beams that trap both ^{87}Sr and ^{88}Sr are derived from a single laser, we cannot capture the isotopes simultaneously. To do true simultaneous trapping would require a parallel set of blue beams optimized for the second isotope. Instead, we exploit a property of the energy level structure of strontium to trap ^{88}Sr atoms first and then hold those atoms in a magnetic trap while we accumulate ^{87}Sr . Afterwards, we pump atoms of both isotopes back from the magnetic trap and into the ground state for transfer into the second-stage red MOT.

Two in 10^5 atoms excited on the 461 nm transition will decay to the $(5s4d)^1D_2$ level [49] instead of to the $(5s^2)^1S_0$ ground state (Fig. 1.1). Subsequently, atoms

decay to either the $(5s5p)^3P_1$ or $(5s5p)^3P_2$ state. Atoms arriving in the $(5s5p)^3P_1$ state decay back to the ground state, but atoms in the $(5s5p)^3P_2$ state do not decay because the $(5s5p)^3P_2$ state is metastable and has a 9 min lifetime [55].

The $(5s5p)^3P_2$ state is dark to the MOT lasers in the experiment, meaning that atoms there are essentially unaffected by light-assisted loss processes that could limit the maximum number. Furthermore, atoms in low-field-seeking magnetic sub-levels can be trapped by the quadrupole magnetic field of the MOT coils (the magnetic trap) [50, 56] which, for our experiment, has a gradient of about 50 G/cm. Therefore, the longer that blue MOT trapping occurs, the larger the number of atoms that accumulates in the $(5s5p)^3P_2$ state. Ultimately, the number of magnetically trapped atoms is limited by the rate of loading and the 22 s trap lifetime (Fig. 2.6) of $(5s5p)^3P_2$ atoms, limited by background gas collisions and blackbody-radiation-induced transitions to states not trapped by the magnetic trap [57].

To create a return path to the ground state for atoms in the magnetic trap, we shine laser light (the “repumping beam”) tuned to the $(5s5p)^3P_2 - (5s4d)^3D_2$ transition. I will say much more about this transition in Chapter 3, but it takes up to 100 ms (Fig. 2.7) for magnetically trapped atoms to decay to the ground state, via the $(5s5p)^3P_1$ level, once they are excited to the $(5s4d)^3D_2$ state. Since applying the repumping laser for longer than about 60 ms results in losses due to light-assisted collisions, particularly for high density samples, we choose a repumping time of about 50 ms.

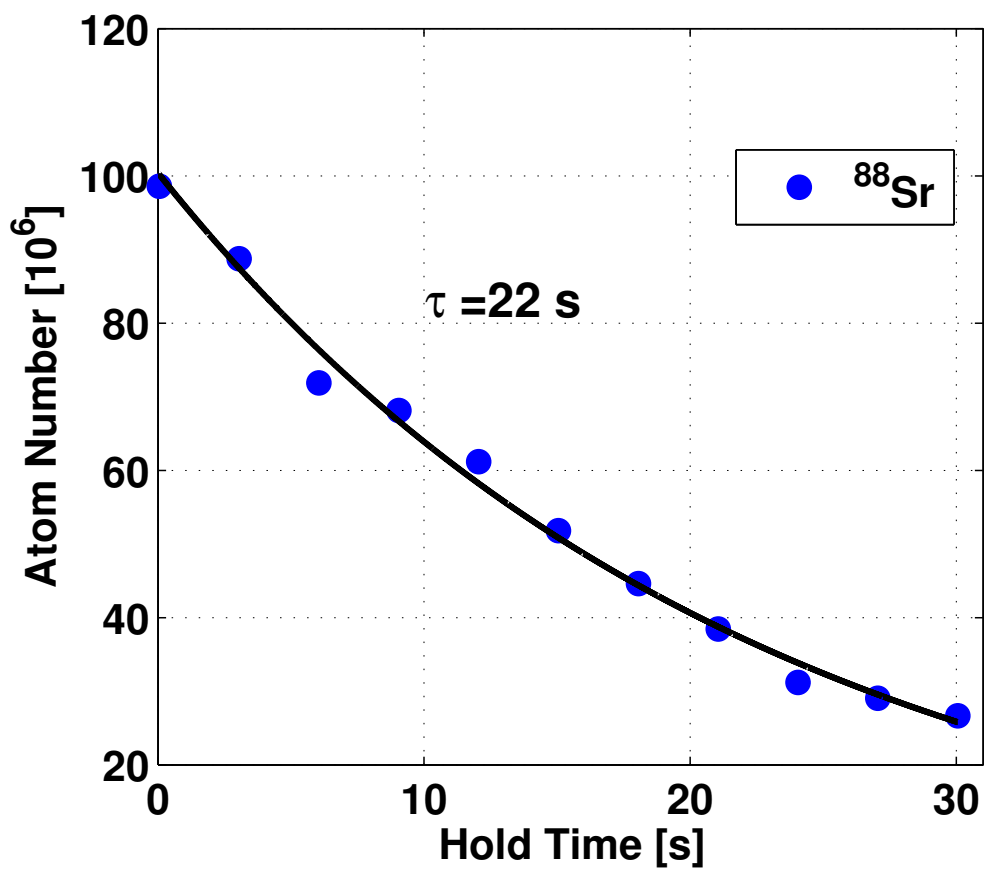


Figure 2.6 : A lifetime study of ^{88}Sr atoms in the $(5s5p)^3\text{P}_2$ state held in our magnetic trap. Atoms were loaded into the magnetic trap from the blue MOT for 1 s and the repumping laser was applied for 36 ms to return the trapped atoms to the ground state for imaging. The trap lifetime is about 22 s, with losses that are primarily due to background gas collisions.

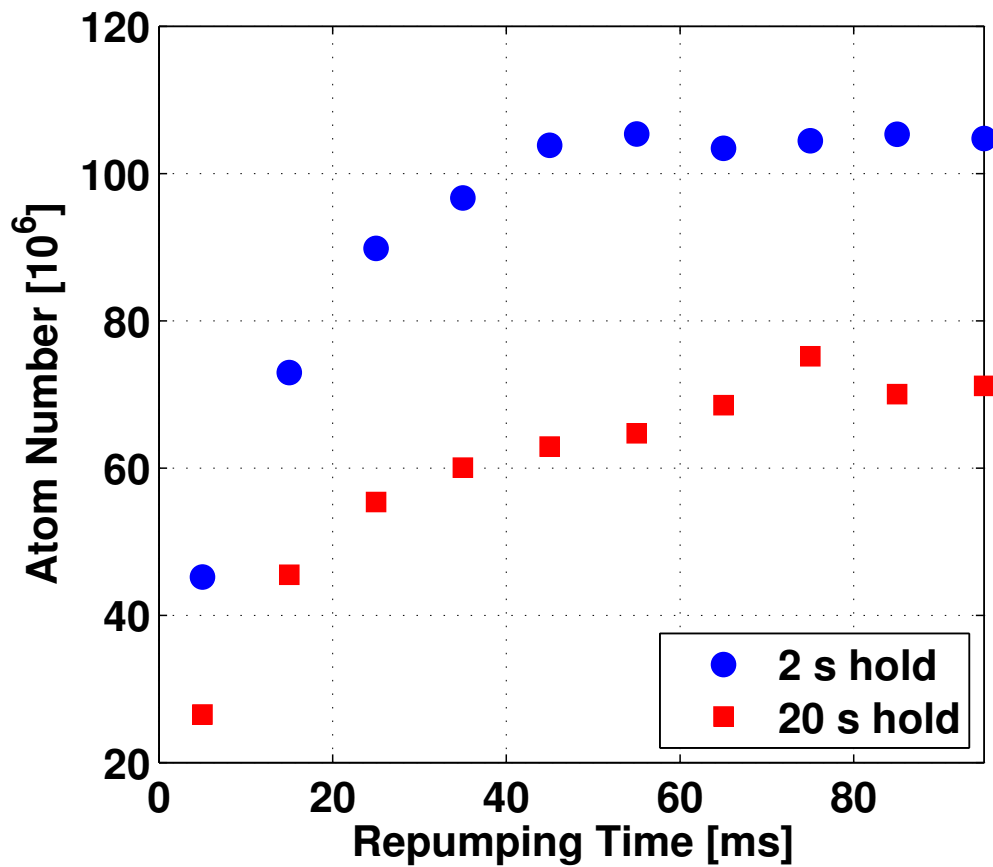


Figure 2.7 : A study of the amount of time needed to repump ^{88}Sr atoms from the magnetic trap to the ground state. Atoms are loaded into the magnetic trap from the blue MOT for 1 s and then held there before the repumping laser is applied for up to 100 ms. For high sample densities (2 s hold time), light-assisted collisions upon return to the ground state may be limiting the total number. For lower sample densities (20 s hold time), the efficiency continues increasing, but after about 50 ms, the increase is not substantial.

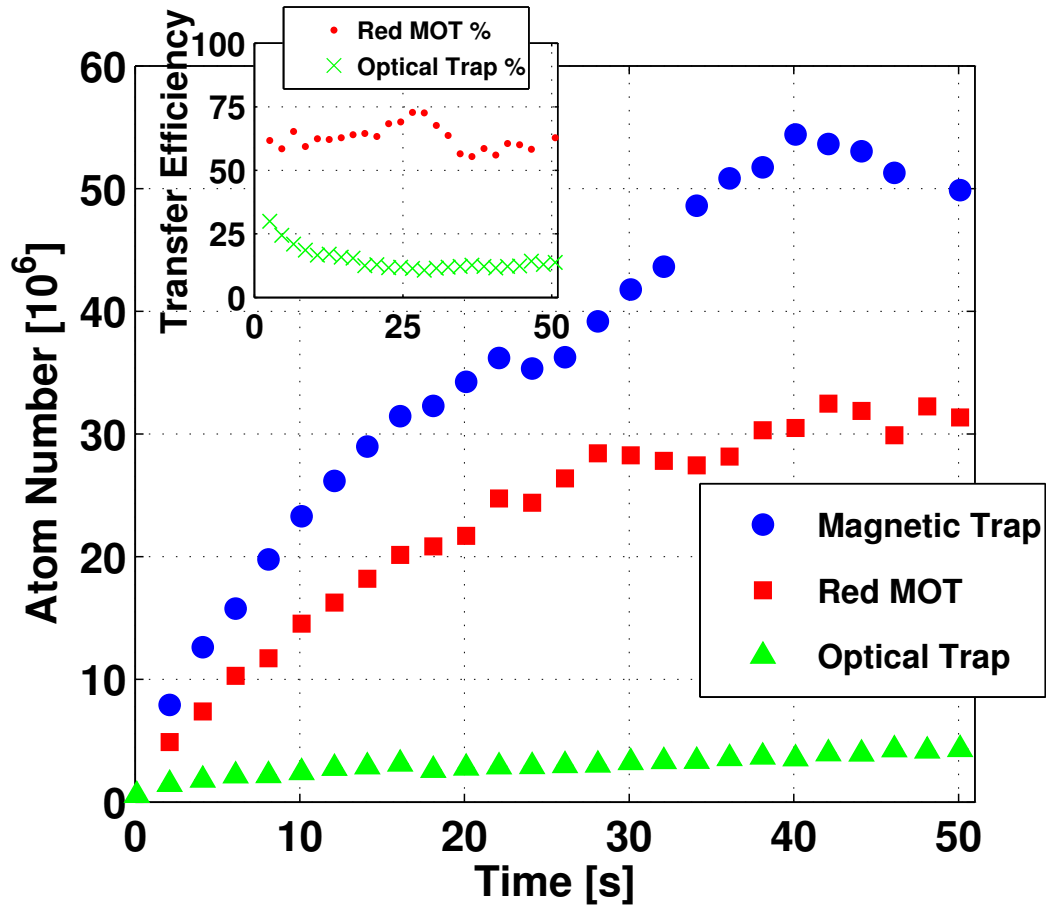


Figure 2.8 : A study of the number of ^{87}Sr atoms in the magnetic trap, red MOT, and optical trap as a function of the loading time. Atoms accumulate in the magnetic trap (blue circles) when the blue MOT and Zeeman slower beams are on, but the repumping laser is off. After an accumulation time that ranges from 100 ms to 50 s, the repumping laser is turned on for about 50 ms with an intensity of 3 W/cm^2 to enable a decay path to the ground state for atoms in the magnetic trap. We image the atoms via absorption imaging once they have returned to the ground state. Atoms in the red MOT (red squares) and the optical trap (green triangles) are shown in order to demonstrate the transfer efficiency for each stage of the process (inset). Transfer from the magnetic trap to the red MOT is $\sim 60\%$ and from the magnetic trap to the optical trap is $\sim 22\%$.

We also study the number of ^{87}Sr atoms as a function of loading time into the magnetic trap by imaging shortly after repumping occurs (Fig. 2.8). The magnetic trap number increases steadily for about 40 s of loading time before leveling off, perhaps due to losses induced by blackbody radiation [57] or background gas collisions. The same figure also shows the number of ^{87}Sr atoms in the red MOT and optical dipole trap as a function of the loading time. While the transfer efficiency of atoms (see inset of Fig. 2.8) into the red MOT seems to stay roughly constant for the entire range of loading time, the transfer efficiency to the optical dipole trap drops to about 22% in the first 20 s. There seem to be severe light-assisted collisional loss for ^{87}Sr on the 689 nm transition, so the transfer to the optical dipole trap is limited.

Accumulation of atoms in the magnetic trap enables experiments with mixtures of ^{87}Sr and ^{88}Sr . Figure 2.9 summarizes the timing for our experiments. First, we set $\delta_{satabs} = 30$ MHz so that the blue MOT beams capture ^{88}Sr atoms. We keep the blue MOT beams on for 3 s to load ^{88}Sr atoms into the magnetic trap. Then, we switch δ_{satabs} to -30 MHz and trap ^{87}Sr for 30 s (These load times are chosen to give us roughly equal numbers of the two isotopes at the beginning of evaporative cooling in the optical dipole trap). Near the end of the ^{87}Sr loading time, the repumping beam returns both ^{87}Sr and ^{88}Sr atoms to the ground state. Initially, the blue MOT beams are still on at the ^{87}Sr frequency to maximize the re-capture of ^{87}Sr atoms and to aid transfer to the red MOT. However, the ^{88}Sr resonance is only ~ 4 natural linewidths away, so re-capturing of ^{88}Sr also occurs. A typical number of re-captured atoms is

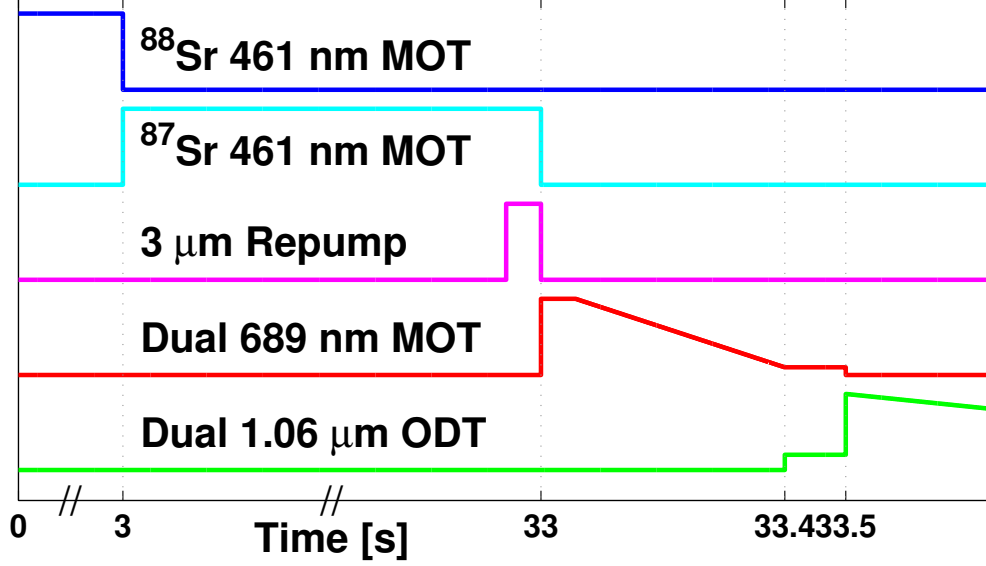


Figure 2.9 : Experimental timing for mixed species trapping.

about 11×10^6 for ^{88}Sr and 30×10^6 for ^{87}Sr atoms. Typical sample temperatures are a few mK for this stage of cooling. For experiments with only one isotope, we do not jump the value of δ_{satabs} and skip the loading phase for the other isotope.

2.2 Narrow Line MOT Operation for ^{87}Sr and ^{88}Sr

Unlike the 461 nm lasers which trap both isotopes, the 689 nm light for second-stage trapping (the red MOT) on the $(5s^2)^1S_0 - (5s5p)^3P_1$ transition is generated separately for ^{87}Sr and ^{88}Sr . In this section, I describe MOT trapping on a narrow line, present details of the lasers used for trapping ^{87}Sr in the red MOT, and then discuss the trade-offs necessary to run the two red MOTs simultaneously.

2.2.1 Red MOT Cooling of ^{87}Sr

To further cool ^{87}Sr , we implement a narrow line MOT for ^{87}Sr following a method outlined by Mukaiyama et al. [16]. I begin by outlining how and why this technique diverges from normal MOT operation.

The simplest MOT cooling schemes occur for $F \rightarrow F + 1$ transitions. In one dimension, incoming light, arriving parallel to the x axis (Fig. 2.10), delivers a momentum kick to atoms in the trap [48]. Using right (σ^+) and left (σ^-) circular polarized light, respectively, drives transitions to the $m_F = +1$ and $m_F = -1$ states. However, an atom at a position $x_0 > 0$ ($x_0 < 0$) needs to preferentially absorb light from the left (right) circularly polarized beam in order to be kicked towards the center of the trap. This asymmetric response is normally accomplished by exploiting the position-dependent Zeeman shift that atoms experience due to the inhomogeneous MOT magnetic field (as in Fig. 2.2(B)). The amount of the Zeeman splitting can be expressed as

$$hf(x) = \left((m_F + 1)\mu_e - m_F\mu_g \right) \frac{dB}{dx} x. \quad (2.5)$$

Here, μ_x are the Zeeman shift coefficients for the ground (g) and excited (e) states ($\mu_x = g_F\mu_B$, where μ_B is the Bohr magneton and $g_F = \frac{F(F+1)+J(J+1)-I(I+1)}{2F(F+1)}$). The Zeeman shifted levels of atoms at $x > 0$ ($x < 0$) and in the $m_F = -1$ ($m_F = +1$) state are more resonant with the σ^- (σ^+) light, thus creating the conditions necessary for preferential absorption. Because the Zeeman shift changes sign on each side of the trap center, if an atom crosses the center, it will begin to absorb photons from the

beam of opposite polarization and end up closer to the center of the MOT.

This picture works well as long as the splitting of the ground state levels is similar to the splitting of the excited state levels ($\mu_e \simeq \mu_g$), as is true for the $F = 0 \rightarrow F = 1$ transition shown in Fig. 2.2(B). However, things are more complicated when the ground state has a closed shell of electrons. Instead of an electronic contribution to the magnetic moment, there is only a nuclear spin contribution, leaving the excited states with a much larger relative magnetic moment ($\mu_e \gg \mu_g$) because they have an open shell of electrons. Then, the excited state splitting is significantly greater than the ground state splitting, and some transitions (e.g. $m_J = -1 \rightarrow m_J = -2$) are no longer red-detuned from the atomic transitions (Fig. 2.11). As a consequence, MOT trapping is ineffective as atoms are lost to the sub-levels in the ground state that are untrapped.

This limitation is overcome by exploiting the asymmetry of the Clebsch-Gordan (CG) coefficients for circularly polarized light [60]. Figure 2.12 shows the spin sub-levels and their relative strengths, under σ^+ light, for the $F = 9/2 \rightarrow F = 11/2$ transition that we use for red MOT trapping. The CG coefficients increase with increasing m_F number so that the $m_F = 9/2 \rightarrow m_F = 11/2$ transition is excited most strongly for σ^+ light. For σ^- light, everything is reversed so that the $m_F = -9/2 \rightarrow m_F = -11/2$ transition is strongest. Therefore, an atom at $x > 0$ and in the $m_F = -9/2$ stretch state absorbs much more strongly from the σ^- beam than the σ^+ beam.

This method works as long as atoms at a given position are in the m_F states

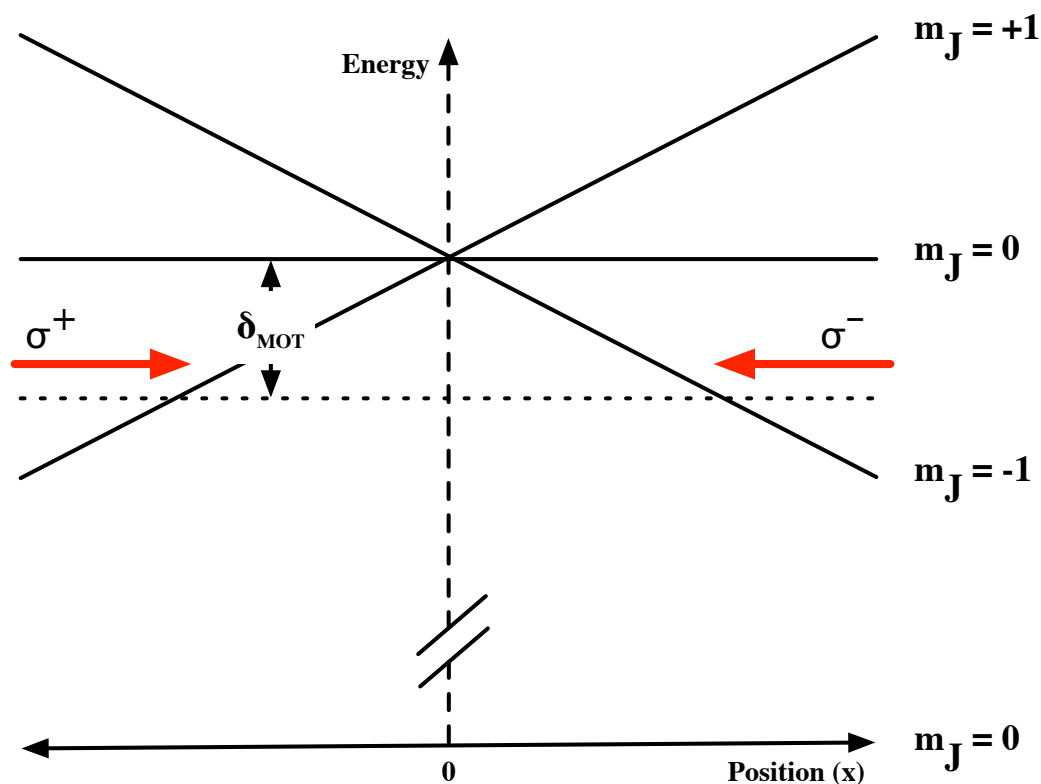


Figure 2.10 : One-dimensional MOT cooling for a $J = 0 \rightarrow J = 1$ transition. The position-dependent Zeeman splitting of the $m_J = \pm 1$ levels allows atoms to preferentially absorb circularly polarized light from the beam that will push them towards the center of the trap. The horizontal dashed line represents the detuning of the MOT lasers (δ_{MOT}) from the atomic resonance. Red-detuned light is necessary for cooling and compression to occur. Figure adapted from [58].

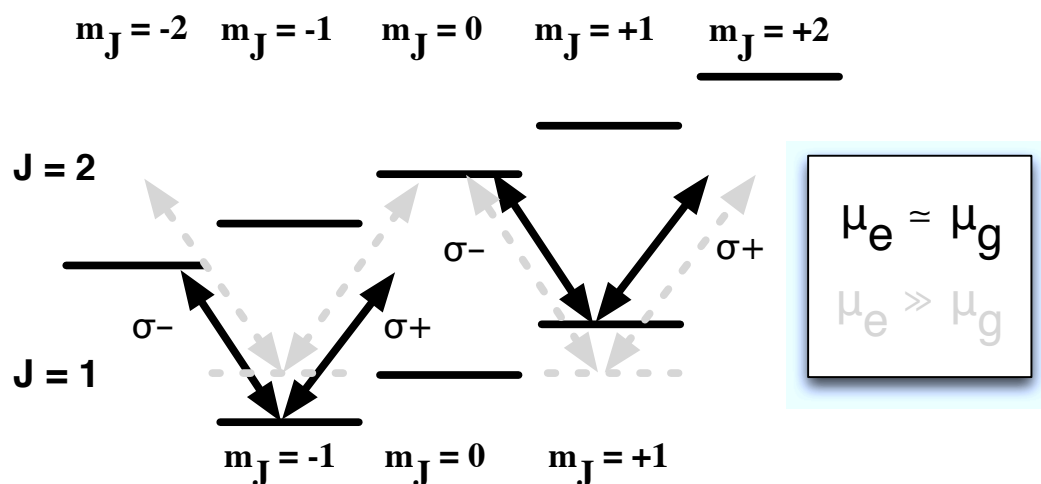


Figure 2.11 : Breakdown of MOT cooling for large excited state Zeeman shifts in atoms with degeneracy in their ground state. When the ground state Zeeman shift is on the order of the excited state shift, then trapping proceeds normally (dark arrows) because all beams are red-detuned from the excited state sub-levels. However, when the excited state Zeeman shift greatly exceeds the ground state shift (gray arrows and levels), some levels are no longer trapped because light is blue-detuned relative to those levels. Figure adapted from [59].

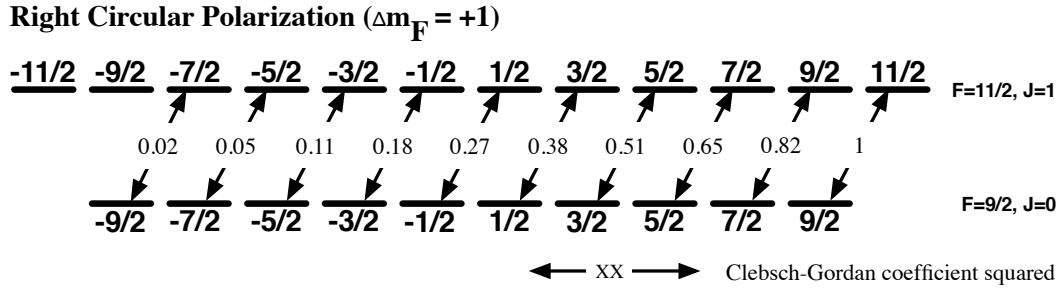


Figure 2.12 : Hyperfine structure, with magnetic sub-levels, for a $F = 9/2 \rightarrow F = 11/2$ transition like the 689 nm $(5s^2)^1S_0 - (5s5p)^3P_1$ transition of ^{87}Sr . The lower manifold of states is for the $(5s^2)^1S_0$ ground state ($J = 0$), while the upper manifold of states is for the $F = 11/2$ level of the $(5s5p)^3P_1$ excited state ($J = 1$). The arrows represent the allowed transitions for right circularly polarized light, and the relative strengths of the transitions are shown as the square of the Clebsch-Gordan (CG) coefficients. Right circularly polarized light, then, interacts with atoms in the $F = 9/2$ stretch state most strongly. For left circularly polarized light, everything is mirrored, with the strongest interaction occurring in the $F = -9/2$ stretch state. The asymmetry in the CG coefficients creates a restoring force for ^{87}Sr red MOT operation.

that absorb from the correct laser polarization. Nominally, the trapping laser will optically pump atoms towards the stretch states (as happens in the blue MOT), but the narrow line width of the 689 nm transition poses a problem. Even a few photon recoils can knock atoms out of resonance with the trapping lasers, making trapping ineffective because atoms end up in untrappable states. To overcome this problem, we introduce an additional laser (the “stir” laser) to randomize the populations of the m_F states. This laser is red-detuned a small amount from the $m_F = 9/2 \rightarrow m_F = 9/2$ transition and stirs the population to be more evenly distributed among the different spin states. The stirring of the population insures that the correct polarization of trapping light can interact with the atoms for more than a few photon recoils. The

stir laser light interacts with atoms for longer than the trapping light because the Zeeman shifts for the $F = 9/2 \rightarrow F = 9/2$ transitions are significantly smaller than for the $F = 9/2 \rightarrow F = 11/2$ transitions (the Landé g-factor for the $F = 9/2$ level is small). Therefore, the atoms stay on resonance longer and are efficiently mixed into m_F states that are suitable for trapping.

The laser beams used for trapping and stirring are generated from diode lasers in a master-slave configuration. The master laser is the frequency-stabilized and narrowed ^{88}Sr red laser, with a linewidth of about 50 kHz [61] that is locked to a saturation absorption cell as an absolute frequency reference [62]. AOMs, shown in Fig. 2.13, offset the frequency of the master laser for different uses in the experiment. The base frequency (f_L) is determined by the frequency of the shift AOM δ_{shift} . Unlike our blue saturated absorption technique, we do not vary the magnetic field to offset the frequency. The other difference for the red saturated absorption set-up is that the frequency of the pump and the probe beams is not the same. We express the frequency of the pump beam relative to the ^{88}Sr resonance as

$$f_L + \vec{k} \cdot \vec{v} = f_{atoms}, \quad (2.6)$$

and the frequency of the probe beam as

$$f_L + \delta_{shift} - \vec{k} \cdot \vec{v} = f_{atoms}, \quad (2.7)$$

where f_{atoms} is the resonance frequency of ^{88}Sr (f_{88}) that we lock to. Neither beam is directly on-resonance with the atoms, but the velocity class that the pump and probe

beams interact with is represented by $\vec{k} \cdot \vec{v}$. Thus, f_L is detuned from the atomic resonance by half of δ_{shift} . For trapping of ^{88}Sr atoms, one additional AOM sets the frequency of the red MOT beams:

$$f_{88trap} = f_L + \delta_{MOT}. \quad (2.8)$$

Reaching the $F = 9/2 \rightarrow F = 11/2$ transition used for trapping ^{87}Sr requires two AOMs (T1 and T2) because of the large shift from resonance (Fig. 1.4):

$$f_{87trap} = f_L + \delta_{T1} + \delta_{T2}. \quad (2.9)$$

Finally, the $F = 9/2 \rightarrow F = 9/2$ transition used to stir the atoms among the different spin sub-levels is:

$$f_{87stir} = f_L + \delta_{stir}. \quad (2.10)$$

These AOMs typically operate with the following frequencies: $\delta_{shift} = 180$ MHz, $\delta_{MOT} = -90$ MHz, $\delta_{T1} = -1251$ GHz, $\delta_{T2} = -80$ MHz, and $\delta_{stir} = 131$ MHz. These values lead to red MOT detunings for ^{88}Sr close (< 1 MHz) to the atomic resonance and trap and stir beam frequencies of $f_{87trap} = 1241$ MHz and $f_{87stir} = 222$ MHz, respectively.

Optimal trapping of ^{87}Sr (Fig. 2.14) by itself requires the trap and stir beams to be on for longer (~ 400 ms) total than the equivalent time for ^{88}Sr (~ 270 ms). During this time, we modulate the laser frequency to capture a larger range of velocities [14]. This frequency modulation is ramped down at a rate of 1.2 kHz/ms to cool the atoms trapped in the 689 nm MOT. We concurrently reduce the detuning of

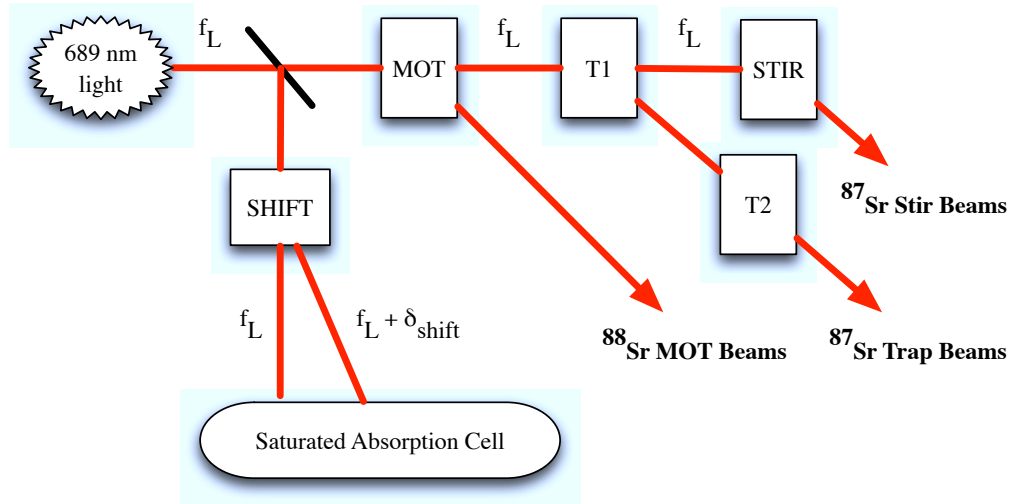


Figure 2.13 : Schematic showing the generation and frequency offset of 689 nm light for trapping and imaging of strontium isotopes. Bold labels indicate light that shines directly on the atoms and rectangles indicate acousto-optic modulators (AOMs) that shift frequencies in the system. As discussed in the text, the AOMs offset the frequency of the red laser light (f_L) for different uses in the experiment.

the stir and trap lasers from the $F = 9/2 \rightarrow F = 9/2$ and $F = 9/2 \rightarrow F = 11/2$ transitions, respectively, beginning around 1 MHz red-detuned and ending within 100 kHz red-detuned of the resonances. Finally, we also ramp the quadrupole magnetic field gradient up to 2 G/cm in 400 ms to compress the atom cloud, thus affecting its shape. We judge the quality of the red MOT by the number and temperature of atoms that are loaded in the trap, as well as the shape of the cloud. Colder sample temperatures and a smaller cloud size are essential for good transfer to the optical dipole trap.

Typical temperatures in the ^{87}Sr red MOT are about $9 \mu\text{K}$. We also note the transfer efficiency of ^{87}Sr red MOT atoms as a function of magnetic trap loading time

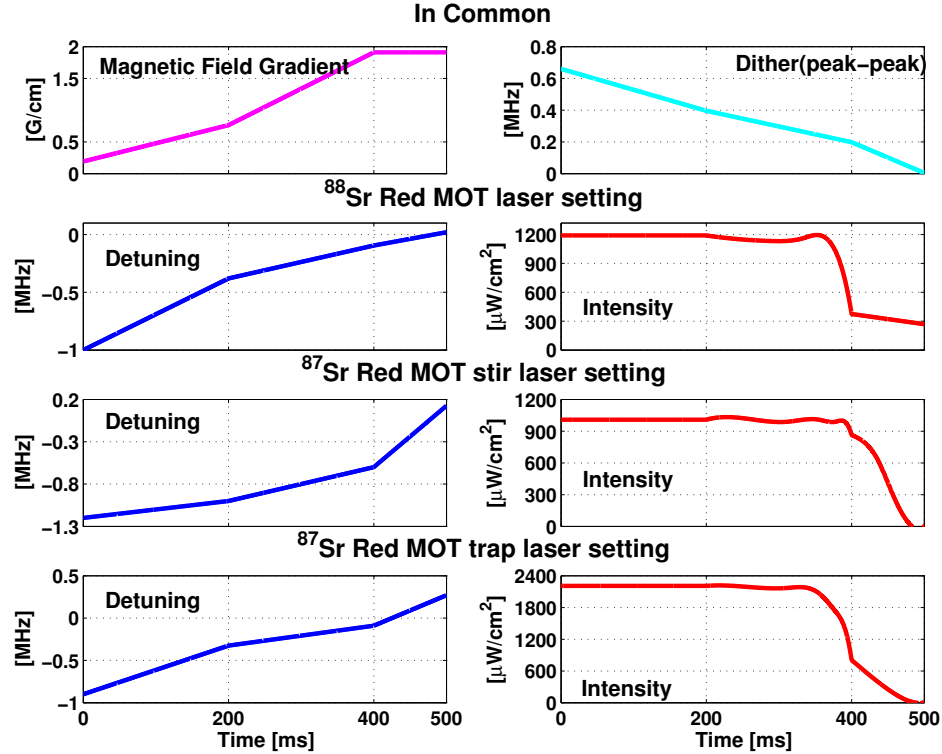


Figure 2.14 : Magnetic field ramps, laser detunings, and laser intensities for all lasers used in trapping ^{87}Sr and ^{88}Sr in the red MOT. The magnetic field ramp and the frequency dither (top row) are shared between ^{87}Sr and ^{88}Sr , while the lasers (rows 2-4) are operated independently of one another. Early in the transfer to the red MOT, the laser frequencies are broadened and the laser intensities are very high in order to maximize capture. Afterwards, captured atoms are compressed by increasing the magnetic field gradient and cooled via single frequency operation of the lasers in preparation for transfer to the optical dipole trap. The detuning of some of the red lasers become positive (blue of the transition) in the final 100 ms of ramping, which we would expect to cause atom loss. However, this 100 ms period is always the time during which atoms are transferred to the optical trap. As will be seen in the following section, the optical trap shifts the energy levels of the atoms. For our optical trap parameters, this AC Stark shift is enough to keep the atoms in the red MOT red-detuned from the 689 nm transition. Figure prepared by Mi Yan.

(recall Fig. 2.8). The loading efficiency stays fairly constant at $\sim 60\%$ which means that, for a typical 30 s load time, as many as $\sim 25 \times 10^6$ atoms are trapped by the red MOT.

To achieve simultaneous loading of the ^{87}Sr and ^{88}Sr red MOTs, we turn on the red MOT lasers for both isotopes at the same time. Because the linewidth of the intercombination line is only 7.4 kHz, the resonance frequencies are widely spaced from one another and the two red MOTs do not interfere with each other. When we trap only ^{88}Sr , the red MOT laser is on for ~ 220 ms, which optimizes the number and temperature of ^{88}Sr samples. However, because the lower number of ^{87}Sr atoms is the limiting factor in our experiments, we seek to avoid changing the ^{87}Sr parameters. Therefore, we re-optimize the ^{88}Sr red MOT parameters; the ramps for ^{87}Sr and ^{88}Sr trapping stay similar in character (Fig. 2.14) except for the optimal magnetic field gradient, which is about a factor of two higher for trapping ^{87}Sr than for trapping ^{88}Sr . The changes in the red MOT trapping parameters for ^{88}Sr result in about 75% fewer ^{88}Sr atoms, but there are still as many ^{88}Sr atoms as ^{87}Sr atoms and the temperature ($\sim 4 \mu\text{K}$) does not appear to have changed significantly.

The red MOT samples of ^{87}Sr and ^{88}Sr , then, are ready to load into the optical dipole trap. When conducting single isotope experiments, we simply leave out the intercombination-line lasers for the other isotope.

2.3 Optical Dipole Trap

Trapping of mixtures of ^{87}Sr and ^{88}Sr in an optical dipole trap is easier than in either the blue and red MOTs because optical dipole traps have the advantage of being able to trap any neutral atom with less regard for the precise frequency of the laser. I explain the underlying physics of optical dipole traps before describing our optical trap setup and its characterization.

2.3.1 Principles of Operation

The simplest dipole trap results from a single laser beam shone onto an atom. A dipole moment is induced in the atom by the electric field of the laser, and the interaction between the laser field and the dipole moment of the atom means the atom experiences a force proportional to the gradient of the Stark shift (“light shift”) of its energy levels:

$$F_{dipole} = -\frac{\delta(\Delta E)}{\delta r}. \quad (2.11)$$

The gradient is along r which, for the usual Gaussian mode and radial symmetry of a laser beam, is zero at the intensity maximum of the laser and increases as the intensity drops off. The energy levels move either towards or away from each other depending on the sign of the detuning of the light from the resonance frequencies of nearby atomic transitions, thus creating a potential that is proportional to the intensity of the laser:

$$U_{dipole}(r) \sim \frac{\Gamma}{\Delta} I(r). \quad (2.12)$$

Here, Γ is the spontaneous decay rate of a transition which is an amount Δ away from the laser frequency. Confinement also occurs in the direction of propagation of the optical trap laser if that laser is focused. In that dimension, the maximum of the intensity will be at the waist of the optical trap beam. For a single beam, however, the gradient tends to be much weaker longitudinally than radially, so the atom cloud elongates as the atoms take the shape of the trap. The sign of the detuning plays a role as well (Fig. 2.15): negatively detuned (red) detuned light moves the ground state energy down, so the trap becomes deeper. But for positively (blue) detuned light, the opposite occurs, creating an anti-trap where atoms are driven away from the intensity maximum. Equation 2.12 is the first of two expressions which encapsulate the key properties of an optical dipole trap. Essentially, it specifies how deep the trapping potential of the optical dipole trap will be for a given laser intensity and frequency.

Losses due to scattering are the second important parameter characterizing an optical dipole trap. Absorption, and subsequent emission, of light from the trap beam can heat atoms so that they are no longer trapped by the optical potential. The losses due to scattering are also a function of the optical trap laser intensity and detuning,

$$\Gamma_{scat}(r) \sim \left(\frac{\Gamma}{\Delta}\right)^2 I(r). \quad (2.13)$$

For an optical trap laser that is tuned on-resonance with an atomic transition ($\Delta = 0$), both the scattering rate and the trap depth diverge, but the heating rate due to scattering is really limited by the rate that atoms can cycle from the excited state to

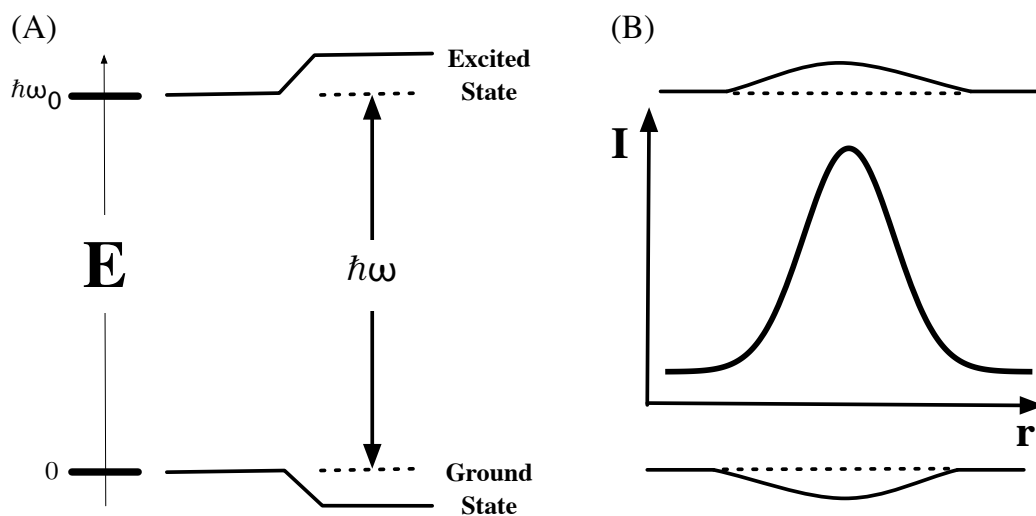


Figure 2.15 : Light shifts of energy levels under the influence of the electric field of an optical dipole trap laser. (A) The energy levels shift with respect to resonance. The shift is negative in the ground state and positive in the excited state, so trapping only occurs for the ground state atoms. (B) The shift is proportional to the intensity of the laser, so for a laser beam with a Gaussian profile (center), the maximum shift is at the center of the beam. Figure adapted from [63].

the ground state. The key difference from Eq. 2.12, however, is that $\Gamma_{scat} \sim 1/\Delta^2$, meaning that the rate of heating drops off more quickly with detuning than does the trap depth. As a consequence, trapping neutral atoms in an optical dipole trap is feasible because we can usually find a laser intensity and detuning for which the trap depth is deep enough, but for which the scattering rate is not too high. Finally, it is worth noting that squaring the detuning means that the loss rate is symmetric on each side of resonance, in stark contrast with the asymmetric behavior of Eq. 2.12.

For strontium, choosing a good wavelength for optically trapping atoms is not simple because there are transitions both red- and blue-detuned from any frequency we might select. Each transition contributes to the light shift and scattering for atoms in proportion to the spontaneous decay rate, Γ , which is proportional to the square of the dipole matrix element (oscillator strength) between the ground and excited states ($\Gamma \sim |\langle e|\mu|g \rangle|^2$). To find an appropriate wavelength, we calculate the aggregate light shifts and scattering rates by summing the contributions from many transitions in strontium (transition rates $\sim 10^5$). Figures 2.16 and 2.17 show the light shifts and scattering rate, respectively, as a function of frequency for a beam that has 1 W of power and 100 μm waists (see also Appendix A). The concentration of transitions between 400 and 700 nm leads to high ($\sim 0.1 \text{ s}^{-1}$) scattering rates, so a wavelength above 800 nm is more desirable for optical trapping. In our experiment, we use 1064 nm light for the optical dipole trap, so the $\sim 80 \text{ kHz}$ light shift for the $(5s^2)^1S_0$ ground state at 1064 nm corresponds to about 4 μK of trap depth (conversion $\sim 5\mu\text{K}/100$

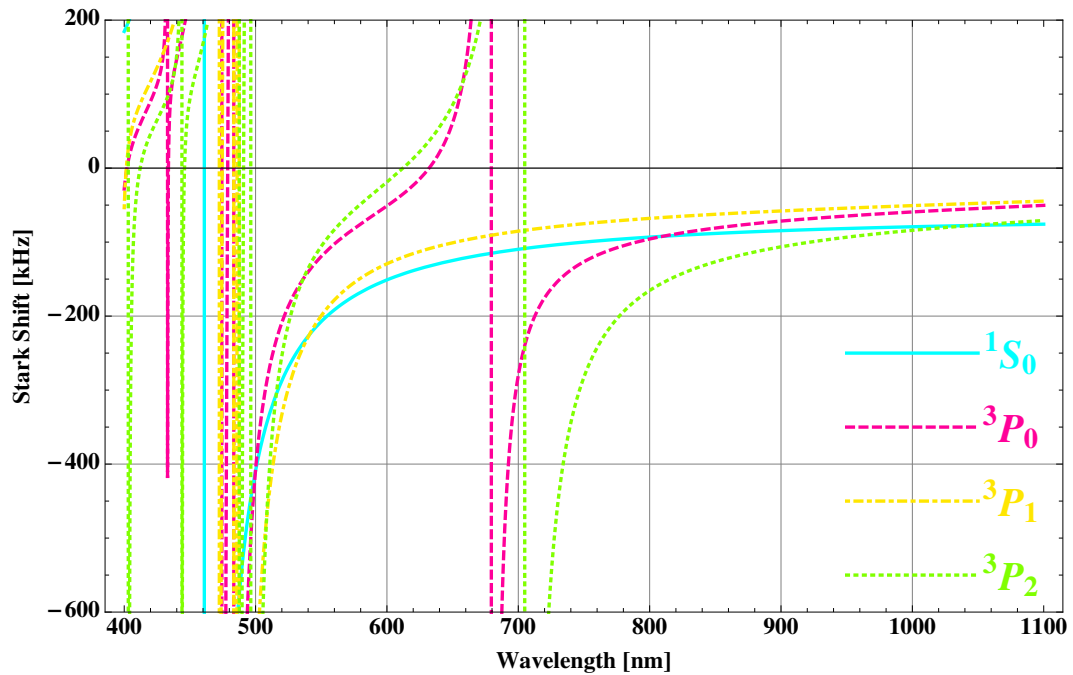


Figure 2.16 : Calculated light shifts as a function of wavelength for a 1 W beam with $100 \mu\text{m}$ waists. The total light shift is a sum of the oscillator strength contributions from many different transitions. We choose a good optical trap laser frequency by looking for a wavelength where the light shift is reasonable, but far enough from a resonance that the scattering rate is low. The optical dipole trap laser we use for our experiments is at 1064 nm. Light shifts are shown in units of kHz (A shift of 100 kHz corresponds to a trap depth of about $5 \mu\text{K}$).

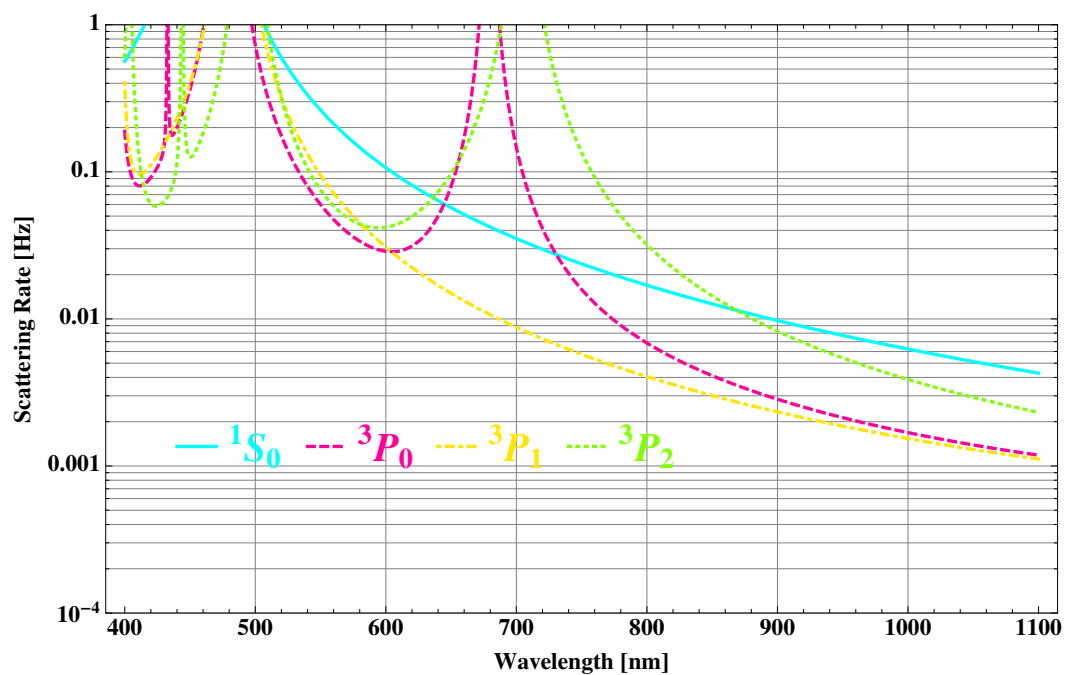


Figure 2.17 : Calculated scattering rates as a function of wavelength for a 1 W beam with $100 \mu\text{m}$ waists. The total scattering rate is a sum of the oscillator strength contributions from many different transitions. We cannot choose a good optical trap laser frequency if the scattering rate is too high (typically $\Gamma_{scat} \gg 0.1 \text{ s}^{-1}$). The optical dipole trap laser we use for our experiments is at 1064 nm.

kHz) for 1 W of light.

2.3.2 Characterization of the Optical Dipole Trap

The configuration we choose for our optical dipole trap is a crossed beam geometry as shown in Fig. 2.18. The source of the beam is a multimode fiber laser operating at 1064 nm with a maximum output power of 20 W. Figure 2.19 summarizes the power control and beam shaping that occurs before the beam goes into the chamber. Lens L1 collimates the beam, L2 focuses the beam so that it can pass through the AOM, L3 re-collimates the beam, and L4 focuses the beam to the $\sim 100 \mu\text{m}$ waist that the atoms see. Afterwards, the input beam is recycled to become the cross beam: lens L5 re-collimates the beam, and L6 focuses to the same $\sim 100 \mu\text{m}$ waist before falling on the atoms. Determination of the waists is one of the primary sources of uncertainty in our knowledge of the trap, and it may change the trap depth by up to 25%. Finally, both the input and cross beams enter the chamber at 10.5° from the horizontal which means that both beams must be overlapped for the trap to hold against gravity.

The AOM allows us to power control the optical dipole trap by monitoring the power level of the first order output beam and feeding back to the AOM to stabilize the power. Our maximum power is reduced from the laser's output of 20 W to about 11 W, limited by the diffraction efficiency of the AOM and the need to power control at a power level below the maximum. It is possible to vary the power quickly and precisely by changing the power control level, a necessary capability for evaporation

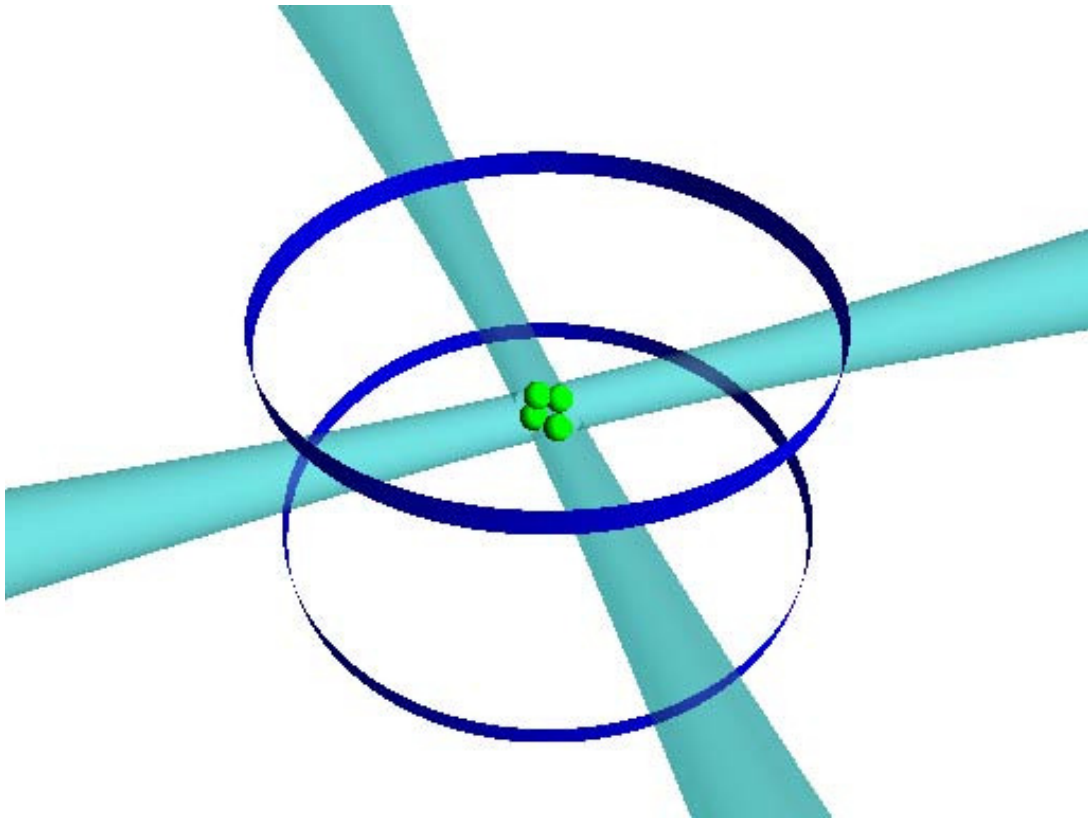


Figure 2.18 : An illustration of the optical dipole trap (ODT) formed by a 1064 nm laser. Atoms held in the optical trap can be evaporated to colder temperatures by reducing the intensity of the beams, thus ejecting the highest energy atoms.

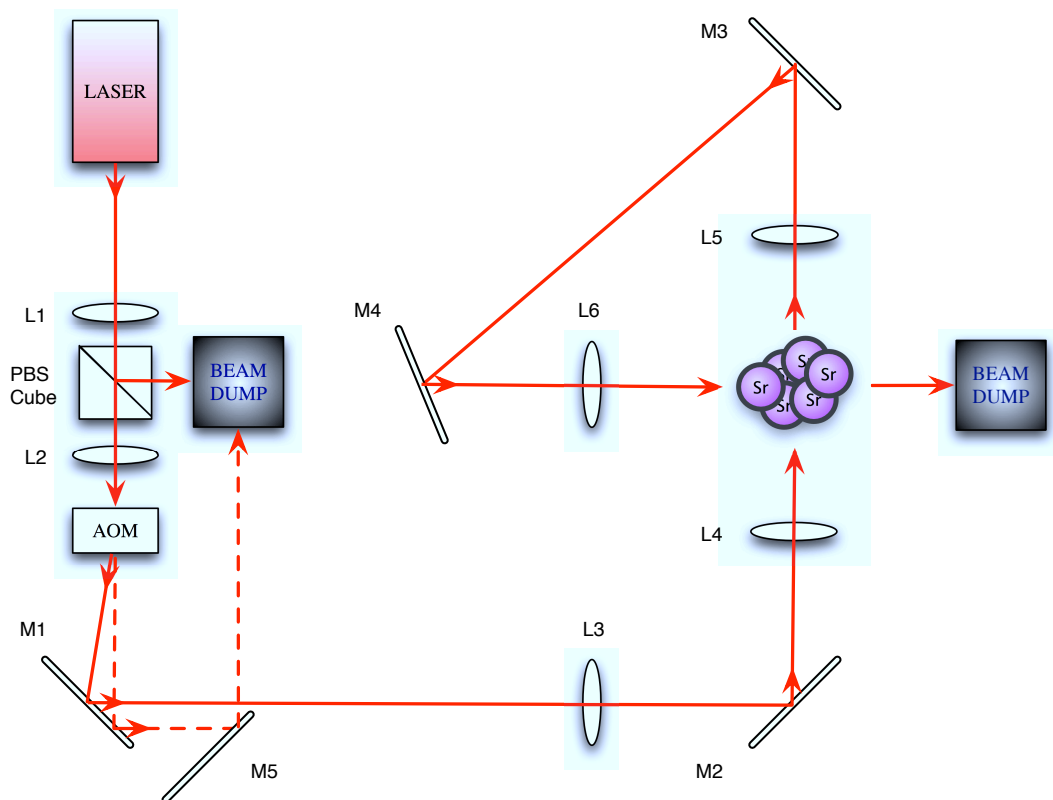


Figure 2.19 : A schematic of the AOMs and optics used to prepare the optical dipole trap beams. The label (L) represents lenses and (M) indicates mirrors. The polarizing beam splitter (PBS) cube splits off a small amount of horizontally polarized light that can be used for other purposes. The AOM is used to power control the beam at a maximum power of about 10 W. After the beam passes through the atoms once, it is recycled for use as the cross beam of the trap, which is about 10% weaker than the input beam.

experiments. For the evaporation experiments, the computer-controlled-voltage-to-power conversion is 0.98 W/V, with the maximum applied voltage being about 10 V. The computer-controlled voltage can also be modulated quickly, which aids in making measurements of the trap frequencies that I will discuss shortly. However, I first discuss preparing samples in the optical trap.

Loading atoms into the optical dipole trap is fairly straight-forward because typical optical trap depths in our experiment, expressed in temperature units, are on the order of 25 μK . For red MOT atoms that are as cold as 1 μK , transfer of atoms from the red MOT to the optical trap is primarily a matter of overlapping the red MOT and the optical trap so that atoms fall into the optical dipole trap potential. Figure 2.20 is an absorption image showing the overlap of the two traps. No quantitative information is extracted from this image because the optical depth is too high, but it is illustrative. Typically, 100 ms of overlap is allowed before turning off the red MOT beams (A) after which atoms that are not trapped by the optical trap fall away. The atoms seen in the individual arms of the optical trap (B) are not trapped. Rather, because of the 10.5 degree inclination of the beams, the longitudinal trapping force of the beams is only strong enough to hold against gravity in the region where the beams are overlapped. 100 ms after the red MOT beams have been extinguished (C), the untrapped atoms in the arms are nearly gone from the image, and at 150 ms after the red MOT is turned off (D), we have a symmetrically shaped trapped sample.

Loading atoms into the dipole trap works better from a shallower trap, typically

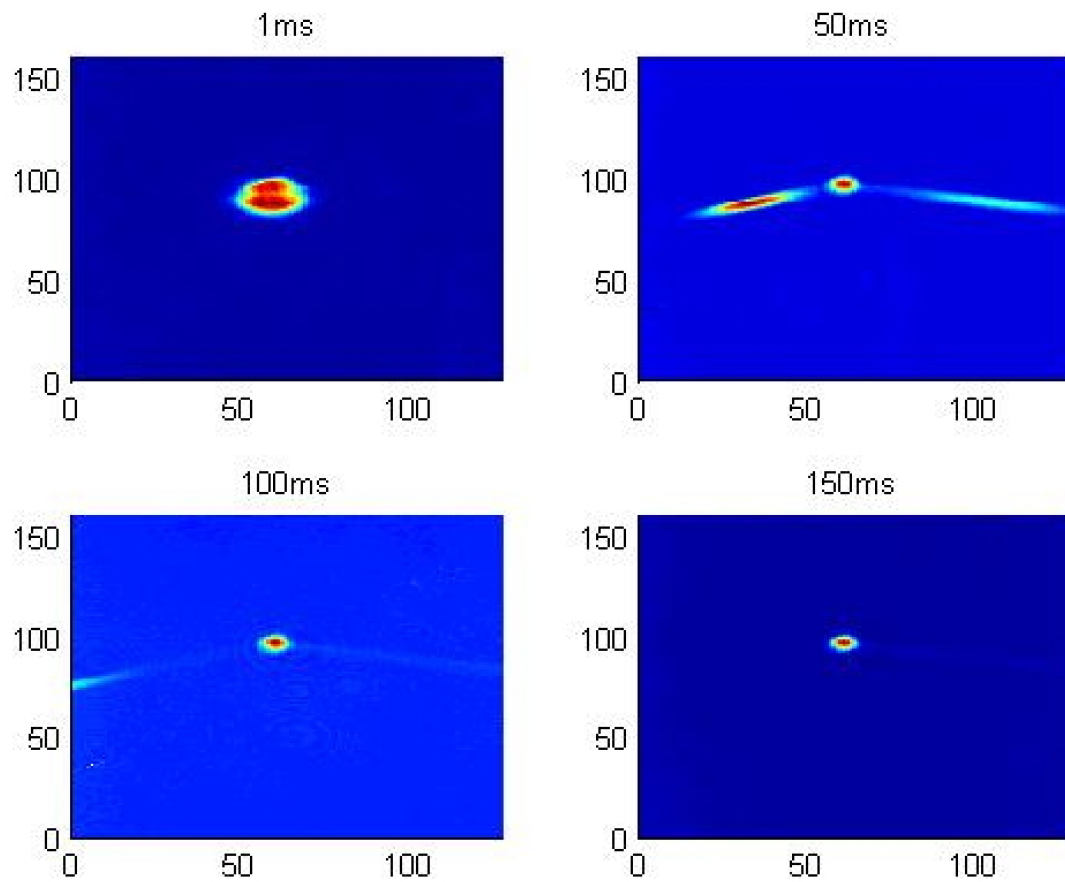


Figure 2.20 : A series of absorption images showing loading of atoms into the optical dipole trap from the red MOT. (A) Initially, the red MOT and the optical trap beams are all applied to the atoms together for 100 ms. (B) After the red MOT beams are turned off, atoms not trapped in the optical trap fall away along the arms of the ODT which are too weak longitudinally to hold against gravity. After enough time has passed (C and D), the atoms which remain are all trapped in the optical dipole trap.

with around 4 W of power in each beam. After the 100 ms overlap time with the red MOT, we ramp the power from 4 W to 7.5 W, corresponding to a final trap depth of about 25 μK , in about 30 ms. For this trap depth and 3 s (30 s) of magnetic trap accumulation of ^{88}Sr (^{87}Sr), we trap about equal numbers of each isotope (3×10^6), with a temperature of about 7 μK and a peak density of $2.5 \times 10^{13} \text{ cm}^{-3}$. Lifetimes in the optical trap are about 30 s (Fig. 2.21) and are thought to be limited by background gas collisions.

Finally, the trap frequencies of an optical dipole trap are its most important property. A harmonic potential, like our optical dipole trap, will have a characteristic frequency (ω_0) in each dimension, which can be determined by parametrically driving the system. In a classical picture, atoms receive a kick each time they reach the turning point at the edge of the trap if the driving frequency is in resonance with the trap frequency. Parametric excitation reveals resonances for the parametric frequency (ω_p),

$$\omega_p = \frac{2\omega_0}{n}, \quad (2.14)$$

with $n = 1, 2, \dots$ and can be observed by modulating the intensity of the optical trap or shaking the beam. The extra energy the atoms receive on-resonance induces heating and leads to loss of atoms from the trap.

We measured the trap frequencies using parametric excitation [64], where we vary the power control voltage to the optical dipole trap to modulate the trap depth. Both the temperature and the number loss show the trap frequencies, though the

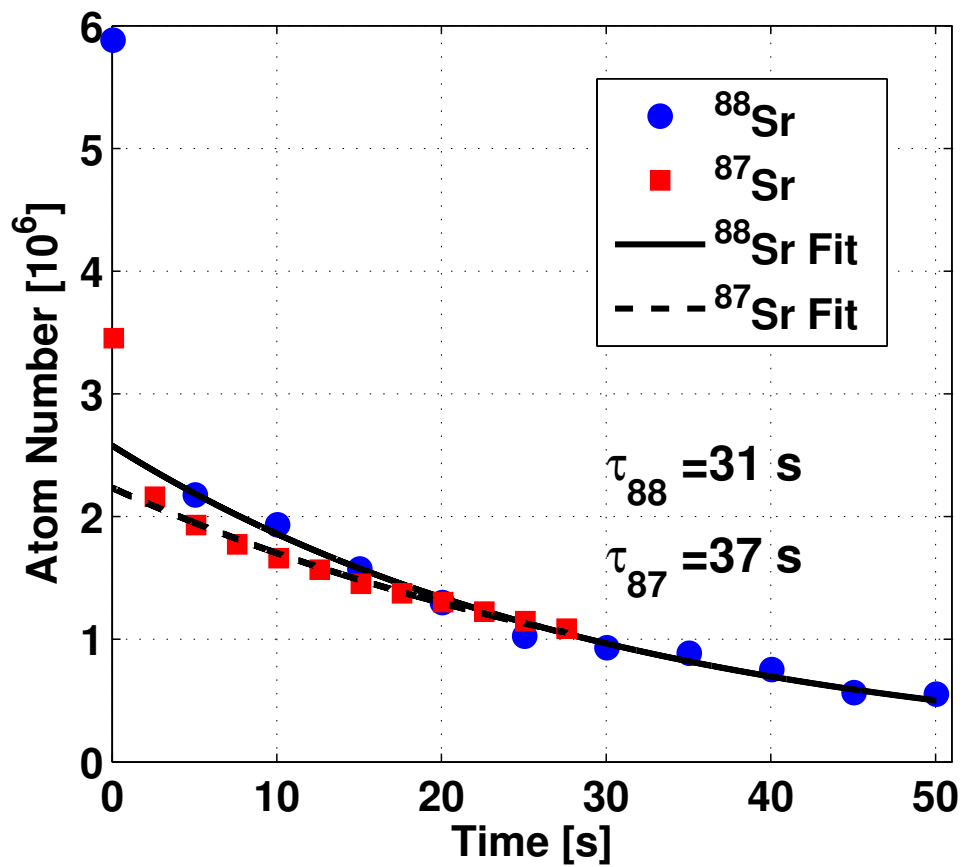


Figure 2.21 : Number of ⁸⁷Sr and ⁸⁸Sr atoms as a function of the time held in the optical dipole trap. The lifetime of samples for a 25 μK trap depth is on the order of 30 s.

temperature tends to be more sensitive because atoms heat up near a resonance even when they are not lost from the trap. Figure 2.22 shows the number of atoms and temperature as a function of the frequency at which we modulate the optical trap power. Data is shown for a shallow ($4 \mu\text{K}$) and a deep ($23 \mu\text{K}$) trap. For the $4 \mu\text{K}$ trap depth, we observe resonances corresponding to $n = 1$ at driving frequencies of about $\omega_x = \omega_z \approx 2\pi \times 160 \text{ Hz}$ and $\omega_y \approx 2\pi \times 230 \text{ Hz}$. Similarly, for a $23 \mu\text{K}$ trap depth, we observe resonances corresponding to $n = 1$ at driving frequencies of about $\omega_x = \omega_z \approx 2\pi \times 290 \text{ Hz}$ and $\omega_y \approx 2\pi \times 420 \text{ Hz}$. Some of the $n = 2$ resonances are also visible at half of the $n = 1$ frequencies: in the shallow trap, we see $\omega_x = \omega_z \approx 2\pi \times 70 \text{ Hz}$ and $\omega_y \approx 2\pi \times 110 \text{ Hz}$. In the deeper trap, we only see $\omega_y \approx 2\pi \times 210 \text{ Hz}$. The x and z axes may be more difficult to excite in a deeper trap, resulting in a weak or non-existent signal.

We can interpret our results in light of our trap geometry, which is very nearly spherical because of the crossed beams. The x and z frequencies should be similar because the x and z axes run parallel with each of the beams, which have nearly identical parameters. Indeed, that the number loss peaks are very broad (such as the $\sim 2\pi \times 290 \text{ Hz}$ peak in panel B of Fig. 2.22) suggests that this frequency is the resonance frequency of two axes. The y frequency, on the other hand, will have the highest value because it is the axis which is most tightly confined. However, as the trap depth is lowered, the y drive frequency will shift ($\Delta\omega_y = \omega_y[deep] - \omega_y[shallow]$) proportionally more than the x and z drive frequencies because the y potential has

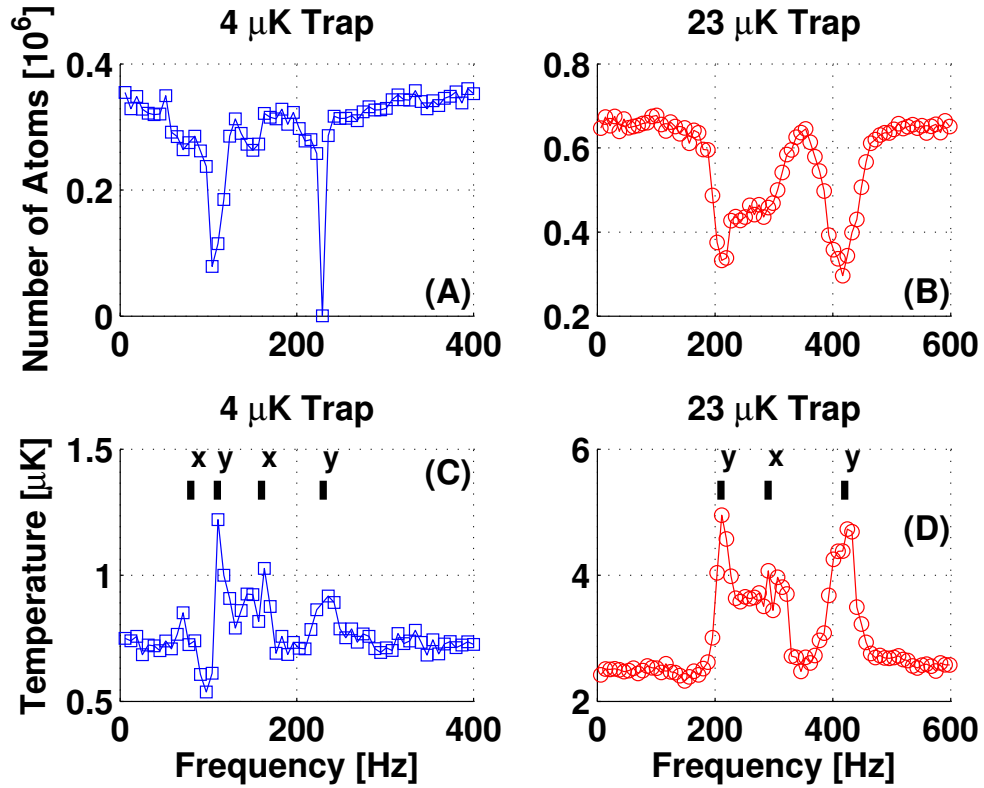


Figure 2.22 : Measurement of optical dipole trap frequencies using optical parametric oscillation of ^{87}Sr . The atom number (A and B) and temperature (C and D) for two different trap depths are shown as a function of the parametric drive frequency. The spherical trap geometry means the x and z trap frequencies will have similar values. The y axis is parallel with gravity, therefore as the trap depth becomes shallower, gravity starts to have a larger effect. Therefore, we expect the y frequencies to shift the most with changing trap depth. Dark lines in the temperature panels (C and D) mark where the drive frequencies appear. The label “ x ” represents both the x and z trap frequencies. This data constrains the possible values of the optical trap beam waists; we can interpolate to find the trap depth and trap frequency for any power of the optical trap beams.

a steeper gradient than the x or z potentials. The data support this interpretation, as $\Delta\omega_y \approx 2\pi \times 200$ Hz while $\Delta\omega_{x,z} \approx 2\pi \times 150$ Hz. Finally, returning to Eq. 2.14, we specify the trap frequencies (as opposed to the drive frequencies) in Table 2.1. One important note is that the trap changes in shape as well as in intensity when we reduce the trap depth. The resulting non-linear reduction of the trap depth means that, unlike in a magnetic trap, the frequencies do not scale as $U^{1/2}$ as one might expect for a linear harmonic potential.

Table 2.1 : Trap frequencies from parametric excitation measurement.

Trap Depth	ω_{0y}	ω_{0x}	ω_{0z}
4 μ K	$2\pi \times 115$ Hz	$2\pi \times 80$ Hz	$2\pi \times 80$ Hz
23 μ K	$2\pi \times 210$ Hz	$2\pi \times 145$ Hz	$2\pi \times 145$ Hz

Ultimately, the trap frequencies are one of the only independent measurements characterizing the trap. While we can profile the optical dipole trap beams outside of the MOT chamber, trap frequencies are the only direct measurement of the optical dipole trap characteristics in the chamber. The measured trap frequencies constrain the possible value of the waist, and the trap depth and trap frequency can be deduced for any optical trap beam power. We get information from these measurements about the optical dipole trap that allows for the subsequent calculation of sample densities or that serves as input to models of trap evaporation.

The optical dipole trap is truly the backbone of our experiments. Having a state-insensitive, low-loss trap in which to load atoms means we can trap and evaporate

mixtures of isotopes with a single laser.

2.4 Imaging Systematics

2.4.1 Imaging of Single Isotopes

Imaging mixtures of isotopes presents unique challenges compared to imaging single isotopes. Before presenting studies of multiple isotope imaging, I review absorption imaging and single isotope imaging.

Absorption imaging, a standard technique in atomic physics, is used to obtain parameters characterizing our cold atom samples: the number of atoms, the size of the atom cloud, the peak density, and the temperature are all determined from the optical depth (OD) of the atom cloud via absorption imaging. Laser light from the imaging beam, which is essentially resonant with the $461 \text{ nm } (5s^2)^1S_0 - (5s5p)^1P_1$ transition, is scattered off of atoms as the beam propagates through the sample. The scattering reduces the light intensity (I_0) according to Beer's law:

$$I(z) = I_0 e^{-OD(x,y)}, \quad (2.15)$$

where $OD(x, y)$, the “optical depth”, is the integral along z of the density distribution multiplied by the frequency-dependent absorption cross section, $\alpha(\nu)$:

$$OD(x, y) = \alpha(\nu) n_0 e^{-\frac{x^2}{2\sigma_x^2}} e^{-\frac{y^2}{2\sigma_y^2}} \int dz e^{-\frac{z^2}{2\sigma_z^2}}. \quad (2.16)$$

The OD is fit by a Gaussian distribution to obtain the number of atoms, N , and the size of the cloud (σ_i) in two dimensions. The third dimension, along which the

imaging occurs, is in the same plane as the horizontal MOT beams and perpendicular to the gravity axis. The size of the third dimension is estimated from the geometric mean of the sizes of the other two dimensions ($\sqrt{\sigma_x \sigma_y}$). Finally, using the number and the size yields an estimate for the peak density of the cloud,

$$n_0 = \frac{N}{(2\pi)^{3/2} \sigma_x \sigma_y \sigma_z}. \quad (2.17)$$

Determining the absorption cross section for ^{88}Sr is straight-forward because it has the same value irrespective of polarization. Due to the $J = 0$ value of the angular momentum in the ground state, atoms subjected to purely polarized light are effectively a two-level system (recall Fig. 2.2(B)). We calculate the value of the absorption cross section, α , using:

$$\alpha = \frac{3\lambda^2}{2\pi} (2J_u + 1) |\hat{\epsilon}_q \cdot \hat{\epsilon}|^2 \begin{pmatrix} J_u & 1 & J_\ell \\ -m_u & q & m_\ell \end{pmatrix}^2, \quad (2.18)$$

where J and m are the quantum numbers of the lower (ℓ) and upper (u) states, $\hat{\epsilon}$ is the light polarization vector, λ is the wavelength of the light, and $q = m_u - m_\ell$. For ^{88}Sr , the ground state has zero angular momentum ($J_\ell = m_\ell = 0$) while the upper states have $J_\ell = 1, m_\ell = 0, \pm 1$. Lastly, the matrix is the $3J$ symbol and can be calculated from the CG coefficients. Each polarization state of the light only drives a single transition and results in the same value of the peak absorption cross section (Table 2.2). Finally, we express the frequency-dependent expression for the ^{88}Sr cross section, proportional to $\alpha_0 = \frac{3\lambda^2}{2\pi}$, as:

$$\alpha_{88}(\nu) = \alpha_0 \times \frac{1}{1 + \frac{I}{I_{sat}} + 4\left(\frac{\Delta}{\Gamma}\right)^2}. \quad (2.19)$$

Table 2.2 : Result of calculating absorption cross sections for ^{88}Sr . Only three configurations have non-zero values of the absorption cross section. These correspond to linearly, right circularly, and left circularly polarized light, respectively.

Polarization	q	$\hat{\epsilon}$	m_u	3-J Symbol	α
π	0	\hat{z}	0	1/3	$3\lambda^2/(2\pi)$
σ^\pm	± 1	$\hat{\epsilon}_{\pm 1}$	± 1	1/3	$3\lambda^2/(2\pi)$

Here, Γ is the linewidth of the transition, $\Delta = \nu - \nu_0$ is the detuning from the atomic resonance frequency, and I_{sat} is the saturation intensity. The image beam intensity is very low compared to $I_{sat} = 42 \text{ mW/cm}^2$; we set the image beam on-resonance, meaning we always see the maximum absorption cross section. As such, determining the number of ^{88}Sr atoms is relatively simple.

Why ever is determining the ^{87}Sr number not as simple as ^{88}Sr ?. For ^{87}Sr , there are multiple ground state levels because of the nuclear spin ($I = 9/2$). Two things occur as a consequence: 1) multiple decay paths exist from a single excited state level, and 2) multiple transitions are driven by a single polarization of light. The net effect is that the atom population is distributed over more ground state levels. Knowledge of this distribution is necessary to determine the absorption cross section of ^{87}Sr . To correctly count the number of ^{87}Sr atoms, we calculate both the excitation rate from a ground state level,

$$R_{m_\ell \rightarrow m_\ell + q}^{F_\ell - F_u} = \frac{I}{I_{sat}} \frac{\Gamma}{2} (2F_u + 1) |\hat{\epsilon}_q \cdot \hat{\epsilon}|^2 \begin{pmatrix} F_u & 1 & F_\ell \\ -(m_\ell + q) & q & m_\ell \end{pmatrix} \frac{1}{1 + \frac{I}{I_{sat}} + (2\Delta/\Gamma)^2}, \quad (2.20)$$

and the decay rate from excited state levels,

$$R_{m_u \rightarrow m_u - q}^{F_u - F_\ell} = \Gamma_0(2F_u + 1) \begin{pmatrix} F_u & 1 & F_\ell \\ -m_u & q & (m_u - q) \end{pmatrix}. \quad (2.21)$$

Here, F and m are the quantum numbers for the lower (ℓ) and upper (u) states, and Γ_0 is the sum of the decay rates due to all three polarizations. We can use these rates to model the population dynamics (Appendix B) as a function of time for a sample of ^{87}Sr atoms.

What we want from this model is a simulation of the imaging of ^{87}Sr : when the image beam is applied to the atoms, what happens to the initial population distribution? Experimentally, we use linearly polarized light, but we do not know the initial distribution of the atom population among the spin states of ^{87}Sr , nor do we know how quickly the atom population is pumped during the 40 - 100 μs that the image beam is on. Therefore, what is the uncertainty in measuring the number of ^{87}Sr atoms?

To answer the first question, we take an evenly distributed population of ^{87}Sr (Fig. 2.23) and compare its dynamics with a population beginning in a single spin state of ^{87}Sr (Fig. 2.24). For these simulations, we take the image beam frequency to be on-resonance with the $F = 9/2 \rightarrow F = 11/2$ transition (though the model also accounts for the effect on the population of the $F = 9/2 \rightarrow F = 9/2$ transition), and the light intensity is set to 2% of the saturation intensity. The relative population of the negative-valued m_F sub-levels is shown as a function of the time that the

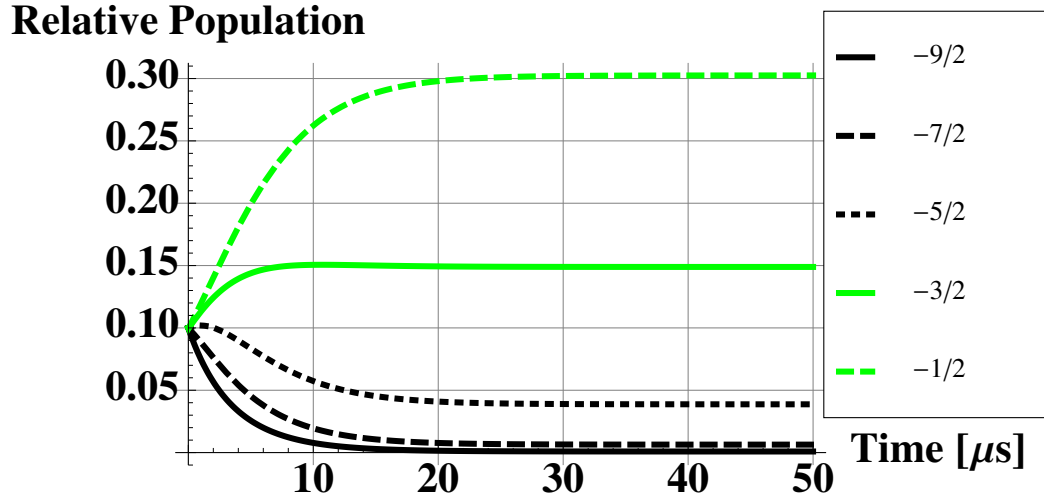


Figure 2.23 : Population dynamics of ^{87}Sr atoms under application of the linearly polarized image beam with $I = 0.02I_{sat}$. The beam is on-resonance with the $F = 9/2 \rightarrow F = 11/2$ transition and optically pumps atoms towards the levels having the strongest CG coefficients. The initial population is distributed evenly between the sub-levels of the ground state. After about $30 \mu\text{s}$ of optical pumping, an equilibrium is reached where no single level contains more than about 30% of the atoms in the sample.

image beam is applied (the positive-valued m_F sub-levels mirror the behavior of the negative-valued ones). After about $30 \mu\text{s}$ of optical pumping with linearly polarized light, the population reaches equilibrium in both cases, with more population in the low-valued m_F sub-levels.

We can understand the equilibrium populations in Figs. 2.23 and 2.24 in light of the decay paths from the $F = 9/2$ and $F = 11/2$ excited states to the $F = 9/2$ ground state (Figs. 2.12 and 2.25). For linearly polarized light, atoms will be excited on any

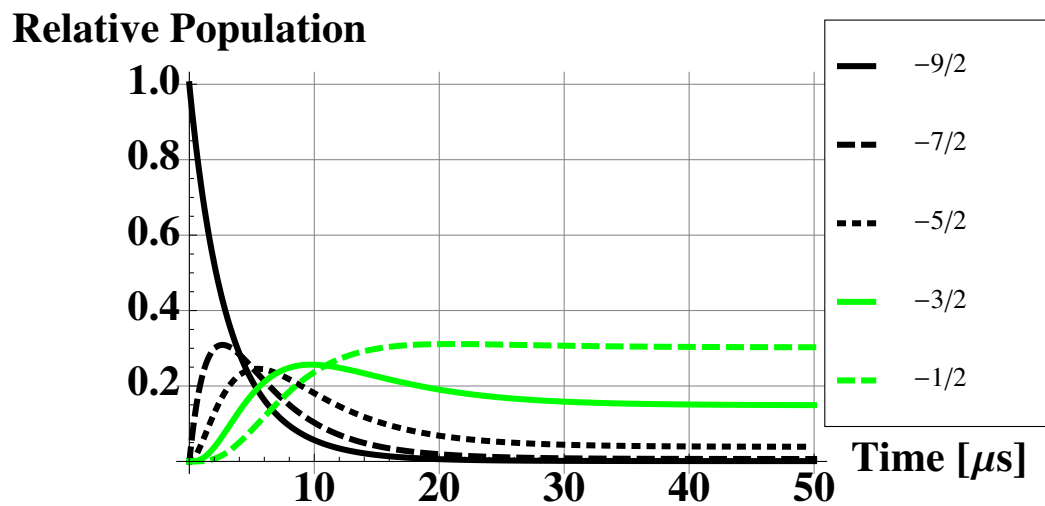


Figure 2.24 : Population dynamics of ^{87}Sr atoms under application of the linearly polarized image beam with $I = 0.02I_{sat}$. The beam is on-resonance with the $F = 9/2 \rightarrow F = 11/2$ transition and optically pumps atoms towards the levels having the strongest CG coefficients. The population is initially polarized in one sub-level, but mixes within about $30 \mu\text{s}$ and ends up distributed similarly to the initially unpolarized population shown in Fig. 2.23.

$\Delta m_F = 0$ transition provided the atoms are aligned with the axis of the magnetic field. From the excited states, decay is possible via any $\Delta m_F = 0, \pm 1$ transition. Because the CG coefficients for the decay favor transitions to smaller $|m_F|$ (Figs. 2.12 and 2.25(A)), atoms will be optically pumped inwards towards the levels with smaller $|m_F|$ values. Though the $F = 9/2 \rightarrow F = 9/2$ transition (Fig. 2.25(B)) has the opposite symmetry (pumping to higher m sub-levels), the 30 MHz detuning of the image beam frequency from the $F = 9/2$ level (it is directly on-resonance with the $F = 11/2$ level), reduces its contribution to the equilibrium population distribution. Our simulation faithfully reflects this conclusion, with nearly 30% of the equilibrium population in the $m_F = -1/2$ state, $\sim 15\%$ in the $m_F = -3/2$ state, and so on. Nor does it matter, in terms of the equilibrium populations, what the initial population distribution is: both Figs. 2.23 and 2.24 show similar final populations.

Given that the atom population is distributed over multiple sub-levels, we desire an answer to the second question asked above: what is the uncertainty in the number of ^{87}Sr atoms that we measure? Because the amount of absorption changes with the population distribution, we introduce an effective cross section (α_{eff}), which is essentially the total excitation rate to the $F = 9/2$ and $F = 11/2$ manifolds weighted by the population in each of the ground state sub-levels:

$$R_{obs} = \sum_{m_\ell} \left\{ n_{m_\ell} \sum_{q=-1}^q [R_{m_\ell \rightarrow m_\ell+q}^{F_\ell-F_{u1}} + R_{m_\ell \rightarrow m_\ell+q}^{F_\ell-F_{u2}}] \right\} = n_{total} \cdot n_{photon} \cdot \alpha_{eff} \cdot \nu_{photon}. \quad (2.22)$$

Here, R_{obs} is the observed excitation rate, and n_{photon} and ν_{photon} are functions of the imaging beam intensity. The effective cross section is reduced by the population

Linear Polarization ($\Delta m_F = 0$)

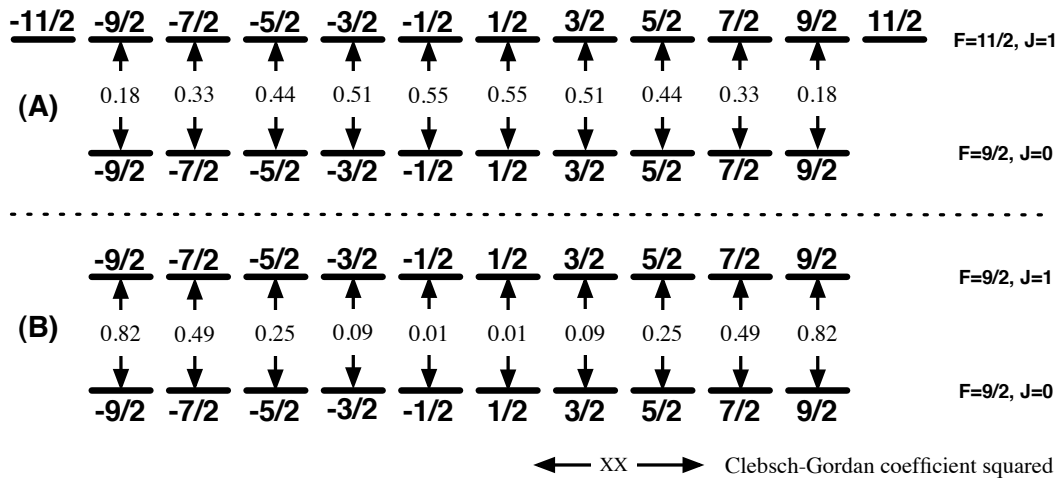


Figure 2.25 : Energy level structure, with magnetic sub-levels, for the $F = 9/2 \rightarrow F = 11/2$ (A) and $F = 9/2 \rightarrow F = 9/2$ (B) transitions. The arrows represent the allowed transitions for linearly polarized light, such as that of the imaging beam, and the relative strengths of the transitions are shown as the square of the CG coefficients. Because of the strength of the CG coefficients and the fact that the imaging beam is on-resonance with the $F = 9/2 \rightarrow F = 11/2$ transition, we expect more atoms will end up in the $m_F = \pm 1/2$ ground states.

distribution compared to the maximum cross section α_0 . In Fig. 2.26, we examine the ratio of the effective absorption cross section to the peak absorption cross section, ($\frac{\alpha}{\alpha_0} = \frac{\alpha}{3\lambda^2/(2\pi)}$). The ratio is shown for the same amount of imaging time as Figs. 2.23 and 2.24, and shows the ratio for both polarized and unpolarized atom populations. During the time that the population is in flux ($t < 30\mu s$), the ratio of the effective cross section to the maximum cross section is changing. Once the population is stable, however, then the ratio is constant at about $\alpha_{eff}/\alpha_0 = 0.52$. For a sample that initially has all atoms in one state, the ratio varies between 0.35 and 0.52. For a sample with a more evenly distributed population, the ratio only varies between 0.46 and 0.52. Our samples of ^{87}Sr usually begin fairly evenly distributed between spin levels, but even in the extreme situation where all the atoms are initially in a single state, the effective cross section will only be off by about 20% during the first 30 μs of imaging. We use this model to approximately account for the population distribution of ^{87}Sr atoms in determining the atom number:

$$\alpha_{87}(\nu) = \alpha_{eff} \times \frac{1}{1 + \frac{I}{I_{sat}} + 4(\frac{\Delta}{\Gamma})^2} \approx 2 \times \alpha_0 \times \frac{1}{1 + \frac{I}{I_{sat}} + 4(\frac{\Delta}{\Gamma})^2}. \quad (2.23)$$

Therefore, when we extract the number of ^{87}Sr atoms, we include this extra factor of two.

Because of the different peak absorption cross sections for ^{87}Sr and ^{88}Sr , we have two imaging protocols. The “88” protocol assumes the value of α is $3\lambda^2/(2\pi)$, per Eq. 2.19. Furthermore, the detuning of the image beam is set to the optimal value for imaging ^{88}Sr . Conversely, the “87” protocol assumes $\alpha = 2 \times 3\lambda^2/(2\pi)$, per Eq. 2.23

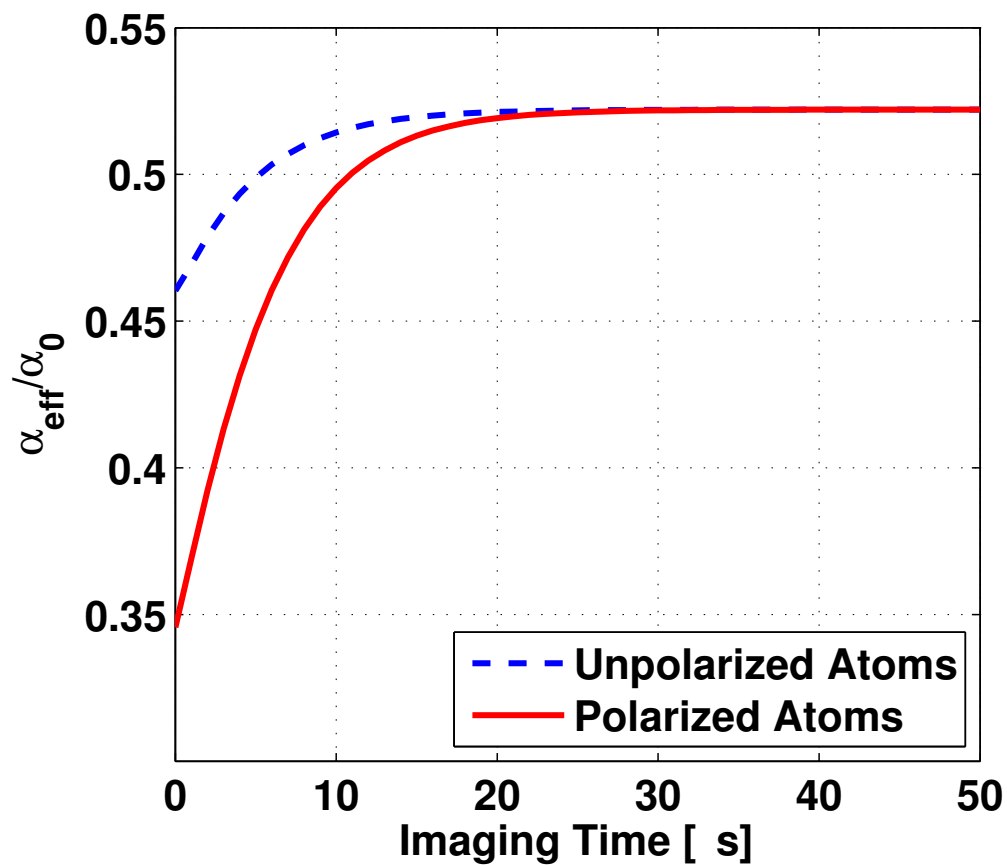


Figure 2.26 : Ratio of effective absorption cross section (α_{eff}) to peak absorption cross section (α_0) for unpolarized and polarized atoms. After about $30 \mu\text{s}$ of optical pumping with linearly polarized light, the population reaches a steady state. The effective cross section at this point for ^{87}Sr atoms is half the value for ^{88}Sr atoms.

(to account for the differences in absorption) and the image beam detuning is set to be optimal for imaging of ^{87}Sr . The desired frequency is shifted by changing δ_{shift} , just as we do to jump the blue MOT laser frequency during the magnetic trapping phase (section 2.1.1). Using the correct protocol to image the isotope being trapped yields an accurate measurement of the number of atoms.

Meanwhile, the temperature of the sample is obtained by observing the velocity of the atoms. After the sample is prepared, all lasers and fields are turned off and the sample falls under the influence of gravity. The change in the root mean square (RMS) size of the atom cloud during the time it is dropped (t_{drop}) determines the average total kinetic energy per atom ($m\bar{v}^2/2$), and setting this equal to the average total energy of an ideal gas ($3k_B T/2$), we get:

$$\frac{1}{2}m\bar{v}^2 = \frac{3}{2}k_B T. \quad (2.24)$$

Here, k_B is Boltzmann's constant, T is the temperature, m is the mass of an atom, and \bar{v} is the RMS velocity distribution of the atoms. Following the equipartition theorem and dividing the total energy between the three axes ($k_B T/2$ per axis), we get:

$$\frac{1}{2}m\left(\frac{\sigma_i}{t_{drop}}\right)^2 = \frac{1}{2}k_B T_i, \quad (2.25)$$

which, reduced and rearranged, yields the temperature in each axis,

$$T_i = \frac{m\sigma_i^2}{k_B t_{drop}^2}. \quad (2.26)$$

This procedure overestimates the change in the size of the sample, and hence the

temperature, because it assumes that the initial size of the cloud is negligible. This approximation only fails for short drop times before the size of the cloud significantly exceeds the initial size. However, because the OD usually remains too high ($OD > 1$) at these short times to accurately count atoms in the sample, we typically drop for longer times anyway. One additional note: the imaging procedure is the same irrespective of whether the sample is in the blue MOT, red MOT, or optical dipole trap. The only significant variation is allowing longer drop times for especially dense samples ($OD > 1$) which occur most frequently in the final stage of optical trapping.

2.4.2 Imaging of Mixtures

While imaging single isotopes is familiar to the Killian lab, imaging of mixtures is a new area. Therefore, we conducted a series of studies to learn about how introducing mixtures changes the imaging process. First, we examine what happens to the sample number and temperature when we try to take two, sequential images of the atoms; this approach could be a strategy for imaging both isotopes in a mixture. Second, we measure the degree to which one isotope “contaminates” images of the other isotope. Finally, I discuss how to mitigate the contamination that we find.

The ideal result of imaging mixtures would be an image, for each component of the mixture, that accurately reflects the number of atoms in the sample and the size of the atom cloud. However, because it is not possible to image both isotopes simultaneously, one image must be taken before the other. If the interaction of the image beam with

the sample during the first image affects the number and temperature of the other isotope in the mixture, then such a method is not feasible.

This scheme is potentially realizable with the camera we normally use for absorption imaging because the camera offers the ability to take two images closely spaced in time. For single isotope imaging, the first of these images is an image of the atoms, and the second is a background image, taken after the atoms have fallen from the trap. Typically, the image beam frequency is the same for both images, and subtracting the background image from the atoms' image results in a clear absorption image of the atom cloud. This kind of image is what we see in the panels of Fig. 2.20.

If, instead, we shorten the time between the images so that the atoms have not yet fallen from the trap for the second image, we can capture two closely spaced images of the sample. Figure 2.27 shows the timing for such an experiment for a sample of ^{87}Sr trapped by itself (panel A) and for a sample of ^{88}Sr trapped by itself (panel B). The first application of the image beam perturbs the sample, while the second application of the image beam probes the effect of the first image beam on the sample number and temperature. To count the number of atoms as accurately as possible, the probing beam always uses the “87” protocol for ^{87}Sr samples and the “88” protocol for ^{88}Sr samples.

The first image beam (“image 1”) can be set to either the “87” or the “88” protocol in order to see the effect of that protocol on the atom sample. Figure 2.28 shows the results of such a procedure. For ^{87}Sr (A and C) and ^{88}Sr (B and D), the number

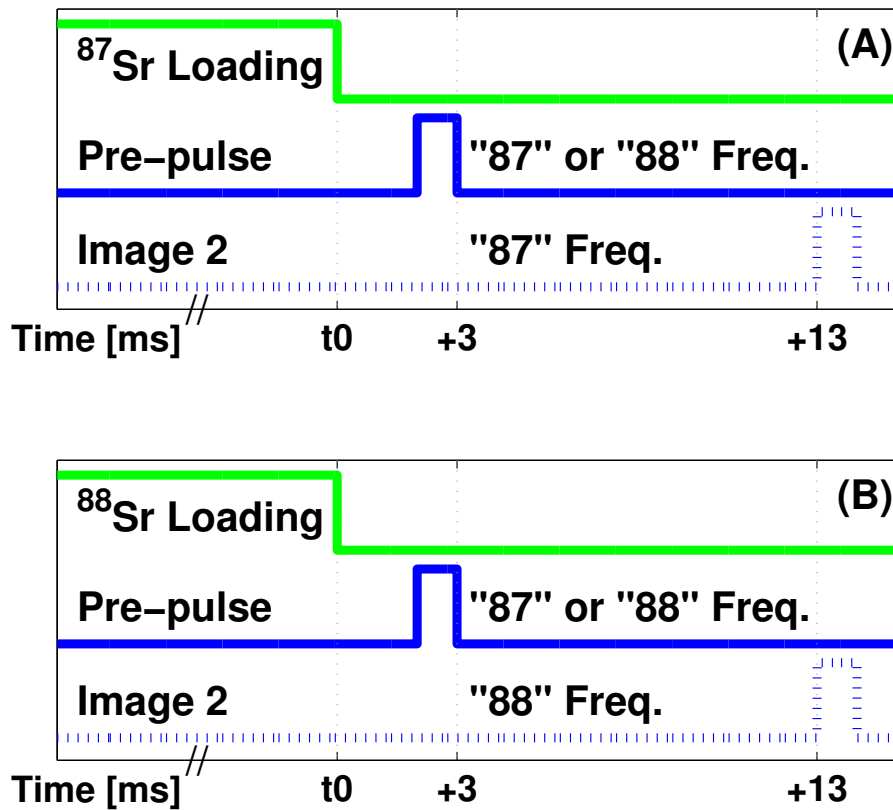


Figure 2.27 : Experimental timing to determine the effect of the image beam on a sample trapped in the optical dipole trap. (A) For ^{87}Sr , the “87” protocol is used for “image 2” which probes how “image 1” affects the sample. (B) Likewise, for ^{88}Sr , the “88” protocol is used for “image 2” to probe the effect of “image 1” on the sample. In both cases, the first application of the image beam can be with either the “87” or the “88” protocol.

of atoms and the temperature are shown for three different situations. The normal image is taken following the usual single isotope imaging procedure and provides a baseline temperature. The other two images probe the sample after the “87” or the “88” protocol has been used. We can compare the effects of the different protocols on the atom cloud with this baseline measurement. What we find is that the image beam significantly heats both ^{87}Sr and ^{88}Sr samples, irrespective of which protocol is used for “image 1”. For example, a sample of ^{87}Sr atoms which experiences the “88” protocol heats up by a factor of five. While, the atom number is not affected as severely, application of the “88” protocol still leads to moderate (20%) number loss. Unfortunately, this study shows that applying the image beam is a destructive measurement. Since we lose information contained in the image, dual imaging of isotopes is not possible using this technique.

What we do instead to image mixtures is to perform two experiments under identical conditions, except that the “87” protocol is used, with normal imaging, in the first experiment to observe the ^{87}Sr component, and the “88” protocol is used in the second experiment to measure the ^{88}Sr component of the mixture. The big disadvantage is that the measurements of the two isotopes in the cloud may be spaced by many minutes as the second experiment cannot be started until the first one is entirely finished. Besides doubling the time required to acquire data, this means drift in the experimental conditions adds some uncertainty to our measurements.

The next question to answer is whether the contamination of an image by the

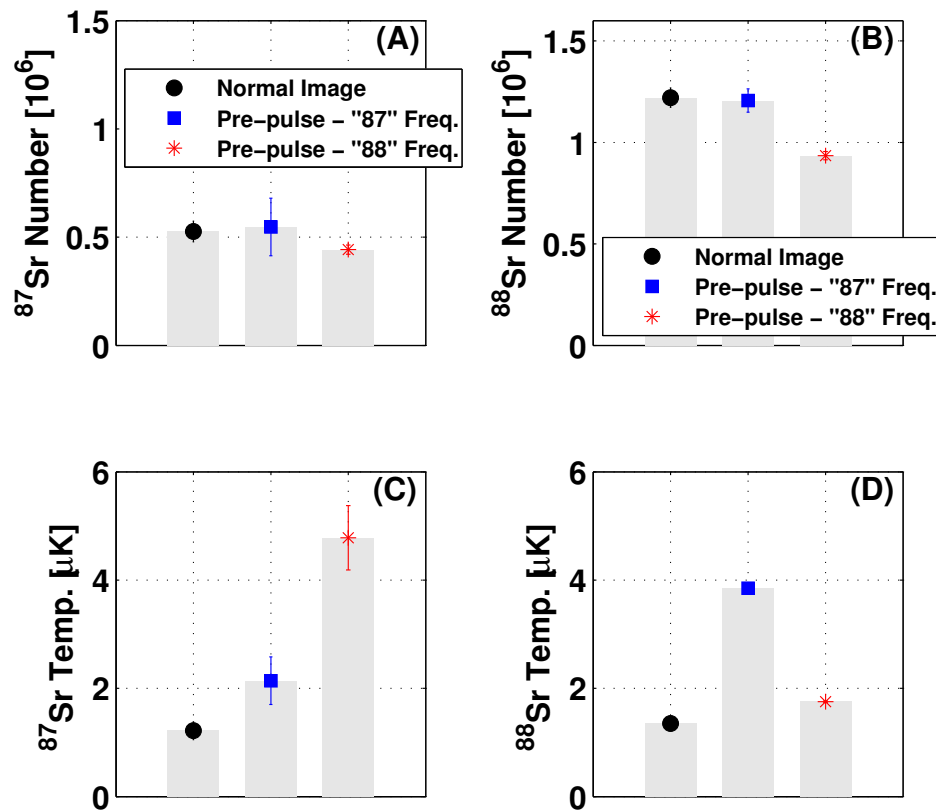


Figure 2.28 : The effect of applying a pre-pulse on the measured number and temperature of atom samples. The “87” and “88” protocols were defined earlier, and the timing for these studies is shown in Fig. 2.27. (A) and (C) show the number and temperature for samples containing only ^{87}Sr , while (B) and (D) show the number and temperature for samples of ^{88}Sr . The overall conclusion we draw is that the image beam heats the samples by a large amount, making such measurements obtained in the manner of Fig. 2.27 unreliable measures of the sample characteristics.

other isotope may be a problem in a mixture of ^{87}Sr and ^{88}Sr . For example, recall Fig. 2.4 which showed the measured number of ^{87}Sr atoms as a function of the image beam frequency. We used it to optimize the imaging frequencies, but it also showed that some ^{87}Sr atoms were still imaged, even 60 MHz away from the peak absorption for ^{87}Sr , suggesting that controlling the contamination may be necessary.

We test this question by again trapping a single isotope at a time, but we use the normal imaging procedure, where only one image is taken in one experimental sequence. We image each isotope with both the “87” and “88” protocols. For ^{88}Sr , using the “88” protocol will provide the true number and temperature of ^{88}Sr atoms in the sample; using the “87” protocol will show the degree to which ^{88}Sr atoms in a mixture might contaminate images of the ^{87}Sr component. We also study the reverse situation, where using the “88” protocol on a ^{87}Sr sample will show the amount of contamination that ^{87}Sr atoms might introduce into a measurement of the ^{88}Sr component of a mixed sample.

As Fig. 2.29 illustrates, contamination is actually a serious concern: a significant number of ^{88}Sr atoms are still seen using the “87” protocol (panel B), $\sim 25\%$ of the total number observed using the correct “88” protocol. Imaging ^{87}Sr atoms with the “88” protocol (panel A) is even worse, where $\sim 40\%$ of the atoms observed using the correct “87” protocol are also seen with the “88” protocol. Furthermore, applying the “88” protocol to an ^{87}Sr sample results in a factor of three increase in the sample temperature (panel C). On the other hand, the “87” protocol does not cause very

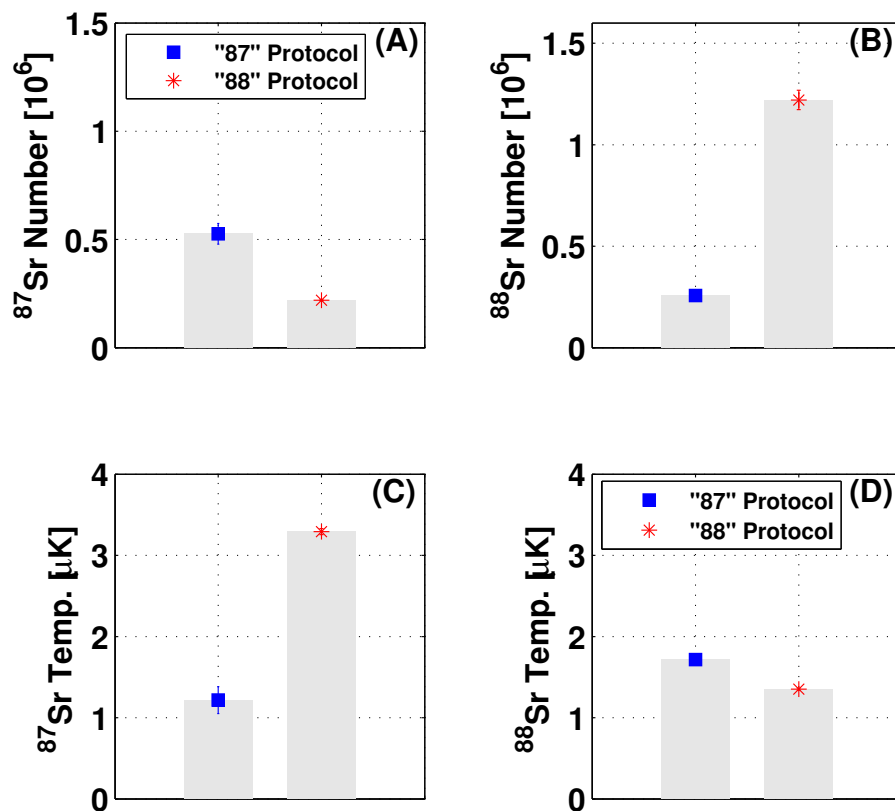


Figure 2.29 : Imaging of ^{87}Sr and ^{88}Sr samples (alone) using the “87” and “88” imaging protocols. (A) An image of ^{87}Sr , even taken far-off-resonance using the “88” protocol, shows $\sim 40\%$ of the true value measured using the “87” protocol. (B) An image of ^{88}Sr taken using the “87” protocol results in $\sim 25\%$ of the real number obtained using the “88” protocol. (C) and (D) Significant heating of samples can also occur when following the “87” and “88” protocols.

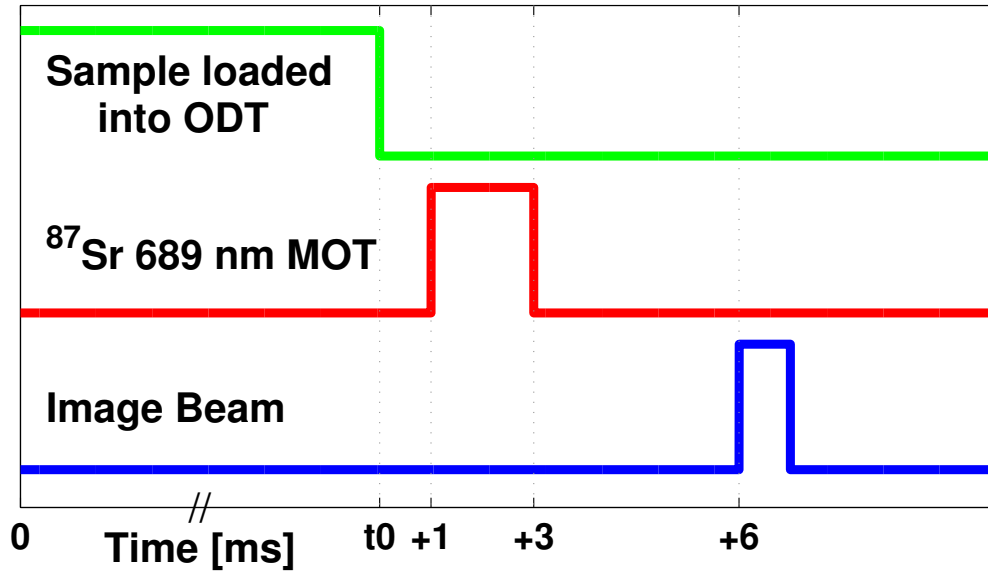


Figure 2.30 : Timing for blowing away the ^{87}Sr component of a mixture of ^{87}Sr and ^{88}Sr atoms. After the sample is loaded into the optical dipole trap, the 689 nm MOT beams for ^{87}Sr are applied for about 2 ms before imaging occurs.

much heating in ^{88}Sr samples (panel D). The relative detuning of the imaging beam frequency may explain the changes in temperature: the “88” protocol shines blue-detuned light onto the ^{87}Sr atoms, which we would expect to cause more heating than the red-detuned light (from the “87” protocol) applied to the ^{88}Sr atoms. Overall, however, the over-counting and heating of atoms will cause problems for measuring mixtures unless we are able to overcome this problem.

The solution we use is relatively simple and is outlined in Fig. 2.30. Before imaging atoms in the normal manner, we turn on the ^{87}Sr 689 nm MOT beams (called “push beams” in this context) for a short amount of time (typically 2 ms) to blow away the atoms of ^{87}Sr before imaging the remaining ^{88}Sr atoms. The results

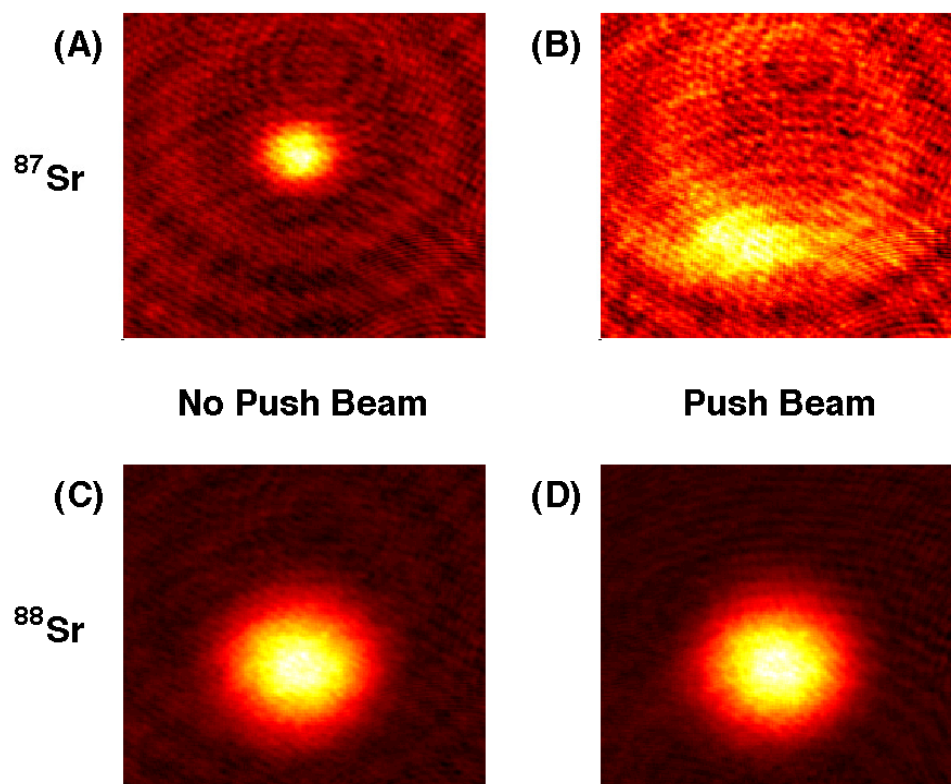


Figure 2.31 : Blowing away the ^{87}Sr component of a mixture of ^{87}Sr and ^{88}Sr . (A) The ^{87}Sr component of the mixture without applying the push beam. (B) The remnants of the ^{87}Sr component of the mixture shortly after the push beam blows away the atoms. (C) and (D) Images of ^{88}Sr with and without the push beam show that the ^{88}Sr component of the mixture remains unaffected by the push beam.

are dramatically illustrated in Fig. 2.31, where panel (A) shows ^{87}Sr atoms when the push beam has not been applied and panel (B) shows these same atoms after having been blown away by the push beam. The image in panel (B) is also the worst case scenario because little time (~ 5 ms) has elapsed between application of the push beam and imaging. In practice, we allow samples to fall under the influence of gravity to make more accurate measurements of the number and temperature. Fortunately, applying the same push beam to the ^{88}Sr atoms (panel D) has no effect, meaning we can successfully eliminate ^{87}Sr atoms from a mixture without disturbing the ^{88}Sr component.

It is possible to similarly remove ^{88}Sr atoms from a mixture, and this is an improvement we will make for future experiments. For the mixed isotope evaporation experiments in this thesis, we correct for the contamination of ^{88}Sr in ^{87}Sr images by subtracting 25% of the ^{88}Sr number from ^{87}Sr images. Ultimately, we are mostly interested in ^{88}Sr for this thesis.

This chapter has outlined the wide range of techniques we use to trap, cool, and image samples of ^{87}Sr and ^{88}Sr . These prepare the samples for the evaporation experiments I will describe in Chapters 4 and 5. However, in the next chapter, I first describe the experiments we did to learn more about repumping atoms from the magnetic trap via the $(5s5p)^3\text{P}_2 - (5s4d)^3\text{D}_2$ transition.

Chapter 3

Repumping and Spectroscopic Measurements Using the $(5s5p)^3P_2 - (5s4d)^3D_2$ Transition

This chapter characterizes the $(5s5p)^3P_2 - (5s4d)^3D_2$ transition used to repump atoms out of the $(5s5p)^3P_2$ state. I discuss the dynamics of repumping to increase the number of atoms in the blue MOT, spectroscopy of the $(5s5p)^3P_2 - (5s4d)^3D_2$ transition for all the stable isotopes of strontium, and how this information applies to the evaporation experiments of Chapter 4. The description of these experiments is largely based on previously published work [1] from the Killian lab.

3.1 Overview

The $(5s5p)^3P_2 - (5s4d)^3D_2$ transition is important to our experiment because a laser operating at the $(5s5p)^3P_2 - (5s4d)^3D_2$ wavelength enables a return path to the ground state for atoms in the metastable $(5s5p)^3P_2$ state (Fig. 3.1). Atoms end up in the $(5s5p)^3P_2$ state because the $(5s5p)^1P_1$ level used for blue MOT operation is not entirely closed: two in 10^5 atoms decay to the $(5s4d)^1D_2$ level, and then to either the $(5s5p)^3P_1$ or $(5s5p)^3P_2$ states. While atoms in the $(5s5p)^3P_1$ have a decay path to the ground state, atoms which end up in the $(5s5p)^3P_2$ state will not decay due to the 17 min lifetime of the $(5s5p)^3P_2$ state [65]. We produce $\sim 3 \mu\text{m}$ light to

excite atoms from the $(5s5p)^3P_2$ state to the $(5s4d)^3D_2$ state with a laser based on optical parametric oscillation (OPO) which requires input from a fiber laser at 1.06 μm . Appendix C documents some of the technical aspects of the OPO laser.

Using 3 μm light to repump atoms out of the $(5s5p)^3P_2$ state is not the only possible solution, and indeed, several strontium experiments [57, 66, 67] use a 707 nm laser to drive atoms to the $(5s6s)^3S_1$ state while another group [31] uses 496 nm light to excite atoms to the $(5s5d)^3D_2$ state. Even past experiments in the Killian lab [50] repumped atoms using the 707 nm transition, but the laser diodes used in the early experiment were expensive and prone to breakage. In search of alternatives, we went so far as to temperature-tune 735 nm laser diodes down to 707 nm with liquid nitrogen [68], an approach that presented its own technical difficulties. Eventually, the availability of the OPO laser as part of a shared equipment grant presented the opportunity to explore the $(5s5p)^3P_2 - (5s4d)^3D_2$ transition and led to the work described here.

3.2 Repumping of Atoms Using the $(5s5p)^3P_2 - (5s4d)^3D_2$ Transition

In this section, I discuss how the repumping laser can be used to significantly increase the number of strontium atoms trapped in the blue MOT. Capturing a high number of atoms in the initial trapping stage is important because the transfer efficiency of atoms from the blue MOT into subsequent cooling stages is limited, as we saw in

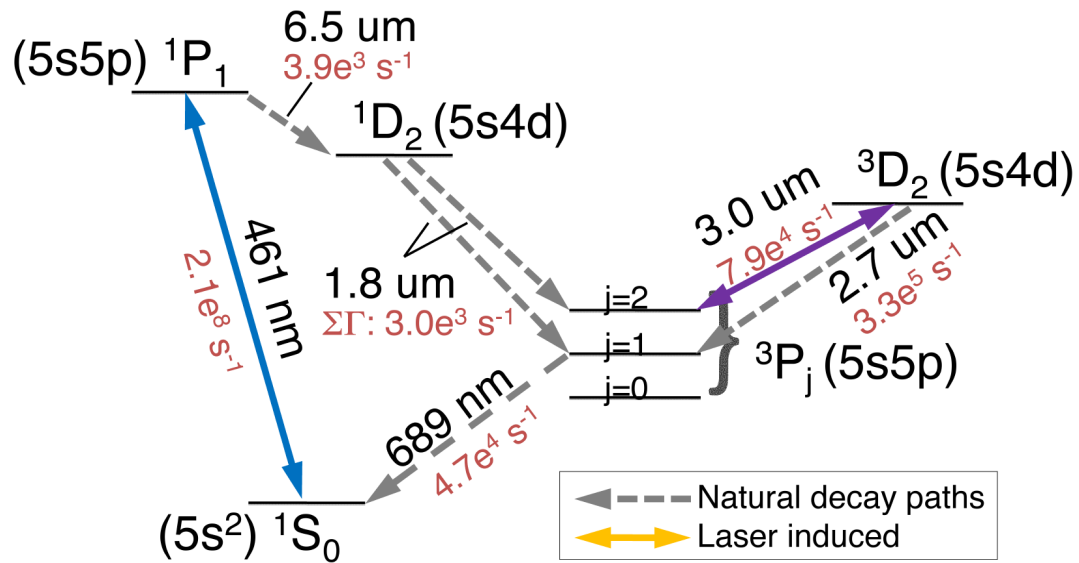


Figure 3.1 : Wavelengths and decay rates for the strontium transitions involved in studying the $(5s5p)^3P_2 - (5s4d)^3D_2$ line. During normal operation of the blue MOT, atoms leaking from the $(5s5p)^1P_1$ level will accumulate in the metastable $(5s5p)^3P_2$ state. Turning on the 3 μm laser excites atoms in the $(5s5p)^3P_2$ state up to the $(5s4d)^3D_2$ state, thus allowing the atoms to decay to the $(5s^2)^1S_0$ state via the intermediate $(5s5p)^3P_1$ state. When the 3 μm laser is applied simultaneously with the blue MOT laser, there will be an enhancement to the number of atoms trapped in the blue MOT. If, instead, the 3 μm laser is turned on only at the end of the blue MOT period, the number of atoms observed depends on how long the blue MOT was on. Spectroscopy of the $(5s5p)^3P_2 - (5s4d)^3D_2$ transition is performed by varying the frequency of the 3 μm laser as atoms are repumped to the ground state. Figure adapted from [1].

Fig. 2.8. Though these concerns apply to both ^{87}Sr and ^{88}Sr , we use repumping of ^{88}Sr as an example. The repumping of ^{87}Sr is complicated by the fact that it has nuclear spin, resulting in atoms being distributed into all of its hyperfine states, and I only briefly cover it because the trade-offs made to trap sufficient numbers of both isotopes were already discussed in section 2.1.2.

In the absence of the repumping laser, up to 50×10^6 ^{88}Sr atoms are trapped using the 461 nm cycling transition between the $(5s^2)^1\text{S}_0$ and $(5s5p)^1\text{P}_1$ states. Atom samples in the blue MOT have a temperature of about 2 mK, a density of around 10^{10} cm^{-3} , and a $1/e$ radius of about 1 mm. We obtain these numbers with a 2D collimation laser cooling stage placed after the atom source and before the Zeeman slowing stage. Without the 2D collimation, the atom loading is reduced by about a factor of 6.

When necessary, we can increase the atom number by using the repumping laser. To do so, we shine the repumping laser on the atom cloud during the blue MOT loading time (see the timing diagram in Fig. 3.2) to create a return path from the $(5s5p)^3\text{P}_2$ state to the ground state via the $(5s4d)^3\text{D}_2$ and $(5s5p)^3\text{P}_1$ levels. Figure 3.3 shows the number of atoms, with and without the repumping laser, as a function of MOT loading time. We introduce the time-dependent number equation for MOT loading to analyze these data:

$$\dot{N} = L_N - \Gamma N - \beta' N^2. \quad (3.1)$$

Here, N is the number of atoms, L_N is the loading rate of atoms into the MOT, Γ is

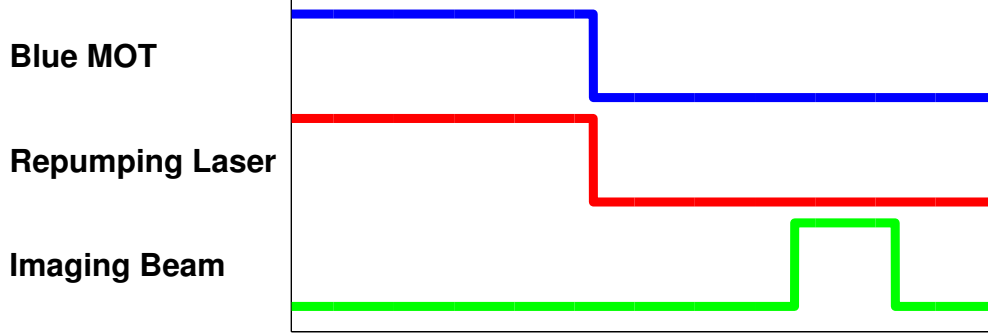


Figure 3.2 : Timing diagram for experiments using repumping during the blue MOT loading stage. The experimental sequence for repumping atoms from the $(5s5p)^3P_2$ metastable level is simple: shine the repumping laser on the atoms concurrent with blue MOT loading, and image the atoms a short time afterwards. For comparison, we block the repumping laser to measure the blue MOT atom number without a repumping enhancement. The timing is not to scale.

the one-body loss rate, and $\beta' = \beta/(2\sqrt{2}V)$, where β is the two-body loss constant and $V = \int d^3r e^{-\frac{r^2}{\sigma^2}}$ is the effective volume for two-body processes (σ is the $1/\sqrt{e}$ radius and r is position). The solution to this differential equation is

$$N(t) = \frac{N_{ss}(1 - e^{-\gamma t})}{(1 + \chi e^{-\gamma t})}, \quad (3.2)$$

where $\gamma = \Gamma + 2\beta'N_{ss}$, N_{ss} is the steady state number of atoms, and χ is the measure of the relative contributions of the one- and two-body loss coefficients:

$$N_{ss} = \frac{-\Gamma + \sqrt{\Gamma^2 + 4\beta'L}}{2\beta'} \quad (3.3)$$

and

$$\chi = \frac{\beta'N_{ss}}{\beta'N_{ss} + \Gamma}. \quad (3.4)$$

This model produces the fits shown in Fig. 3.3.

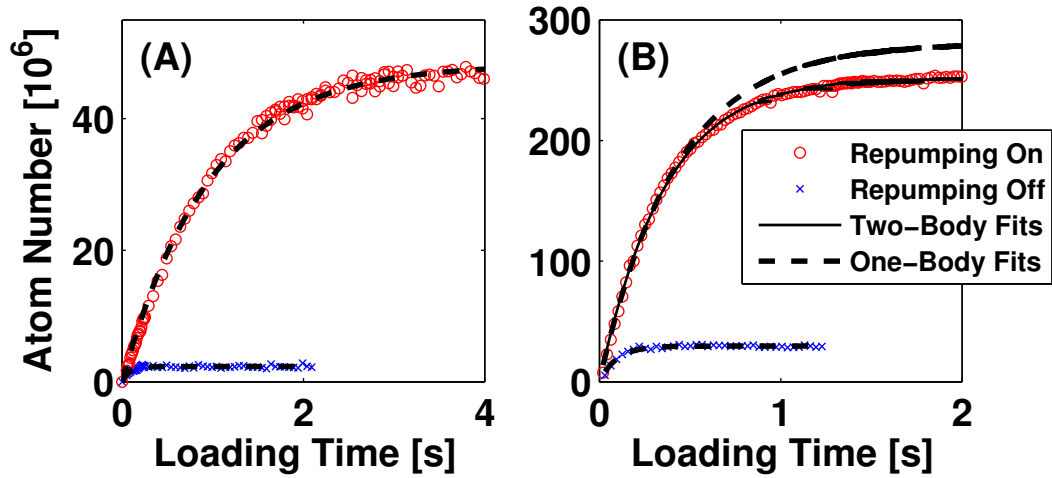


Figure 3.3 : Loading of ^{88}Sr atoms into the blue MOT with and without the $3\ \mu\text{m}$ repumping laser. Absent the repumping laser, atoms accumulate in the $(5s5p)^3\text{P}_2$ dark state and cannot return to the ground state, thus limiting the number in the blue MOT. Turning on the repumping laser pumps atoms out of the $(5s5p)^3\text{P}_2$ state and into the $(5s4d)^3\text{D}_2$ state, providing a decay path to the ground state and increasing the number of atoms that can be captured in the blue MOT. The curves fit to the data are from a model of MOT dynamics which accounts for the loading rate, one-body loss processes, and two-body loss processes. We observe an enhancement of a factor of twenty if the overall atom number is less than a few million (A), but the enhancement is limited by light-assisted collisions for higher overall atom number (B). Figure adapted from [1].

The measured MOT lifetime ($1/\Gamma$) is consistent both with other experiments and with a theoretical estimate for our experimental conditions. When the repumping laser is off, this lifetime is determined by losses to the $(5s5p)^3P_2$ level. We set $\beta = 0$, in the low density limit, and achieve a good fit to the data with Γ as the sole free parameter. The fit value, Γ , is of order 10 s^{-1} , which is consistent with the $\Gamma = 59 \text{ s}^{-1}$ quoted by Dinneen et al. [66], as we show by accounting for the larger detuning from resonance and the lower intensity of the MOT beams.

For this consistency check, I compare the calculated and measured fraction of atoms in the excited state. Using our laser detuning and intensity, we can calculate the loss from the MOT cycling transition. Because atoms decaying from the $(5s4d)^1D_2$ state to the $(5s5p)^3P_1$ state are recycled to the ground state and do not factor in as losses, we begin by estimating the loss to the $(5s5p)^3P_2$ level:

$$\Gamma = f\gamma_{P-D}L, \quad (3.5)$$

where f is the fraction of atoms in the excited state of the MOT transition ($(5s5p)^1P_1$), γ_{P-D} is the decay rate out of the $(5s5p)^1P_1$ state to the $(5s4d)^1D_2$ level, and L is the branching ratio to the $(5s5p)^3P_2$ state. Using $\gamma_{P-D} = 3850 \text{ s}^{-1}$ [69] and $L = 0.3$ [66] and rearranging the equation, we obtain an excited state fraction for our value of Γ of about 1%. For comparison with this experimentally determined excited state fraction, we now calculate the fraction of atoms in the $(5s5p)^1P_1$ state using the expression for the population of an excited state [58]:

$$\rho_{es} = \frac{s_0/2}{1 + s_0 + (2\delta/\gamma)^2}, \quad (3.6)$$

where s_0 is the saturation parameter, defined as the ratio of the laser intensity to the saturation intensity of the transition (I/I_s), δ is the laser detuning from resonance, and $\gamma = 2 \times 10^8$ Hz is the decay rate from the $(5s5p)^1P_1$ to the $(5s^2)^1S_0$ states. The saturation intensity is $I_s \equiv \pi h c / 3 \lambda^3 \tau$, with h as Planck's constant, c as the speed of light, and λ and τ as the wavelength and lifetime, respectively, of the $(5s5p)^1P_1 - (5s^2)^1S_0$ transition. For a laser intensity of $I = 13.8$ mW/cm² (an average of 2.3 mW/cm² per beam for six MOT beams) and detuning of $\delta = 60$ MHz from resonance, we get an excited state fraction of $\rho_{es} = 0.01$, in good agreement with the measured value. Moreover, once the differences in MOT laser intensity and detuning are taken into account, the excited state fraction of this experiment closely matches that of Dinneen et al.

Another interesting aspect of this study is that the observed repumping enhancement varies with density. For the analysis that was just presented (Fig. 3.3(A)), we kept the number of atoms low for both loading curves by turning off the 2D collimation beams and observed a repumping enhancement of about a factor of 20. When we fit these loading data with Eq. 3.2, we conclude that two-body losses are not significant for this low atom number because $\beta = 0$. To produce the larger atom numbers seen in Fig. 3.3(B), we turn on the 2D collimation beams and get a factor of six more atoms in the system, only to find a smaller repumping enhancement than the factor of twenty observed with fewer atoms in the system. There are several factors that could account for the decreased enhancement. First, the results of a fit using

Eq. 3.2, with $\beta = 6 \pm 2 \times 10^{-10} \text{ s}^{-1}$ and $\Gamma = 2.4 \pm 0.1 \text{ s}^{-1}$, suggest that two-body light-assisted losses (from the non-zero β value) are becoming important. Second, Γ has increased, indicating more one-body loss. Finally, the size of the atom cloud is substantially larger ($\sim 2 \text{ mm}$) with the repumping laser applied, and its shape is non-Gaussian which could lead to systematic uncertainty in number measurements. Attempts to assign systematic uncertainty resulting from this non-ideal density distribution are inconclusive, but the value of β does seem to agree with that seen by [66].

Finally, we note that the lifetime ($1/\Gamma = 0.96 \pm 0.01 \text{ s}$) is much shorter than the 25 s lifetime of $(5s5p)^3P_2$ atoms observed in the magnetic trap of the MOT quadrupole magnets. While it is not clear why such a discrepancy exists, we suspect that atoms may be escaping the trapping region before repumping occurs.

While the hyperfine structure of ^{87}Sr , which I discuss in more detail in the following section, complicates its repumping, we still observe a MOT repumping enhancement of up to a factor of 3. Without the repumping laser, the atom number is $\sim 8 \times 10^6$. However, as will be seen in section 3.4, the enhancement with the repumping laser varies moderately with the detuning of the laser, so choosing the optimum frequency will be important for repumping both ^{87}Sr and ^{88}Sr in mixed isotope experiments.

3.3 Spectroscopy of ^{84}Sr , ^{86}Sr , ^{87}Sr , and ^{88}Sr

We also use the repumping enhancement as a diagnostic to perform spectroscopy of the $(5s5p)^3\text{P}_2 - (5s4d)^3\text{D}_2$ transition for all the stable isotopes of strontium. As we change the frequency of the 3 μm laser, the number of atoms imaged varies, thus revealing the structure of the isotopes seen in Figs. 3.4 and 3.5.

Because the natural abundances of the isotopes differ, we vary the experimental procedure for each isotope to optimize the signal obtained. For samples of ^{86}Sr and ^{88}Sr which have strong signals, lowering the repumping laser intensity is acceptable and results in splitting of the lines. On the other hand, high repumping laser intensity is needed to observe the other stable isotopes, ^{84}Sr and ^{87}Sr . The different procedures change how the zero frequency (the resonance frequency of the transition when the atom is unperturbed by magnetic fields) for each isotope is specified. Therefore, before discussing the topic of isotope shifts, I examine the spectral structure in more detail.

We observe structure in the spectra of ^{86}Sr and ^{88}Sr due to the Zeeman effect under the influence of the 50 G cm^{-1} MOT magnetic field gradient (Fig. 3.5). We see how the laser intensity affects the line shape in more detail in Fig. 3.6(A). Applying the highest laser intensity results in a power-broadened line while applying lower intensities reveals the more complicated structure. If we assume that the atoms being repumped are distributed between all the $(5s5p)^3\text{P}_2$ magnetic sub-levels, we would expect to observe peaks corresponding to all the possible transitions, for all

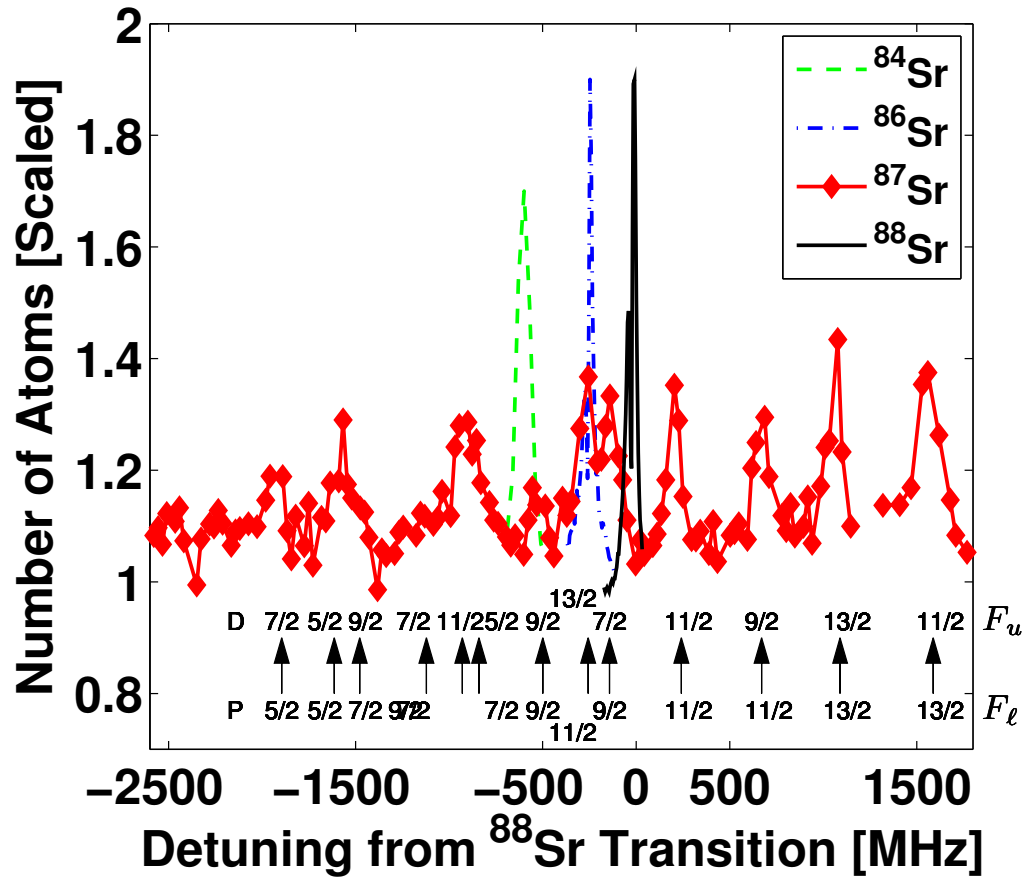


Figure 3.4 : Spectroscopy of the $(5s5p)^3P_2 - (5s4d)^3D_2$ transition for all the stable isotopes of strontium. Shifts are measured relative to the zero of the ⁸⁸Sr spectrum. For ⁸⁶Sr, ⁸⁷Sr, and ⁸⁸Sr, the number is normalized to the number observed without the repumping laser. For ⁸⁴Sr, the scaling is arbitrary because large repumping efficiency is necessary to observe a spectrum. The structure in the ⁸⁷Sr spectrum is due to the hyperfine interaction: the fermionic isotope of strontium has nuclear spin, I , equal to $9/2$. Transition assignments (arrows) can be made for all of the observed peaks (upper and lower spin states marked by F_u and F_l), and the isotope shift of ⁸⁷Sr is determined by the shift of the centroid of the energy level manifold from the ⁸⁸Sr zero. Figure adapted from [1].

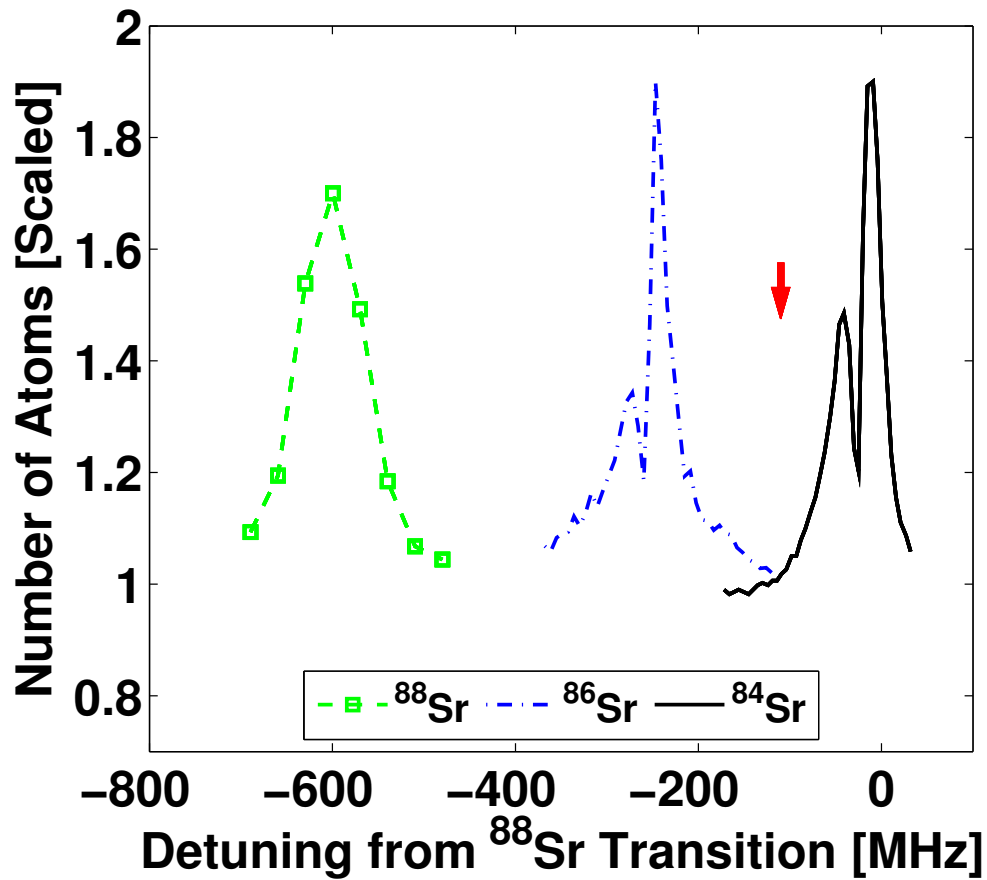


Figure 3.5 : Spectroscopy of the $(5s5p)^3P_2 - (5s4d)^3D_2$ transition for ^{84}Sr , ^{86}Sr , and ^{88}Sr . This represents a smaller frequency range of the spectrum in Fig. 3.4 and shows details of the spectroscopy. The position of the centroid of the ^{87}Sr manifold is marked with an arrow. Zeeman splitting from the 50 G cm^{-1} MOT magnetic field gradient causes the structure seen in the ^{86}Sr and ^{88}Sr spectra. A model of this splitting, described in the text, determines where to place the frequency zero for ^{88}Sr . Because ^{84}Sr and ^{87}Sr are observed only at high repumping laser power, the Zeeman structure is washed out in their spectra. Figure adapted from [1].

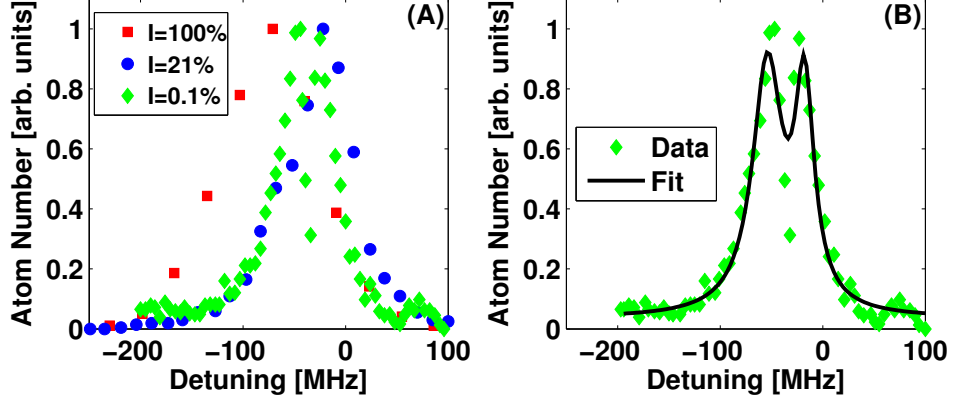


Figure 3.6 : Line shapes of ^{88}Sr spectra. (A) The number of atoms varies as a function of repumping laser intensity. At high intensity, the spectrum is shifted and we observe no structure because the line is power-broadened, while at lower intensities, structure appears due to Zeeman splitting in the MOT magnetic field. (B) We fit the lowest intensity data to a double Lorentzian line shape. We believe that the leftmost peak is the transition from the $(5s5p)^3P_2$ $m_j = 2$ sub-level to the $(5s4d)^3D_2$ $m_j = 1$ sub-level, and the rightmost peak is the transition from the $(5s5p)^3P_2$ $m_j = 2$ sub-level to the $(5s4d)^3D_2$ $m_j = 2$ sub-level. The frequency splitting of the two peaks helps determine the frequency of the transition when it is unperturbed by the magnetic field. The fit also shows that the upper limit on the line width of the repumping laser is about 35 MHz.

the polarizations, from the $m_j = \pm 2, \pm 1$, and 0 sub-levels of the $(5s5p)^3P_2$ state to the $(5s4d)^3D_2$ state as seen in Fig. 3.7. Though we do not model the population distribution of atoms among the five sub-levels, not all of the sub-levels are magnetically trapped by the magnetic field gradient of the MOT [50], leading to the escape of atoms not in the $m_j = +2$ or $m_j = +1$ levels from the trapping region of the MOT before repumping occurs.

We can calculate the splitting between the transitions accounting for the magnetic moments of the upper and lower states, the magnetic field gradient, and the

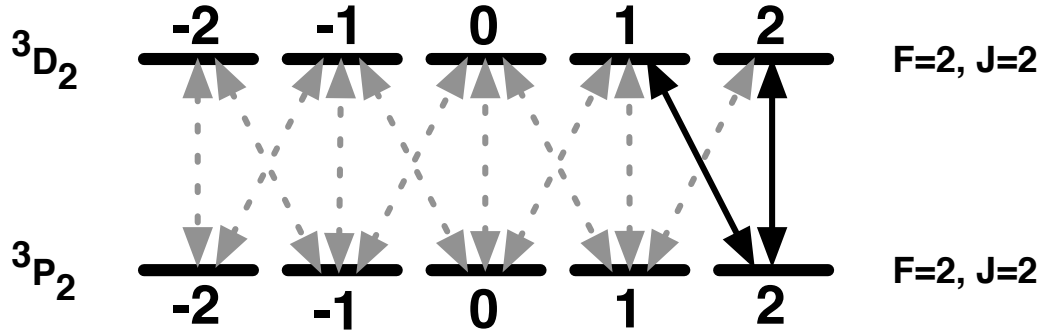


Figure 3.7 : Schematic of energy levels for even-numbered isotopes of strontium. Because atoms in the $m_j = +2$ level are trapped most strongly by the magnetic field gradient of the MOT, We expect that the structure seen in the spectra of Figs. 3.5 and 3.6(B) is due to transitions from that state to Zeeman sub-levels in the $(5s4d)^3D_2$ manifold (solid black arrows). Inactive transitions have dashed gray arrows for clarity. The level structure of ^{87}Sr is not shown here because the laser intensity required to repump ^{87}Sr washes out any structure that could be seen.

temperature of the atoms in the MOT (Appendix D). Assuming that the two peaks we see correspond to the transitions out of the $(5s5p)^3P_2$ $m_j = 2$ sub-level, then the frequency of the unperturbed ($B=0$) resonance is about 20 MHz blue-detuned of the righthand peak. This sets the zero of the frequency axis in Figs. 3.4 and 3.6 and allows the determination of the isotope shift of ^{86}Sr from ^{88}Sr . Because high repumping laser intensity is required to achieve good signal for the other stable isotopes— ^{84}Sr has a low natural abundance (0.56%) and ^{87}Sr has poor repumping efficiency because the atom population is distributed between the 13 spin states—any structure due to magnetic sub-levels is washed out and we do not correct for the magnetic field shift. For these isotopes, the measured frequency is taken as the center of the line.

Unlike the structure observed in ^{86}Sr and ^{88}Sr , the structure seen in ^{87}Sr (Fig. 3.4) is hyperfine structure caused by the ^{87}Sr nuclear spin of $I = 9/2$. The laser intensity used to repump ^{87}Sr is too high to allow observation of the magnetic sub-levels of ^{87}Sr . We predict the spacing of the transitions between the hyperfine levels using the Casimir formula:

$$\Delta E_F = A \frac{K}{2} + B \left[\frac{3/4K(K+1) - I(I+1)J(J+1)}{I(2I-1)2J(2J-1)} \right]. \quad (3.7)$$

Here, $K = F(F+1) - J(J+1) - I(I+1)$, and A and B are the magnetic dipole and electric quadrupole factors, respectively. We use experimentally determined values of A and B for the $(5s4d)^3\text{D}_2$ [70] and $(5s5p)^3\text{P}_2$ [71] levels. For the $(5s5p)^3\text{P}_2 - (5s4d)^3\text{D}_2$ transition, the total angular momentum, F , ranges from $5/2$ to $13/2$, for both the upper and lower states of the transition, because $J = 2$ and $I = 9/2$. The arrows in Fig. 3.4 are the calculated positions of the transitions. When the observed peaks are matched to these calculated positions by overlaying the two, the agreement is good to within 30 MHz (see Table 3.1).

The isotope shifts of ^{84}Sr , ^{86}Sr , and ^{87}Sr relative to ^{88}Sr are summarized in Table 3.1. The zero frequency of ^{84}Sr is taken as the center of the power-broadened line, and the zero frequency of ^{86}Sr and ^{88}Sr were specified in the discussion of the Zeeman splitting. To determine the isotope shift of ^{87}Sr , we measure the shift of the centroid of the ^{87}Sr energy levels with respect to the ^{88}Sr zero. The principal sources of uncertainty for these measurements are the statistical uncertainty from fitting the line shapes and possible drift in the calibration of the wavemeter. Additionally, the

King plot in Fig. 3.8, a common method to analyze isotope shifts [72, 73], compares this work with measurements of the $(5s^2)^1S_0 - (5s5p)^1P_1$ [54] and $(5s^2)^1S_0 - (5s5p)^3P_1$ [74] lines. For the figure, I plot the modified isotope shift ($\delta\nu_M$),

$$\delta\nu_M = (\delta\nu_{IS} - \delta\nu_{NMS}) \frac{A_1 A_2}{A_1 - A_2}, \quad (3.8)$$

where A_1 and A_2 are the mass numbers of the isotopes in atomic mass units (amu), $\delta\nu_{IS}$ is the observed isotope shift, and $\delta\nu_{NMS} = (\nu m_e / m_p) \times (A_1 - A_2) / A_1 A_2$ is the normal mass shift caused by the reduced mass of the atom. Further, ν is the frequency of the transition, and m_e and m_p are electron and proton masses. The King plot is consistent with a linear relationship between the isotope shifts of different transitions that is expected when the nuclear spin does not contribute to the isotope shift [73].

Table 3.1 : Isotope shifts and uncertainties of the $(5s5p)^3P_2 - (5s4d)^3D_2$ transition at $\lambda=3012$ nm in strontium.

Isotope Pair	Isotope Shift [MHz] at λ
87–88	-110(30)
86–88	-270(40)
84–88	-600(50)

To complete the discussion of shifts in the resonance frequencies of the isotopes, an absolute frequency measurement is needed. We used absorption spectroscopy of ammonia [75] to calibrate the wavemeter absolutely [76]. For ^{88}Sr , which provides the zero frequency for the relative shifts, we find a value of $3320.226 \pm 0.0025 \text{ cm}^{-1}$ for the unperturbed resonance wave number of the $(5s5p)^3P_2 - (5s4d)^3D_2$ transition.

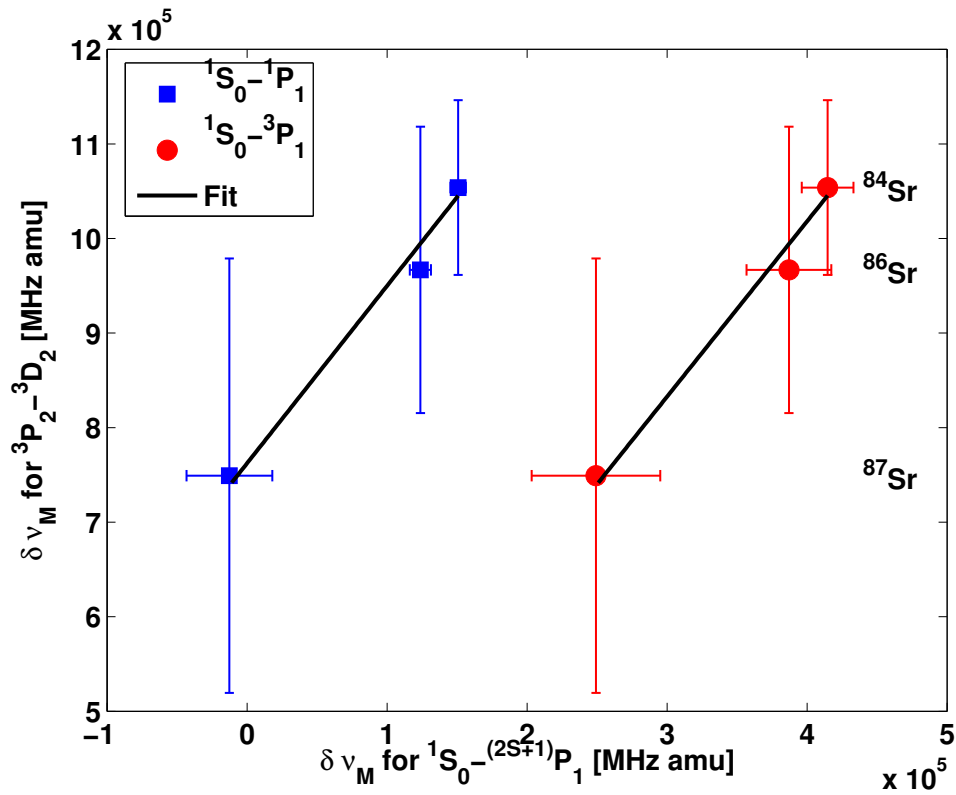


Figure 3.8 : A King plot of the modified isotope shifts, $\delta \nu_M$, of the $(5s5p)^3P_2 - (5s4d)^3D_2$ transition versus the modified isotope shifts of the 461 nm $(5s^2)^1S_0 - (5s5p)^1P_1$ [54] and 689 nm $(5s^2)^1S_0 - (5s5p)^3P_1$ [74] transitions of strontium. The data reflects the linear relationship between the isotope shifts for the different transitions expected when no unusual structure is observed. Figure adapted from [1].

This measurement represents a small shift from and improvement to the $(5s5p)^3P_2 - (5s4d)^3D_2$ transition wave number compared to the previously published value of 3320.232 cm^{-1} [77].

Taken collectively, these measurements of the $(5s5p)^3P_2 - (5s4d)^3D_2$ transition enhance our understanding of its dynamics and enable us to effectively repump atoms to the ground state.

3.4 Experimental Considerations for Trapping Mixtures

The spectroscopy described in this chapter suggests several experimental considerations. Recall the procedure for trapping mixtures of ^{87}Sr and ^{88}Sr described in section 2.1.2. There, we first load ^{88}Sr into the magnetic trap, then load ^{87}Sr , before repumping both isotopes back to the ground state for transfer into the red MOT. Figure 3.4 helps determine the best operating frequency for the repumping laser to simultaneously repump the two isotopes. At first glance, setting the repumping laser frequency near the ^{88}Sr resonance seems logical because of the overlap between the ^{87}Sr and ^{88}Sr transitions. However, in practice, we find that the repumping efficiency for ^{87}Sr is the limiting factor for mixed species trapping. Spectroscopy of both ^{87}Sr and ^{88}Sr (Fig. 3.9) shows that in order to maximize the number of ^{87}Sr atoms repumped from the magnetic trap, we should set the frequency to about +1500 MHz detuned, or 3320.255 cm^{-1} . We also keep the laser intensity high to optimize the repumping efficiency of ^{87}Sr , effectively washing out structure due to Zeeman splitting. Despite the reduction

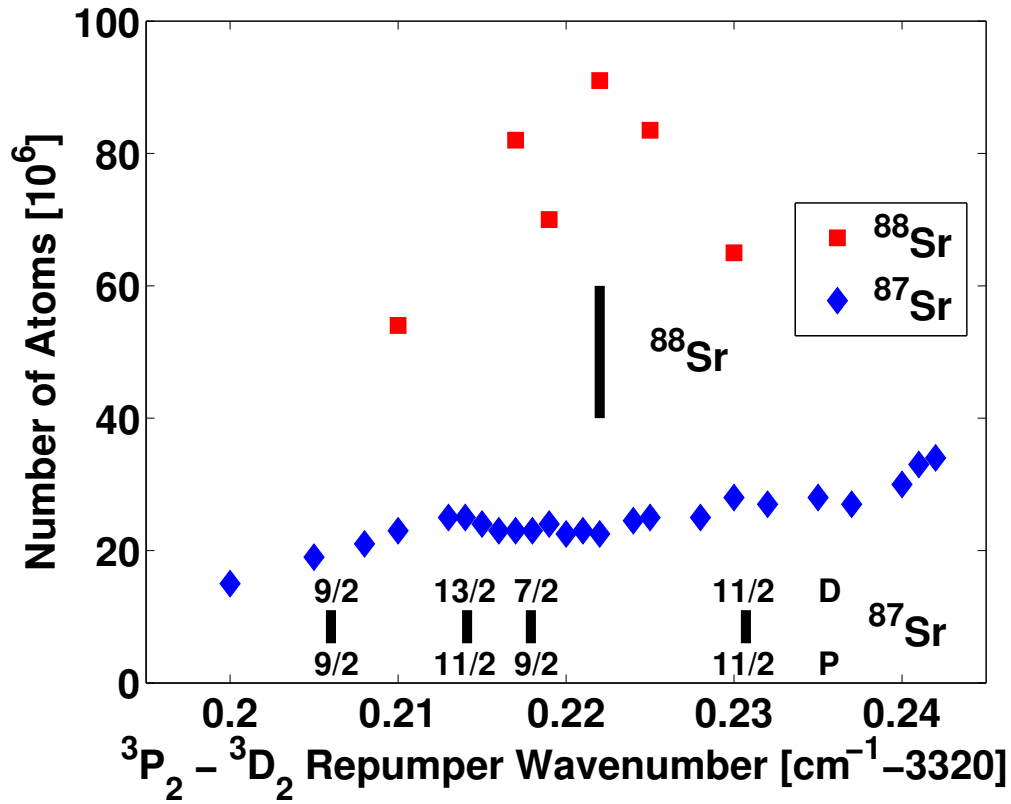


Figure 3.9 : Repumping efficiency as a function of repumping laser frequency for ^{87}Sr and ^{88}Sr . Despite falling off quickly away from resonance, the efficiency of ^{88}Sr repumping is superior to that of ^{87}Sr for most of the range shown. For this reason, we tune the repumping laser to the highest frequency measured (around 3320.255 cm^{-1}) to produce the greatest enhancement for ^{87}Sr .

in the repumping efficiency of ^{88}Sr at this frequency, we can still repump about the same number of ^{88}Sr as ^{87}Sr atoms, so it is a reasonable frequency to choose.

Other schemes, which we have not yet implemented, may help us increase the number of ^{87}Sr atoms. For example, scanning the frequency of the repumping laser on the time scale of the repumping time (Fig. 2.7 showed 10 - 100 ms) could allow atoms trapped in the other spin states to be repumped from the magnetic trap.

Assuming an equal population distribution among the 5 spin sub-levels, an upper limit would be a factor of 5 more than pumping from a single level. However, the CG coefficients for each transition vary, so the repumping efficiency would not be the same for all the states, leading to less than a factor of 5. Technically, we might be able to achieve this frequency change by ramping the current controller of the repumping laser. Even without an improved repumping laser, however, the current repumping scheme is able to transfer as many as 3×10^6 ^{87}Sr into the optical dipole trap, which turns out to be enough for the evaporation experiments described in the next chapter.

Chapter 4

Unforced Evaporation in the Optical Dipole Trap

Here I describe the evaporation experiments that form the core of this thesis and lead to the production of a Bose-Einstein condensate (BEC) of ^{88}Sr . Previous chapters explained how to create mixtures of ^{87}Sr and ^{88}Sr in the optical dipole trap. In this chapter, I discuss the properties of ^{87}Sr and ^{88}Sr , both alone and in mixtures.

4.1 Spin-Polarization of ^{87}Sr

Simply put, spin-polarization is the degree to which the atoms in a sample occupy the same spin state. For a fermionic atom such as ^{87}Sr , if more atoms are in the same spin state, interactions between atoms in the sample decrease because Pauli's exclusion principle forbids collisions between fermions in the same state. On one extreme, atoms in an ^{87}Sr sample with equal populations in each of the ten energy sub-levels of the $(5s^2)^1\text{S}_0$ ground state will interact with all but the 10% of the atoms which are in the same sub-level. This corresponds to a low degree of spin-polarization. At the opposite extreme, a high degree of spin-polarization corresponds to having all the atoms in a single spin state, and no collisions occur between atoms in the sample.

4.1.1 Evidence for Spin-Polarization

Because the distribution of atoms among different spin states affects the scattering properties of ^{87}Sr , we conduct three kinds of studies to determine the spin-polarization of ^{87}Sr and its effect on unforced evaporation. First, we can alter the polarization by applying a laser beam to optically pump atoms into different spin states. Second, we can probe the spin-polarization by applying a magnetic field to separate the spin levels and then performing spectroscopy. Finally, we can look at unforced evaporation of ^{87}Sr , which is sensitive to the degree of spin-polarization because the rate of evaporation depends on the frequency of collisions in the sample.

Since spin-polarization is the degree to which the atoms in a sample occupy the same spin state, we can alter the spin-polarization of a sample of ^{87}Sr by optically pumping atoms to other spin states. The beam used for this purpose (the “pump” beam) is derived from the ^{87}Sr stir laser; it drives the $F = 9/2 \rightarrow F = 9/2$, $(5s^2)^1\text{S}_0 - (5s5p)^3\text{P}_1$ transition which is 222 MHz blue-detuned from the 689 nm resonance for ^{88}Sr (Fig. 4.1). The axis of quantization of the sample is defined by a weak magnetic field (~ 2 Gauss) in the vertical direction, and the pump beam travels along this axis. To change the spin-polarization of the sample, the pump beam is applied to the atoms for up to 30 ms with as much as $1 \text{ mW}/\text{cm}^2$ of intensity. The circular polarization of the pump laser means atoms will move towards the $m_F = \pm 9/2$ in the ground state manifold (Fig. 4.2), with the sign depending on whether the pump laser is left or right circularly polarized. In our case, the helicity of the polarization is σ^+ ,

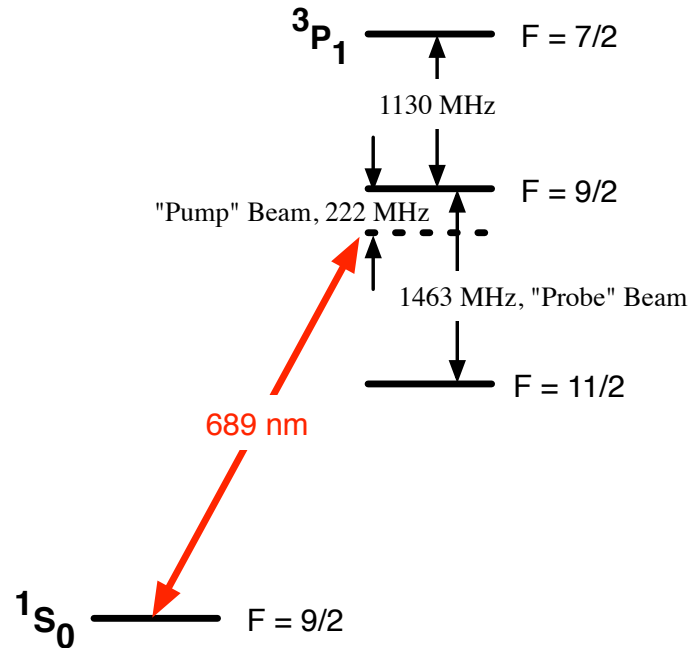


Figure 4.1 : Hyperfine structure of the $(5s5p)^3P_1$ state of ^{87}Sr (—), showing the level spacings and the detuning from the ^{88}Sr (\cdots) resonance. The pump beam used to spin-polarize samples operates on the $F = 9/2 \rightarrow F = 9/2$ transition, and the probe beam used for spectroscopy operates on the $F = 9/2 \rightarrow F = 11/2$ transition.

as we will see from our data (Fig. 4.4). Fig. 4.2 illustrates the distribution of the magnetic sub-levels and the allowed transitions if the light is right circularly polarized. Applying the pump beam for long enough should therefore concentrate atoms into the $m_F = 9/2$ dark state (i.e. atoms remain where there is no allowed transition from a ground state sub-level for right circularly polarized light). Not applying the pump beam to the atoms means the degree of spin-polarization should not change. For the rest of this discussion, I refer to samples which we have not optically pumped as “unpolarized,” and samples which we have pumped as “polarized.”

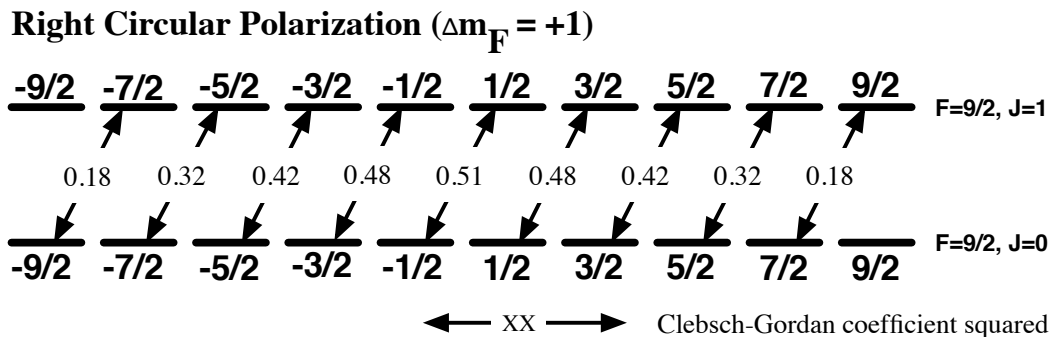


Figure 4.2 : Hyperfine structure, with magnetic sub-levels, for a $F = 9/2 \rightarrow F = 9/2$ transition such as the 689 nm $(5s^2)^1S_0 - (5s5p)^3P_1$ transition of ^{87}Sr . The lower manifold of states is for the $(5s^2)^1S_0$ ground state ($J = 0$), while the upper manifold of states is for the $F = 9/2$ level of the $(5s5p)^3P_1$ excited state ($J = 1$). The arrows represent the allowed transitions for right circularly polarized light, and the relative strengths of the transitions are shown as the square of the Clebsch-Gordan coefficients. If the pump laser is right circularly polarized, atoms are driven towards the $m_F = 9/2$ level of the $(5s^2)^1S_0$ ground state.

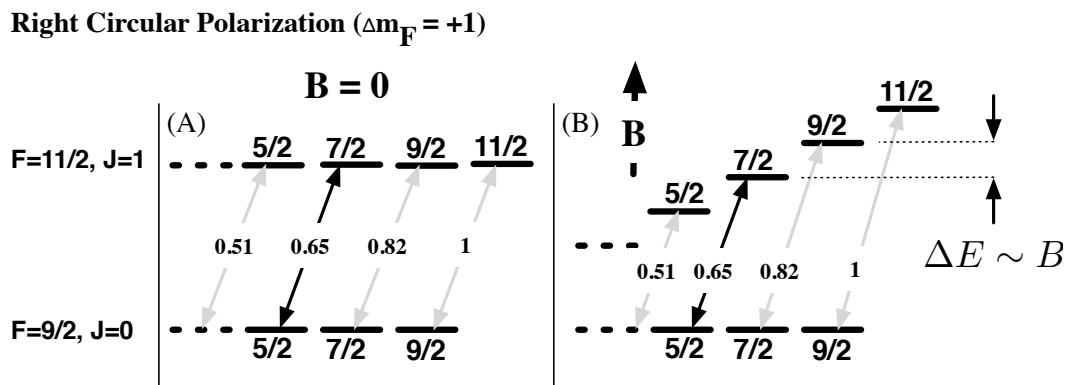


Figure 4.3 : A subset of the magnetic sub-levels for a $F = 9/2 \rightarrow F = 11/2$ transition. (A) Without an applied magnetic field, the levels and transitions are unperturbed. (B) When a magnetic field is applied to the sub-levels, however, the degeneracy of the excited state is lifted and the levels are split by an amount proportional to the m_F quantum number and the magnetic field, B . The lower manifold of states remains unaffected by the magnetic field because it has $J = 0$. The shift of the excited state levels separates the frequencies of the allowed transitions, thus enabling spectroscopy of the individual sub-levels using circularly polarized probe light.

One way in which we probe the spin-polarization of ^{87}Sr is to perform spectroscopy using a laser beam (the “probe” beam) operating on the $F = 9/2 \rightarrow F = 11/2$, $(5s^2)^1\text{S}_0 - (5s5p)^3\text{P}_1$ transition, which is 1463 MHz red-detuned from the pump beam frequency (Fig. 4.1). For spectroscopy, the probe beam is applied for 200 ms with an intensity of ~ 0.1 mW/cm². Under the influence of the ~ 2 Gauss magnetic field that determines the quantization axis, the degeneracy of the excited state manifold is broken, as shown in Fig. 4.3(B). The amount by which the sub-levels shift is determined by

$$\Delta f_{s7} = \frac{g_F \mu_B B}{h}, \quad (4.1)$$

where g_F is the Landé g-factor, μ_B is the Bohr magneton, B is the applied magnetic field, and h is Planck’s constant. For the excited state, the spacing between the levels is about 0.75 MHz. Meanwhile, the energies of the ground state levels do not shift relative to one another because there is no electronic angular momentum and the g-factor equals zero. From the diagram, it can also be seen that for a single frequency of purely polarized light, atoms in a ground state sub-level can be excited only to a single excited state sub-level. Furthermore, resolving individual transitions is possible because the scattering rate is proportional to the number of atoms in the ground state of any transition that is resonantly excited by the probe laser. Therefore, we expect to see resonances only when a ground state sub-level is occupied and the probe frequency matches an allowed transition to the excited state sub-levels.

Experimentally, when these two conditions are met, atoms are ejected from the

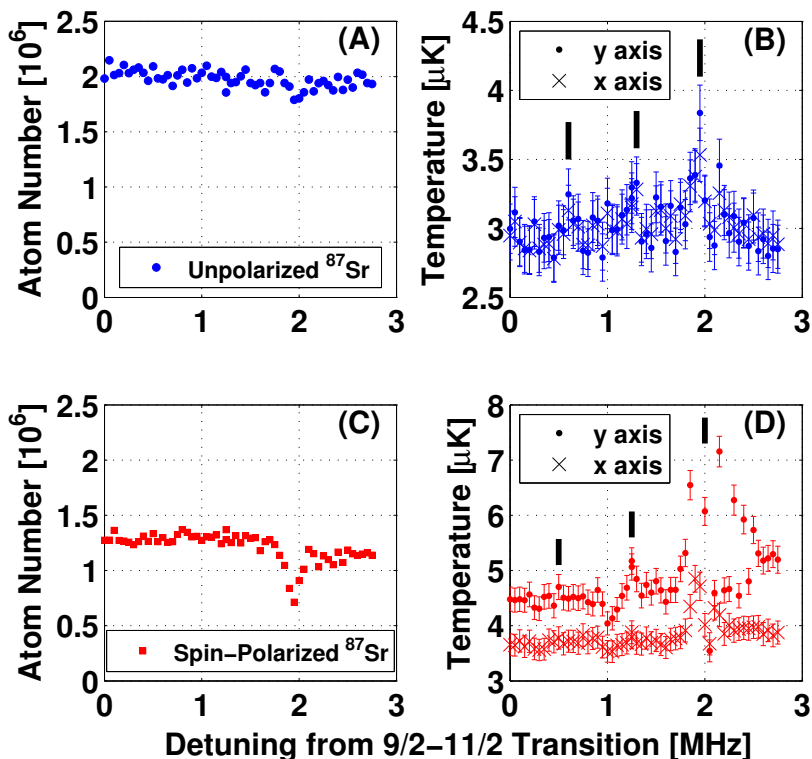


Figure 4.4 : Spectra comparing spin-polarized ^{87}Sr to unpolarized ^{87}Sr . Resonances appear when a spin state is occupied and the probe beam causes loss from the trap. (A) The number of atoms as a function of the frequency of the probe beam when no pump beam has been applied. (B) The sample temperature without applying the pump beam, also as a function of the probe beam frequency. Peaks in the temperature which are thought to correspond to resonances are marked by solid black lines. The frequency splitting between these resonances is ~ 0.75 MHz, a value consistent with the calculated splitting from Eq. 4.1. The temperature is arguably a better measure of the spectrum because it is more sensitive to population in a spin level than is the number loss. (C) and (D) contain the number and temperature spectra taken with the pump beam applied. This data shows that our light must be σ^+ polarized because excitation appears blue-detuned from resonance. In the case of (D), the temperature calculated from the size in the vertical (y) axis is thought to be warmer than that in the horizontal (x) axis because the pump beam runs parallel to the vertical axis. The relative size of different peaks in a number spectrum (either A or C) is not by itself indicative of the atom population of that sub-level because the Clebsch-Gordan coefficients differ between the transitions. However, the growth of one peak in the polarized spectrum of panel (C) relative to the same peak in the unpolarized spectrum in panel (A) suggests that we are changing the spin-polarization of the sample.

trap due to heating. Though this atom loss indicates that atoms were present, the temperature of the sample is often a more sensitive probe because heating from the probe laser occurs even when there is no number loss. Figure 4.4 shows the spectrum obtained from such a measurement: both the number of atoms and the temperature of the sample are plotted against the detuning relative to the $F = 9/2 \rightarrow F = 11/2$ resonance. Panels (A) and (B) show the spectrum of the unpolarized sample. The lack of clear structure in the number spectrum implies that the atoms are not concentrated in one state. Further, the temperature spectrum reveals heating at multiple frequencies, also implying that atoms are in multiple states. Both results are consistent with a relatively unpolarized sample. In contrast, panels (C) and (D), corresponding to the spin-polarized sample, contain a more prominent resonance. The increased amplitude of the loss relative to the same resonance in the unpolarized spectrum indicates that we have indeed altered the spin-polarization of the sample.

We can optimize the optical pumping process by varying how long the pump beam is applied (Fig. 4.5) and with how much intensity (Fig. 4.6). For these studies, the frequency of the probe laser is set to a frequency 1.95 MHz blue-detuned from the $F = 9/2 \rightarrow F = 11/2$ resonance, the location of the largest resonance in Fig. 4.4. Because most of the atoms are pumped into the 1.95 MHz-detuned state, when we probe the cloud with that light frequency, atom loss is induced and the changing amplitude of the resonance is our measure of the optical pumping efficiency. The first study shows the number of atoms in the 1.95 MHz-detuned state as a function

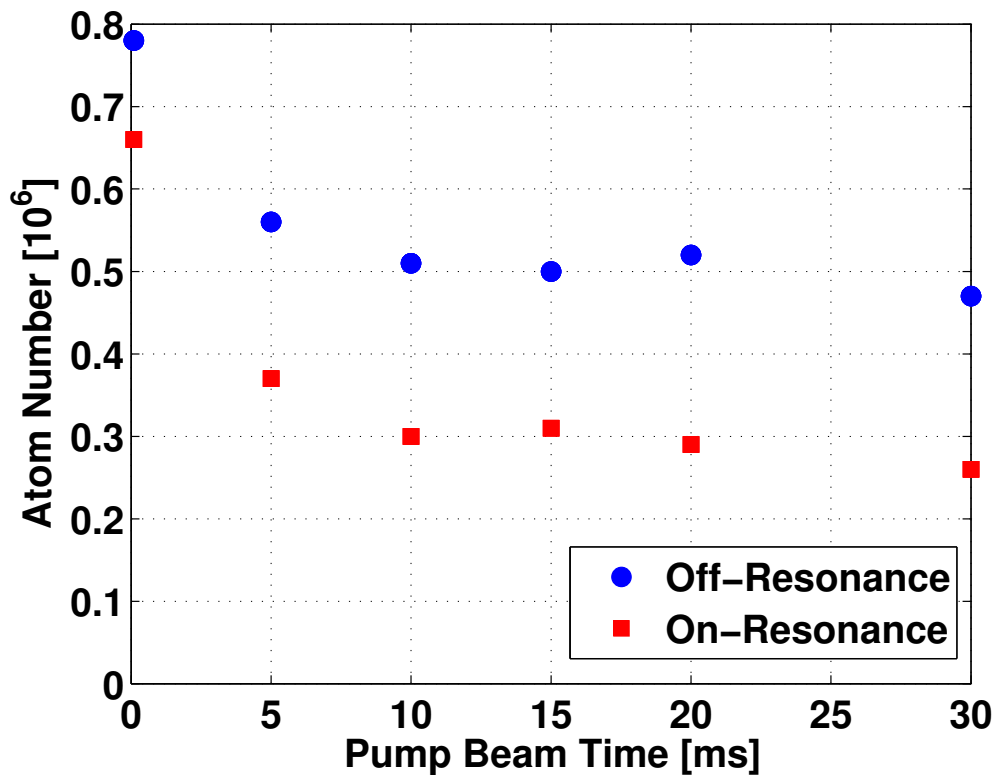


Figure 4.5 : Study of the number of atoms versus the amount of time that the pump beam is on when the pump beam is 1.95 MHz blue-detuned from the $F = 9/2 \rightarrow F = 11/2$ transition. The number from when the pump beam is far off-resonance is also plotted for comparison. Observing more loss implies that more atoms have accumulated in this sub-level when the probe beam is applied. After about 10 ms, it appears that the amount of optical pumping stops increasing. This result is consistent with a scenario where all atoms have been pumped into the dark $F = 9/2$ sub-level of the ground state.

of the time that the pump laser is applied to the atoms with an intensity of 0.5 mW/cm². For comparison, the number of atoms with the pump beam off-resonance is also plotted; because some atoms remain in other states, we look at the difference between the two data sets for optimization. When the pumping laser is on-resonance, the number loss initially increases with more pumping time. Then, after about 10 ms of pumping time, we observe no further increase in the difference in the loss. If the sample is mostly spin-polarized at this point, it makes sense that atom loss would cease: atoms may have accumulated in the $F = 9/2$ dark state where no loss will occur because atoms there cannot scatter right circularly polarized light. The second study (Fig. 4.6) shows the number of atoms as a function of the pump beam intensity. Here, the pump beam is on for 10 ms. Once the pump beam exceeds 0.5 mW/cm², the loss stops increasing. As in the study of the pump time, this result is consistent with the transfer of atoms to the $m_F = 9/2$ dark state. Taken together, these studies suggest that we are able to significantly increase the spin-polarization of our ⁸⁷Sr samples.

Another question we answer about spin-polarized samples is how long the spin-polarization lasts. To check for persistence of the spin-polarization, we hold atoms in the optical dipole trap for either 0.75 s (short) or 5 s (long) after extinguishing the pump beam and then probe the sample by scanning the probe laser across the resonance that is 1.95 MHz blue-detuned from the $F = 9/2 \rightarrow F = 11/2$ transition. If the spin-polarization diminishes during the long hold time, the amplitude of the

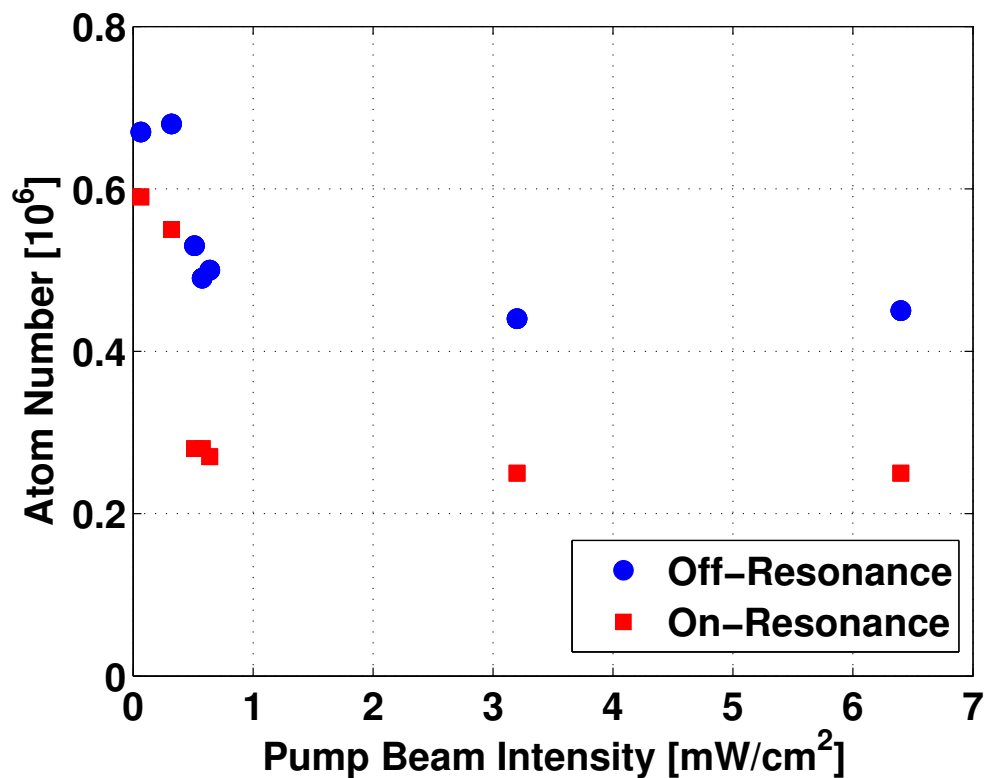


Figure 4.6 : Study of the number of atoms versus the pump beam intensity when the pump laser is 1.95 MHz blue-detuned from the $F = 9/2 \rightarrow F = 11/2$ transition. For comparison, the number of atoms from when the pump beam is far off-resonance is also shown. For the 10 ms that the pump beam is on, it appears that no further loss is seen above an intensity of ~ 0.5 mW/cm², implying that atoms are concentrated in the dark $F = 9/2$ sub-level which is unaffected by right circularly polarized light.

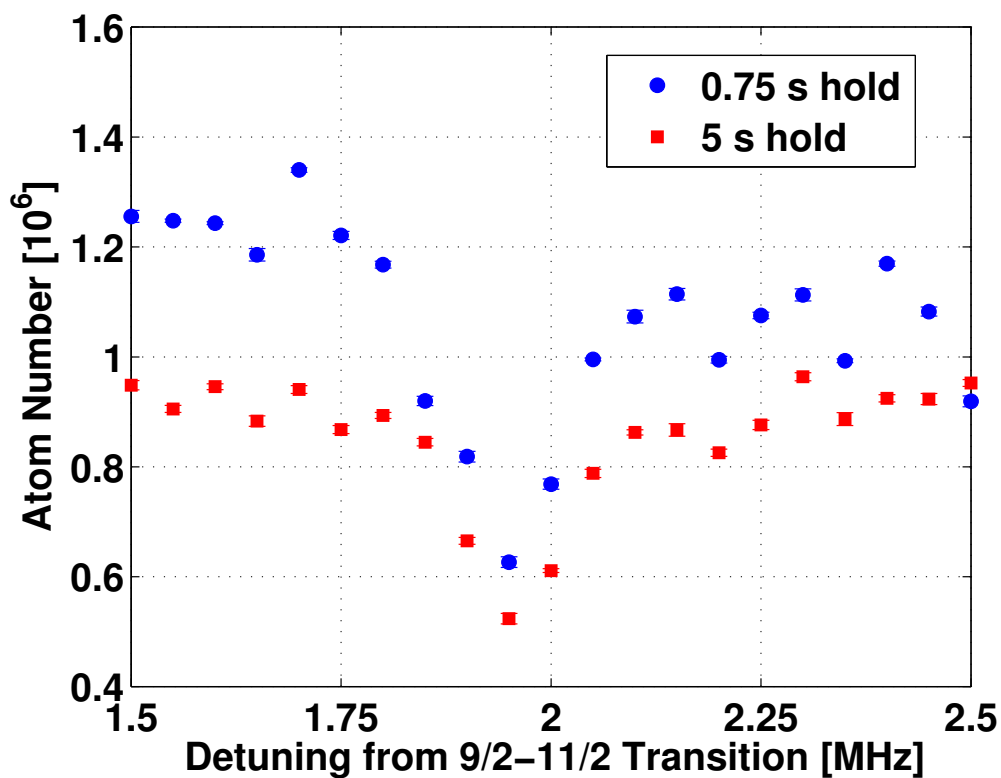


Figure 4.7 : Study of the duration of the spin-polarization. In one case, the spin-polarized sample is probed shortly after the pump beam is applied (0.75 s), while in the other case, the sample is probed a longer time (5 s) after the pump beam is applied. Qualitatively, the spectra look similar. The small amount of background loss is ascribed to processes such as one-body losses and evaporation in the optical dipole trap. Otherwise, the relative amplitude of the two data sets is comparable, thereby indicating that the degree of polarization is not changing substantially on a longer time scale.

resonance will decrease relative to the amplitude for the short hold time. Figure 4.7 compares the spin-polarization for the two hold times. Qualitatively, the spectra look similar, though the spectrum taken after being held in the optical dipole trap for 5 s has a lower overall number of atoms due to normal decay processes. More importantly, the relative amplitudes of the resonance at 1.95 MHz, at both short and long hold times, are of the same order. This measurement is an approximate one, and it is possible that the spin-polarization is slowly relaxing over time due to something like misalignment of the pump beam with the quantization axis defined by the magnetic field. However, we can rule out decay of the polarization on a time scale as fast as hundreds of milliseconds.

The final measurement that demonstrates spin-polarization is unforced evaporation of ^{87}Sr in the optical dipole trap. The rate of evaporation shows the spin-polarization of a sample because the rate of collisions that lead to evaporation depends on the distribution among the spin states of fermionic atoms. For low spin-polarization, evaporation will occur nearly as quickly as with samples of ^{84}Sr ($a_{84} = 123a_0$ [41, 78]). Conversely, if a sample of ^{87}Sr atoms is 100% spin-polarized, it will behave more like ^{88}Sr ($a_{88} = -1.4a_0$ [41, 78]), where the small background scattering length means effectively that no interactions take place and evaporation is slow. Unforced evaporation experiments are a good way to study spin-polarized samples because the number and temperature evolution of the atoms reflect the rate of evaporation of the system and allow us to quantify the degree of spin-polarization.

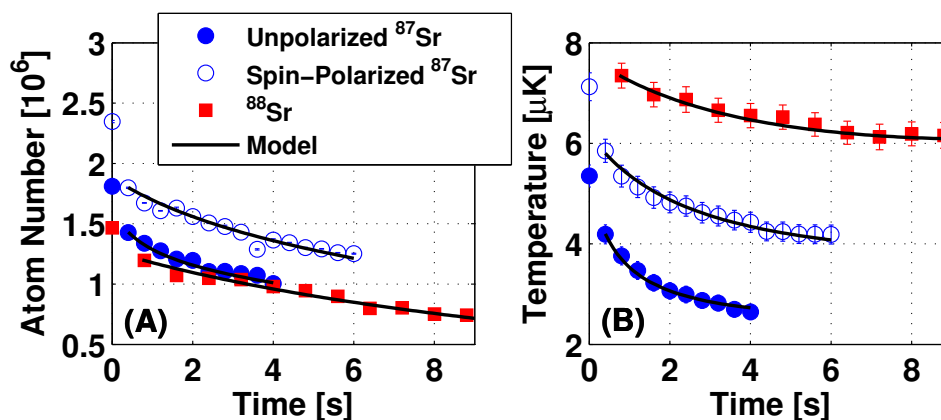


Figure 4.8 : A comparison of spin-polarized ⁸⁷Sr to unpolarized ⁸⁷Sr. (A) The number of atoms during the unforced evaporation trajectory decreases due to one-body loss and evaporation. (B) The sample temperature during this same time decreases as evaporative processes remove the most energetic atoms. Spin-polarized ⁸⁷Sr does not evaporate efficiently by itself and thus behaves more like the weakly interacting ⁸⁸Sr. The unpolarized sample of ⁸⁷Sr cools most quickly because it has atoms distributed among more spin states. Fits from the model of evaporative cooling discussed in the text are shown. No attempt is made to fit the model to the earliest time point in each data set because, at that point, many atoms that are not in the optical dipole trap are still present in the images, thus skewing the number and temperature measurement.

To compare the scattering properties of unpolarized and spin-polarized ^{87}Sr , we examine the number and temperature evolution of the samples (Fig. 4.8). For the spin-polarized sample of ^{87}Sr , the pump beam has been applied for 10 ms with an intensity of 0.5 mW/cm^2 . Data is collected by holding the sample in the optical dipole trap for times up to 10 seconds. During this time, the number of atoms decreases due to one-body losses and evaporation of the sample, while the average temperature decreases as a result of evaporation of the hottest atoms from the trap. The rates at which these processes occur reflect the scattering properties of the system. ^{88}Sr , with its weak interactions, cools more slowly than either ^{87}Sr sample. The spin-polarized ^{87}Sr shows a slower decrease in the atom number and temperature than unpolarized ^{87}Sr . Qualitatively, this behavior is consistent with a large scattering length and unpolarized sample, where fast collisions efficiently remove energetic atoms and decrease the temperature.

4.1.2 Modeling Unforced Evaporation of ^{87}Sr

To quantify the behavior, we use a model of the collisional dynamics [79] to reproduce the evolution of the sample and extract a value of the scattering length for each experimental dataset. The model is simplified, however, and can only treat single atom species with a single scattering length. Thus, for ^{87}Sr , in which identical states do not interact, the value of the scattering length extracted from the model is only an effective scattering length. Quantifying the exact effect is complicated, but as

an approximation, we note that evaporation is most sensitive to the average elastic collision rate (R_{el}) in the sample. To determine how much the spin-polarization would affect R_{el} and the observed effective scattering length, we introduce an approximate form for the elastic scattering rate, as suggested by [27]:

$$R_{el} = \frac{q-1}{p} n \sigma_{87} \bar{v}, \quad (4.2)$$

where $\sigma_{87} = 4\pi a_{87}^2$ is the elastic collision cross section for non-identical particles, n is the density, \bar{v} is the mean relative velocity of the particles, p is the total number of possible spin states atoms can occupy, and q is the actual number of spin states that are occupied. Atoms only collide with atoms in other spin states, so the collision rate is reduced by a factor of $(q-1)/p$. The numerical model assumes that the elastic collision cross section is for identical bosons ($\sigma_{obs} = 8\pi a_{obs}^2$), so this suggests a relationship between the true scattering length and the scattering length from the model of

$$a_{obs} = \sqrt{\frac{q-1}{2p}} a_{87}. \quad (4.3)$$

Here, $p = 10$, so when atoms are distributed evenly over all ten states ($q = 10$), the observed scattering length should be nearly $65a_0$, as seen in Fig. 4.9. When all the atoms are in a single spin state ($q = 1$), then the effective scattering length should be zero as no interactions will take place.

To test the validity of the model, we examine data showing the evolution of ^{84}Sr in the optical dipole trap. Unlike ^{87}Sr , where spin complicates the picture, and ^{88}Sr , which has weak, attractive interactions, the analysis of ^{84}Sr is more straight-

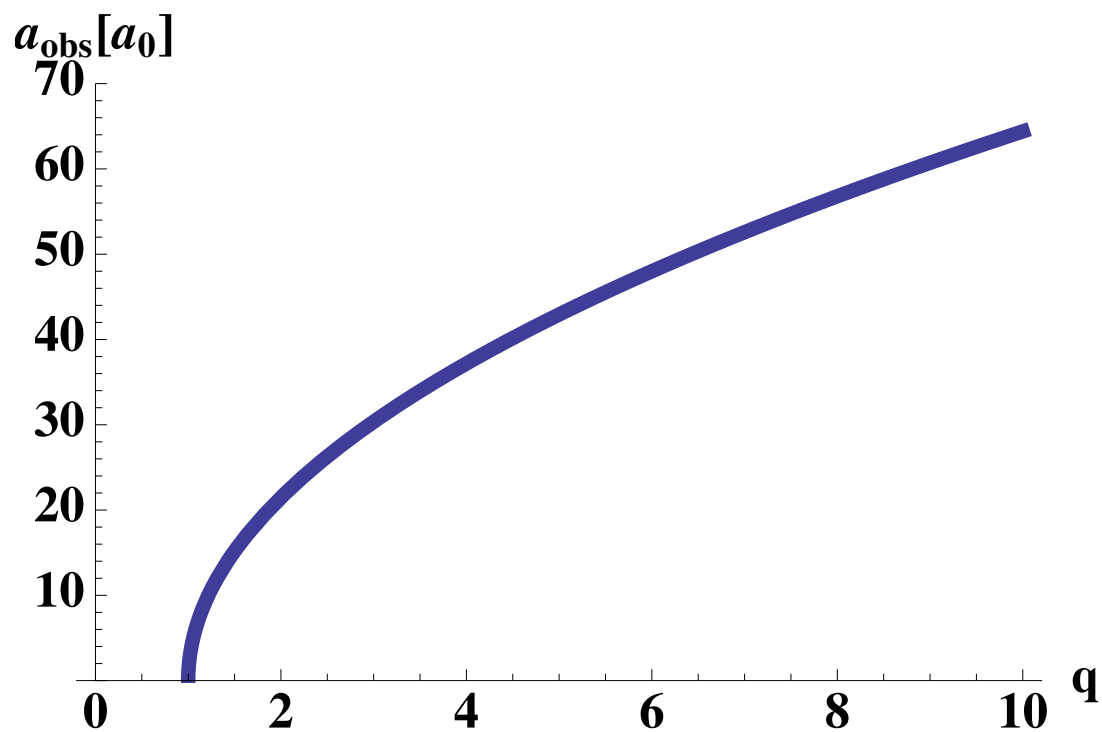


Figure 4.9 : Effective scattering length as a function of q , the number of occupied states. If there is little spin-polarization and atoms are evenly spread among all 10 spin levels ($q = 10$), the effective scattering length is about $64a_0$. At the opposite extreme, a completely spin-polarized sample has no interactions and has an effective scattering length of zero. Our model and data suggest that both the “unpolarized” ($q = 2.8$) and “polarized” ($q = 1.3$) samples have a high degree of spin-polarization.

forward because it is a boson and because it has strong, repulsive interactions. Seeing reasonable behavior for ^{84}Sr will build confidence in the results for the other isotopes. Experimental details of the trapping and cooling of ^{84}Sr are beyond the scope of this thesis [53], but Fig. 4.10 parallels Fig. 4.8 in showing the number and temperature of ^{84}Sr as a function of the time held in the optical dipole trap. The same numerical model [79] shows fits to the data and yields a scattering length, $120 \pm 20 a_0$, close to the $122.7 \pm 0.3 a_0$ measured in the two-photon photoassociation experiment [41]. Finally, the ratio of the trap depth to the temperature of the atoms, η , is about 14.

As another check of the validity of our model, we use a different numerical model of evaporation as developed by Comparat et al. [80] to see if, for similar conditions, it predicts similarly large values of η . The η values for ^{84}Sr that the Comparat approach predicts ($\eta = \sim 14$) are in good agreement with the range of values produced by our model, giving us more confidence in the accuracy of the numerical model used throughout this chapter.

Table 4.1 summarizes the values of the scattering length determined from our model. The values for ^{87}Sr are much lower than the value measured by two-photon photoassociation [41], suggesting that the samples could be highly spin-polarized. Turning Eq. 4.3 around and putting in the observed scattering lengths from Table 4.1, we find $q = 2.8$ for the unpolarized ^{87}Sr samples and $q = 1.3$ for the spin-polarized sample. These results are consistent with the qualitative picture from the spectroscopy in Fig. 4.4, where fewer peaks appeared in the spectrum of the polarized

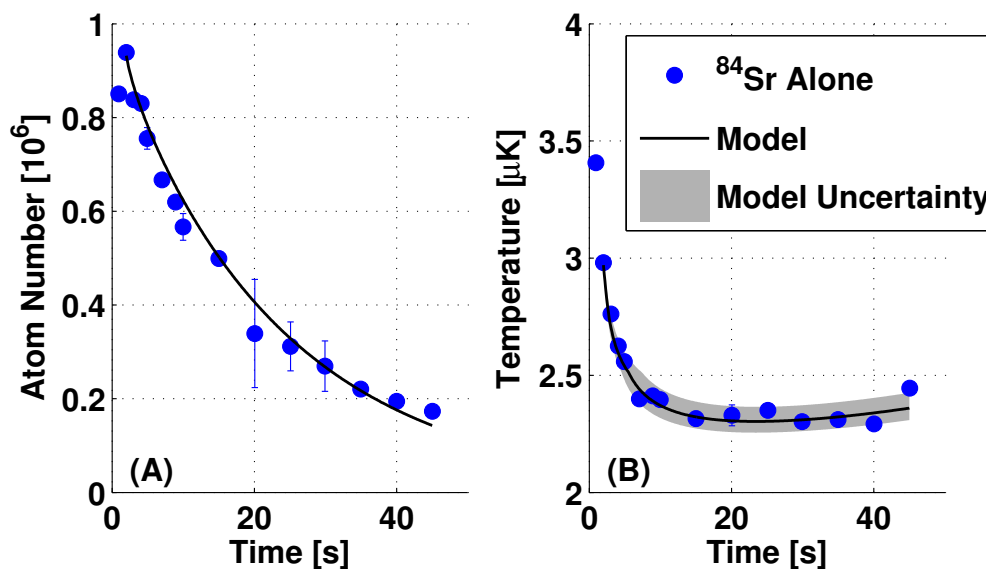


Figure 4.10 : Time evolution of a sample of ^{84}Sr . (A) The number of atoms during the unforced evaporation trajectory decreases due to one-body loss and evaporation. (B) The sample temperature during this same time decreases as evaporation processes remove the most energetic atoms in the sample. Compared to ^{87}Sr and ^{88}Sr , interpretation of the dynamics of ^{84}Sr is straightforward because it is a boson with a relatively large and positive scattering length. Therefore, it is a good system with which to test the numerical model of sample evolution discussed in the text. The model represents our best guess for the optical dipole trap power and waist values. For these parameters, the scattering length is found to be $120 \pm 20a_0$, in reasonable agreement with previous measurements of the scattering length [41, 78]. The shaded area represents the $\pm 20a_0$ region of the model. For the trap depths considered here, η values for ^{84}Sr are around 14.

sample as compared to unpolarized samples.

Table 4.1 : Scattering lengths, extracted from a model of collisional dynamics [79], for unpolarized ^{87}Sr , spin-polarized ^{87}Sr , and ^{84}Sr . All isotopes in this study are loaded by themselves in the optical dipole trap. I list values of the scattering length obtained from two-photon photoassociation spectroscopy [41] for comparison. The rough agreement of the ^{84}Sr scattering length with the value from 2-photon photoassociation spectroscopy (PAS) supports the accuracy of the model, so the fact that the observed scattering lengths of ^{87}Sr are much smaller than the 2-photon PAS scattering lengths suggests that the samples have a high degree of spin-polarization.

Isotope	Spin-Polarized?	From Model	From 2-photon PAS
^{87}Sr	No	$29 \pm 2a_0$	$96a_0$
^{87}Sr	Yes	$12 \pm 2a_0$	$96a_0$
^{88}Sr	N/A	$6 \pm 2a_0$	$-1.4a_0$
^{84}Sr	N/A	$120 \pm 20a_0$	$123a_0$

It is worth mentioning that the approach to spin-polarization presented here is not especially useful for increasing the phase space density in samples of ^{87}Sr because the pump laser reduces the atom number and increases the temperature. Future work will focus on methods for spin-polarization without the attendant loss of phase space density, with application to producing fermionic quantum degenerate gases of ^{87}Sr . Meanwhile, because the current work benefits from the higher number of collisions that occur in a less spin-polarized sample, the ^{87}Sr samples studied in the remainder of this thesis are unpolarized.

4.2 Mixtures of ^{87}Sr and ^{88}Sr

One can learn more about the scattering properties of ^{87}Sr and ^{88}Sr by loading a mixture of the two into the optical dipole trap and comparing the interactions of the mixture to how the isotopes behave by themselves. As in the previous section, samples are studied by observing them in the optical dipole trap for times up to 10 seconds, and values of the scattering length are obtained for each dataset using the same model of collisional dynamics [79].

First, we briefly examine the behavior of the isotopes trapped alone. Figure 4.11 summarizes the number and temperature evolution of ^{87}Sr (unpolarized) and ^{88}Sr ; Table 4.1 lists the values of the scattering length obtained for the single (unmixed) isotopes in Fig. 4.11. As previously discussed, the slow temperature evolution of ^{88}Sr alone in the optical dipole trap reflects its small background scattering length. Atoms in this situation are weakly interacting, and elastic collisions are too infrequent to lead to significant evaporative cooling. Two-photon photoassociation gives the scattering length as the limit of $a = \sqrt{\sigma/(8\pi)}$ as the collision energy approaches zero. However, at temperatures of a few μK , the energy dependence is significant, thus changing the effective scattering length. Figure 4.12 shows the cross section, σ , as a function of the collision energy. Averaging over the collision energies present in the thermal sample means that the cross section never reaches zero, consistent with the value of the scattering length ($6a_0$) we extract from the model (Table 4.1). On the other hand, the larger background scattering length of ^{87}Sr means that ^{87}Sr by itself reaches

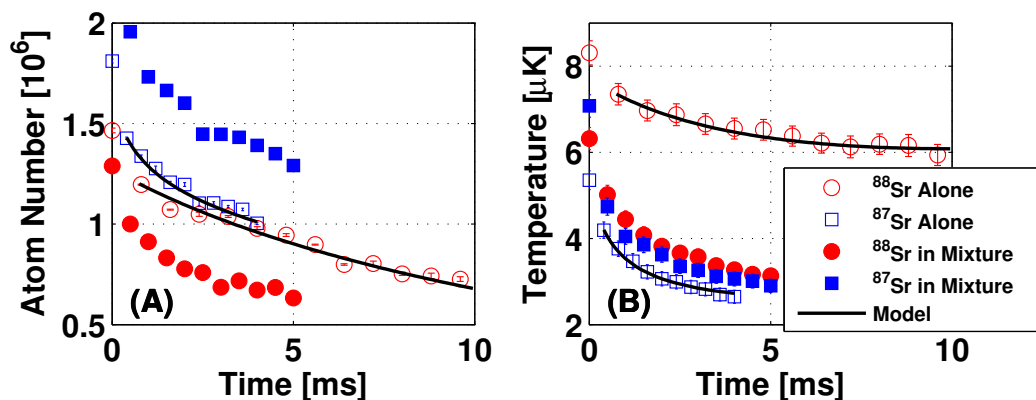


Figure 4.11 : Comparison of the lifetimes of single or mixed isotopes loaded in the optical dipole trap. (A) The number of atoms during the unforced evaporation trajectory decreases due to one-body loss and evaporation. Here, the initial number of ^{87}Sr atoms is about twice the initial number of ^{88}Sr . (B) The sample temperature during this same time decreases as evaporation processes remove the most energetic atoms in the sample. ^{88}Sr , with its small background scattering length, cools very slowly when it is alone in the trap. In contrast, ^{87}Sr evaporates to a colder temperature more quickly because of its considerably larger background scattering length. When mixed, however, ^{87}Sr and ^{88}Sr equilibrate at an intermediate temperature reflecting the role of ^{87}Sr as an intermediary for ^{88}Sr collisions. That ^{88}Sr ends up significantly colder in a mixture than when alone is strong evidence that ^{87}Sr is sympathetically cooling ^{88}Sr . A model describing both the number and temperature evolution of the sample matches the data and provides an estimate of the scattering length for each of the isotopes when alone in the trap. The model does not account for multiple species with different scattering lengths, so no model fit is shown for the mixed isotope data.

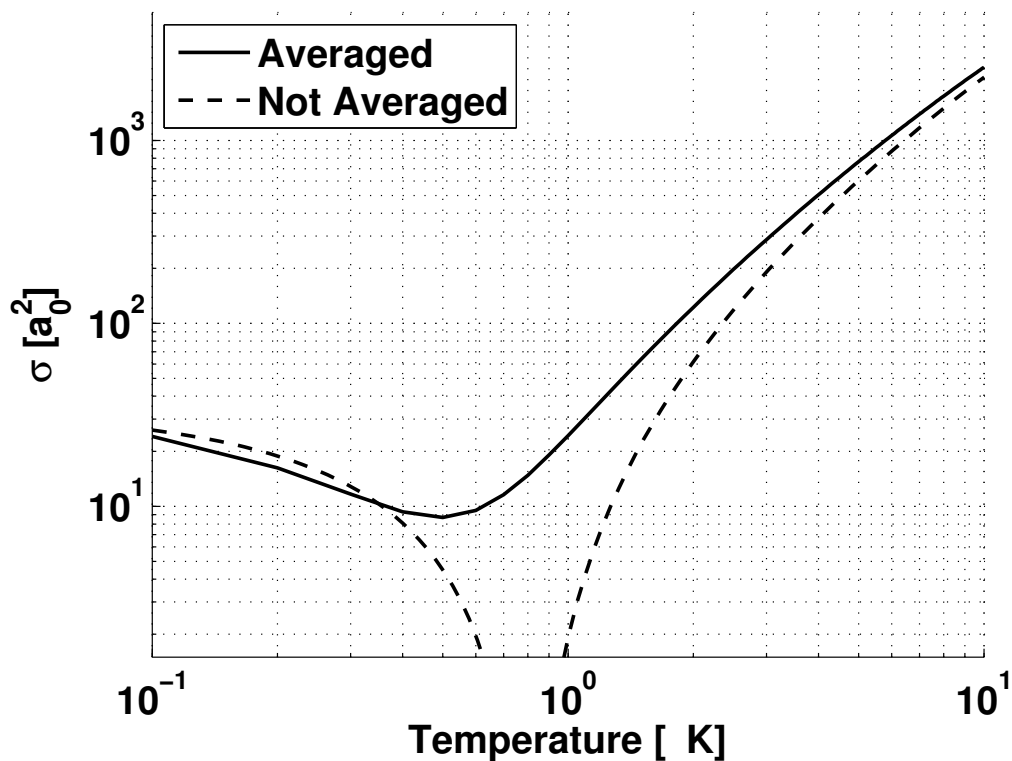


Figure 4.12 : Collision cross section as a function of temperature. For a thermal sample with a Maxwell-Boltzmann distribution of energies, thermal averaging means that the scattering cross section does not become zero-valued. Averaging of the collision cross section accounts for the higher value ($a_{scat} = \pm 6a_0$) of the ^{88}Sr scattering length than one would expect from two-photon photoassociation experiments ($a_{scat} = -1.4a_0$).

significantly lower temperatures than ^{88}Sr alone because more frequent collisions lead to increased evaporation.

More interesting behavior, however, occurs when we mix ^{87}Sr and ^{88}Sr , with about twice as many ^{87}Sr as ^{88}Sr atoms in the mixture. The presence of ^{87}Sr in the system allows ^{88}Sr atoms to evaporate more efficiently, and as a consequence, ^{88}Sr atoms

reach a colder temperature than when they are alone in the trap. The large ^{87}Sr - ^{88}Sr scattering length insures that their temperature evolution is similar for most of the evaporation trajectory. Atoms of ^{87}Sr , of course, are heated by being in the mixture, but this thesis emphasizes cooling the boson, ^{88}Sr , rather than the fermion, ^{87}Sr . No value of the scattering length is obtained for the mixture, but future work may extend our model to treat mixtures of particles with different collision cross sections.

Another important aspect of the data in Fig. 4.11 is the thermalization time for ^{87}Sr and ^{88}Sr . Thermalization, the time scale on which the temperatures of the species converge, occurs as a result of collisions between species. There is a slight offset in the final temperature of ^{88}Sr in the mixture, relative to ^{87}Sr , but it is roughly constant ($\sim 2 \mu\text{K}$) after about 0.5 s of evaporation time. We believe the offset results from having blown away ^{87}Sr atoms for imaging using the $F = 9/2 \rightarrow F = 11/2$, $(5s^2)^1\text{S}_0 - (5s5p)^3\text{P}_1$ transition. At 0.5 s hold time, the two isotopes already have about the same temperature, so 0.5 s should be an upper limit for the thermalization time. To check this claim, I calculate the elastic scattering rate of atoms for a high- η trap (trap depth \gg atom temperature) [79]:

$$\Gamma_{el} = \frac{\sqrt{2}}{2^{3/\gamma}} \sigma_{el} \bar{v} n_0. \quad (4.4)$$

Here, γ is a power which varies by the type of potential experienced by the atoms, σ_{el} is the elastic collision cross section, \bar{v} is the mean atomic velocity, $[(8k_B T)/(\pi m)]^{1/2}$, and n_0 is the peak density of the sample. For a mixture of ^{87}Sr and ^{88}Sr in a parabolic trap ($\gamma = 2$), σ_{el} will be the $4\pi a_{scat}^2$ for distinguishable particles, with a value of a_{87-88}

$= 55a_0$ [41].

Figure 4.13 shows the collision time ($\tau_{collision} = 1/\Gamma_{el}$), calculated from Eq. 4.4, as a function of temperature for values of the peak density of $0.5 \times 10^{19} \text{ m}^{-3}$, $1 \times 10^{19} \text{ m}^{-3}$, and $5 \times 10^{19} \text{ m}^{-3}$. The densities of ^{87}Sr and ^{88}Sr are roughly equal, so for a density of about $1 \times 10^{19} \text{ m}^{-3}$ and a temperature of about $6 \mu\text{K}$, Fig. 4.13 gives $\tau_{collision} \approx 0.05 \text{ s}$. Therefore, in 0.5 s , around 10 collisions ought to occur. Since previous theoretical results have shown that it only takes about 2.7 collisions for gases to thermalize [81], it is reasonable to expect that ^{87}Sr and ^{88}Sr will thermalize in less than 0.5 s of unforced evaporation.

The dramatic decrease in the temperature of ^{88}Sr when it is mixed with ^{87}Sr is a promising development. Being able to sympathetically cool with ^{87}Sr means that producing the conditions for quantum degeneracy of ^{88}Sr is possible with forced evaporation of atoms from the optical dipole trap, as will be seen in chapter 5.

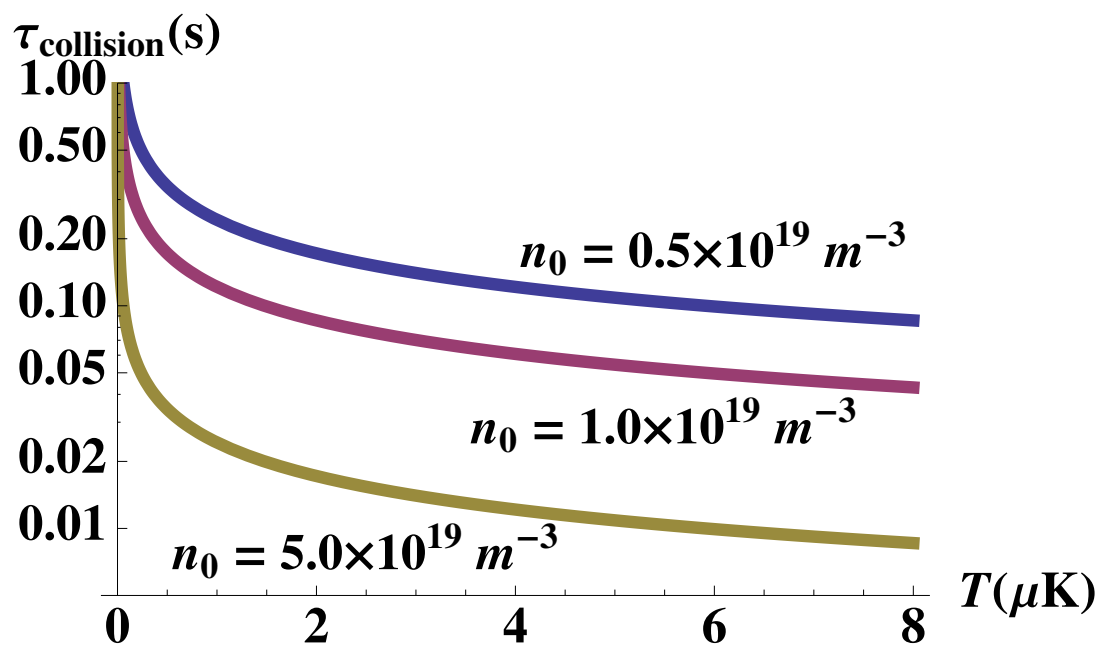


Figure 4.13 : Calculation of the time per elastic collision as a function of temperature for three different sample densities. Thermalization rates in a mixture of ^{87}Sr and ^{88}Sr depend on how quickly collisions occur. For experimental densities on the order of 10^{19} m^{-3} , nearly 10 collisions per second occur. Because 2.7 collisions are required for thermalization [81], thermalization in our samples should occur on a time scale on the order of a hundred milliseconds.

Chapter 5

Production of BEC by Forced Evaporation of Mixtures of ^{87}Sr and ^{88}Sr

The addition of ^{87}Sr to sympathetically cool ^{88}Sr is the crucial step which overcomes the weak interaction of ^{88}Sr atoms and enables forced evaporation to quantum degeneracy. I describe the forced evaporation trajectory before presenting the evidence which supports the observation of a BEC of ^{88}Sr .

5.1 Forced Evaporation Trajectory

Forced evaporation is necessary to increase the phase space density because unforced evaporation at a fixed trap depth becomes a less efficient process as the sample temperature decreases [82]. Forced evaporation overcomes the limitations of a fixed trap by slowly lowering the trapping potential to eject the highest energy atoms in the sample (Fig. 5.1), and leaving the remaining trapped atoms with less overall energy. However, sustaining evaporation requires the remaining atoms to continuously re-thermalize as the potential gets shallower [83]. This requirement means atoms must re-populate the high energy tail of the Maxwell-Boltzmann distribution. We allow re-thermalization by maintaining a roughly constant ratio of the trap depth to the sample temperature ($\eta = U / k_B T$) as long as we can. Our evaporation trajectory

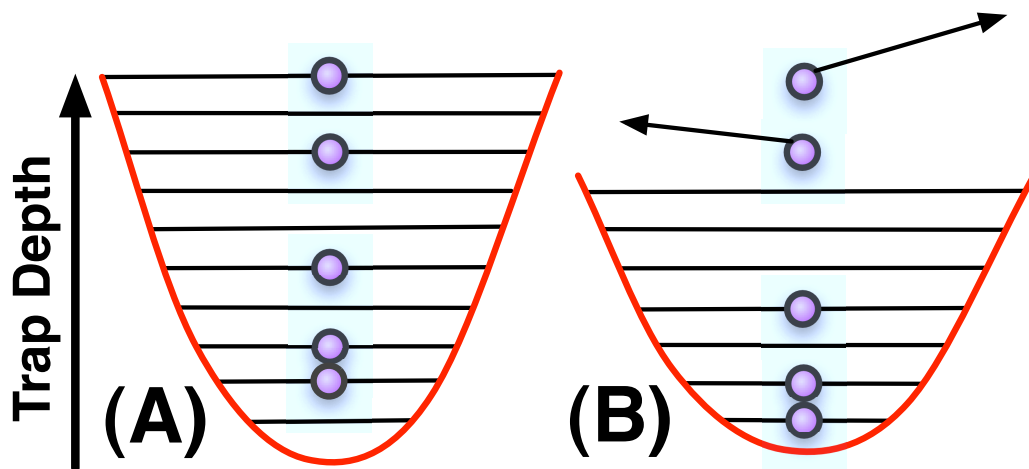


Figure 5.1 : A cartoon depicting forced evaporation of atoms. (A) A thermal sample of trapped atoms before evaporation has a Maxwell-Boltzmann distribution. (B) When the potential is lowered, high energy atoms are ejected, and the remaining atoms have less overall energy. Before the trap depth can be lowered again, the remaining atoms must re-thermalize if the phase space density is to be increased. In a magnetic trap, the gradient of the potential is maintained. However, in an optical dipole trap like the one used for our experiments, lowering the trap power changes the confinement.

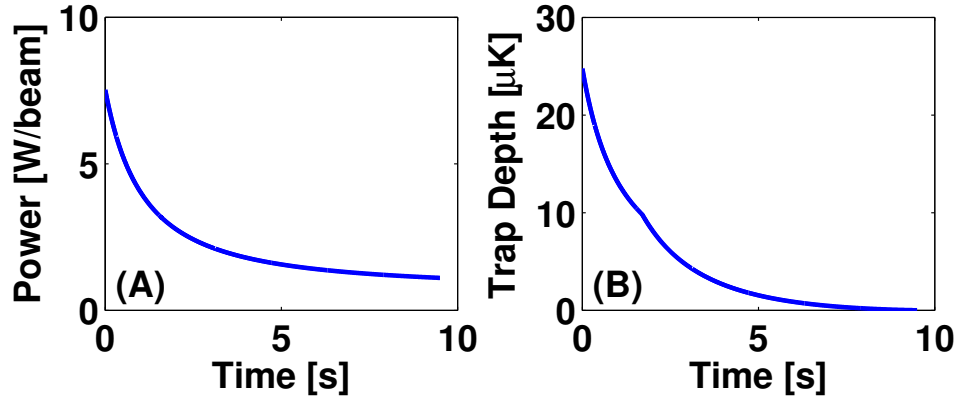


Figure 5.2 : Evaporation trajectory used to produce BEC of ^{88}Sr . (A) The power of each optical trap beam as a function of evaporation time. The optical trap beam power (P), shown as a function of evaporation time, is slowly lowered to eliminate the highest energy atoms from the trap. (B) The trap depth produced by the geometry of the beams. Unlike the beam power, the slope of the trap depth steepens at one point during the trajectory. The trap has weakened enough at this point that gravity begins to have a larger effect on the atoms. Nevertheless, as the overall temperature of the sample is reduced, the phase space density of the remaining atoms increases.

(Fig. 5.2) is based on the scaling laws derived by O'Hara et al. [84]. The trajectory,

lasts about 10 seconds and is described by

$$P(t) = \frac{P_i}{\left(1 + \frac{t}{\tau}\right)^\beta} + P_{offset}, \quad (5.1)$$

where P is the optical trap power and t is the time held in the optical dipole trap. τ

is related to η and the initial collision rate, γ_i , as

$$\frac{1}{\tau} = \frac{2}{3}\eta'(\eta - 4)\exp(-\eta)\gamma_i, \quad (5.2)$$

and β is related to η as

$$\beta = -2(\eta' - 3)\eta'. \quad (5.3)$$

In both Eqs. 5.2 and 5.3, $\eta' = \eta + (\eta - 5)/(\eta - 4)$. O'Hara et al. design this trajectory neglecting gravity [84], but for strontium in this trap, gravity has a substantial effect near the end of evaporation. Therefore, P_{offset} is set near the minimum optical trap power that still holds atoms against gravity. The values used for our experiment are $P_i = 6.9$ W, μK , $\tau = 1.5$, $\beta = 1.4$, and $P_{offset} = 0.7$ W.

While the power of the optical trap beam shown in Fig. 5.2(A) is a smoothly varying function, the slope of the trap depth steepens at one point in the trajectory (B). We determine the trap depth by starting at the minimum at the center of the trap and searching for the saddle point along each axis. One saddle point (y) will be along the direction of gravity, and the other two saddle points (x and z) will be along each of the beams. The axis with the lowest saddle point determines the overall trap depth. Figure 5.3 shows the trap depth of each axis for the evaporation trajectory. The x and z trap depths are very similar, only differing because the recycled cross beam has 90% of the power of the input beam. The y trap depth, however, has a different character because of gravity. Early in the trajectory when the trap is deeper, gravity is only a minor perturbation to the trap depth, but as the power in the beams is reduced, gravity plays an increasingly large role. Just before 2 s of evaporation time, the trap depth in the y direction becomes shallower than the trap depth in the z direction, resulting in the change of slope seen in Fig. 5.2(B). Despite the change in slope of the trap depth, this trajectory should increase the phase space density (PSD) of the sample with only moderate loss of atoms from the trap.

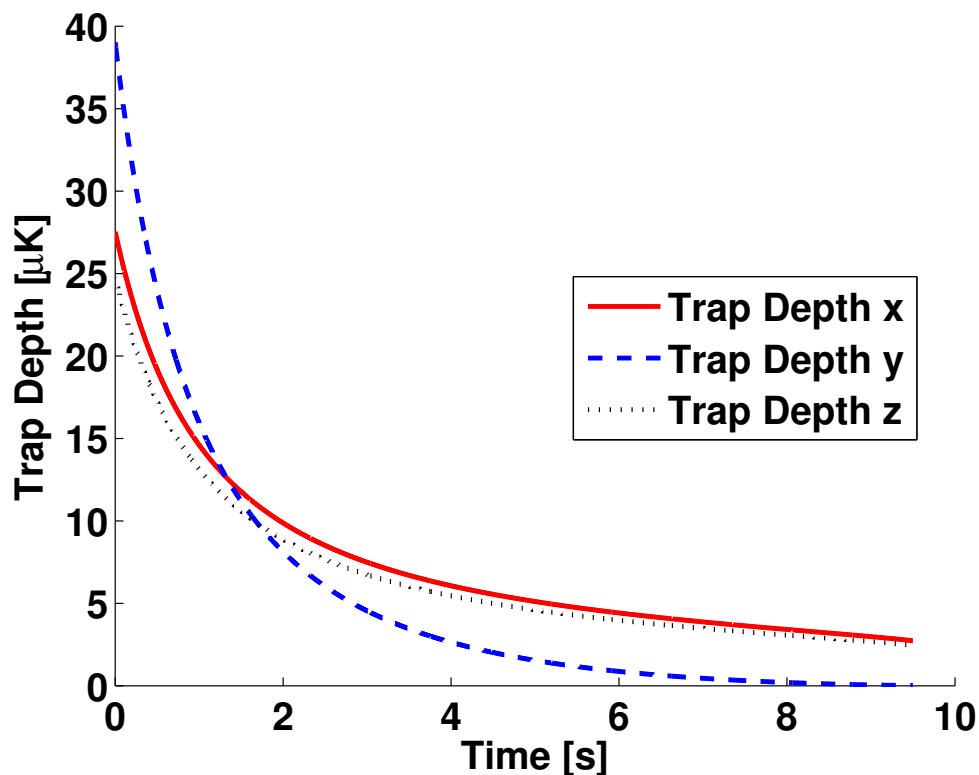


Figure 5.3 : Trap depths for each axis of the optical trap during evaporation. We calculate the trap depth in each axis independently (x is along one beam, z is along the other beam, and y is the direction of gravity). The axis with the lowest trap depth determines the overall depth of the trap at any given point in the trajectory. Early on, the z beam (which has only 90% of the power in the x beam) is the weakest axis. However, as we progress through the evaporation trajectory, the power of the beams is reduced and gravity begins to affect the y axis disproportionately. The slope of each of the axes is different, so when the trap depth in y becomes the weakest axis, there is a change in slope of the overall trap depth (Fig. 5.2(B)).

Applying this forced evaporation trajectory to the mixture of ^{87}Sr and ^{88}Sr successfully reduces the temperature of the mixture. In Fig. 5.4(A), we begin with about 1.3 times more ^{87}Sr atoms than ^{88}Sr atoms. However, the ratio changes such that there are about half as many atoms of ^{87}Sr than ^{88}Sr by the end of the evaporation trajectory. The final ratio is best seen in Fig. 5.4(C), which shows the final 3 seconds of evaporation. The changing ratio is consistent with a picture of evaporation where ^{87}Sr atoms collide both with other ^{87}Sr atoms and with ^{88}Sr atoms. Conversely, ^{88}Sr atoms primarily collide with ^{87}Sr atoms in the mixture, thus experiencing less overall loss.

Sympathetic cooling of the ^{88}Sr atoms by ^{87}Sr occurs as long as there remains a reasonable number of ^{87}Sr atoms, so the evaporation efficiency at the end may be reduced because of the smaller ^{87}Sr number. Ideally, the number of ^{87}Sr would not limit evaporation, but this is the disadvantage of using the number-limited (Fig. 2.8) ^{87}Sr to sympathetically cool ^{88}Sr . Here, the initial temperatures of the isotopes are different (Fig. 5.4(B)), but they come into equilibrium with each other and stay that way to the end of the trajectory. The overall reduction in temperature, in combination with the moderate number loss in ^{88}Sr , suggests that the sample may be approaching the conditions necessary for Bose-Einstein condensation of ^{88}Sr .

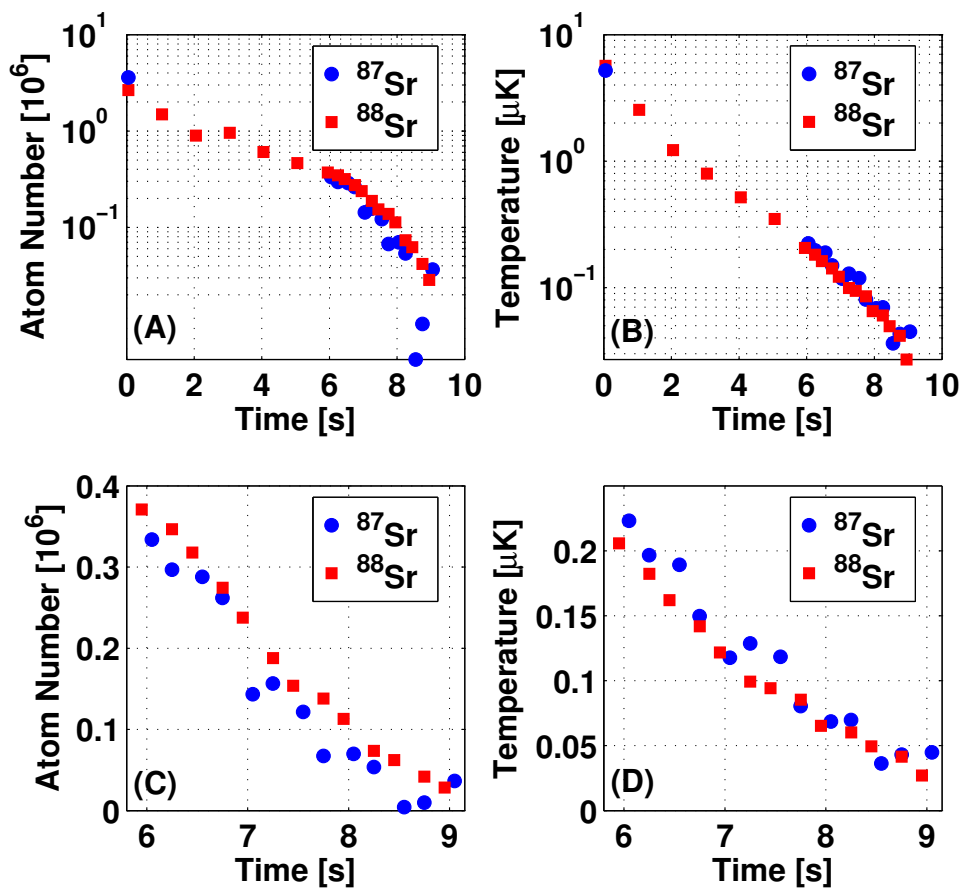


Figure 5.4 : Atom number (left) and temperature (right) evolution during forced evaporation of the mixture of ^{87}Sr and ^{88}Sr as ^{88}Sr approaches the transition to Bose-Einstein condensation. (A) and (B) have a log scale showing the number and temperature for the full evaporation trajectory, while (C) and (D) have a linear scale showing the final 3 seconds of evaporation in detail. We initially load about 1.5 times the number of ^{87}Sr atoms as ^{88}Sr atoms into the optical trap. More ^{87}Sr atoms are lost during evaporation, but the temperature of ^{87}Sr and ^{88}Sr atoms stays the same for most of the trajectory. Because of the sympathetic cooling that trapping ^{87}Sr enables, we are able to observe a Bose-Einstein condensate of ^{88}Sr near the end of this (typical) evaporation trajectory.

5.2 Evidence for Bose-Einstein Condensation

We see evidence of Bose-Einstein condensation in Fig. 5.5. The absorption images and density profiles are from select points of the sample evolution shown in Fig. 5.4. At first, around 5 s and 356 nK, the sample is still a thermal gas, but as evaporation proceeds, we see non-classical behavior in the deviation of the fits from the data. After 7.5 s and 77 nK, the high density peak of a BEC is visible, and finally, we end up with a pure condensate after about 9 s of evaporation.

We obtain quantitative information about the thermal cloud and the BEC by fitting images of the atom cloud with the distribution function for a Bose gas (solid lines). The column density, $n_{th}(x, y)$, is fit to [85]

$$n_{th}(x, y) = n_{th,peak} \frac{Li_2 \left[\zeta e^{\frac{x^2}{2\sigma_x} + \frac{y^2}{2\sigma_y}} \right]}{Li_2[\zeta]}, \quad (5.4)$$

with $n_{th,peak}$ as the peak density, σ_i as the horizontal or vertical cloud size, and $\zeta = e^{\mu/k_B T}$ as the fugacity. Further, μ is the chemical potential, k_B is Boltzmann's constant, T is the sample temperature, and $Li_n(\zeta) = \sum_{k=1}^{\infty} \zeta^k / k^n$ is the poly-logarithmic function of order n . We also fit the absorption images with a Maxwell-Boltzmann distribution (dashed lines), as we would treat a normal thermal gas. For a temperature well above the critical temperature (T_c) for formation of a BEC, a Bose distribution matches a Maxwell-Boltzmann distribution for the temperature of the atoms. The earliest panel of Fig. 5.5 shows that both fits essentially overlap one another. As the sample temperature drops, however, Bose statistics begin to affect the distribution

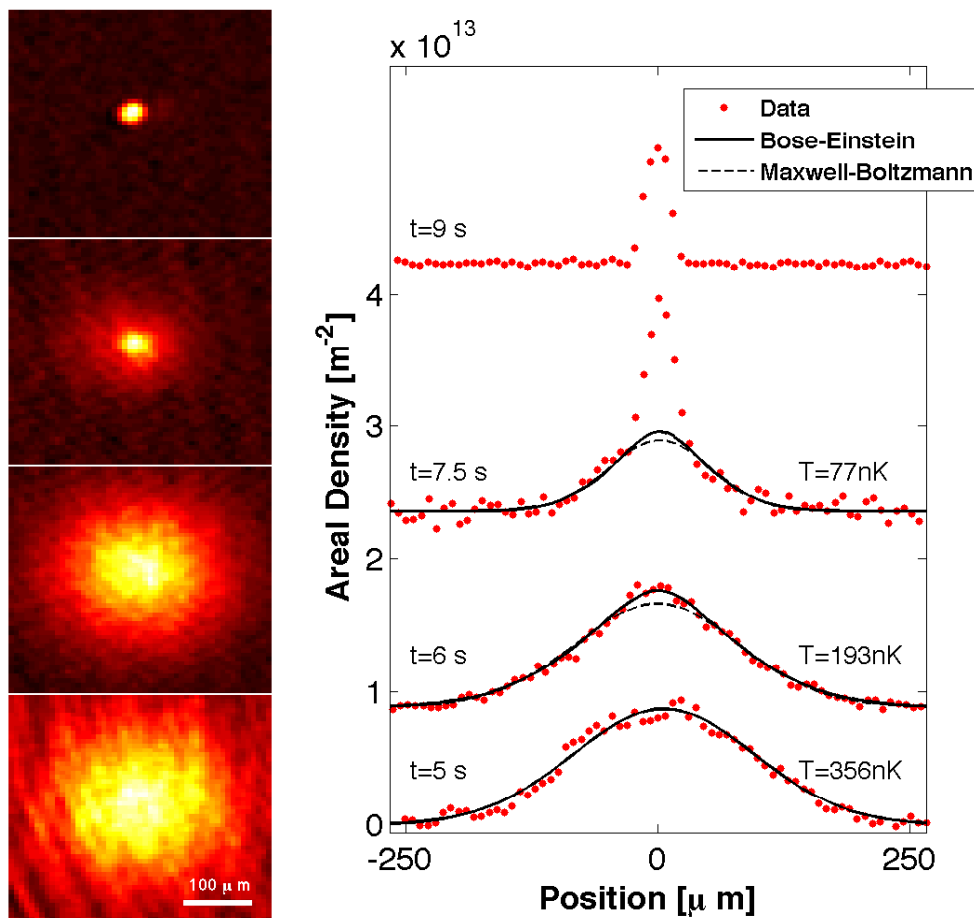


Figure 5.5 : Emergence of Bose-Einstein condensation of ^{88}Sr in absorption images (left) and areal density profiles (right). The evaporation times (t) and temperatures (T) for each sample are marked next to the areal density profiles which are from a vertical cut through the center of the cloud. We determine the temperature from a fit to the edges of the cloud using a two-dimensional Bose distribution function (solid line). For colder temperatures, this distribution differs from a Maxwell-Boltzmann distribution (dashed line) even for a non-degenerate gas (e.g. $t = 6$ s). At early times in the evaporation trajectory, there is only a thermal cloud of ^{88}Sr ($t = 5$ s). The bimodal distribution characteristic to Bose-Einstein condensation clearly appears around 7.5 s and a pure BEC of ^{88}Sr is observed at 9 s of evaporation.

even before the onset of quantum degeneracy. Figs. 5.5 and 5.6 both show the difference between a fit using the Bose-Einstein distribution and a fit using the classical Maxwell-Boltzmann distribution. As one should expect, the two fits diverge most strongly in the center of the sample where the density is highest. In the wings of the sample where the density is lower, atoms still have a Maxwell-Boltzmann velocity distribution, so the two fits match pretty well. The value of the fugacity for these fits is $\zeta \approx 1$, which implies that the sample must be nearing the critical temperature. These data clearly illustrate how Bose-Einstein statistics are more appropriate for fitting the sample than classical Maxwell-Boltzmann statistics even though no BEC has been observed at this point in the evaporation trajectory.

Unlike the data in Fig. 5.6, Bose-Einstein statistics are not sufficient to describe a bimodal distribution such as the one in the $t = 7.5$ s panel of Fig. 5.5. Here, the critical temperature for the sample has been passed: atoms in the dense core form the BEC, while the surrounding atoms remain thermally distributed. We treat this by fitting the thermal atoms in the wings using Bose-Einstein statistics (and setting $\zeta = 1$), while fitting the BEC component separately. To extract number and temperature information about the thermal component of the sample, we exclude a central region corresponding to the BEC and fit the wings of the distribution using Eq. 5.4. Figure 5.7(A) shows how the central region is excluded from the fit so that the Bose-Einstein fit is a good description of the behavior of the surrounding atoms. We obtain the temperatures shown in Fig. 5.5 from these fits to the wings.

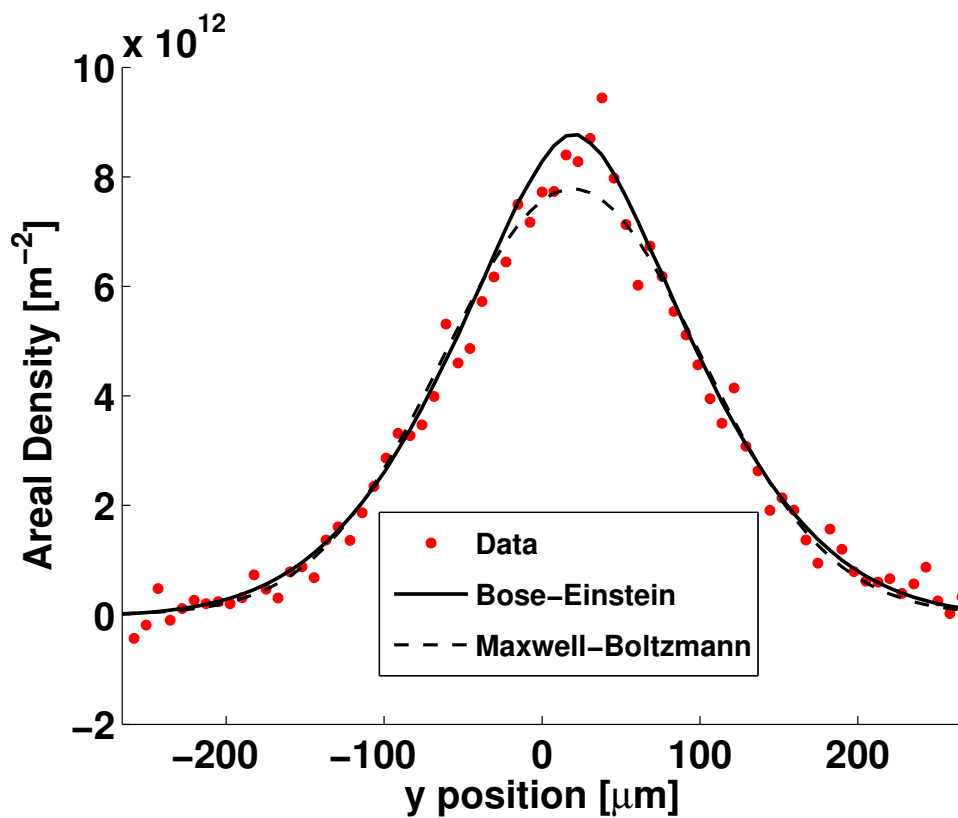


Figure 5.6 : Fitting of samples which are nearly quantum degenerate, but still have temperatures above the critical temperature. A fit using Bose-Einstein statistics (solid line; Eq. 5.4) describes the distribution better than a fit using Maxwell-Boltzmann statistics (dashed line). We extract the temperature of the sample using the Bose-Einstein statistics.

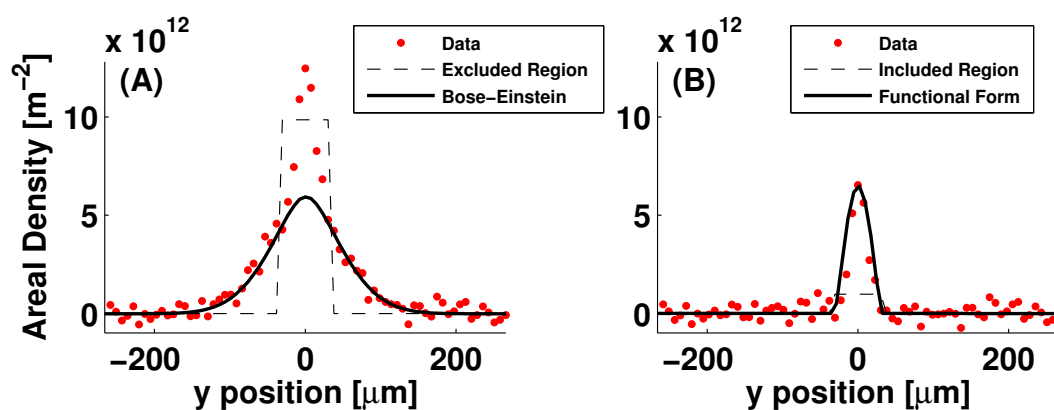


Figure 5.7 : An illustration of the procedure used to determine the temperature of the atom cloud when there is a bimodal distribution. (A) To accurately measure the temperature, we exclude a central region which encompasses the emerging BEC (dashed black line) and fit the remaining data with the Bose-Einstein distribution of Eq. 5.4 (solid black line), while setting the fugacity value equal to unity (i.e. the chemical potential is equal to zero). (B) The residuals from the fit, obtained by subtracting the fit from the data, show the BEC component of the overall cloud. As in (A), the dashed black line defines the region excluded from the fit. The BEC component is fit by the functional form defined in Eq. 5.5. For clarity in both panels, only a slice of the vertical axis through the cloud center is shown, but the entire cloud is fit in two dimensions to determine the temperature.

On the other hand, the pure BEC component shown in Fig. 5.7(B) is the difference between the bimodal distribution and the fit using Bose-Einstein statistics, and it can be fit using the functional form [86]

$$n(x, y) = \frac{5N_0}{2\pi R_x R_y} \left(1 - \frac{x^2}{R_x^2} - \frac{y^2}{R_y^2}\right)^{3/2} \theta \left(1 - \frac{x^2}{R_x^2} - \frac{y^2}{R_y^2}\right). \quad (5.5)$$

Here, N_0 is the number of atoms in the condensate, and R_x and R_y are the radii of the condensate. The Heaviside function (θ) is used because the parabolic form used to fit the BEC is ill-defined outside the BEC region. We use Eq. 5.5 to extract the number of condensate atoms.

A condensate of ^{88}Sr has a limited size because of the negative scattering length of ^{88}Sr . This means that the condensate will grow until the critical number of condensate atoms (N_{cr}) has been reached [87]:

$$N_{cr} = 0.575 \frac{a_{ho}}{|a_{88}|}. \quad (5.6)$$

Here, $a_{ho} = [\hbar/(m\bar{\omega})]^{1/2}$ is the harmonic oscillator length, where m is the atomic mass, \hbar is the reduced Planck constant, and $\bar{\omega}$ is the geometric average of the oscillator frequency. When the critical number is exceeded, the attractive interactions due to the negative scattering length cause collapse of the BEC [88, 89]. Once collapse occurs, the BEC forms anew, resulting in a cycle of formation and collapse that lasts as long as the conditions for BEC remain. For our estimated trap frequencies of 70 Hz at the later evaporation times, $N_{cr} \sim 10,000$. Further, the data showing the pure BEC at 9 s of evaporation time in Fig. 5.5 has one of the largest condensate numbers that

we observed, $N_0 \sim 9,700$ atoms and does not appear to exceed the critical number for the condensate. Studies of the collapse dynamics are ongoing in the Killian lab, but these results are consistent with those for an attractive condensate.

In conclusion, we have demonstrated the production of quantum degenerate ^{88}Sr via sympathetic cooling with ^{87}Sr . It promises to enable myriad studies, such as the observation of low-loss optical Feshbach resonances, that benefit from or require quantum degenerate strontium. The BEC of ^{88}Sr represents the exciting culmination of the ^{87}Sr - ^{88}Sr mixed isotope experiments.

Chapter 6

Conclusion

This thesis has demonstrated the trapping and evaporation of mixtures of ^{87}Sr and ^{88}Sr , thereby facilitating the production of the first Bose-Einstein condensate of ^{88}Sr . Mixing ^{87}Sr with ^{88}Sr was the key step to producing quantum degeneracy because the larger inter-species scattering length allowed for more efficient evaporation of ^{88}Sr . Techniques new to the Killian lab were implemented to enable the lab's first mixture of ultracold gases in an optical dipole trap: we showed how ^{87}Sr is trapped by itself, we experimented with a method of spin-polarizing ^{87}Sr samples, we explored how to accurately image mixtures of isotopes, and we learned the compromises necessary to simultaneously trap two isotopes. Finally, we derived new knowledge of the scattering and spectroscopic properties of strontium from these experiments.

While a BEC of ^{88}Sr is not even the first instance of quantum degeneracy in strontium (that honor belongs to ^{84}Sr [53]), it promises much for the study of quantum degenerate gases in the alkaline earth atoms. Condensates of ^{84}Sr [37], the least abundant strontium isotope, are already larger in number compared to condensates of ytterbium [26] and calcium [28]. The ^{88}Sr BEC shown in this work is limited in size by its attractive scattering length, but fortunately, the small magnitude of the ^{88}Sr scattering length makes it an ideal system with which to tune the scattering

length using an optical Feshbach resonance [33, 90, 91]. Tuning from a scattering length of order $-2a_0$ [78] is possible for very reasonable laser intensities on the order of 10 W/cm^2 . If the promise of low-loss tunability via optical Feshbach resonances is realized, then the higher natural abundance of ^{88}Sr may enable the production of still larger condensates.

Optical Feshbach resonances may also allow the creation of stable two-dimensional solitons in quantum degenerate ^{88}Sr . So-called “soliton management” [92] involves modulating the sign of the scattering length between positive and negative values in order to stabilize the soliton. Lasers offer the precision and speed necessary to change the scattering properties quickly and on a length scale as small as the wavelength of the light.

At the same time, the presence of the fermionic ^{87}Sr in our mixtures should not be ignored. It may only have played a supporting role in the production of Bose-Einstein condensation, but newer experiments in the Killian lab have already hinted at the existence of Fermi quantum degeneracy in ^{87}Sr . Ongoing work seeks to characterize the Fermi degeneracy, as well as to explore the possibility of Bose-Fermi mixtures.

Strontium maintains its relevance in the very active area of ultracold atomic gases in multiple ways: as a system for studying cold collisions [41, 78]; as a robust optical frequency standard [13, 35, 44]; as a promising system for quantum computation [18, 19]; and as a system which may exhibit novel quantum phases [20, 21]. Quantum degeneracy simply adds another layer to what is already an exciting body of work.

Appendix A

Calculation of Optical Trap Light Shifts and Scattering Rates

This appendix presents the calculation of the light shift and scattering rate for an atom due to a 1 W and 100 μm laser beam. The values of the oscillator strengths were taken from the following references [93, 94], with experimentally determined values being preferred over theoretically calculated values whenever possible. Our approach follows that described by Katori et. al in [95], and it successfully reproduces the calculations of Katori et. al within $\sim 20\%$ for similar beam parameters (note: that comparison is not shown here). We believe that the differences between the Katori and the Killian calculations arise for two reasons: 1) the oscillator strengths we used as inputs for the sums may not match those of Katori et. al; 2) we may not have included all of the same transitions in the sums as Katori et. al.

The Mathematica notebook which is included in this appendix can be found at the following path: “//Strontium86/studentfolders/pascal/Doctoral Thesis/Analysis/ODT Light Shifts/Dipole Calculations 20100415.nb”

Calculating dipole potential depth and scattering rate for the ground singlet S and triplet P states

Pascal Mickelson, July 2003 (updated April 2010)

General: Constants and Formulas

■ Constants and Definitions

```
In[530]:= Clear[c, h, e0, j2, k, m2, q1]
c = 2.998 * 10^7; h = 6.6262 * 10^-34; h = 6.6262 * 10^-34 / (2 * Pi);
e0 = 8.854 * 10^-12;
j2 = k = 1; m2 = q1
```

k and q are associated with tensors. k is the rank and q can take values from -k to +k. In our case, k will always be one and q will represent the polarization of our light (-1, 0, and +1 are left circularly, linearly, and right circularly polarized light respectively).

■ Formulas

The damping rate (Γ) corresponds to the spontaneous decay rate of the excited level. The damping rate is calculated using the dipole matrix element between the ground and excited states. This first quantity is the on-resonance damping rate.

The calculation of the dipole potential and the scattering rate incorporates the damping rate. As it turns out, the dipole potential is equal to the Stark shift in the ground state due to all the excited states that have allowed transitions to that ground state. This makes it easier to calculate how deep the potential will be.

j1 and m1 represent the initial state of the system, while j and m represent the final (upper) state of the system. What the final state can be is limited by the selection rules and the polarization of the laser.

```
In[530]:= Clear[Gamma, omega, r, Int, omega, depth, P, PeakPower, lambda, lambdaE,
Summand, Summand2, StarkSum, ScatSum, scat, j, m, j1, m1]
omega = 2 * Pi * c
lambdaE = lambda * 10^-9;
omega[lambda_] := 2 * Pi * c
lambda * 10^-9
Int = 2 * PeakPower * 10^-3 (* single beam intensity *)
Pi * (x * 10^-6)^2
m = m1 + q;
P[j1_, m1_, j_] := ClebschGordan[{j1, m1}, {j2, m2}, {j, m}]
Summand[lambda_] := (Gamma * P[j1, m1, j]^2 * (1 / (omega - omega[lambda]) + 1 / (omega + omega[lambda]))) / omega^3
Summand2[lambda_] := (omega[lambda]^3 * (Gamma * P[j1, m1, j]^2) * (1 / (omega - omega[lambda]) + 1 / (omega + omega[lambda]))) / (3 * Pi * c^2)
depth[lambda_] := - (2 * h / (2 * h)) * Int * StarkSum[lambda]
scat[lambda_] := (3 * Pi * c^2 / (2 * h)) * Int * ScatSum[lambda]
In[540]:= PeakPower = 1000; r = 100; (* Laser power in mW and beam waist in microns *)
```

It is in the expression for the dipole potential so that the light shifts come out in units of Hz.

■ Plotting Parameters

I define global plotting parameters to make it easier to change things on a mass scale. First are the x and y ranges. Then, the colors for each of the states.

```
In[550]:= Clear[xlow1, xlow2, xmid1, xmid2, xhigh1, xhigh2, ylow1, ylow2, ymid1, ymid2, yhigh1, yhigh2]
xlow1 = 400; xlow2 = 1100; xmid1 = 2000; xmid2 = 3000; xhigh1 = 5000; xhigh2 = 10000;
ylow1 = -1000; ylow2 = 200; ymid1 = -200; ymid2 = 1000; yhigh1 = -400; yhigh2 = 100;
Clear[colorS0a, colorS0b, colorP0a, colorP0b,
colorP1a, colorP1b, colorP2a, colorP2b, colorP2c,
colorS0a = 0.5; colorS0b = 0.6; colorP0a = 0.9; colorP0b = 0.8; colorP1a = 0.15;
colorP1b = 0.05; colorP2a = 0.25; colorP2b = 0.35; colorP2c = 0.45;
```

■ Parameters

The parameters that will need to be entered are the peak laser power density (I, in milliwatts/cm²), the waist of the Gaussian beam (in micrometers), the transition or resonance wavelength (lambda, in nm), the spontaneous decay rate for the excited state (Gamma, in Hz), and the parameters necessary to calculate the Clebsch-Gordan coefficients (initial |j1 m1> and final |j2 m2> states, as well as the polarization of light, q). For this program, though, the C-G coefficient only needs the initial state's j and m, the final state's j and the polarization q in order to figure out what the final state will be. Careful thought will be required to make sure I am specifying the correct final state when I enter the initial state and q.

The total light shift for a particular ground state level is determined by the sum over the light shifts caused by possible excited states. This means that I will need to iterate through a list of parameters for all the excited states up to some limit. The Kato paper goes to n=11, so I will strive to match that. Likewise, the scattering rate requires an iteration through that same list of values.

Ground State Light Shift

- $m=0, q=0$ (linear polarization)
 - Transition Data
- The form of the list data is as follows: List[*resonance wavelength, transition probability, final j, initial j*].

```
Data from PPT1976
s5p05 = List[460.862, 2.10*10^6, 1, 0];
s5p06 = List[293.269, 1.96*10^6, 1, 0];
s5p07 = List[257.024, 5.59*10^6, 1, 0];
s5p08 = List[235.029, 1.92*10^7, 1, 0];
s5p09 = List[230.797, 1.20*10^7, 1, 0];
s5p10 = List[227.601, 6.96*10^6, 1, 0];
s5p11 = List[225.395, 3.90*10^6, 1, 0];
d4p05 = List[242.884, 1.76*10^7, 1, 0];

Data from WGTG1992
s5p05 = List[460.862, 2.01*10^6, 1, 0];
s5p06 = List[293.269, 1.86*10^6, 1, 0];
s5p07 = List[257.024, 5.40*10^6, 1, 0];
s5p08 = List[235.029, 1.84*10^7, 1, 0];
s5p09 = List[230.797, 1.17*10^7, 1, 0];
s5p10 = List[227.601, 6.96*10^6, 1, 0];
s5p11 = List[225.395, 3.90*10^6, 1, 0];
d4p05 = List[242.884, 1.69*10^7, 1, 0];

Data from WGTG1992
mi = 0; q = 0;
Clear[groundstatelinear];
s5p05 = List[460.862, 2.10*10^6, 1, 0];
s5p06 = List[293.269, 1.96*10^6, 1, 0];
s5p07 = List[257.024, 5.59*10^6, 1, 0];
s5p08 = List[235.029, 1.92*10^7, 1, 0];
s5p09 = List[230.797, 1.20*10^7, 1, 0];
s5p10 = List[227.601, 6.96*10^6, 1, 0];
s5p11 = List[225.395, 3.90*10^6, 1, 0];
d4p05 = List[242.884, 1.76*10^7, 1, 0];
groundstatelinear = Out[{-8, -7, -6, -5, -4, -3, -2, -1}];
```

```
In[554]:=
mi = 0; q = 0;
Clear[groundstatelinear];
s5p05 = List[460.862, 2.10*10^6, 1, 0];
s5p06 = List[293.269, 1.96*10^6, 1, 0];
s5p07 = List[257.024, 5.59*10^6, 1, 0];
s5p08 = List[235.029, 1.92*10^7, 1, 0];
s5p09 = List[230.797, 1.20*10^7, 1, 0];
s5p10 = List[227.601, 6.96*10^6, 1, 0];
s5p11 = List[225.395, 3.90*10^6, 1, 0];
d4p05 = List[242.884, 1.76*10^7, 1, 0];
groundstatelinear = Out[{-8, -7, -6, -5, -4, -3, -2, -1}];
```

Calculating the Light Shifts

```
In[565]:= Clear[max, gs00d, gs00s]
max = Length[groundstatelinear];
StartSum[λ_] = 0;
ScatSum[λ_] = 0;
For[i = 1, i ≤ max, i++,
  (
    Ar = Part[Part[groundstatelinear, i], 1];
    I = Part[Part[groundstatelinear, i], 2];
    J = Part[Part[groundstatelinear, i], 3];
    j1 = Part[Part[groundstatelinear, i], 4];
    StartSum[λ_] = StartSum[λ] + Summand[λ];
    ScatSum[λ_] = ScatSum[λ] + Summand[λ];
  )
]
gs00d[λ_] = depth[λ];
gs00s[λ_] = scat[λ];
In[572]:= gs00d[1.064]/10^3
Out[572]= -76.888

■ Plotting the Light Shifts
In[573]:= Clear[dr3a, dr2a, dr3a, sr1a, sr2a, sr3a]
dr3a = Plot[10^3, {λ, xlow1, xlow2}, PlotRange → {ylow1, ylow2},
  PlotStyle → {Blue[Color$0a], Thick}, GridLines → Automatic,
  Frame → True, FrameLabel → {"Wavelength (nm)", "Stark Shift (kHz)",
    "Light Shift for GS Coupled to Singlet States, m = 0, (λ < 1100 nm)", ""}],
  dr2a = Plot[10^3, {λ, xmid1, xmid2}, PlotRange → {ymid1, ymid2},
  PlotStyle → {Blue[Color$0a], Thick}, GridLines → Automatic,
  Frame → True, FrameLabel → {"Wavelength (nm)", "Stark Shift (kHz)",
    "Light Shift for GS Coupled to Singlet States, m = 0, (2000 nm < λ < 3000 nm)", ""}],
  dr3a = Plot[10^3, {λ, xhigh1, xhigh2}, PlotRange → {yhigh1, yhigh2},
  PlotStyle → {Blue[Color$0a], Thick}, GridLines → Automatic,
  Frame → True, FrameLabel → {"Wavelength (nm)", "Stark Shift (kHz)",
    "Light Shift for GS Coupled to Singlet States, m = 0, (5000 < λ < 10000 nm)", ""}],
  sr1a = LogPlot[gs00s[λ], {λ, xlow1, xlow2}, PlotRange → {0.0001, 1},
  PlotStyle → {Blue[Color$0a], Thick}, Frame → True, GridLines → Automatic,
  FrameLabel → {"Wavelength (nm)", "Scattering Rate (Hz)",
    "Scattering Rate for GS Coupled to Singlet States, m = 0, (λ < 1100 nm)", ""}],
  sr2a = LogPlot[gs00s[λ], {λ, xmid1, xmid2}, PlotRange → {0.0001, 1},
  PlotStyle → {Blue[Color$0a], Thick}, Frame → True, GridLines → Automatic,
  FrameLabel → {"Wavelength (nm)", "Scattering Rate (Hz)",
    "Scattering Rate for GS Coupled to Singlet States, m = 0, (2000 nm < λ < 3000 nm)", ""}],
  sr3a = LogPlot[gs00s[λ], {λ, xhigh1, xhigh2}, PlotRange → {1.1^-6, 1},
  PlotStyle → {Blue[Color$0a], Thick}, Frame → True, GridLines → Automatic,
  FrameLabel → {"Wavelength (nm)", "Scattering Rate (Hz)",
    "Scattering Rate for GS Coupled to Singlet States, m = 0, (5000 < λ < 10000 nm)", ""}];
```

m=0, q=1 (circular polarization)

Transition Data

The form of the list data is as follows: List[{resonance wavelength, transition probability, final j, initial j}].

```
Data from PR1976
s5p05 = List[460.862, 2.10*10^6, 1, 0];
s5p06 = List[293.269, 1.96*10^6, 1, 0];
s5p07 = List[257.024, 5.59*10^6, 1, 0];
s5p08 = List[235.029, 1.92*10^6, 1, 0];
s5p09 = List[230.797, 1.20*10^6, 1, 0];
s5p10 = List[227.601, 6.96*10^6, 1, 0];
s5p11 = List[225.395, 3.90*10^6, 1, 0];
d4p05 = List[242.884, 1.76*10^6, 1, 0];

Data from WGN1992
s5p05 = List[460.862, 2.01*10^6, 1, 0];
s5p06 = List[293.269, 1.86*10^6, 1, 0];
s5p07 = List[257.024, 5.40*10^6, 1, 0];
s5p08 = List[235.029, 1.84*10^6, 1, 0];
s5p09 = List[230.797, 1.17*10^6, 1, 0];
s5p10 = List[227.601, 6.96*10^6, 1, 0];
s5p11 = List[225.395, 3.90*10^6, 1, 0];
Data from WGN1992
d4p05 = List[242.884, 1.69*10^6, 1, 0];

Clear[groundstatecircular]
m1 = 0; q = 1;
s5p05 = List[460.862, 2.10*10^6, 1, 0];
s5p06 = List[293.269, 1.96*10^6, 1, 0];
s5p07 = List[257.024, 5.59*10^6, 1, 0];
s5p08 = List[235.029, 1.92*10^6, 1, 0];
s5p09 = List[230.797, 1.20*10^6, 1, 0];
s5p10 = List[227.601, 6.96*10^6, 1, 0];
s5p11 = List[225.395, 3.90*10^6, 1, 0];
d4p05 = List[242.884, 1.76*10^6, 1, 0];
groundstatecircular = Out[{-6, -7, -6, -5, -4, -3, -2, -1}];
```

Calculating the Light Shifts

```
in[501]:= Clear[max, gs01d, gs01s]
max = Length[groundstatecircular];
StarkSum[λ_] := 0
ScatSum[λ_] := 0
For[i = 1, i ≤ max, i++,
  Ar = Part[Part[groundstatecircular, i], 1];
  l0 = Part[Part[groundstatecircular, i], 2];
  J = Part[Part[groundstatecircular, i], 3];
  J1 = Part[Part[groundstatecircular, i], 4];
  StarkSum[λ_] = StarkSum[λ] + Summand[λ];
  ScatSum[λ_] = ScatSum[λ] + Summand2[λ];
}
gs01d[λ_] = depth[λ];
gs01s[λ_] = scat[λ];

Plotting the Light Shifts
in[508]:= Clear[dr1b, dr2b, dr3b, sr1b, sr2b, sr3b]
dr1b = Plot[ $\frac{gs01d[\lambda]}{10^3}$ , {λ, xlow1, xlow2}, PlotRange → {ylo1, ylow2},
  PlotStyle → {Hue[ColorS0b]}, Thick], GridLines → Automatic,
  Frame → True, FrameLabel → {"Wavelength (nm)", "Stark Shift (kHz)",
  "Light Shift for GS Coupled to Singlet States, m = ±1, (λ < 1100 nm)", ""}]
dr2b = Plot[ $\frac{gs01d[\lambda]}{10^3}$ , {λ, xmid1, xmid2}, PlotRange → {ymid1, ymid2},
  PlotStyle → {Hue[ColorS0b]}, Thick], GridLines → Automatic,
  Frame → True, FrameLabel → {"Wavelength (nm)", "Stark Shift (kHz)",
  "Light Shift for GS Coupled to Singlet States, m = ±1, (2000 nm < λ < 3000 nm)", ""}]
dr3b = Plot[ $\frac{gs01d[\lambda]}{10^3}$ , {λ, xhigh1, xhigh2}, PlotRange → {yhigh1, yhigh2},
  PlotStyle → {Hue[ColorS0b]}, Thick], GridLines → Automatic,
  Frame → True, FrameLabel → {"Wavelength (nm)", "Stark Shift (kHz)",
  "Light Shift for GS Coupled to Singlet States, m = ±1, (5000 < λ < 10000 nm)", ""}]
sr1b = LogPlot[gs01s[λ], {λ, xlow1, xlow2}, PlotRange → {0.0001, 1},
  PlotStyle → {Hue[ColorS0b]}, Thick], Frame → True, GridLines → Automatic,
  FrameLabel → {"Wavelength (nm)", "Scattering Rate (Hz)",
  "Scattering Rate for GS Coupled to Singlet States, m = ±1, (λ < 1100 nm)", ""}]
sr2b = LogPlot[gs01s[λ], {λ, xmid1, xmid2}, PlotRange → {0.0001, 1},
  PlotStyle → {Hue[ColorS0b]}, Thick], Frame → True, GridLines → Automatic,
  FrameLabel → {"Wavelength (nm)", "Scattering Rate (Hz)",
  "Scattering Rate for GS Coupled to Singlet States, m = ±1, (2000 nm < λ < 3000 nm)", ""}]
sr3b = LogPlot[gs01s[λ], {λ, xhigh1, xhigh2}, PlotRange → {1.*^-6, 1},
  PlotStyle → {Hue[ColorS0b]}, Thick], Frame → True, GridLines → Automatic,
  FrameLabel → {"Wavelength (nm)", "Scattering Rate (Hz)",
  "Scattering Rate for GS Coupled to Singlet States, m = ±1, (5000 < λ < 10000 nm)", ""}]
```

```

In[600]:= Solve[depth[x]/10^3 == 400, x]
Solve[depth[x]/10^3 == -600, x]
List[depth[1000]/10^3, depth[800]/10^3, depth[700]/10^3, depth[600]/10^3, depth[300]/10^3]
List[scat[900], scat[800], scat[600], scat[300]]
Out[600]= {{(λ -> -429.331), (λ -> -293.231), (λ -> -256.971), (λ -> -242.759), (λ -> -234.912),
(λ -> -230.729), (λ -> -227.564), (λ -> -225.375), (λ -> 225.375), (λ -> 227.564),
(λ -> 230.729), (λ -> 234.912), (λ -> 242.759), (λ -> 256.971), (λ -> 293.231), (λ -> 429.331)}}
Out[600]= {{(λ -> -486.436), (λ -> -293.291), (λ -> -257.057), (λ -> -242.962), (λ -> -235.101),
(λ -> -230.837), (λ -> -227.623), (λ -> -225.407), (λ -> 225.407), (λ -> 227.623),
(λ -> 230.837), (λ -> 235.101), (λ -> 242.962), (λ -> 257.057), (λ -> 293.291), (λ -> 486.436)}}
Out[607]= {-79.2708, -93.2229, -109.714, -151.062, 39.2209}
Out[608]= {0.00975324, 0.016933, 0.106576, 0.563924, 0.0777879}

```

■ All polarizations

```

In[609]:= Show[dt1a, dr1b], Frame -> True, FrameLabel -> {"Wavelength (nm)", "Stark Shift (kHz)",
"Light Shift for GS Coupled to Singlet States (λ < 1100 nm)", ""}
Show[dt2a, dr2b], Frame -> True, FrameLabel -> {"Wavelength (nm)", "Stark Shift (kHz)",
"Light Shift for GS Coupled to Singlet States (2000 nm < λ < 3000 nm)", ""}
Show[dt3a, dr3b], Frame -> True, FrameLabel -> {"Wavelength (nm)", "Stark Shift (kHz)",
"Light Shift for GS Coupled to Singlet States (5000 nm < λ < 10000 nm)", ""}
Show[sr1a, sr1b], Frame -> True, FrameLabel -> {"Wavelength (nm)", "Stark Shift (kHz)",
"Scattering Rate for GS Coupled to Singlet States (λ < 1100 nm)", ""}
Show[sr2a, sr2b], Frame -> True, FrameLabel -> {"Wavelength (nm)", "Stark Shift (kHz)",
"Scattering Rate for GS Coupled to Singlet States (2000 nm < λ < 3000 nm)", ""}
Show[sr3a, sr3b], Frame -> True, FrameLabel -> {"Wavelength (nm)", "Stark Shift (kHz)",
"Scattering Rate for GS Coupled to Singlet States (5000 nm < λ < 10000 nm)", ""}

```

Linear and circular polarization are the same, just as one would expect for a transition beginning in the ground state $|0\rangle$.

Triplet P0 State Light Shift

- $m=0, q=0$ (linear polarization)

The form of the list data is as follows: List[*resonance wavelength, transition probability, j upper, j lower*].

■ Transition Data

```

Experimental Data
s5506 = List[679.290, 9.16 * 10^6, 1, 0];
s5507 = List[432.770, 2.37 * 10^6, 1, 0];
s5404 = List[2603.13, 2.71 * 10^6, 1, 0];
s5405 = List[483.340, 4.66 * 10^6, 1, 0];
s5406 = List[394.190, 1.72 * 10^6, 1, 0];
p5p05 = List[474.320, 4.84 * 10^6, 1, 0];
Theoretical Numbers
s5506 = List[679.290, 7.13 * 10^6, 1, 0];
s5507 = List[432.770, 1.75 * 10^7, 1, 0];
s5508 = List[378.160, 8.22 * 10^6, 1, 0];
s5509 = List[355.450, 4.53 * 10^6, 1, 0];
s5510 = List[343.520, 2.77 * 10^6, 1, 0];
s5604 = List[2603.13, 4.32 * 10^6, 1, 0];
s5605 = List[483.340, 5.83 * 10^6, 1, 0];
s5606 = List[394.190, 2.67 * 10^7, 1, 0];
s5607 = List[363.020, 1.42 * 10^7, 1, 0];
s5608 = List[347.840, 8.51 * 10^6, 1, 0];
s5609 = List[339.090, 5.51 * 10^6, 1, 0];
p5p05 = List[474.320, 6.10 * 10^6, 1, 0];
Clear[tripletOstetelinear0]
m1 = 0; q = 0;
s5506 = List[679.290, 9.16 * 10^6, 1, 0];
s5507 = List[432.770, 2.37 * 10^6, 1, 0];
s5508 = List[378.160, 8.22 * 10^6, 1, 0];
s5509 = List[355.450, 4.53 * 10^6, 1, 0];
s5510 = List[343.520, 2.77 * 10^6, 1, 0];
s5404 = List[2603.13, 2.71 * 10^6, 1, 0];
s5405 = List[483.340, 4.66 * 10^6, 1, 0];
s5406 = List[394.190, 1.72 * 10^6, 1, 0];
s5407 = List[363.020, 8.40 * 10^6, 1, 0];
s5408 = List[347.840, 5.02 * 10^6, 1, 0];
s5409 = List[339.090, 3.25 * 10^6, 1, 0];
p5p05 = List[474.320, 4.84 * 10^6, 1, 0];
tripletOstetelinear0 = Out[{-12, -11, -10, -9, -8, -7, -6, -5, -4, -3, -2, -1}];

```

- Calculating the Light Shifts

```

In[630]:=
Clear[max, ts00d, ts00s]
max = Length[tripletOscatellinear0];
StarSum[λ_] := 0
For[i = 1, i ≤ max, i++,
  (
    Ar = Part[Part[tripletOscatellinear0, i], 1];
    T = Part[Part[tripletOscatellinear0, i], 2];
    J = Part[Part[tripletOscatellinear0, i], 3];
    j1 = Part[Part[tripletOscatellinear0, i], 4];
    StarSum[λ_] = StarSum[λ] + Summand[λ];
    StarSum[λ_] = StarSum[λ] + Summand2[λ];
  )
];
ts00d[λ_] = depth[λ];
ts00s[λ_] = scat[λ];

In[637]:=
Clear[dr1c, dr2c, dr3c, sr1c, sr2c, sr3c]
dr1c = Plot[ $\frac{10^3}{ts00d[\lambda]}$ , {λ, xlow1, xlow2}, PlotRange → {ylow1, ylow2},
  PlotStyle → {Hue[ColorF0a], Dashed, Thick}, GridLines → Automatic, Frame → True,
  FrameLabel → {"Wavelength (nm)", "Stark Shift (kHz)", "Light Shift for Triplet P1
  State Coupled to Higher Triplet States, m = 0, (λ < 1100 nm)", ""}],
  dr2c = Plot[ $\frac{10^3}{ts00d[\lambda]}$ , {λ, xmid1, xmid2}, PlotRange → {ymid1, ymid2},
  PlotStyle → {Hue[ColorF0a], Dashed, Thick}, GridLines → Automatic, Frame → True,
  FrameLabel → {"Wavelength (nm)", "Stark Shift (kHz)", "Light Shift for Triplet P1 State
  Coupled to Higher Triplet States, m = 0, (2000 nm < λ < 3000 nm)", ""}],
  dr3c = Plot[ $\frac{10^3}{ts00d[\lambda]}$ , {λ, xhigh1, xhigh2}, PlotRange → {yhigh1, yhigh2},
  PlotStyle → {Hue[ColorF0a], Dashed, Thick}, GridLines → Automatic, Frame → True,
  FrameLabel → {"Wavelength (nm)", "Stark Shift (kHz)", "Light Shift for Triplet P1 State
  Coupled to Higher Triplet States, m = 0, (5000 < λ < 10000 nm)", ""}],
  sr1c = LogPlot[ts00s[λ], {λ, xlow1, xlow2}, PlotRange → {0.0001, 1},
  PlotStyle → {Hue[ColorF0a], Dashed, Thick}, Frame → True, GridLines → Automatic,
  FrameLabel → {"Wavelength (nm)", "Scattering Rate (Hz)", "Scattering Rate for Triplet
  P1 State Coupled to Higher Triplet States, m = 0, (λ < 1100 nm)", ""}],
  sr2c = LogPlot[ts00s[λ], {λ, xmid1, xmid2}, PlotRange → {0.0001, 1},
  PlotStyle → {Hue[ColorF0a], Dashed, Thick}, Frame → True, GridLines → Automatic,
  FrameLabel → {"Wavelength (nm)", "Scattering Rate (Hz)", "Scattering Rate for Triplet P1
  State Coupled to Higher Triplet States, m = 0, (2000 nm < λ < 3000 nm)", ""}],
  sr3c = LogPlot[ts00s[λ], {λ, xhigh1, xhigh2}, PlotRange → {1. * 10-6, 1},
  PlotStyle → {Hue[ColorF0a], Dashed, Thick}, Frame → True, GridLines → Automatic,
  FrameLabel → {"Wavelength (nm)", "Scattering Rate (Hz)", "Scattering Rate for Triplet P1
  State Coupled to Higher Triplet States, m = 0, (5000 < λ < 10000 nm)", ""}]]

```

```

In[641]:=
Solve[depth[λ] / 103 == 100, λ]
Solve[depth[λ] / 103 == 200, λ]
Solve[depth[λ] / 103 == 300, λ]
List[depth[3500] / 103]
Out[641]=
{{(λ → -2112.23), (λ → -655.929), (λ → -479.04), (λ → -435.62), (λ → -422.334), (λ → -386.805),
(λ → -373.715), (λ → -360.053), (λ → -353.459), (λ → -346.149), (λ → -342.255), (λ → -337.29),
(λ → 337.29), (λ → 342.255), (λ → 346.149), (λ → 353.459), (λ → 360.053), (λ → 373.715),
(λ → 386.805), (λ → 422.334), (λ → 435.62), (λ → 479.04), (λ → 655.929), (λ → 2112.23)}}
Out[642]=
{{(λ → -2277.8), (λ → -664.492), (λ → -479.318), (λ → -447.478),
(λ → -431.418), (λ → -391.002), (λ → -376.723), (λ → -361.923), (λ → -354.863),
(λ → -347.283), (λ → -343.201), (λ → -338.726), (λ → -338.726), (λ → -343.201),
(λ → -347.283), (λ → -354.863), (λ → -361.923), (λ → -376.723), (λ → -391.002),
(λ → -431.418), (λ → -447.478), (λ → -479.318), (λ → -664.492), (λ → -2277.8)}}
Out[643]=
{{(λ → -2350.02), (λ → -668.027), (λ → -479.545), (λ → -455.171),
(λ → -432.105), (λ → -392.113), (λ → -377.276), (λ → -362.324), (λ → -355.092),
(λ → -347.494), (λ → -343.329), (λ → -338.876), (λ → -338.876), (λ → -343.329),
(λ → -347.494), (λ → -355.092), (λ → -362.324), (λ → -377.276), (λ → -392.113),
(λ → -432.105), (λ → -455.171), (λ → -479.545), (λ → -668.027), (λ → -2350.02)}}
Out[647]=
{-232.81}

```

- m=0, q=1 (circular polarization)

The form of the list data is as follows: List[resonance wavelength, transition probability, j1, m1, q].

- Transition Data

```

Experimental Data
s5806 = List[679.290, 9.16 * 106, 1, 0];
s5807 = List[432.770, 2.37 * 106, 1, 0];
s5804 = List[2603.13, 2.71 * 106, 1, 0];
s5805 = List[483.340, 4.66 * 106, 1, 0];
s5806 = List[394.190, 1.72 * 106, 1, 0];
p5905 = List[474.320, 4.84 * 107, 1, 0];
Theoretical Numbers
s5806 = List[679.290, 7.13 * 107, 1, 0];
s5807 = List[432.770, 1.75 * 107, 1, 0];
s5808 = List[378.160, 8.22 * 106, 1, 0];
s5809 = List[395.450, 4.53 * 106, 1, 0];
s5810 = List[343.520, 2.77 * 106, 1, 0];
s5804 = List[2603.13, 4.32 * 106, 1, 0];
s5805 = List[483.340, 5.83 * 106, 1, 0];
s5806 = List[394.190, 2.67 * 106, 1, 0];
s5807 = List[363.020, 1.42 * 106, 1, 0];
s5808 = List[347.840, 9.51 * 106, 1, 0];
s5809 = List[339.090, 5.51 * 106, 1, 0];
p5905 = List[474.320, 6.10 * 107, 1, 0];

```

```

In[64]:= Clear[tripletOstatecircular0]
m1 = 0; q = 1;
s5s06 = List[679.290, 9.16 * 10^6, 1, 0];
s5s07 = List[432.770, 2.37 * 10^6, 1, 0];
s5s08 = List[378.160, 8.22 * 10^6, 1, 0];
s5s09 = List[355.450, 4.53 * 10^6, 1, 0];
s5s10 = List[343.520, 2.77 * 10^6, 1, 0];
s5d04 = List[2603.13, 2.71 * 10^6, 1, 0];
s5d05 = List[483.340, 4.66 * 10^7, 1, 0];
s5d06 = List[394.190, 1.72 * 10^7, 1, 0];
s5d07 = List[363.020, 8.40 * 10^6, 1, 0];
s5d08 = List[347.840, 5.02 * 10^6, 1, 0];
s5d09 = List[339.090, 3.25 * 10^7, 1, 0];
p5p05 = List[474.320, 4.84 * 10^7, 1, 0];
tripletOstatecircular0 = Out[{-12, -11, -10, -9, -8, -7, -6, -5, -4, -3, -2, -1}];

```

Calculating the Light Shifts

```

In[65]:= Clear[max, ts01d, ts01s];
max = Length[tripletOstatecircular0];
StackSum[λ_] := 0
For[i = 1, i ≤ max, i++,
(
  λr = Part[Part[tripletOstatecircular0, i], 1];
  r = Part[Part[tripletOstatecircular0, i], 2];
  j = Part[Part[tripletOstatecircular0, i], 3];
  j1 = Part[Part[tripletOstatecircular0, i], 4];
  StackSum[λ_] = StackSum[λ] + Summand[λ];
  StackSum[λ_] = StackSum[λ] + Summand2[λ];
)
]
ts01d[λ_] = depth[λ];
ts01s[λ_] = scat[λ];

```

Plotting the Light Shifts

```

In[70]:= Clear[dr1d, dr2d, dr3d, sr1d, sr2d, sr3d]
dr1d = Plot[
  10^3 / ts01d[λ],
  {λ, xlow1, xlow2}, PlotRange → {ylow1, ylow2},
  PlotStyle → {Blue[ColorP0b]}, Dashed, Thick, GridLines → Automatic, Frame → True,
  FrameLabel → {"Wavelength (nm)", "Stark Shift (kHz)", "Light Shift for Triplet P1
  State Coupled to Higher Triplet States, m = ±1 (λ < 1100 nm)", ""}]
dr2d = Plot[
  10^3 / ts01d[λ],
  {λ, xmid1, xmid2}, PlotRange → {ymid1, ymid2},
  PlotStyle → {Blue[ColorP0b]}, Dashed, Thick, GridLines → Automatic, Frame → True,
  FrameLabel → {"Wavelength (nm)", "Stark Shift (kHz)", "Light Shift for Triplet P1 State
  Coupled to Higher Triplet States, m = ±1 (2000 nm < λ < 3000 nm)", ""}]
dr3d = Plot[
  10^3 / ts01d[λ],
  {λ, xhigh1, xhigh2}, PlotRange → {yhigh1, yhigh2},
  PlotStyle → {Blue[ColorP0b]}, Dashed, Thick, GridLines → Automatic, Frame → True,
  FrameLabel → {"Wavelength (nm)", "Stark Shift (kHz)", "Light Shift for Triplet P1 State
  Coupled to Higher Triplet States, m = ±1 (5000 < λ < 10000 nm)", ""}]
sr1d = LogPlot[ts01s[λ], {λ, xlow1, xlow2}, PlotRange → {0.0001, 1},
  PlotStyle → {Blue[ColorP0b]}, Dashed, Thick, Frame → True, GridLines → Automatic,
  FrameLabel → {"Wavelength (nm)", "Scattering Rate (Hz)", "Scattering Rate for Triplet
  P1 State Coupled to Higher Triplet States, m = ±1 (λ < 1100 nm)", ""}]
sr2d = LogPlot[ts01s[λ], {λ, xmid1, xmid2}, PlotRange → {0.0001, 1},
  PlotStyle → {Blue[ColorP0b]}, Dashed, Thick, Frame → True, GridLines → Automatic,
  FrameLabel → {"Wavelength (nm)", "Scattering Rate (Hz)", "Scattering Rate for Triplet P1
  State Coupled to Higher Triplet States, m = ±1 (2000 nm < λ < 3000 nm)", ""}]
sr3d = LogPlot[ts01s[λ], {λ, xhigh1, xhigh2}, PlotRange → {1.*^-6, 1},
  PlotStyle → {Blue[ColorP0b]}, Dashed, Thick, Frame → True, GridLines → Automatic,
  FrameLabel → {"Wavelength (nm)", "Scattering Rate (Hz)", "Scattering Rate for Triplet P1
  State Coupled to Higher Triplet States, m = ±1 (5000 < λ < 10000 nm)", ""}]

```

All Polarizations

```

In[77]:= Show[
  {dr1c, dr1d},
  FrameLabel → {"Wavelength (nm)", "Stark Shift (kHz)", "Light Shift for Triplet
  P1 State Coupled to Triplet S, P, & D; m = 0, ±1, (λ < 1100 nm)", ""}]
Show[
  {dr2c, dr2d},
  FrameLabel → {"Wavelength (nm)", "Stark Shift (kHz)",
  "Light Shift for Triplet P1 State Coupled to Triplet
  S, P, & D; m = 0, ±1, (2000 nm < λ < 3000 nm)", ""}]
Show[
  {dr3c, dr3d},
  FrameLabel → {"Wavelength (nm)", "Stark Shift (kHz)",
  "Light Shift for Triplet P1 State Coupled to Triplet
  S, P, & D; m = 0, ±1, (5000 nm < λ < 10000 nm)", ""}]
Show[
  {sr1c, sr1d},
  FrameLabel → {"Wavelength (nm)", "Scattering Rate (Hz)",
  "Scattering Rate for Triplet P1 State Coupled to Triplet
  S, P, & D; m = 0, ±1, (λ < 1100 nm)", ""}]
Show[
  {sr2c, sr2d},
  FrameLabel → {"Wavelength (nm)", "Scattering Rate (Hz)",
  "Scattering Rate for Triplet P1 State Coupled to Triplet
  S, P, & D; m = 0, ±1, (2000 nm < λ < 3000 nm)", ""}]
Show[
  {sr3c, sr3d},
  FrameLabel → {"Wavelength (nm)", "Scattering Rate (Hz)",
  "Scattering Rate for Triplet P1 State Coupled to Triplet
  S, P, & D; m = 0, ±1, (5000 nm < λ < 10000 nm)", ""}]

```

Triplet P1 State Light Shift

- m=0, q=0 (linear polarization)

The form of the list data is as follows: List[resonance wavelength, transition probability, j, j, j].

▪ Transition Data

```
Experimental Data
s5506 = List[688.021, 2.54 * 107, 1, 1];
s5507 = List[436.293, 6.31 * 106, 1, 1];
s5508 = List[380.850, 8.22 * 106, 1, 1];
s5509 = List[357.822, 4.53 * 106, 1, 1];
s5510 = List[345.743, 1.83 * 107, 1, 1];
s554a = List[2736.20, 1.75 * 105, 1, 1];
s554b = List[2692.19, 3.31 * 105, 2, 1];
s554c = List[487.743, 1.83 * 107, 1, 1];
s554d = List[487.385, 5.56 * 106, 2, 1];
s554e = List[397.116, 1.35 * 107, 1, 1];
s554f = List[397.038, 2.01 * 107, 2, 1];
p552b = List[478.565, 4.08 * 106, 1, 1];
p552c = List[472.359, 3.77 * 107, 2, 1];
Theoretical Numbers
s5506 = List[688.021, 7.13 * 107, 1, 1];
s5507 = List[436.293, 1.75 * 107, 1, 1];
s5508 = List[380.850, 8.22 * 106, 1, 1];
s5509 = List[357.822, 4.53 * 106, 1, 1];
s5510 = List[345.743, 2.77 * 106, 1, 1];
s554a = List[487.743, 5.83 * 107, 1, 1];
s554b = List[487.385, 5.83 * 107, 2, 1];
s554c = List[397.116, 2.60 * 107, 1, 1];
s554d = List[397.038, 2.60 * 107, 2, 1];
s554e = List[365.500, 6.17 * 106, 1, 1];
s554f = List[350.070, 1.11 * 107, 2, 1];
s554g = List[350.110, 3.69 * 106, 1, 1];
s554h = List[341.260, 2.39 * 106, 2, 1];
p552a = List[483.346, 6.10 * 107, 0, 1];
p552b = List[478.565, 6.10 * 107, 1, 1];
p552c = List[472.359, 6.10 * 107, 2, 1];
```

```
in[683]: Clear[tripletstatalinear0];
m1 = 0; q = 0;
s5506 = List[688.021, 2.54 * 107, 1, 1];
s5507 = List[436.293, 6.31 * 106, 1, 1];
s5508 = List[380.850, 8.22 * 106, 1, 1];
s5509 = List[357.822, 4.53 * 106, 1, 1];
s5510 = List[345.743, 2.77 * 106, 1, 1];
s554a = List[2736.20, 1.75 * 105, 1, 1];
s554b = List[2692.19, 3.31 * 105, 2, 1];
s554c = List[487.743, 1.83 * 107, 1, 1];
s554d = List[487.385, 5.56 * 106, 2, 1];
s554e = List[397.116, 1.35 * 107, 1, 1];
s554f = List[397.038, 2.01 * 107, 2, 1];
s554g = List[365.500, 6.17 * 106, 1, 1];
s554h = List[350.110, 3.69 * 106, 1, 1];
s554i = List[350.070, 6.65 * 106, 2, 1];
s554j = List[341.260, 2.39 * 106, 1, 1];
s554k = List[341.260, 4.30 * 106, 2, 1];
p552a = List[478.565, 4.08 * 106, 1, 1];
p552b = List[472.359, 3.77 * 107, 2, 1];
tripletstatalinear0 = Out[[-20, -19, -18, -17, -16,
-15, -14, -13, -12, -11, -10, -9, -8, -7, -6, -5, -4, -3, -2, -1]];

```

▪ Calculating the Light Shifts

```
in[708]: Clear[ts104, ts105];
max = Length[tripletstatalinear0];
StarkSum[λ_] := 0
For[i = 1, i ≤ max, i++,
(
  λr = Part[Part[tripletstatalinear0, i], 1];
  r = Part[Part[tripletstatalinear0, i], 2];
  j = Part[Part[tripletstatalinear0, i], 3];
  j1 = Part[Part[tripletstatalinear0, i], 4];
  StarkSum[λ_] = StarkSum[λ] + Summand[λ];
  StarkSum[λ_] = StarkSum[λ] + Summand2[λ];
);
ts104[λ_] = depth[λ];
ts105[λ_] = scat[λ];
```

- Plotting the Light Shifts

```

Clear[dr1e, dr2e, dr3e, sr1e, sr2e, sr3e]
dr1e = Plot[ $\frac{10^3}{\text{ts10d}[\lambda]}$ , { $\lambda$ , xlow1, xlow2}, PlotRange -> {ylow1, ylow2},
PlotStyle -> {Hue[ColorPIa], Dotted, Thick},
GridLines -> Automatic, Frame -> True, FrameLabel ->
{"Wavelength (nm)", "Stark Shift (kHz)", "Light Shift for Triplet P1 State Coupled
to Higher Triplet States, m = 0, ( $\lambda < 1100$  nm)", ""}]
dr2e = Plot[ $\frac{10^3}{\text{ts10d}[\lambda]}$ , { $\lambda$ , xmid1, xmid2}, PlotRange -> {ymid1, ymid2},
PlotStyle -> {Hue[ColorPIa], Dotted, Thick},
GridLines -> Automatic, Frame -> True, FrameLabel ->
{"Wavelength (nm)", "Stark Shift (kHz)", "Light Shift for Triplet P1 State Coupled
to Higher Triplet States, m = 0, (2000 nm <  $\lambda < 3000$  nm)", ""}]
dr3e = Plot[ $\frac{10^3}{\text{ts10d}[\lambda]}$ , { $\lambda$ , xhigh1, xhigh2}, PlotRange -> {yhigh1, yhigh2},
PlotStyle -> {Hue[ColorPIa], Dotted, Thick},
GridLines -> Automatic, Frame -> True, FrameLabel ->
{"Wavelength (nm)", "Stark Shift (kHz)", "Light Shift for Triplet P1 State Coupled
to Higher Triplet States, m = 0, (5000 <  $\lambda < 10000$  nm)", ""}]
sr1e = LogPlot[ts10s[\lambda], { $\lambda$ , xlow1, xlow2}, PlotRange -> {0.0001, 1},
Frame -> True, GridLines -> Automatic, PlotStyle -> {Hue[ColorPIa], Dotted, Thick},
FrameLabel -> {"Wavelength (nm)", "Scattering Rate (Hz)", "Scattering Rate for Triplet P1 State
Coupled to Higher Triplet States, m = 0, ( $\lambda < 1100$  nm)", ""}]
sr2e = LogPlot[ts10s[\lambda], { $\lambda$ , xmid1, xmid2}, PlotRange -> {0.0001, 1},
Frame -> True, GridLines -> Automatic, PlotStyle -> {Hue[ColorPIa], Dotted, Thick},
FrameLabel -> {"Wavelength (nm)", "Scattering Rate (Hz)", "Scattering Rate for Triplet P1 State
Coupled to Higher Triplet States, m = 0, (2000 nm <  $\lambda < 3000$  nm)", ""}]
sr3e = LogPlot[ts10s[\lambda], { $\lambda$ , xhigh1, xhigh2}, PlotRange -> {1.1*^-6, 1},
FrameLabel -> {"Wavelength (nm)", "Scattering Rate (Hz)", "Scattering Rate for Triplet P1
State Coupled to Higher Triplet States, m = 0, (5000 <  $\lambda < 10000$  nm)", ""}]
O4[F20]= Solve[depth[\lambda]/10^3 == 100, \lambda]
Solve[depth[\lambda]/10^3 == 208.3, \lambda]
Solve[depth[\lambda]/10^3 == 300, \lambda]
List[depth[3500]/10^3]
O4[F20]= {{(\lambda -> 2200.54), (\lambda -> 486.005), (\lambda -> 474.818), (\lambda -> 415.435), (\lambda -> 384.585)},
{(\lambda -> 361.56), (\lambda -> 348.234), (\lambda -> 340.071), (\lambda -> 340.071), (\lambda -> 348.234),
(\lambda -> 361.56), (\lambda -> 384.585), (\lambda -> 415.435), (\lambda -> 474.818), (\lambda -> 486.005), (\lambda -> 2200.54)}}
O4[F21]= {{(\lambda -> 2370.77), (\lambda -> 486.007), (\lambda -> 475.099), (\lambda -> 439.648), (\lambda -> 393.7)},
{(\lambda -> 364.32), (\lambda -> 349.556), (\lambda -> 340.906), (\lambda -> 340.96), (\lambda -> 369.556)},
{(\lambda -> 364.32), (\lambda -> 393.7), (\lambda -> 439.648), (\lambda -> 475.099), (\lambda -> 486.007), (\lambda -> 2370.77)}}
O4[F22]= {{(\lambda -> 2443.55), (\lambda -> 486.081), (\lambda -> 475.371), (\lambda -> 450.301), (\lambda -> 395.073)},
{(\lambda -> 364.738), (\lambda -> 349.753), (\lambda -> 341.077), (\lambda -> 341.077), (\lambda -> 349.753)},
{(\lambda -> 364.738), (\lambda -> 395.073), (\lambda -> 450.301), (\lambda -> 475.371), (\lambda -> 486.081), (\lambda -> 2443.55)}}
O4[F23]= {-232.879}

```

- m=1, q=0 (linear polarization)

The form of the list data is as follows: List[resonance wavelength, transition probability, j1, ml, q1].

- Transition Data

```

Experimental Data
s5806 = List[688.021, 2.54 * 10^7, 1, 1];
s5807 = List[436.293, 6.31 * 10^6, 1, 1];
s584a = List[2736.20, 1.75 * 10^6, 1, 1];
s584b = List[2692.19, 3.31 * 10^7, 2, 1];
s585a = List[487.743, 1.83 * 10^7, 1, 1];
s585b = List[487.385, 5.56 * 10^7, 2, 1];
s586a = List[397.116, 1.35 * 10^7, 1, 1];
s586b = List[397.038, 2.01 * 10^7, 2, 1]; p586a = List[483.346, 1.97 * 10^6, 0, 1];
p586b = List[478.565, 4.08 * 10^7, 1, 1];
p586c = List[472.359, 3.77 * 10^7, 2, 1];
Theoretical Numbers
s5806 = List[688.021, 7.13 * 10^7, 1, 1];
s5807 = List[436.293, 1.75 * 10^7, 1, 1];
s5808 = List[380.850, 8.22 * 10^6, 1, 1];
s5809 = List[357.822, 4.53 * 10^6, 1, 1];
s5810 = List[345.743, 2.77 * 10^6, 1, 1];
s585a = List[487.743, 5.83 * 10^7, 1, 1];
s585b = List[487.385, 5.83 * 10^7, 2, 1];
s586a = List[397.116, 2.60 * 10^7, 1, 1];
s586b = List[397.038, 2.60 * 10^7, 2, 1];
s587a = List[365.500, 6.17 * 10^7, 1, 1];
s587b = List[365.400, 1.11 * 10^7, 2, 1];
s588a = List[350.110, 3.69 * 10^6, 1, 1];
s588b = List[350.070, 6.65 * 10^6, 2, 1];
s589a = List[341.260, 2.39 * 10^6, 1, 1];
s589b = List[341.260, 4.30 * 10^6, 2, 1];
p589a = List[483.346, 6.10 * 10^7, 0, 1];
p589b = List[478.565, 6.10 * 10^7, 1, 1];
p589c = List[472.359, 6.10 * 10^7, 2, 1];

```

```

In[724]:= Clear[triplettslist];
ml = j; q = 0;
s506 = List[688.021, 2.54*10^7, 1, 1];
s507 = List[436.293, 6.31*10^6, 1, 1];
s508 = List[380.850, 8.22*10^6, 1, 1];
s509 = List[357.822, 4.53*10^6, 1, 1];
s510 = List[345.743, 2.77*10^6, 1, 1];
s511 = List[2736.20, 1.75*10^6, 1, 1];
s512 = List[2692.19, 3.31*10^6, 2, 1];
s513 = List[487.743, 1.83*10^7, 1, 1];
s514 = List[487.385, 5.56*10^7, 2, 1];
s515 = List[397.116, 1.35*10^7, 1, 1];
s516 = List[397.038, 2.01*10^7, 2, 1];
s517 = List[365.500, 6.17*10^6, 1, 1];
s518 = List[365.400, 1.11*10^7, 2, 1];
s519 = List[350.110, 3.69*10^7, 1, 1];
s520 = List[350.070, 6.65*10^6, 2, 1];
s521 = List[341.260, 2.39*10^6, 1, 1];
s522 = List[341.260, 4.30*10^7, 2, 1];
p55b = List[478.565, 4.08*10^7, 1, 1];
p55c = List[472.359, 3.77*10^7, 2, 1];
triplettslist =
Out[724]= {-19, -18, -17, -16, -15, -14, -13, -12, -11, -10, -9, -8, -7, -6, -5, -4, -3, -2, -1}];

```

Calculating the Light Shifts

```

In[725]:= Clear[max, tslist, tslist];
max = Length[triplettslist];
StackSum[λ_] := 0
ScatSum[λ_] := 0
For[i = 1, i ≤ max, i++,
  (
  λr = Part[Part[triplettslist, i], 1];
  λi = Part[Part[triplettslist, i], 2];
  λj = Part[Part[triplettslist, i], 3];
  λl = Part[Part[triplettslist, i], 4];
  StackSum[λ_] = StackSum[λ] + Summand[λ];
  ScatSum[λ_] = ScatSum[λ] + Summand2[λ];
  )
]
tslist[λ_] = depth[λ];
tslist[λ_] = scat[λ];

```

Plotting the Light Shifts

```

In[726]:= Clear[dr1f, dr2f, dr3f, sr1f, sr2f, sr3f];
dr1f = Plot[10^3, {λ, xlow1, xlow2}, PlotRange -> {ylo1, ylow2},
  PlotStyle -> {Blue[ColorPib], Dotted, Thick, Thick},
  GridLines -> Automatic, Frame -> True, FrameLabel ->
  {"Wavelength (nm)", " Stark Shift (kHz)", "Light Shift for Triplet P1 State Coupled
  to Higher Triplet States, m = ±1 (λ < 1100 nm)", ""}]
dr2f = Plot[10^3, {λ, xmid1, xmid2}, PlotRange -> {ymid1, ymid2},
  PlotStyle -> {Blue[ColorPib], Dotted, Thick, Thick},
  GridLines -> Automatic, Frame -> True, FrameLabel ->
  {"Wavelength (nm)", " Stark Shift (kHz)", "Light Shift for Triplet P1 State Coupled
  to Higher Triplet States, m = ±1 (2000 nm < λ < 3000 nm)", ""}]
dr3f = Plot[10^3, {λ, xhigh1, xhigh2}, PlotRange -> {yhigh1, yhigh2},
  PlotStyle -> {Blue[ColorPib], Dotted, Thick, Thick},
  GridLines -> Automatic, Frame -> True, FrameLabel ->
  {"Wavelength (nm)", " Stark Shift (kHz)", "Light Shift for Triplet P1 State Coupled
  to Higher Triplet States, m = ±1 (5000 < λ < 10000 nm)", ""}]
sr1f = LogPlot[tslist[λ], {λ, xlow1, xlow2}, PlotRange -> {0.0001, 1},
  Frame -> True, GridLines -> Automatic, FrameLabel ->
  {"Wavelength (nm)", "Scattering Rate (Hz)", "Scattering Rate for Triplet P1 State
  Coupled to Higher Triplet States, m = ±1 (λ < 1100 nm)", ""}]
sr2f = LogPlot[tslist[λ], {λ, xmid1, xmid2}, PlotRange -> {0.0001, 1},
  Frame -> True, GridLines -> Automatic, FrameLabel ->
  {"Wavelength (nm)", "Scattering Rate (Hz)", "Scattering Rate for Triplet P1 State
  Coupled to Higher Triplet States, m = ±1 (2000 nm < λ < 3000 nm)", ""}]
sr3f = LogPlot[tslist[λ], {λ, xhigh1, xhigh2}, PlotRange -> {1.*^-6, 1},
  Frame -> True, GridLines -> Automatic, FrameLabel ->
  {"Wavelength (nm)", "Scattering Rate (Hz)", "Scattering Rate for Triplet P1 State
  Coupled to Higher Triplet States, m = ±1 (5000 < λ < 10000 nm)", ""}]

```

■ All Polarizations

```

In[700]:= Show[{dr1e, dr1f},
FrameLabel->{"Wavelength (nm)", "Stark Shift (kHz)", "Light Shift for Triplet
P1 State Coupled to Triplet S, P, & D; m = 0, z1, ( $\lambda < 1100$  nm)", ""}],
Show[{dr2e, dr2f}, FrameLabel->{"Wavelength (nm)", "Stark Shift (kHz)",
"Light Shift for Triplet P1 State Coupled to Triplet
S, P, & D; m = 0, z1, (2000 nm <  $\lambda < 3000$  nm)", ""}],
Show[{dr3e, dr3f}, FrameLabel->{"Wavelength (nm)", "Stark Shift (kHz)",
"Light Shift for Triplet P2 State Coupled to Triplet
S, P, & D; m = 0, z1, (5000 nm <  $\lambda < 10000$  nm)", ""}],
Show[{sr1e, sr1f}, FrameLabel->{"Wavelength (nm)", "Scattering Rate (Hz)",
"Scattering Rate for Triplet P State Coupled
to Triplet S, P, & D; m = 0, z1, ( $\lambda < 1100$  nm)", ""}],
Show[{sr2e, sr2f}, FrameLabel->{"Wavelength (nm)", "Scattering Rate (Hz)",
"Scattering Rate for Triplet P State Coupled to Triplet
S, P, & D; m = 0, z1, (2000 nm <  $\lambda < 3000$  nm)", ""}],
Show[{sr3e, sr3f}, FrameLabel->{"Wavelength (nm)", "Scattering Rate (Hz)",
"Scattering Rate for Triplet P State Coupled to Triplet
S, P, & D; m = 0, z1, (5000 nm <  $\lambda < 10000$  nm)", ""}]]

```

Triplet P2 State Light Shift

■ m=0, q=0 (linear polarization)

The form of the list data is as follows: List[resonance wavelength, transition probability, j1, m1, q1].

■ Transition Data

```

Experimental Data
s5s06 = List[704.960, 4.25 * 107, 1, 2];
s5s07 = List[443.930, 1.02 * 107, 1, 2];
s5s08 = List[386.650, 7.44 * 106, 1, 2];
s5d4a = List[3067.02, 8.30 * 107, 1, 2];
s5d4b = List[3011.84, 7.89 * 107, 2, 2];
s5d4c = List[2923.37, 3.45 * 108, 3, 2];
s5d5a = List[497.310, 1.80 * 106, 1, 2];
s5d5b = List[496.930, 1.62 * 107, 2, 2];
s5d5c = List[496.360, 7.16 * 107, 3, 2];
s5d6a = List[403.430, 8.12 * 106, 1, 2];
s5d6b = List[403.350, 8.20 * 106, 2, 2];
s5d6c = List[403.150, 2.93 * 107, 3, 2];
p5p5b = List[487.770, 6.54 * 107, 1, 2];
p5p5c = List[481.320, 1.15 * 108, 2, 2];

Theoretical Numbers
s5s06 = List[704.960, 7.13 * 107, 1, 2];
s5s07 = List[443.930, 1.75 * 106, 1, 2];
s5s08 = List[386.650, 8.22 * 106, 1, 2];
s5s09 = List[362.940, 4.53 * 106, 1, 2];
s5s10 = List[350.520, 2.77 * 106, 1, 2];
s5d4a = List[3067.02, 4.32 * 106, 1, 2];
s5d4b = List[3011.84, 4.32 * 107, 2, 2];
s5d4c = List[2923.37, 4.32 * 108, 3, 2];
s5d5a = List[497.310, 5.83 * 107, 1, 2];
s5d5b = List[496.930, 5.83 * 107, 2, 2];
s5d5c = List[496.360, 5.83 * 107, 3, 2];
s5d6a = List[403.430, 2.67 * 107, 1, 2];
s5d6b = List[403.350, 2.67 * 107, 2, 2];
s5d6c = List[403.150, 2.67 * 107, 3, 2];
s5d7a = List[370.840, 3.94 * 106, 1, 2];
s5d7b = List[370.770, 3.55 * 106, 2, 2];
s5d7c = List[370.700, 1.42 * 106, 3, 2];
s5d8a = List[395.010, 2.36 * 106, 1, 2];
s5d8b = List[394.970, 2.13 * 106, 2, 2];
s5d8c = List[394.910, 8.51 * 105, 3, 2];
s5d9a = List[345.910, 1.53 * 106, 1, 2];
s5d9b = List[345.910, 1.38 * 106, 2, 2];
s5d9c = List[345.850, 5.51 * 105, 3, 2];
p5p5b = List[487.770, 6.10 * 107, 1, 2];
p5p5c = List[481.320, 6.10 * 107, 2, 2];

```

```

In[700]:= Clear[triplet2statalinear0]
m1 = 0; q = 0;
s5s06 = List[704.960, 4.25*10^7, 1, 2];
s5s07 = List[443.930, 1.02*10^7, 1, 2];
s5s08 = List[386.650, 7.44*10^6, 1, 2];
s5s09 = List[362.940, 4.53*10^6, 1, 2];
s5s10 = List[350.520, 2.77*10^6, 1, 2];
s5d4a = List[3067.02, 8.30*10^5, 1, 2];
s5d4b = List[3011.84, 7.89*10^4, 2, 2];
s5d4c = List[2923.37, 3.45*10^5, 3, 2];
s5d5a = List[497.310, 1.80*10^6, 1, 2];
s5d5b = List[496.930, 1.62*10^7, 2, 2];
s5d5c = List[496.360, 7.16*10^7, 3, 2];
s5d6a = List[403.430, 8.12*10^5, 1, 2];
s5d6b = List[403.350, 8.20*10^6, 2, 2];
s5d6c = List[403.150, 2.93*10^7, 3, 2];
s5d7a = List[370.840, 3.94*10^5, 1, 2];
s5d7b = List[370.770, 3.55*10^6, 2, 2];
s5d7c = List[370.700, 1.42*10^7, 3, 2];
s5d8a = List[385.010, 2.36*10^5, 1, 2];
s5d8b = List[354.970, 2.13*10^6, 2, 2];
s5d8c = List[354.910, 8.51*10^6, 3, 2];
s5d9a = List[345.910, 1.53*10^5, 1, 2];
s5d9b = List[345.910, 1.38*10^6, 2, 2];
s5d9c = List[345.850, 5.51*10^6, 3, 2];
p5p5b = List[487.770, 6.54*10^7, 1, 2];
p5p5c = List[481.320, 1.15*10^8, 2, 2];
triplet2statalinear0 = Out[{-25, -24, -23, -22, -21, -20, -19, -18,
-17, -16, -15, -14, -13, -12, -11, -10, -9, -8, -7, -6, -5, -4, -3, -2, -1}];

```

■ Calculating the Light Shifts

```

In[701]:= Clear[max, ts20d, ts20s]
max = Length[triplet2statalinear0];
StartSum[λ_] := 0
ScatSum[λ_] := 0
For[i = 1, i ≤ max, i++,
(
  λc = Part[Part[triplet2statalinear0, i], 1];
  T = Part[Part[triplet2statalinear0, i], 2];
  j = Part[Part[triplet2statalinear0, i], 3];
  j1 = Part[Part[triplet2statalinear0, i], 4];
  StartSum[λ_] = StartSum[λ] + Summand[λ];
  ScatSum[λ_] = ScatSum[λ] + Summand2[λ];
)
];
ts20d[λ_] = depth[λ];
ts20s[λ_] = scat[λ];

```

■ Plotting the Light Shifts

```

In[801]:= Clear[dr1g, dr2g, dr3g, sr1g, sr2g, sr3g]
dr1g = Plot[ $\frac{10^3}{ts20d[\lambda]}$ , {λ, xlow1, xlow2}], PlotRange → {ylow1, ylow2},
PlotStyle → {Blue[ColorP2a], Dotted, Thick}, GridLines → Automatic, Frame → True,
FrameLabel → {"Wavelength (nm)", "Stark Shift (kHz)", "Light Shift for Triplet P1
State Coupled to Higher Triplet States, m = 0, (λ < 1100 nm)", ""}]
dr2g = Plot[ $\frac{10^3}{ts20d[\lambda]}$ , {λ, xmid1, xmid2}], PlotRange → {ymid1, ymid2},
PlotStyle → {Blue[ColorP2a], Dotted, Thick}, GridLines → Automatic, Frame → True,
FrameLabel → {"Wavelength (nm)", "Stark Shift (kHz)", "Light Shift for Triplet P1 State
Coupled to Higher Triplet States, m = 0, (2000 nm < λ < 3000 nm)", ""}]
dr3g = Plot[ $\frac{10^3}{ts20d[\lambda]}$ , {λ, xhigh1, xhigh2}], PlotRange → {yhigh1, yhigh2},
PlotStyle → {Blue[ColorP2a], Dotted, Thick}, GridLines → Automatic, Frame → True,
FrameLabel → {"Wavelength (nm)", "Stark Shift (kHz)", "Light Shift for Triplet P1 State
Coupled to Higher Triplet States, m = 0, (5000 < λ < 10000 nm)", ""}]
sr1g = LogPlot[ts20s[λ], {λ, xlow1, xlow2}], PlotRange → {0.0001, 1},
PlotStyle → {Blue[ColorP2a], Dotted, Thick}, Frame → True, GridLines → Automatic,
FrameLabel → {"Scattering Rate (Hz)", "Scattering Rate for Triplet
P1 State Coupled to Higher Triplet States, m = 0, (λ < 1000 nm)", ""}]
sr2g = LogPlot[ts20s[λ], {λ, xmid1, xmid2}], PlotRange → {0.0001, 1},
PlotStyle → {Blue[ColorP2a], Dotted, Thick}, Frame → True, GridLines → Automatic,
FrameLabel → {"Wavelength (nm)", "Scattering Rate (Hz)", "Scattering Rate for Triplet P1
State Coupled to Higher Triplet States, m = 0, (2000 nm < λ < 3000 nm)", ""}]
sr3g = LogPlot[ts20s[λ], {λ, xhigh1, xhigh2}], PlotRange → {1.*^-6, 1},
PlotStyle → {Blue[ColorP2a], Dotted, Thick}, Frame → True, GridLines → Automatic,
FrameLabel → {"Wavelength (nm)", "Scattering Rate (Hz)", "Scattering Rate for Triplet P1
State Coupled to Higher Triplet States, m = 0, (5000 < λ < 10000 nm)", ""}]

```

```

In[608]:= Solve[depth[λ]/10³ = 100, λ]
Solve[depth[λ]/10³ = 208.3, λ]
Solve[depth[λ]/10³ = 300, λ]
List[depth[3500./10³]]

Out[608]= {{λ -> -3064.69}, {λ -> -2309.75}, {λ -> -653.957}, {λ -> -497.295}, {λ -> -491.119},
{λ -> -450.701}, {λ -> -433.764}, {λ -> -403.425}, {λ -> -393.676}, {λ -> -384.298},
{λ -> -370.838}, {λ -> -367.182}, {λ -> -361.954}, {λ -> -355.008}, {λ -> -352.998},
{λ -> -349.947}, {λ -> -345.909}, {λ -> -344.251}, {λ -> -344.251}, {λ -> -345.909},
{λ -> -349.947}, {λ -> -352.998}, {λ -> -355.008}, {λ -> -361.954}, {λ -> -367.182},
{λ -> -370.838}, {λ -> -384.298}, {λ -> -393.676}, {λ -> -403.425}, {λ -> -433.764},
{λ -> -450.701}, {λ -> -491.119}, {λ -> -497.295}, {λ -> -653.957}, {λ -> -2309.75}, {λ -> -3064.69}}

Out[609]= {{λ -> -3064.87}, {λ -> -2503.34}, {λ -> -672.112}, {λ -> -497.296}, {λ -> -491.424},
{λ -> -476.792}, {λ -> -460.83}, {λ -> -442.768}, {λ -> -425.79}, {λ -> -412.297},
{λ -> -376.838}, {λ -> -369.909}, {λ -> -362.679}, {λ -> -355.009}, {λ -> -352.997},
{λ -> -350.382}, {λ -> -345.909}, {λ -> -345.463}, {λ -> -345.463}, {λ -> -345.909},
{λ -> -350.382}, {λ -> -354.287}, {λ -> -355.008}, {λ -> -362.679}, {λ -> -369.448},
{λ -> -370.838}, {λ -> -386.043}, {λ -> -399.318}, {λ -> -403.425}, {λ -> -441.806},
{λ -> -464.737}, {λ -> -491.424}, {λ -> -497.296}, {λ -> -672.112}, {λ -> -2503.34}, {λ -> -3064.87}}

Out[610]= {{λ -> -3065.01}, {λ -> -2591.94}, {λ -> -679.865}, {λ -> -497.296}, {λ -> -491.688},
{λ -> -471.971}, {λ -> -442.768}, {λ -> -403.425}, {λ -> -400.688}, {λ -> -386.285},
{λ -> -370.838}, {λ -> -369.907}, {λ -> -362.781}, {λ -> -355.009}, {λ -> -354.521},
{λ -> -350.437}, {λ -> -345.909}, {λ -> -345.617}, {λ -> -345.617}, {λ -> -345.909},
{λ -> -350.437}, {λ -> -354.521}, {λ -> -355.009}, {λ -> -362.781}, {λ -> -369.907},
{λ -> -370.838}, {λ -> -386.285}, {λ -> -400.688}, {λ -> -403.425}, {λ -> -442.768},
{λ -> -471.971}, {λ -> -491.688}, {λ -> -497.296}, {λ -> -679.865}, {λ -> -2591.94}, {λ -> -3065.01}}

Out[611]= {-393.747}

■ m=1, q=0 (linear polarization)

The form of the list data is as follows: List[resonance wavelength, transition probability, j1, m1, q].

```

■ Transition Data

Experimental Data

```

s5506 = List[704.960, 4.25 * 10⁷, 1, 2];
s5507 = List[443.930, 1.02 * 10⁷, 1, 2];
s5508 = List[386.650, 7.44 * 10⁶, 1, 2];
s554a = List[3067.02, 8.30 * 10⁷, 1, 2];
s554b = List[3011.84, 7.89 * 10⁷, 2, 2];
s554c = List[2923.37, 3.45 * 10⁷, 3, 2];
s555a = List[497.310, 1.80 * 10⁶, 1, 2];
s555b = List[496.930, 1.62 * 10⁷, 2, 2];
s555c = List[496.360, 7.16 * 10⁷, 3, 2];
s556a = List[403.430, 8.12 * 10⁶, 1, 2];
s556b = List[403.350, 8.20 * 10⁶, 2, 2];
s556c = List[403.150, 2.93 * 10⁷, 3, 2];
p555b = List[487.770, 6.54 * 10⁷, 1, 2];
p555c = List[481.320, 1.15 * 10⁸, 2, 2];
Theoretical Numbers
s5506 = List[704.960, 7.13 * 10⁷, 1, 2];
s5507 = List[443.930, 1.75 * 10⁷, 1, 2];
s5508 = List[386.650, 8.22 * 10⁶, 1, 2];
s5509 = List[362.940, 4.53 * 10⁷, 1, 2];
s5510 = List[350.520, 2.77 * 10⁶, 1, 2];
s554a = List[3067.02, 4.32 * 10⁶, 1, 2];
s554b = List[3011.84, 4.32 * 10⁶, 2, 2];
s554c = List[2923.37, 4.32 * 10⁶, 3, 2];
s555a = List[497.310, 5.83 * 10⁷, 1, 2];
s555b = List[496.930, 5.83 * 10⁷, 2, 2];
s555c = List[496.360, 5.83 * 10⁷, 3, 2];
s556a = List[403.430, 2.67 * 10⁷, 1, 2];
s556b = List[403.350, 2.67 * 10⁷, 2, 2];
s556c = List[403.150, 2.67 * 10⁷, 3, 2];
s557a = List[370.840, 3.94 * 10⁵, 1, 2];
s557b = List[370.770, 3.55 * 10⁶, 2, 2];
s557c = List[370.700, 1.42 * 10⁷, 3, 2];
s558a = List[395.010, 2.36 * 10⁵, 1, 2];
s558b = List[394.970, 2.13 * 10⁶, 2, 2];
s558c = List[394.910, 8.51 * 10⁶, 3, 2];
s559a = List[345.910, 1.53 * 10⁵, 1, 2];
s559b = List[345.910, 1.38 * 10⁶, 2, 2];
s559c = List[345.850, 5.51 * 10⁶, 3, 2];
p555b = List[487.770, 6.10 * 10⁷, 1, 2];
p555c = List[481.320, 6.10 * 10⁷, 2, 2];

```

```

In[62]:=
mi = j; q = 0;
s506 = List[704.960, 4.25*10^7, 1, 2];
s507 = List[443.930, 1.02*10^7, 1, 2];
s508 = List[386.650, 7.44*10^6, 1, 2];
s509 = List[362.940, 4.53*10^6, 1, 2];
s510 = List[350.520, 2.77*10^6, 1, 2];
s511 = List[3067.02, 8.30*10^5, 1, 2];
s512 = List[3011.84, 7.89*10^5, 2, 2];
s513 = List[2923.37, 3.45*10^5, 3, 2];
s514 = List[497.310, 1.80*10^6, 1, 2];
s515 = List[496.930, 1.62*10^7, 2, 2];
s516 = List[496.360, 7.16*10^7, 3, 2];
s517 = List[403.430, 8.12*10^6, 1, 2];
s518 = List[403.350, 8.20*10^6, 2, 2];
s519 = List[403.150, 2.93*10^7, 3, 2];
s520 = List[370.840, 3.94*10^6, 1, 2];
s521 = List[370.770, 3.55*10^6, 2, 2];
s522 = List[370.700, 1.42*10^7, 3, 2];
s523 = List[385.010, 2.36*10^6, 1, 2];
s524 = List[354.970, 2.13*10^6, 2, 2];
s525 = List[354.910, 8.51*10^6, 3, 2];
s526 = List[345.910, 1.53*10^6, 1, 2];
s527 = List[345.910, 1.38*10^6, 2, 2];
s528 = List[345.850, 5.51*10^6, 3, 2];
p529 = List[487.770, 6.54*10^7, 1, 2];
p530 = List[481.320, 1.15*10^8, 2, 2];
triplet2state1inear1 = Out[25, 24, -23, -22, -21, -20, -19, -18,
-17, -16, -15, -14, -13, -12, -11, -10, -9, -8, -7, -6, -5, -4, -3, -2, -1]];

```

■ Calculating the Light Shifts

```

In[63]:=
Clear[max, ts2id, ts2is]
max = Length[triplet2state1inear1];
ScatSum[λ_] := 0
ScatSum[λ_] := 0
For[i = 1, i ≤ max, i++,
  λr = Part[Part[triplet2state1inear1, i], 1];
  r = Part[Part[triplet2state1inear1, i], 2];
  j = Part[Part[triplet2state1inear1, i], 3];
  j1 = Part[Part[triplet2state1inear1, i], 4];
  ScatSum[λ_] = ScatSum[λ] + Summand[i];
  ScatSum[λ_] = ScatSum[λ] + Summand2[i];
];
ts2id[λ_] = depth[λ];
ts2is[λ_] = scat[λ];

```

■ Plotting the Light Shifts

```

In[847]:=
Clear[dr3b, dr2h, dr3h, dr3b, sr1h, sr2h, sr3h]
dr3b = Plot[
  10^3, {λ, xlow1, xlow2}, PlotRange → {ylow1, ylow2},
  PlotStyle → {Blue[ColorP2b]}, Dotted, Thick, GridLines → Automatic, Frame → True,
  FrameLabel → {"Wavelength (nm)", "Stark Shift (kHz)", "Light Shift for Triplet P1
  State Coupled to Higher Triplet States, m = ±1 (λ < 1100 nm)", ""}],
  dr2h = Plot[
  10^3, {λ, xmid1, xmid2}, PlotRange → {ymid1, ymid2},
  PlotStyle → {Blue[ColorP2b]}, Dotted, Thick, GridLines → Automatic, Frame → True,
  FrameLabel → {"Wavelength (nm)", "Stark Shift (kHz)", "Light Shift for Triplet P1 State
  Coupled to Higher Triplet States, m = ±1 (2000 nm < λ < 3000 nm)", ""}],
  dr3h = Plot[
  10^3, {λ, xhigh1, xhigh2}, PlotRange → {yhigh1, yhigh2},
  PlotStyle → {Blue[ColorP2b]}, Dotted, Thick, GridLines → Automatic, Frame → True,
  FrameLabel → {"Wavelength (nm)", "Stark Shift (kHz)", "Light Shift for Triplet P1 State
  Coupled to Higher Triplet States, m = ±1 (5000 < λ < 10000 nm)", ""}],
  sr1h = LogPlot[ts2is[λ], {λ, xlow1, xlow2}, PlotRange → {0.0001, 1},
  PlotStyle → {Blue[ColorP2b]}, Dotted, Thick, Frame → True, GridLines → Automatic,
  FrameLabel → {"Scattering Rate (Hz)", "Scattering Rate for Triplet
  P1 State Coupled to Higher Triplet States, m = ±1 (λ < 1100 nm)", ""}],
  sr2h = LogPlot[ts2is[λ], {λ, xmid1, xmid2}, PlotRange → {0.0001, 1},
  PlotStyle → {Blue[ColorP2b]}, Dotted, Thick, Frame → True, GridLines → Automatic,
  FrameLabel → {"Wavelength (nm)", "Scattering Rate (Hz)", "Scattering Rate for Triplet P1
  State Coupled to Higher Triplet States, m = ±1 (2000 nm < λ < 3000 nm)", ""}],
  sr3h = LogPlot[ts2is[λ], {λ, xhigh1, xhigh2}, PlotRange → {1.*^-6, 1},
  PlotStyle → {Blue[ColorP2b]}, Dotted, Thick, Frame → True, GridLines → Automatic,
  FrameLabel → {"Wavelength (nm)", "Scattering Rate (Hz)", "Scattering Rate for Triplet P1
  State Coupled to Higher Triplet States, m = ±1 (5000 < λ < 10000 nm)", ""}],

```

■ m=2, q=0 (linear polarization)

The form of the list data is as follows: List[resonance wavelength, transition probability, j1, m1, q].

```

In[84]:= Clear[triplet2stateilinear2]
ma = 2; q = 0;
s5d6b = List[704.960, 4.25 * 107, 1, 2];
s5s06 = List[704.960, 4.25 * 107, 1, 2];
s5s07 = List[443.930, 1.02 * 107, 1, 2];
s5s08 = List[386.650, 7.44 * 106, 1, 2];
s5d4a = List[3067.02, 8.30 * 103, 1, 2];
s5d4b = List[3011.84, 7.89 * 104, 2, 2];
s5d4c = List[2923.37, 3.45 * 105, 3, 2];
s5d5a = List[497.310, 1.80 * 106, 1, 2];
s5d5b = List[496.930, 1.62 * 107, 2, 2];
s5d5c = List[496.360, 7.16 * 107, 3, 2];
s5d6a = List[403.430, 8.12 * 105, 1, 2];
s5d6b = List[403.350, 8.20 * 106, 2, 2];
s5d6c = List[403.150, 2.93 * 107, 3, 2];
p5p5b = List[487.770, 6.54 * 107, 1, 2];
p5p5c = List[481.320, 1.15 * 108, 2, 2];

Theoretical Numbers
s5s06 = List[704.960, 7.13 * 107, 1, 2];
s5s07 = List[443.930, 1.75 * 106, 1, 2];
s5s08 = List[386.650, 8.22 * 106, 1, 2];
s5s09 = List[362.940, 4.53 * 106, 1, 2];
s5s10 = List[350.520, 2.77 * 106, 1, 2];
s5d4a = List[3067.02, 4.32 * 106, 1, 2];
s5d4b = List[3011.84, 4.32 * 106, 2, 2];
s5d4c = List[2923.37, 4.32 * 106, 3, 2];
s5d5a = List[497.310, 5.83 * 107, 1, 2];
s5d5b = List[496.930, 5.83 * 107, 2, 2];
s5d5c = List[496.360, 5.83 * 107, 3, 2];
s5d6a = List[403.430, 2.67 * 107, 1, 2];
s5d6b = List[403.350, 2.67 * 107, 2, 2];
s5d6c = List[403.150, 2.67 * 107, 3, 2];
s5d7a = List[370.840, 3.94 * 105, 1, 2];
s5d7b = List[370.770, 3.55 * 106, 2, 2];
s5d7c = List[370.700, 1.42 * 107, 3, 2];
s5d8a = List[355.010, 2.36 * 105, 1, 2];
s5d8b = List[354.970, 2.13 * 106, 2, 2];
s5d8c = List[354.910, 8.51 * 106, 3, 2];
s5d9a = List[345.910, 1.53 * 105, 1, 2];
s5d9b = List[345.850, 1.38 * 106, 2, 2];
s5d9c = List[345.850, 5.51 * 106, 3, 2];
p5p5b = List[487.770, 6.10 * 107, 1, 2];
p5p5c = List[481.320, 6.10 * 107, 2, 2];

Experimental Data
s5d6b = List[3011.84, 7.89 * 104, 2, 2];
s5d4c = List[2923.37, 3.45 * 105, 3, 2];
s5d5b = List[496.930, 1.62 * 107, 2, 2];
s5d5c = List[496.360, 7.16 * 107, 3, 2];
s5d6b = List[403.350, 8.20 * 106, 2, 2];
s5d4c = List[403.150, 2.93 * 107, 3, 2];
s5d7b = List[370.770, 3.55 * 106, 2, 2];
s5d7c = List[370.700, 1.42 * 107, 3, 2];
s5d8b = List[354.970, 2.13 * 106, 2, 2];
s5d8c = List[354.910, 8.51 * 106, 3, 2];
s5d9b = List[345.910, 1.53 * 105, 1, 2];
s5d9c = List[345.850, 5.51 * 106, 3, 2];
p5p5b = List[481.320, 1.15 * 108, 2, 2];
triplet2stateilinear2 = Out[{-13, -12, -11, -10, -9, -8, -7, -6, -5, -4, -3, -2, -1}];

■ Calculating the Light Shifts
In[870]:= Clear[max, ts22d, ts22s]
max = Length[triplet2stateilinear2];
StarkSum[λ_] := 0
ScatSum[λ_] := 0
For[i = 1, i ≤ max, i++,
(
Ar = Part[Part[triplet2stateilinear2, i], 1];
t = Part[Part[triplet2stateilinear2, i], 2];
j = Part[Part[triplet2stateilinear2, i], 3];
jl = Part[Part[triplet2stateilinear2, i], 4];
StarkSum[λ_] = StarkSum[λ] + Summand[λ];
ScatSum[λ_] = ScatSum[λ] + Summand2[λ];
)
)
ts22d[λ_] = depth[λ];
ts22s[λ_] = scat[λ];

```

- Plotting the Light Shifts

```
(q877)=
Clear[dr1i, dr2i, dr3i, sr1i, sr2i, sr3i]

dr1i = Plot[ $\frac{10^3}{ts22d[\lambda]}$ , { $\lambda$ , xlow1, xlow2}, PlotRange -> {ylow1, ylow2},
  PlotStyle -> {Hue[ColorP2c], Dotted, Thick}, GridLines -> Automatic, Frame -> True,
  FrameLabel -> {"Wavelength (nm)", "Stark Shift (kHz)", "Light Shift for Triplet P1
  State Coupled to Higher Triplet States, m = z1 ( $\lambda < 1100$  nm)", ""}],
  { $\lambda$ , xmid1, xmid2}, PlotRange -> {ymid1, ymid2},
  PlotStyle -> {Hue[ColorP2c], Dotted, Thick}, GridLines -> Automatic, Frame -> True,
  FrameLabel -> {"Wavelength (nm)", "Stark Shift (kHz)", "Light Shift for Triplet P1 State
  Coupled to Higher Triplet States, m = z1 (2000 nm <  $\lambda < 3000$  nm)", ""}],
  { $\lambda$ , xhigh1, xhigh2}, PlotRange -> {yhigh1, yhigh2},
  PlotStyle -> {Hue[ColorP2c], Dotted, Thick}, GridLines -> Automatic, Frame -> True,
  FrameLabel -> {"Wavelength (nm)", "Stark Shift (kHz)", "Light Shift for Triplet P1 State
  Coupled to Higher Triplet States, m = z1 (5000 <  $\lambda < 10000$  nm)", ""}],
  LogPlot[ts22s[\lambda], { $\lambda$ , xlow1, xlow2}, PlotRange -> {0, 0.001}, 1},
  PlotStyle -> {Hue[ColorP2c], Dotted, Thick}, Frame -> True, GridLines -> Automatic,
  FrameLabel -> {"Wavelength (nm)", "Scattering Rate (Hz)", "Scattering Rate for Triplet
  P1 State Coupled to Higher Triplet States, m = z1 ( $\lambda < 1100$  nm)", ""}],
  LogPlot[ts22s[\lambda], { $\lambda$ , xmid1, xmid2}, PlotRange -> {0, 0.001}, 1},
  PlotStyle -> {Hue[ColorP2c], Dotted, Thick}, Frame -> True, GridLines -> Automatic,
  FrameLabel -> {"Wavelength (nm)", "Scattering Rate (Hz)", "Scattering Rate for Triplet P1
  State Coupled to Higher Triplet States, m = z1 (2000 nm <  $\lambda < 3000$  nm)", ""}],
  LogPlot[ts22s[\lambda], { $\lambda$ , xhigh1, xhigh2}, PlotRange -> {1, 10^6}, 1},
  PlotStyle -> {Hue[ColorP2c], Dotted, Thick}, Frame -> True, GridLines -> Automatic,
  FrameLabel -> {"Wavelength (nm)", "Scattering Rate (Hz)", "Scattering Rate for Triplet P1
  State Coupled to Higher Triplet States, m = z1 (5000 <  $\lambda < 10000$  nm)", ""}],
  State Coupled to Higher Triplet States, m = z1 (5000 <  $\lambda < 10000$  nm)", ""]]]
```

- m=0, q=1 (circular polarization)

The form of the list data is as follows: List[resonance wavelength, transition probability, j1, m1, q].

- Transition Data

```
(q878)=
ExperimentalData
s5a06 = List[704.960, 4.25 * 10^6, 1, 2];
s5a07 = List[443.930, 1.02 * 10^6, 1, 2];
s5a08 = List[386.650, 7.44 * 10^6, 1, 2];
s5d4a = List[3067.02, 8.30 * 10^6, 1, 2];
s5d4b = List[3011.84, 7.89 * 10^6, 2, 2];
s5d4c = List[2923.37, 3.45 * 10^6, 3, 2];
s5d5a = List[497.310, 1.80 * 10^6, 1, 2];
s5d5b = List[496.930, 1.62 * 10^6, 2, 2];
s5d5c = List[496.360, 7.16 * 10^6, 3, 2];
s5d6a = List[403.430, 8.12 * 10^6, 1, 2];
s5d6b = List[403.350, 8.20 * 10^6, 2, 2];
s5d6c = List[403.150, 2.93 * 10^6, 3, 2];
p5p5b = List[487.770, 6.54 * 10^6, 1, 2];
p5p5c = List[481.320, 1.15 * 10^6, 2, 2];
TheoreticalNumbers
s5a06 = List[704.960, 7.13 * 10^6, 1, 2];
s5a07 = List[443.930, 1.75 * 10^6, 1, 2];
s5a08 = List[386.650, 8.22 * 10^6, 1, 2];
s5d09 = List[362.940, 4.53 * 10^6, 1, 2];
s5d10 = List[350.520, 2.77 * 10^6, 1, 2];
s5d4a = List[3067.02, 4.32 * 10^6, 1, 2];
s5d4b = List[3011.84, 4.32 * 10^6, 2, 2];
s5d4c = List[2923.37, 4.32 * 10^6, 3, 2];
s5d5a = List[497.310, 5.83 * 10^6, 1, 2];
s5d5b = List[496.930, 5.83 * 10^6, 2, 2];
s5d5c = List[496.360, 5.83 * 10^6, 3, 2];
s5d6a = List[403.430, 2.67 * 10^6, 1, 2];
s5d6b = List[403.350, 2.67 * 10^6, 2, 2];
s5d6c = List[403.150, 2.67 * 10^6, 3, 2];
s5d7a = List[370.840, 3.94 * 10^6, 1, 2];
s5d7b = List[370.770, 3.55 * 10^6, 2, 2];
s5d7c = List[370.700, 1.42 * 10^6, 3, 2];
s5d8a = List[355.010, 2.36 * 10^6, 1, 2];
s5d8b = List[354.970, 2.13 * 10^6, 2, 2];
s5d8c = List[354.910, 8.51 * 10^6, 3, 2];
s5d9a = List[345.910, 1.53 * 10^6, 1, 2];
s5d9b = List[345.910, 1.38 * 10^6, 2, 2];
s5d9c = List[345.850, 5.51 * 10^6, 3, 2];
p5p5b = List[487.770, 6.10 * 10^6, 1, 2];
p5p5c = List[481.320, 6.10 * 10^6, 2, 2];
```

```

In[88]:= Clear[triplet2statecircular0]
m1 = 0; q = 1;
s5s06 = List[704.960, 4.25*10^7, 1, 2];
s5s07 = List[443.930, 1.02*10^7, 1, 2];
s5s08 = List[386.650, 7.44*10^6, 1, 2];
s5s09 = List[362.940, 4.53*10^6, 1, 2];
s5s10 = List[350.520, 2.77*10^6, 1, 2];
s5d4a = List[3067.02, 8.30*10^5, 1, 2];
s5d4b = List[3011.84, 7.89*10^4, 2, 2];
s5d4c = List[2923.37, 3.45*10^5, 3, 2];
s5d5a = List[497.310, 1.80*10^6, 1, 2];
s5d5b = List[496.930, 1.62*10^7, 2, 2];
s5d6a = List[496.360, 7.16*10^5, 3, 2];
s5d6b = List[403.350, 8.20*10^6, 2, 2];
s5d6c = List[403.150, 2.93*10^7, 3, 2];
s5d7a = List[370.840, 3.94*10^6, 1, 2];
s5d7b = List[370.770, 3.55*10^6, 2, 2];
s5d8a = List[370.700, 1.42*10^7, 3, 2];
s5d8b = List[354.970, 2.13*10^6, 2, 2];
s5d8c = List[354.910, 8.51*10^6, 3, 2];
s5d9a = List[345.910, 1.53*10^6, 1, 2];
s5d9b = List[345.910, 1.38*10^6, 2, 2];
s5d9c = List[345.850, 5.51*10^6, 3, 2];
p5p5b = List[487.770, 6.54*10^7, 1, 2];
p5p5c = List[481.320, 1.15*10^8, 2, 2];
triplet2statecircular0 = Out[(-25, -24, -23, -22, -21, -20, -19, -18,
-17, -16, -15, -14, -13, -12, -11, -10, -9, -8, -7, -6, -5, -4, -3, -2, -1)];

```

■ Calculating the Light Shifts

```

In[92]:= Clear[max, ts201d, ts201s]
max = Length[triplet2statecircular0];
StartSum[λ_] := 0
ScatSum[λ_] := 0
For[i = 1, i ≤ max, i++,
(
λc = Part[Part[triplet2statecircular0, i], 1];
T = Part[Part[triplet2statecircular0, i], 2];
j = Part[Part[triplet2statecircular0, i], 3];
j1 = Part[Part[triplet2statecircular0, i], 4];
StartSum[λ_] = StartSum[λ] + Summand[λ];
ScatSum[λ_] = ScatSum[λ] + Summand2[λ];
);
];
ts201d[λ_] = depth[λ];
ts201s[λ_] = scat[λ];

```

■ Plotting the Light Shifts

```

In[93]:= Clear[dr1j, dr2j, dr3j, sr1j, sr2j, sr3j]
dr1j = Plot[
10^3
-----, {λ, xLow1, xLow2}, PlotRange → {yLow1, yLow2},
ts201d[λ]
PlotStyle → {Blue[ColorP2a], Dotted, Thick}, GridLines → Automatic, Frame → True,
FrameLabel → {"Wavelength (nm)", "Stark Shift (kHz)", "Light Shift for Triplet P1
State Coupled to Higher Triplet States, m = 0, (λ < 11000 nm)", ""}]
dr2j = Plot[
10^3
-----, {λ, xmid1, xmid2}, PlotRange → {ymid1, ymid2},
ts201d[λ]
PlotStyle → {Blue[ColorP2a], Dotted, Thick}, GridLines → Automatic, Frame → True,
FrameLabel → {"Wavelength (nm)", "Stark Shift (kHz)", "Light Shift for Triplet P1 State
Coupled to Higher Triplet States, m = 0, (2000 nm < λ < 30000 nm)", ""}]
dr3j = Plot[
10^3
-----, {λ, xhigh1, xhigh2}, PlotRange → {yhigh1, yhigh2},
ts201d[λ]
PlotStyle → {Blue[ColorP2a], Dotted, Thick}, GridLines → Automatic, Frame → True,
FrameLabel → {"Wavelength (nm)", "Stark Shift (kHz)", "Light Shift for Triplet P1 State
Coupled to Higher Triplet States, m = 0, (5000 < λ < 100000 nm)", ""}]
sr1j = LogPlot[ts201s[λ], {λ, xLow1, xLow2}, PlotRange → {0.0001, 1},
PlotStyle → {Blue[ColorP2a], Dotted, Thick}, Frame → True, GridLines → Automatic,
FrameLabel → {"Scattering Rate (Hz)", "Scattering Rate for Triplet
P1 State Coupled to Higher Triplet States, m = 0, (λ < 1100 nm)", ""}]
sr2j = LogPlot[ts201s[λ], {λ, xmid1, xmid2}, PlotRange → {0.0001, 1},
PlotStyle → {Blue[ColorP2a], Dotted, Thick}, Frame → True, GridLines → Automatic,
FrameLabel → {"Wavelength (nm)", "Scattering Rate (Hz)", "Scattering Rate for Triplet P1
State Coupled to Higher Triplet States, m = 0, (2000 nm < λ < 30000 nm)", ""}]
sr3j = LogPlot[ts201s[λ], {λ, xhigh1, xhigh2}, PlotRange → {1, 10^6, 10^7},
PlotStyle → {Blue[ColorP2a], Dotted, Thick}, Frame → True, GridLines → Automatic,
FrameLabel → {"Wavelength (nm)", "Scattering Rate (Hz)", "Scattering Rate for Triplet P1
State Coupled to Higher Triplet States, m = 0, (5000 < λ < 100000 nm)", ""}]

```

```

In[628]= Solve[depth[λ]/10³ = 100, λ]
          Solve[depth[λ]/10³ = 208.3, λ]
          Solve[depth[λ]/10³ = 300, λ]
List[depth[3000]/10³]

Out[628]= {{λ -> -3066.52}, {λ -> -2992.1}, {λ -> -2346.02}, {λ -> -691.706}, {λ -> -497.307},
           {λ -> -496.811}, {λ -> -491.659}, {λ -> -486.843}, {λ -> -444.714}, {λ -> -427.052},
           {λ -> -403.429}, {λ -> -403.298}, {λ -> -391.516}, {λ -> -385.656}, {λ -> -370.839},
           {λ -> -367.025}, {λ -> -362.649}, {λ -> -353.099}, {λ -> -350.374}, {λ -> -345.896},
           {λ -> -344.613}, {λ -> -344.613}, {λ -> -345.896}, {λ -> -350.374}, {λ -> -353.099},
           {λ -> -362.649}, {λ -> -367.025}, {λ -> -370.839}, {λ -> -385.656}, {λ -> -391.516},
           {λ -> -403.298}, {λ -> -403.429}, {λ -> -427.052}, {λ -> -444.714}, {λ -> -486.843},
           {λ -> -496.811}, {λ -> -497.307}, {λ -> -691.706}, {λ -> -2346.02}, {λ -> -2992.1}, {λ -> -3066.52}}

Out[627]= {{λ -> -3066.56}, {λ -> -2993.04}, {λ -> -2546.75}, {λ -> -696.645}, {λ -> -497.307},
           {λ -> -496.812}, {λ -> -492.094}, {λ -> -486.955}, {λ -> -451.283}, {λ -> -442.712},
           {λ -> -403.429}, {λ -> -403.3}, {λ -> -399.316}, {λ -> -386.485}, {λ -> -370.839},
           {λ -> -370.754}, {λ -> -369.578}, {λ -> -362.874}, {λ -> -354.377}, {λ -> -350.486},
           {λ -> -345.897}, {λ -> -345.539}, {λ -> -345.897}, {λ -> -350.486}, {λ -> -354.377},
           {λ -> -362.874}, {λ -> -369.578}, {λ -> -370.754}, {λ -> -370.839}, {λ -> -386.485}, {λ -> -399.316},
           {λ -> -403.3}, {λ -> -403.429}, {λ -> -442.712}, {λ -> -451.283}, {λ -> -486.955}, {λ -> -492.094},
           {λ -> -496.812}, {λ -> -497.307}, {λ -> -696.645}, {λ -> -2546.75}, {λ -> -2993.04}, {λ -> -3066.56}}

Out[626]= {{λ -> -3066.58}, {λ -> -2993.85}, {λ -> -2633.79}, {λ -> -698.648}, {λ -> -497.307},
           {λ -> -496.814}, {λ -> -492.431}, {λ -> -487.034}, {λ -> -459.7}, {λ -> -443.506},
           {λ -> -403.429}, {λ -> -403.301}, {λ -> -400.821}, {λ -> -386.555}, {λ -> -370.839},
           {λ -> -370.754}, {λ -> -370.009}, {λ -> -362.59}, {λ -> -354.583}, {λ -> -350.5},
           {λ -> -345.898}, {λ -> -345.664}, {λ -> -345.664}, {λ -> -345.898}, {λ -> -350.5},
           {λ -> -362.59}, {λ -> -370.009}, {λ -> -370.754}, {λ -> -370.839}, {λ -> -387.533}, {λ -> -400.821},
           {λ -> -403.3}, {λ -> -403.429}, {λ -> -444.714}, {λ -> -487.034}, {λ -> -492.431},
           {λ -> -496.814}, {λ -> -497.307}, {λ -> -698.648}, {λ -> -2633.79}, {λ -> -2993.85}, {λ -> -3066.58}}

Out[625]= {-347.89}

■ m=1, q=0 (linear polarization)
The form of the list data is as follows: List[resonance wavelength, transition probability, j1, m1, q].

```

■ Transition Data

Experimental Data

```

s5506 = List[704.960, 4.25 * 10⁷, 1, 2];
s5507 = List[443.930, 1.02 * 10⁷, 1, 2];
s5508 = List[386.650, 7.44 * 10⁶, 1, 2];
s554a = List[3067.02, 8.30 * 10⁷, 1, 2];
s554b = List[3011.84, 7.89 * 10⁷, 2, 2];
s554c = List[2923.37, 3.45 * 10⁷, 3, 2];
s555a = List[497.310, 1.80 * 10⁶, 1, 2];
s555b = List[496.930, 1.62 * 10⁷, 2, 2];
s555c = List[496.360, 7.16 * 10⁷, 3, 2];
s556a = List[403.430, 8.12 * 10⁶, 1, 2];
s556b = List[403.350, 8.20 * 10⁶, 2, 2];
s556c = List[403.150, 2.93 * 10⁷, 3, 2];
p555b = List[487.770, 6.54 * 10⁷, 1, 2];
p555c = List[481.320, 1.15 * 10⁸, 2, 2];

```

Theoretical Numbers

```

s5506 = List[704.960, 7.13 * 10⁷, 1, 2];
s5507 = List[443.930, 1.75 * 10⁷, 1, 2];
s5508 = List[386.650, 8.22 * 10⁶, 1, 2];
s5509 = List[362.940, 4.53 * 10⁷, 1, 2];
s5510 = List[350.520, 2.77 * 10⁶, 1, 2];
s554a = List[3067.02, 4.32 * 10⁶, 1, 2];
s554b = List[3011.84, 4.32 * 10⁷, 2, 2];
s554c = List[2923.37, 4.32 * 10⁸, 3, 2];
s555a = List[497.310, 5.83 * 10⁷, 1, 2];
s555b = List[496.930, 5.83 * 10⁷, 2, 2];
s555c = List[496.360, 5.83 * 10⁷, 3, 2];
s556a = List[403.430, 2.67 * 10⁷, 1, 2];
s556b = List[403.350, 2.67 * 10⁷, 2, 2];
s556c = List[403.150, 2.67 * 10⁷, 3, 2];
s557a = List[370.840, 3.94 * 10⁵, 1, 2];
s557b = List[370.770, 3.55 * 10⁶, 2, 2];
s557c = List[370.700, 1.42 * 10⁷, 3, 2];
s558a = List[395.010, 2.36 * 10⁵, 1, 2];
s558b = List[394.970, 2.13 * 10⁶, 2, 2];
s558c = List[394.910, 8.51 * 10⁶, 3, 2];
s559a = List[345.910, 1.53 * 10⁵, 1, 2];
s559b = List[345.910, 1.38 * 10⁶, 2, 2];
s559c = List[345.850, 5.51 * 10⁶, 3, 2];
p555b = List[487.770, 6.10 * 10⁷, 1, 2];
p555c = List[481.320, 6.10 * 10⁷, 2, 2];

```

```

In[600]:= Clear[triplet2statecircularl]
m1 = j; q = -j;
s506 = List[704.960, 4.25*10^7, 1, 2];
s507 = List[443.930, 1.02*10^7, 1, 2];
s508 = List[386.650, 7.44*10^6, 1, 2];
s509 = List[362.940, 4.53*10^6, 1, 2];
s510 = List[350.520, 2.77*10^6, 1, 2];
s511 = List[305.02, 8.30*10^5, 1, 2];
s512 = List[301.84, 7.89*10^5, 2, 2];
s513 = List[292.37, 3.45*10^5, 3, 2];
s514 = List[497.310, 1.80*10^6, 1, 2];
s515 = List[496.930, 1.62*10^7, 2, 2];
s516 = List[496.360, 7.16*10^7, 3, 2];
s517 = List[403.430, 8.12*10^6, 1, 2];
s518 = List[403.350, 8.20*10^6, 2, 2];
s519 = List[403.150, 2.93*10^7, 3, 2];
s520 = List[370.840, 3.94*10^6, 1, 2];
s521 = List[370.770, 3.55*10^6, 2, 2];
s522 = List[370.700, 1.42*10^7, 3, 2];
s523 = List[385.010, 2.36*10^6, 1, 2];
s524 = List[354.970, 2.13*10^6, 2, 2];
s525 = List[354.910, 8.51*10^6, 3, 2];
s526 = List[345.910, 1.53*10^6, 1, 2];
s527 = List[345.910, 1.38*10^6, 2, 2];
s528 = List[345.850, 5.51*10^6, 3, 2];
p529 = List[487.770, 6.54*10^7, 1, 2];
p530 = List[481.320, 1.15*10^8, 2, 2];
triplet2statecircularl = Out[{-25, -24, -23, -22, -21, -20, -19, -18,
-17, -16, -15, -14, -13, -12, -11, -10, -9, -8, -7, -6, -5, -4, -3, -2, -1}];

```

■ Calculating the Light Shifts

```

In[601]:= Clear[max, ts211d, ts211s]
max = Length[triplet2statecircularl];
StarSum[λ_] := 0
ScatSum[λ_] := 0
For[i = 1, i ≤ max, i++,
  λr = Part[Part[triplet2statecircularl, i], 1];
  r = Part[Part[triplet2statecircularl, i], 2];
  j = Part[Part[triplet2statecircularl, i], 3];
  j1 = Part[Part[triplet2statecircularl, i], 4];
  StarSum[λ_] = StarSum[λ] + Summand[λ];
  ScatSum[λ_] = ScatSum[λ] + Summand2[λ];
]
ts211d[λ_] = depth[λ];
ts211s[λ_] = scat[λ];

```

■ Plotting the Light Shifts

```

In[602]:= Clear[dr1b, dr2h, dr3h, sr1b, sr2h, sr3h]
dr1b = Plot[ $\frac{10^3}{ts211d[\lambda]}$ , {λ, xlow1, xlow2}, PlotRange → {ylow1, ylow2},
  PlotStyle → {Blue[ColorP2b], Dotted, Thick}, GridLines → Automatic, Frame → True,
  FrameLabel → {"Wavelength (nm)", "Stark Shift (kHz)", "Light Shift for Triplet P1
  State Coupled to Higher Triplet States, m = ±1 (λ < 1100 nm)", ""}]
dr2h = Plot[ $\frac{10^3}{ts21id[\lambda]}$ , {λ, xmid1, xmid2}, PlotRange → {ymid1, ymid2},
  PlotStyle → {Blue[ColorP2b], Dotted, Thick}, GridLines → Automatic, Frame → True,
  FrameLabel → {"Wavelength (nm)", "Stark Shift (kHz)", "Light Shift for Triplet P1 State
  Coupled to Higher Triplet States, m = ±1 (2000 nm < λ < 3000 nm)", ""}]
dr3h = Plot[ $\frac{10^3}{ts21id[\lambda]}$ , {λ, xhigh1, xhigh2}, PlotRange → {yhigh1, yhigh2},
  PlotStyle → {Blue[ColorP2b], Dotted, Thick}, GridLines → Automatic, Frame → True,
  FrameLabel → {"Wavelength (nm)", "Stark Shift (kHz)", "Light Shift for Triplet P1 State
  Coupled to Higher Triplet States, m = ±1 (5000 < λ < 10000 nm)", ""}]
sr1b = LogPlot[ts21s[λ], {λ, xlow1, xlow2}, PlotRange → {0.0001, 1},
  PlotStyle → {Blue[ColorP2b], Dotted, Thick}, Frame → True, GridLines → Automatic,
  FrameLabel → {"Scattering Rate (Hz)", "Scattering Rate for Triplet
  P1 State Coupled to Higher Triplet States, m = ±1 (λ < 100 nm)", ""}]
sr2h = LogPlot[ts21s[λ], {λ, xmid1, xmid2}, PlotRange → {0.0001, 1},
  PlotStyle → {Blue[ColorP2b], Dotted, Thick}, Frame → True, GridLines → Automatic,
  FrameLabel → {"Wavelength (nm)", "Scattering Rate (Hz)", "Scattering Rate for Triplet P1
  State Coupled to Higher Triplet States, m = ±1 (2000 nm < λ < 3000 nm)", ""}]
sr3h = LogPlot[ts21s[λ], {λ, xhigh1, xhigh2}, PlotRange → {1.*^-6, 1},
  PlotStyle → {Blue[ColorP2b], Dotted, Thick}, Frame → True, GridLines → Automatic,
  FrameLabel → {"Wavelength (nm)", "Scattering Rate (Hz)", "Scattering Rate for Triplet P1
  State Coupled to Higher Triplet States, m = ±1 (5000 < λ < 10000 nm)", ""}]

```

■ m=2, q=0 (linear polarization)

The form of the list data is as follows: List[resonance wavelength, transition probability, j1, m1, q].

- Transition Data

```

Experimental Data
s5s06 = List[704.960, 4.25 * 107, 1, 2];
s5s07 = List[443.930, 1.02 * 107, 1, 2];
s5s08 = List[386.650, 7.44 * 106, 1, 2];
s5d4a = List[3067.02, 8.30 * 103, 1, 2];
s5d4b = List[3011.84, 7.89 * 104, 2, 2];
s5d4c = List[2923.37, 3.45 * 105, 3, 2];
s5d5a = List[497.310, 1.80 * 106, 1, 2];
s5d5b = List[496.930, 1.62 * 107, 2, 2];
s5d5c = List[496.360, 7.16 * 107, 3, 2];
s5d6a = List[403.430, 8.12 * 105, 1, 2];
s5d6b = List[403.350, 8.20 * 106, 2, 2];
s5d6c = List[403.150, 2.93 * 107, 3, 2];
p5p5b = List[487.770, 6.54 * 107, 1, 2];
p5p5c = List[481.320, 1.15 * 108, 2, 2];
Theoretical Numbers
s5s06 = List[704.960, 7.13 * 107, 1, 2];
s5s07 = List[443.930, 1.75 * 106, 1, 2];
s5s08 = List[386.650, 8.22 * 106, 1, 2];
s5s09 = List[362.940, 4.53 * 106, 1, 2];
s5s10 = List[350.520, 2.77 * 106, 1, 2];
s5d4a = List[3067.02, 4.32 * 106, 1, 2];
s5d4b = List[3011.84, 4.32 * 106, 2, 2];
s5d4c = List[2923.37, 4.32 * 106, 3, 2];
s5d5a = List[497.310, 5.83 * 107, 1, 2];
s5d5b = List[496.930, 5.83 * 107, 2, 2];
s5d5c = List[496.360, 5.83 * 107, 3, 2];
s5d6a = List[403.430, 2.67 * 107, 1, 2];
s5d6b = List[403.350, 2.67 * 107, 2, 2];
s5d6c = List[403.150, 2.67 * 107, 3, 2];
s5d7a = List[370.840, 3.94 * 105, 1, 2];
s5d7b = List[370.770, 3.55 * 106, 2, 2];
s5d7c = List[370.700, 1.42 * 107, 3, 2];
s5d8a = List[355.010, 2.36 * 105, 1, 2];
s5d8b = List[354.970, 2.13 * 106, 2, 2];
s5d8c = List[354.910, 8.51 * 106, 3, 2];
s5d9a = List[345.910, 1.53 * 105, 1, 2];
s5d9b = List[345.910, 1.38 * 106, 2, 2];
s5d9c = List[345.850, 5.51 * 106, 3, 2];
p5p5b = List[487.770, 6.10 * 107, 1, 2];
p5p5c = List[481.320, 6.10 * 107, 2, 2];

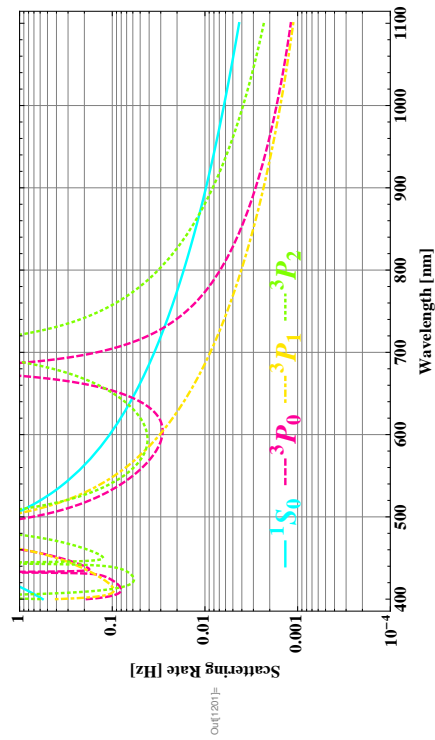
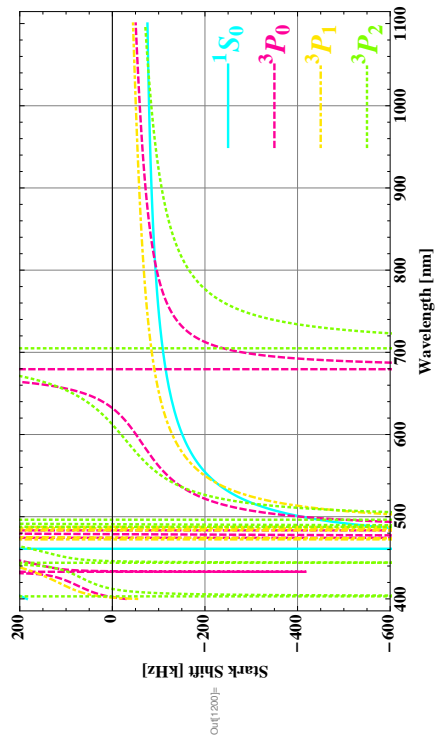
```

```

In[92]:= Clear[triplet2stateilinear2];
ma = 2; q = 0;
s5d4b = List[3011.84, 7.89 * 104, 2, 2];
s5d4c = List[2923.37, 3.45 * 105, 3, 2];
s5d5b = List[496.930, 1.62 * 107, 2, 2];
s5d5c = List[496.360, 7.16 * 107, 3, 2];
s5d6b = List[403.350, 8.20 * 106, 2, 2];
s5d6c = List[403.150, 2.93 * 107, 3, 2];
s5d7b = List[370.770, 3.55 * 106, 2, 2];
s5d7c = List[370.700, 1.42 * 107, 3, 2];
s5d8b = List[354.970, 2.13 * 106, 2, 2];
s5d8c = List[354.910, 8.51 * 106, 3, 2];
s5d9b = List[345.910, 1.38 * 106, 2, 2];
s5d9c = List[345.850, 5.51 * 106, 3, 2];
p5p5c = List[481.320, 1.15 * 108, 2, 2];
triplet2stateilinear2 = Out[{-13, -12, -11, -10, -9, -8, -7, -6, -5, -4, -3, -2, -1}];

■ Calculating the Light Shifts
In[98]:= Clear[max, ts22d, ts22s];
max = Length[triplet2stateilinear2];
StartSum[λ_] := 0
ScatSum[λ_] := 0
For[i = 1, i ≤ max, i++,
(
Ar = Part[Part[triplet2stateilinear2, i], 1];
t = Part[Part[triplet2stateilinear2, i], 2];
j = Part[Part[triplet2stateilinear2, i], 3];
jl = Part[Part[triplet2stateilinear2, i], 4];
ScatSum[λ_] = ScatSum[λ] + Summand[λ];
ScatSum[λ_] = ScatSum[λ] + Summand2[λ];
)
)
ts22d[λ_] = depth[λ];
ts22s[λ_] = scat[λ];

```

■ $m=1, q=0$ (linear polarization)

Appendix B

Effective Cross Section for Imaging

This appendix explicates the model used to determine the absorption cross sections of ^{87}Sr and ^{88}Sr in section 2.4.1. The first part of the appendix describes the model itself, and the second part includes an implementation of the model in Mathematica.

B.1 Deriving the Peak Absorption Cross Section

The treatment of ^{87}Sr differs from that of ^{88}Sr due to the more complicated level structure of ^{87}Sr . The model for ^{88}Sr is shown first, followed by the development of the model for ^{87}Sr .

B.1.1 Cross Section for ^{88}Sr

With ^{88}Sr , we are spoiled because we do not typically have to worry about Clebsch-Gordan coefficients to calculate transition rates, beyond knowing the selection rules. For example, the peak absorption cross section for the $^1\text{S}_0$ – $^1\text{P}_1$ transition (wavelength of $\lambda = 461$ nm) in ^{88}Sr is

$$\alpha_0 = 6\pi\left(\frac{\lambda}{2\pi}\right)^2 = \frac{3\lambda^2}{2\pi}, \quad (\text{B.1})$$

which, for off-resonant light, becomes

$$\alpha = \frac{\alpha_0}{1 + 4\left(\frac{\Delta}{\Gamma}\right)^2}. \quad (\text{B.2})$$

Here, $\Delta = 2\pi \times (f - f_0)$ is the detuning of the laser light from resonance and $\Gamma = 1/\tau \approx 2\pi \times 30.5$ MHz is the linewidth for the 461 nm transition. Each polarization of light (π, σ^+ , or σ^-) drives a single transition for ^{88}Sr due to the selection rules (as in Fig. 2.2(B)).

Generally, the absorption cross section, on-resonance with a transition $J_\ell, M_\ell \rightarrow J_u, M_u$, can be written as it was in Eq. 2.18:

$$\alpha = \frac{3\lambda^2}{2\pi} (2J_u + 1) |\hat{\epsilon}_q \cdot \hat{\epsilon}|^2 \left(\begin{array}{ccc} J_u & 1 & J_\ell \\ -M_u & q & M_\ell \end{array} \right)^2. \quad (\text{B.3})$$

If $\Delta M = q = M_u - M_\ell$, we get $\hat{\epsilon}_0 = \hat{z}$ for $\hat{\epsilon} = \pi$ polarization and $\hat{\epsilon}_{\pm 1} = \mp(\hat{x} \pm i\hat{y})/\sqrt{2}$ for $\hat{\epsilon} = \sigma^\pm$ polarizations. Equation B.3 utilizes the $3J$ symbol which is related to the Clebsch-Gordan coefficients:

$$(2J_u + 1) \left(\begin{array}{ccc} J_u & 1 & J_\ell \\ -M_u & q & M_\ell \end{array} \right)^2 = CG[\{J_\ell, M_\ell\}, \{1, q\}, \{J_u, M_u\}]^2, \quad (\text{B.4})$$

$$(2J_u + 1) \left(\begin{array}{ccc} J_u & 1 & J_\ell \\ -M_u & q & M_\ell \end{array} \right)^2 = |\langle J_\ell, M_\ell; 1, q | J_\ell, 1; J_u, M_u \rangle|^2. \quad (\text{B.5})$$

There are only three non-vanishing cross sections; if we pick the optimal light polarization, $J_\ell = M_\ell = 0$ and $J_u = 1$, we get the results shown in Table 2.2, which I reprint here (Table B.1) for reference.

Table B.1 : Result of calculating absorption cross sections for ^{88}Sr . Only three configurations have non-zero values of the absorption cross section. These correspond to linearly, right circularly, and left circularly polarized light, respectively.

Polarization	q	$\hat{\epsilon}$	m_u	3-J Symbol	α
π	0	\hat{z}	0	1/3	$3\lambda^2/(2\pi)$
σ^\pm	± 1	$\hat{\epsilon}_{\pm 1}$	± 1	1/3	$3\lambda^2/(2\pi)$

B.1.2 Decay Rates From Excited States

Thus far, we have only discussed the rate of excitation due to laser light. Now we turn to the decay rates, assuming only magnetic sub-level degeneracy in the ground state. The natural decay rate cannot depend on the magnetic sub-level (or the hyperfine state, neglecting perturbations). For the $^1\text{P}_1$ state of ^{88}Sr , each state only has one decay channel (Fig. B.1), but in general, each state of an atom can radiatively decay to three other states by three possible paths: $\Delta M = \pm 1, 0$. Each path has a rate $\Gamma_q = \Gamma_\pi, \Gamma_{\sigma^\pm}$, so the total decay rate from an excited state level is $\Gamma_0 = \Gamma_\pi + \Gamma_{\sigma^+} + \Gamma_{\sigma^-}$.

Everything said about the rates so far is also true for ^{87}Sr with the valid quantum number being F instead of J because the nuclear contribution to the angular momentum is now included: $J_u \rightarrow F_u$ and $J_\ell \rightarrow F_\ell$. The general expression for the transition rate is written as,

$$\Gamma_q^{F_u, M_u} = \Gamma_0 (2F_u + 1) \left(\begin{array}{ccc} F_u & 1 & F_\ell \\ -M_u & q & M_\ell = M_u - q \end{array} \right)^2, \quad (\text{B.6})$$

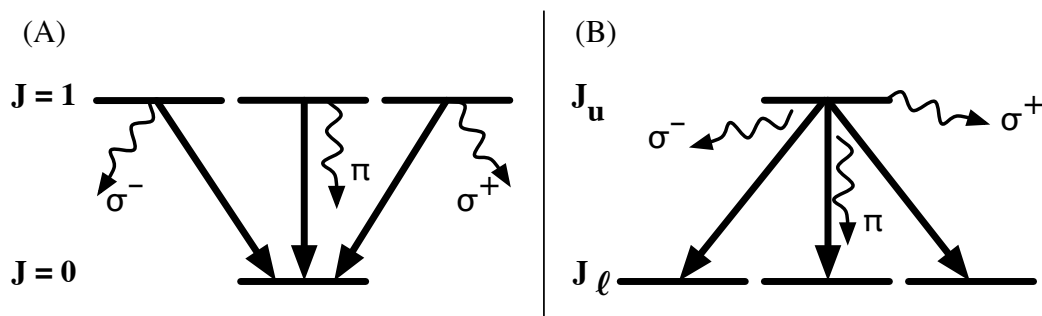


Figure B.1 : Decay paths from excited state levels. (A) A $J = 0 \rightarrow J = 1$ system where decay from the excited state levels only goes to a single ground state (this is like the $^1S_0 - ^1P_1$ transition in ^{88}Sr). In these systems, each state only has one decay channel, with a single light polarization for the radiated photon. (B) More generally, an excited state can decay to one of three lower energy levels, with the light polarization of the radiated photon differing along each decay path (this more closely resembles the structure of ^{87}Sr). The total decay rate in this situation would be a sum over the rates of all the possible decay paths.

noting that the sum of the $3J$ symbols over all the transitions is unity:

$$(2F_u + 1) \sum_{q=0,\pm 1} \left(\begin{array}{ccc} F_u & 1 & F_\ell \\ -M_u & q & M_\ell = M_u - q \end{array} \right)^2 = 1 \quad (\text{B.7})$$

B.1.3 Relating Excitation and Decay Rates to Laser Parameters

Now that we have defined these rates for absorption and decay, let us related these quantities to experimental parameters that we know. The saturation intensity of a transition, neglecting the Clebsch-Gordan coefficients, is

$$I_{sat} = \Gamma \frac{hc\pi}{3\lambda^3}. \quad (\text{B.8})$$

The intensity in terms of the photon density, n , is $I = nh\nu c$. Since the rate of excitation per second per atom, neglecting saturation, is

$$R = n\sigma\nu = \frac{I\alpha}{h\nu}, \quad (\text{B.9})$$

we can plug in the expression for the cross section from above (Eq. B.3), add the dependence on the detuning, replace J_u with F_u , and get

$$R = \frac{I}{hc} \frac{3\lambda^2}{2\pi} (2F_u + 1) |\hat{\epsilon}_q \cdot \hat{\epsilon}|^2 \left(\begin{array}{ccc} F_u & 1 & F_\ell \\ -M_u & q & M_\ell \end{array} \right)^2 \frac{1}{1 + 4(\frac{\Delta}{\Gamma})^2}. \quad (\text{B.10})$$

If we include the effect of saturation, we have

$$R = \frac{I}{I_{sat}} \frac{\Gamma}{2} (2F_u + 1) |\hat{\epsilon}_q \cdot \hat{\epsilon}|^2 \left(\begin{array}{ccc} F_u & 1 & F_\ell \\ -M_u & q & M_\ell \end{array} \right)^2 \frac{1}{1 + \frac{I}{I_{sat}} + 4(\frac{\Delta}{\Gamma})^2}. \quad (\text{B.11})$$

So, to summarize what we have derived so far, we write the total excitation (Eq. B.12) and the total decay (Eq. B.13) rates:

$$R_{M_\ell \rightarrow M_\ell + q}^{F_\ell - F_u} = \frac{I}{I_{sat}} \frac{\Gamma}{2} (2F_u + 1) |\hat{\epsilon}_q \cdot \hat{\epsilon}|^2 \left(\begin{array}{ccc} F_u & 1 & F_\ell \\ -(M_\ell + q) & q & M_\ell \end{array} \right)^2 \frac{1}{1 + \frac{I}{I_{sat}} + 4(\frac{\Delta}{\Gamma})^2}, \quad (\text{B.12})$$

$$R_{M_u \rightarrow M_u - q}^{F_u - F_\ell} = \Gamma_0 (2F_u + 1) \left(\begin{array}{ccc} F_u & 1 & F_\ell \\ -M_u & q & M_\ell = M_u - q \end{array} \right)^2. \quad (\text{B.13})$$

A short-hand for these two equations, which will be used henceforth, looks like $R_{M_\ell \rightarrow M_\ell + q}^{F_\ell - F_u} = R[F_d, q, F_u, M_d]$ and $R_{M_u \rightarrow M_u - q}^{F_u - F_\ell} = \Gamma[F_\ell, q, F_u, M_\ell]$. The d is used for the lower level when referring to excitation, and the ℓ is used to refer to the lower level for decay.

B.1.4 Rate Equations for ^{87}Sr Ground State Levels

Any ground level is connected to three upper levels by excitation (roughly like Fig. B.1(A)) and any excited state is connected to three lower levels by decay (like Fig. B.1(B)). So, if we are to determine the population of a particular energy level, we need to sum all the population loss (gain) from a level due to excitations and all the population gain (loss) to the level due to decay from higher energy states. We will discuss this treatment specifically for ^{87}Sr because it is its effective absorption cross section that we are interested in.

The manifold of energy states of ^{87}Sr for linearly polarized image beam light is as in Fig. 2.25. For a ground state ($F = 9/2, J = 0$) level, excitation reduces the population as atoms are driven into higher energy states. Conversely, ground state population increases from any decay allowed by the selection rules. We will refer to the population of a lower, ground state level as $down[M_d]$ and the populations of higher energy, excited states as $up[M_u]$. The rate of population change can be expressed as the sum of the excitation and decay rates:

$$\begin{aligned} \dot{down}[M_d](t) = & -down[M_d] \sum_{q=-1}^1 \left\{ R[F_d, q, F_{u2}, M_d] + R[F_d, q, F_{u1}, M_d] \right\} \\ & + \sum_{q=-1}^1 \left\{ up_{F_{u2}}[M_d + q] \times \Gamma[F_d, q, F_{u2}, M_d] + up_{F_{u1}}[M_d + q] \times \Gamma[F_d, q, F_{u1}, M_d] \right\}, \end{aligned} \tag{B.14}$$

Here, we assume that excitation can only be to two higher energy levels, $F = F_{u1}$ and $F = F_{u2}$, and the initial population distribution of this ground state manifold

is $down[M_d](0) = \frac{1}{2F_d+1}$ for an unpolarized sample. For ^{87}Sr , this corresponds to the $F_{u1} = 9/2$ and $F_{u2} = 11/2$ manifolds; we neglect the $F = 7/2$ manifold because it is detuned more than one linewidth (30.5 MHz) from the $F = 9/2 \rightarrow F = 11/2$ transition used for imaging.

Similarly, we write down the expressions for the rate of population change in the excited states F_{u1} and F_{u2} states, assuming initial excited state populations of zero ($up_{F_{u1}}[M_u](0) = 0, up_{F_{u2}}[M_u](0) = 0$):

$$\dot{up}_{F_{u1}}[M_u] = -up_{F_{u1}}[M_u]\Gamma_0 + \sum_{q=-1}^1 down[M_u - q] \times R[F_d, q, F_{u1}, M_u - q] \quad (\text{B.15})$$

$$\dot{up}_{F_{u2}}[M_u] = -up_{F_{u2}}[M_u]\Gamma_0 + \sum_{q=-1}^1 down[M_u - q] \times R[F_d, q, F_{u2}, M_u - q] \quad (\text{B.16})$$

Thus far, we have ignored one key part of the level structure in determining the populations of the various levels. That is, some excited state levels only decay to a single ground state level (instead of the usual three levels as shown in Fig. B.1(B)) because of the selection rules. For example, when atoms are in the $F = 11/2, M_F = \pm 11/2$ state, they can only decay to one ground state level (the $F = 9/2, M_F = \pm 9/2$ level). Another example is the $F = 11/2, M_F = \pm 9/2$ state which can only decay to two ground state levels ($F = 9/2, M_F = \pm 9/2$ and $F = 9/2, M_F = \pm 7/2$).

We considered two solutions to treat this problem. The first is to suppose that the excited states always have three levels that they can decay to; there will always be at least one real level, with “ghost” levels filling whichever ones do not exist in the ground state manifold. By artificially defining the population in these “ghost”

levels, we can set their population to zero without affecting the overall dynamics. Alternatively, we can write special expressions to treat the levels which cannot decay to three ground state levels. Adding these special expressions to the expressions for the population of all the other levels will allow a correct treatment of the population dynamics. The advantage of using the first solution is that we do not change much in the model. However, the second solution is more physical. After all, there do not exist “ghost” levels in the atoms. For this reason, we choose to add the special expressions to correctly model the population dynamics.

To correctly model the *down* population, we add Eq. B.14 to the following expression for the rate of population change of the $F_d = 9/2$ ground state:

$$\begin{aligned} \dot{down}[\pm 9/2] = & -down[\pm 9/2] \sum_{q=-1}^1 \left\{ R[9/2, q, F_{u2}, \pm 9/2] + R[9/2, q, F_{u1}, \pm 9/2] \right\} \\ + \sum_{q=-1}^1 & \left\{ up_{F_{u2}}[\pm 9/2 + q] \times \Gamma[9/2, q, F_{u2}, \pm 9/2] + up_{F_{u1}}[\pm 9/2 + q] \times \Gamma[9/2, q, F_{u1}, \pm 9/2] \right\}, \end{aligned} \quad (\text{B.17})$$

In similar fashion, we add the following expressions (Eqs. B.18 and B.19) to Eqs. B.15 and B.16:

$$\dot{up}_{F_{u1}}[\pm 9/2] = -up_{F_{u1}}[\pm 9/2]\Gamma_0 + \sum_{q=-1}^1 down[\pm 9/2 - q] \times R[F_d, q, 9/2, \pm 9/2 - q] \quad (\text{B.18})$$

$$\begin{aligned}
ip_{F_{u2}}[\pm 9/2] &= -up_{F_{u2}}[\pm 9/2]\Gamma_0 + \sum_{q=-1}^1 \text{down}[\pm 9/2 - q] \times R[F_d, q, 11/2, \pm 9/2 - q] \\
ip_{F_{u2}}[\pm 11/2] &= -up_{F_{u2}}[\pm 11/2]\Gamma_0 + \text{down}[\pm 11/2 \mp 1] \times R[F_d, q, 11/2, \pm 11/2 \mp 1]
\end{aligned} \tag{B.19}$$

B.1.5 Effective Absorption Cross Section for ⁸⁷Sr

The purpose of this calculation is to get an effective cross section to find the number of atoms from our absorption images, so we need to relate our parameters to the optical depth. Beer's law is

$$I = I_0 e^{-\int dz \sum_{M_d} n_{M_d} \alpha_{M_d}} \tag{B.20}$$

Now, we define an effective cross section (α_{eff}) which is the sum of the population over all the levels:

$$I = I_0 e^{-\int dz \alpha_{eff} \sum_{M_d} n_{M_d}} = I_0 e^{-\int dz \alpha_{eff} n_{total}} \tag{B.21}$$

Our model above allows us to determine $n_{total} = \sum_{M_d} n_{M_d}$, so we can write:

$$\frac{I}{h\nu} \alpha_{eff} \sum_{M_d} n_{M_d} = \alpha_0 \sum_{M_d} n_{M_d} \times \sum_{q=-1}^1 \left\{ R[F_d, q, F_{u2}, M_d] + R[F_d, q, F_{u1}, M_d] \right\}, \tag{B.22}$$

where α_0 is the peak cross section ($\frac{3\lambda_2}{2\pi}$) due to the maximum possible excitation rate, $R_{max} = \frac{I}{I_{sat}} \frac{\Gamma}{2}$, due to the imaging beam. We can express the ratio of the effective cross section to the peak cross section as

$$\frac{\alpha_{eff}}{\alpha_0} = \frac{1}{R_{max}} \frac{1}{\sum_{M_d} n_{M_d}} \sum_{M_d} \left\{ n_{M_d} \sum_{q=-1}^1 R[F_d, q, F_{u2}, M_d] + R[F_d, q, F_{u1}, M_d] \right\} \tag{B.23}$$

Equation B.23 is the expression that we plot in Fig. 2.26. As we can see from the expression, the cross section of atoms is reduced by the detuning of the imaging beam and the population distribution. Therefore, for ^{87}Sr atoms, which can be distributed among the different spin sub-levels, the effective cross section is less than that observed for ^{88}Sr atoms.

B.2 Model Implementation in Mathematica

The Mathematica notebook which is included in this appendix can be found at the following path: “//Strontium86/studentfolders/pascal/Doctoral Thesis/Analysis/Imaging Mixtures/TransitionRates87Sr.nb”.

Here are the run time instructions for this Mathematica code:

1. Quit the local kernel;
2. Set the following quantities:
 - The saturation parameter (e.g. $S_0 = 0.02$);
 - The polarization factor $[-q] = [\dot{\epsilon}_q \cdot \dot{\epsilon}]^2$. For a particular light polarization, set the desired light polarization to 1 while the other two polarizations are zero. e.g. linear polarization $\rightarrow [-1] = 0$ for σ^- , $[0] = 1$ for π , and $[+1] = 0$ for σ^+ . Conversely, for unpolarized light, set each value to $1/3$;
 - The detuning, Δ_{11} , from the $F_d = 9/2 \rightarrow F_u = 11/2$ transition (e.g. 0 MHz) and the detuning, Δ_9 , from the $F_d = 9/2 \rightarrow F_u = 9/2$ transition

(e.g. 30 MHz);

3. Evaluate all the initialization cells;
4. Look at the population and the effective cross section plots. Change the plot titles manually to reflect new conditions.

Note : the kernel must be quit and restarted with new parameters to switch between plotting an unpolarized sample and plotting a polarized atom sample (i.e. between samples where all atoms begin evenly distributed and samples where all atoms begin in a single state).

The remainder of this appendix shows a condensed version of the code developed to model the population distribution among the ground state energy levels as a function of time that the image beam is applied to the atoms.

```

In[1]:=
Fu = 9 / 2;
Fd = 9 / 2;
(* we have extended the sums to run over Md from -Fd-
  2 to Fd+2 so we will have simple forms of all the population dynamic
  equations. We will artificially define Fd levels with Md=-Fd-2,
  -Fd-1, Fd+1, and Fd+2. Their populations will always be zero. CG
  coefficients involving these levels will always be zero. *)
For[q = -2, q < 1, q++; For[Md = -Fd - 3, Md < Fd + 2, Md++;
  CGsq[Fd, q, Fu, Md] = (ClebschGordan[{Fd, Md}, {1, q}, {Fu, Md + q}])^2]]
(*q=0;
  For[Md=-Fd-3, Md<Fd+2, Md++;Print[CGsq[Fd,q,Fu,Md]]] *)
q = 1;
ListPlot[Table[CGsq[Fd, q, Fu, Md], {Md, -Fd - 2, Fd + 2, 1}], GridLines -> Automatic]
q = 0;
ListPlot[Table[CGsq[Fd, q, Fu, Md], {Md, -Fd - 2, Fd + 2, 1}], GridLines -> Automatic]
q = 1;
ListPlot[Table[CGsq[Fd, q, Fu, Md], {Md, -Fd - 2, Fd + 2, 1}], GridLines -> Automatic]

```

Constants for Defining Excitation and Decay Rates

After you change these, you need to quit the kernel (local) and then evaluate initialization cells. Then you can evaluate and plot the level populations

```

In[20]:=
scalefactor = 10^6; (* change Hz to MHz and rates to per mus *)
r0 = 2 * pi * 30.5 * 10^7 / scalefactor (* in MHz *)
S0 = .02; (* saturation parameter *)
polarizationfactor[-1] = 0;
(* square of dot product of light polarization and transition polarization vector *)
polarizationfactor[0] = 1; (*PI transition *)
polarizationfactor[1] = 0;
d11 = 2 * pi * 0000; (* detuning from 11/2 upper level in MHz *)
d9 = 2 * pi * 30; (* detuning from 9/2 upper level in MHz *)
lineshapefactor11 = 1 + 1 / (1 + S0 * (2*d11 / r0)^2)
lineshapefactor9 = 1 + 1 / (1 + S0 * (2*d9 / r0)^2)
Rmax = S0 * r0 / 2

```

This notebook solves the population equations derived in Appendix B of Pascal's PhD thesis.

Run time instructions:

- 1) Quit local kernel;
- 2) Set A) saturation parameter (e.g. S0 = 0.02)
 B) polarization factor [-q] = $|\epsilon_q|^2$.
 Set the desired light polarization to 1 while the other two polarizations are zero.
 $|-1| = 1$ for σ^-
 $|0| = 1$ for π
 $|+1| = 1$ for σ^+
 Set each to 1/3 for unpolarized light.
 C) Δ_{11} = detuning from $F_J = 9/2 \rightarrow F_u = 11/2$ e.g. 0 MHz
 Δ_9 = detuning from $F_J = 9/2 \rightarrow F_u = 9/2$ e.g. 30 MHz
- 3) Evaluate all initialization cells
- 4) Look at population and effective cross section plots; change plot titles to reflect new conditions

Initialization

```

In[6]= Needs["PlotLegends`"]
(ClebschGordan[{F1, M1}, {1, q}, {Fu, Mu}])^2 =
(2 * Fu + 1) * N[ThreeSymbol[{Fu, -Mu}, {1, q}, {F1, M1}]]^2
ThreeSymbol[{j1, m1}, {j2, m2}, {j3, m3}] gives the values of the Wigner 3-j symbol.

```

Defining CG Coefficients

```

In[6]=
Fu = 11 / 2;
Fd = 9 / 2;
(* we have extended the sums to run over Md from -Fd-
  2 to Fd+2 so we will have simple forms of all the population dynamic
  equations. We will artificially define Fd levels with Md=-Fd-2,
  -Fd-1, Fd+1, and Fd+2. Their populations will always be zero. CG
  coefficients involving these levels will always be zero. *)
For[q = -2, q < 1, q++; For[Md = -Fd - 3, Md < Fd + 2, Md++;
  CGsq[Fd, q, Fu, Md] = (ClebschGordan[{Fd, Md}, {1, q}, {Fu, Md + q}])^2]]
(*q=0;
  For[Md=-Fd-3, Md<Fd+2, Md++;Print[CGsq[Fd,q,Fu,Md]]] *)
q = 1;
ListPlot[Table[CGsq[Fd, q, Fu, Md], {Md, -Fd - 2, Fd + 2, 1}], GridLines -> Automatic]
q = 0;
ListPlot[Table[CGsq[Fd, q, Fu, Md], {Md, -Fd - 2, Fd + 2, 1}], GridLines -> Automatic]
q = 1;
ListPlot[Table[CGsq[Fd, q, Fu, Md], {Md, -Fd - 2, Fd + 2, 1}], GridLines -> Automatic]

```

Define Excitation and Decay Rates (detuning and polarization information is in here)

```

In[3]:=
Fu = 11 / 2;
Fd = 9 / 2;
For[q = -2, q < 1, q++]
  For[Md = -Fd - 3, Md < Fd + 2, Md++] Γ[Fd, q, Fu, Md] = r0 * CGsq[Fd, q, Fu, Md]]]
  (* Level resolved decay rates*)
  For[q = -2, q < 1, q++] For[Md = -Fd - 3, Md < Fd + 2, Md++]
    R[Fd, q, Fu, Md] = S0 +  $\frac{r0}{\Gamma}$  * LineshapeFactor11 * polarizationFactor[q] * CGsq[Fd, q, Fu, Md]]]
    (* Level resolved excitation rate *)
  Fu = 9 / 2;
  For[q = -2, q < 1, q++]
    For[Md = -Fd - 3, Md < Fd + 2, Md++] Γ[Fd, q, Fu, Md] = r0 * CGsq[Fd, q, Fu, Md]]]
    (* Level resolved decay rates*)
  For[q = -2, q < 1, q++] For[Md = -Fd - 3, Md < Fd + 2, Md++]
    R[Fd, q, Fu, Md] = S0 +  $\frac{r0}{\Gamma}$  * LineshapeFactor9 * polarizationFactor[q] * CGsq[Fd, q, Fu, Md]]]
    (* Level resolved excitation rate *)
  (*eq0;
  For[Md = -Fd - 3, Md < Fd + 2, Md++] Print[CGsq[Fd, q, Fu, Md]]] *)
  Fu = 11 / 2;
  q = -1;
  ListPlot[Table[R[Fd, q, Fu, Md], {Md, -Fd - 2, Fd + 2, 1}], GridLines -> Automatic]
  q = 0;
  ListPlot[Table[R[Fd, q, Fu, Md], {Md, -Fd - 2, Fd + 2, 1}], GridLines -> Automatic]
  q = 1;
  ListPlot[Table[R[Fd, q, Fu, Md], {Md, -Fd - 2, Fd + 2, 1}], GridLines -> Automatic]

```

Testing Subset Solutions

Solve the Rate Equations : Full Simulation

To start with a polarized sample of atoms, insert down[-9/2][0] = 1, Table[down[Md][0] == 0, {Md, -7/2, 9/2}] right after the space marked (* Here *) in the "eqs" expression below.
 To start with an unpolarized sample of atoms, replace the above with Table[down[Md][0] == 1/(2*Fd + 1), {Md, -9/2, 9/2}] right after the space marked (* Here *) in the "eqs" expression below.

```

In[4]:=
Fu2 = 11 / 2;
Fu1 = 9 / 2;
Fd = 9 / 2;

```

```

Table[down[Md][0] = 1 / (2 * Fd + 1), {Md, -9 / 2, 9 / 2}] (* unpolarized atoms *)
(* down[-9/2][0] = 1, Table[down[Md][0] = 0, {Md, -7/2, 9/2}] *) (* Polarized atoms *)
eqs = {Table[down[Md][x] = -down[Md][x] +  $\sum_{q=-1}^1$  R[Fd, q, Fu2, Md] + R[Fd, q, Fu1, Md]] +
 $\sum_{q=-1}^1$  (upFu2[Md + q][x] * Γ[Fd, q, Fu2, Md] - upFu1[Md + q][x] * Γ[Fd, q, Fu1, Md]),
{Md, -Fd + 1, Fd - 1}], {down[-9 / 2][x] =
-down[-9 / 2][x] +  $\sum_{q=-1}^1$  (R[Fd, q, Fu2, -9 / 2] + R[Fd, q, Fu1, -9 / 2]) +
 $\sum_{q=0}^1$  (upFu1[-9 / 2 + q][x] * Γ[Fd, q, Fu1, -9 / 2]) +
 $\sum_{q=-1}^1$  (upFu2[-9 / 2 + q][x] * Γ[Fd, q, Fu2, -9 / 2])},
{down[9 / 2][x] = -down[9 / 2][x] +  $\sum_{q=-1}^1$  (R[Fd, q, Fu2, 9 / 2] + R[Fd, q, Fu1, 9 / 2]) +
 $\sum_{q=-1}^0$  (upFu1[9 / 2 + q][x] * Γ[Fd, q, Fu1, 9 / 2]) +
 $\sum_{q=-1}^1$  (upFu2[9 / 2 + q][x] * Γ[Fd, q, Fu2, 9 / 2])},
(* Here! *) down[-9 / 2][0] = 1, Table[down[Md][0] = 0, {Md, -7 / 2, 9 / 2}],
Table[upFu1[Mu][x] = -upFu1[Mu][x] +  $\sum_{q=-1}^1$  down[Mu - q][x] * R[Fd, q, Fu1, Mu - q],
{Mu, -Fu1 + 1, Fu1 - 1}],
{upFu1[-9 / 2][x] = -upFu1[-9 / 2][x] +  $\sum_{q=-1}^0$  down[-9 / 2 - q][x] * R[Fd, q, Fu1, -9 / 2 - q]},
{upFu1[9 / 2][x] = -upFu1[9 / 2][x] +  $\sum_{q=0}^1$  down[9 / 2 - q][x] * R[Fd, q, Fu1, 9 / 2 - q]},
Table[upFu1[Mu][0] = 0, {Mu, -Fu1, Fu1}],
Table[upFu2[Mu][x] = -upFu2[Mu][x] +  $\sum_{q=-1}^1$  down[Mu - q][x] * R[Fd, q, Fu2, Mu - q],
{Mu, -Fu2 + 1, Fu2 - 1}],

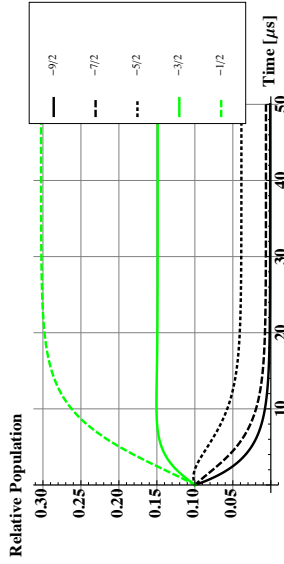
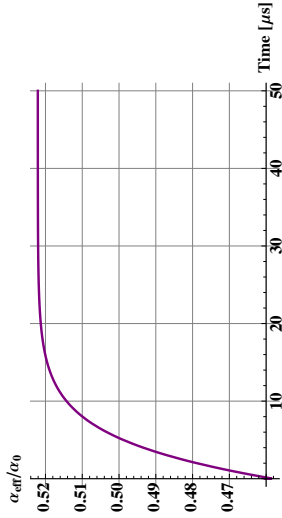
```

```
(Mu, -Fu2 * 2, Fu2 - 2),
{upFu2[-9/2][x] == -upFu2[-9/2][x] r0 + Sum[down[-9/2 - q][x] * R[Fd, q, Fu2, -9/2 - q],
q == -1],
{upFu2[9/2][x] == -upFu2[9/2][x] r0 + Sum[down[9/2 - q][x] * R[Fd, q, Fu2, 9/2 - q],
q == 0],
{upFu2[-11/2][x] == -upFu2[-11/2 + 1][x] * R[Fd, -1, Fu2, -11/2 + 1],
upFu2[11/2][x] == -upFu2[11/2][x] r0 + down[11/2 - 1][x] * R[Fd, 1, Fu2, 11/2 - 1],
Table[upFu2[Mu][0] == 0, {Mu, -Fu2, Fu2}];
Solve == {down[-9/2], down[-7/2], down[-5/2], down[-3/2], down[-1/2],
down[1/2], down[3/2], down[5/2], down[7/2], down[9/2], down[11/2],
upFu2[-9/2], upFu2[-7/2], upFu2[-5/2], upFu2[-3/2], upFu2[-1/2],
upFu2[1/2], upFu2[3/2], upFu2[5/2], upFu2[7/2], upFu2[9/2], upFu2[11/2],
upFu1[-9/2], upFu1[-7/2], upFu1[-5/2], upFu1[-3/2], upFu1[-1/2],
upFu1[1/2], upFu1[3/2], upFu1[5/2], upFu1[7/2], upFu1[9/2]};
First[NDSolve[eqns, {down[-9/2], down[-7/2], down[-5/2], down[-3/2], down[-1/2],
down[1/2], down[3/2], down[5/2], down[7/2], down[9/2], down[11/2],
upFu2[-9/2], upFu2[-7/2], upFu2[-5/2], upFu2[-3/2], upFu2[-1/2],
upFu2[1/2], upFu2[3/2], upFu2[5/2], upFu2[7/2], upFu2[9/2], upFu2[11/2],
upFu1[-9/2], upFu1[-7/2], upFu1[-5/2], upFu1[-3/2], upFu1[-1/2],
upFu1[1/2], upFu1[3/2], upFu1[5/2], upFu1[7/2], upFu1[9/2]};
(* For [Mds-Fd-3, Mds-Fd-2, Mds-Fd-1, Mds] == Solution[[Mds-Fd-3]]] doesn't work *)
down[-9/2] := Solution[[1]]; down[-7/2] := Solution[[2]]; down[-5/2] := Solution[[3]];
down[-3/2] := Solution[[4]]; down[-1/2] := Solution[[5]]; down[1/2] := Solution[[6]];
down[3/2] := Solution[[7]]; down[5/2] := Solution[[8]]; down[7/2] := Solution[[9]];
upFu2[-7/2] := Solution[[10]]; upFu2[-5/2] := Solution[[11]]; upFu2[-3/2] := Solution[[12]];
upFu2[-1/2] := Solution[[13]]; upFu2[1/2] := Solution[[14]];
upFu2[3/2] := Solution[[15]]; upFu2[5/2] := Solution[[16]]; upFu2[7/2] := Solution[[17]];
upFu2[9/2] := Solution[[18]]; upFu2[11/2] := Solution[[19]]; upFu1[-7/2] := Solution[[20]];
upFu1[-5/2] := Solution[[21]]; upFu1[-3/2] := Solution[[22]]; upFu1[-1/2] := Solution[[23]];
upFu1[1/2] := Solution[[24]]; upFu1[3/2] := Solution[[25]]; upFu1[5/2] := Solution[[26]];
upFu1[7/2] := Solution[[27]]; upFu1[9/2] := Solution[[28]]; upFu1[11/2] := Solution[[29]];
upFu1[13/2] := Solution[[30]]; upFu1[15/2] := Solution[[31]]; upFu1[17/2] := Solution[[32]];
TotalDownPopulation[x_] := Sum[down[Md][x],
Md == 2],
(*TotalDownPopulation[x_] := down[-9/2][x] + down[-7/2][x] + down[-5/2][x] + down[-3/2][x] +
down[-1/2][x] + down[1/2][x] + down[3/2][x] + down[5/2][x] + down[7/2][x] + down[9/2][x] +
DownPopulationWeightedExcitationRate[x_] :=
Sum[down[Md][x] * Sum[R[Fd, q, Fu1, Md] + R[Fd, q, Fu2, Md]],
Md == 9/2],
(*Plot[Evaluate[Table[down[Md][x], {Md, -13/2, 13/2}], {x, 0, 10}], *)
(*Plot[Evaluate[Table[upFu2[Mu][x], {Mu, -11/2, 11/2}], {x, 0, 0.5}], PlotRange -> All], *)
Out[69] = {down[-9/2][0] == 1/10, down[-7/2][0] == 1/10, down[-5/2][0] == 1/10,
down[-3/2][0] == 1/10, down[-1/2][0] == 1/10, down[1/2][0] == 1/10,
down[3/2][0] == 1/10, down[5/2][0] == 1/10, down[7/2][0] == 1/10, down[9/2][0] == 1/10}
```

- Thesis Plots
- Initially Unpolarized Atom Population

Run these first plots only if you chose run the code for the unpolarized sample above.

```
popRatio = Plot[DownPopulationWeightedExcitationRate[x] / Rmax, {x, 0, 50},
AxesLabel -> All, PlotStyle -> {Directive[Thick, Purple]}, GridLines -> Automatic,
AspectRatio -> {"Time [μs]", "αeff/r0"}, LabelStyle -> Directive[Bold, 14]]
popRatio = Plot[Evaluate[Table[down[Md][x], {Md, -13/2, 13/2}], {x, 0, 50},
PlotStyle -> {Directive[Thick, Green, Dotted]}, GridLines -> Automatic,
AxesLabel -> {"Time [μs]", "αeff/r0"}, LabelStyle -> Directive[Thick, Screen, Dashed],
Directive[Thick, Green, Dotted], Directive[Thick, Green, Dotted],
Directive[Thick, Green, Dotted], Directive[Thick, Red, Dotted],
PlotLegend -> {"-9/2", "-7/2", "-5/2", "-3/2", "-1/2"}, LegendPosition -> {-6, -45},
LegendStyle -> {None, LegendTextSpace -> 2, LegendShadow -> None, GridLines -> Automatic,
AxesLabel -> {"Time [μs]", "Relative Population"}, LabelStyle -> Directive[Bold, 14]]
```



Export data if you want to ...

Appendix C

OPO Laser

The OPO (optical parametric oscillation) laser we use for repumping on the $(5s5p)^3P_2 - (5s4d)^3D_2$ transition is pumped by a fiber laser operating at 1064 nm [96]. This appendix briefly summarizes the intensity measurement of the laser and the calibration of the wavemeter.

C.1 OPO Beam Intensity

Measurements of the OPO beam size are made using a knife edge technique. A photodiode is used to measure the power while a razor edge is used to clip the beam a little bit at a time. The resulting curve is the cumulative distribution function for the Gaussian probability distribution. Figure C.1 shows the beam profile for a measurement near the output of the laser and for a measurement made before the beam is incident upon the atoms. Because the beam diverges a fair amount by the time it is measured near the atoms, it is necessary to place a lens to collect all the light onto the photodetector.

The maximum power in Fig. C.1 corresponds to the entire beam falling on the detector. When the power is cut in half (“half power”) by occluding the beam with the knife edge, we are at the peak of the gaussian intensity distribution; let us call

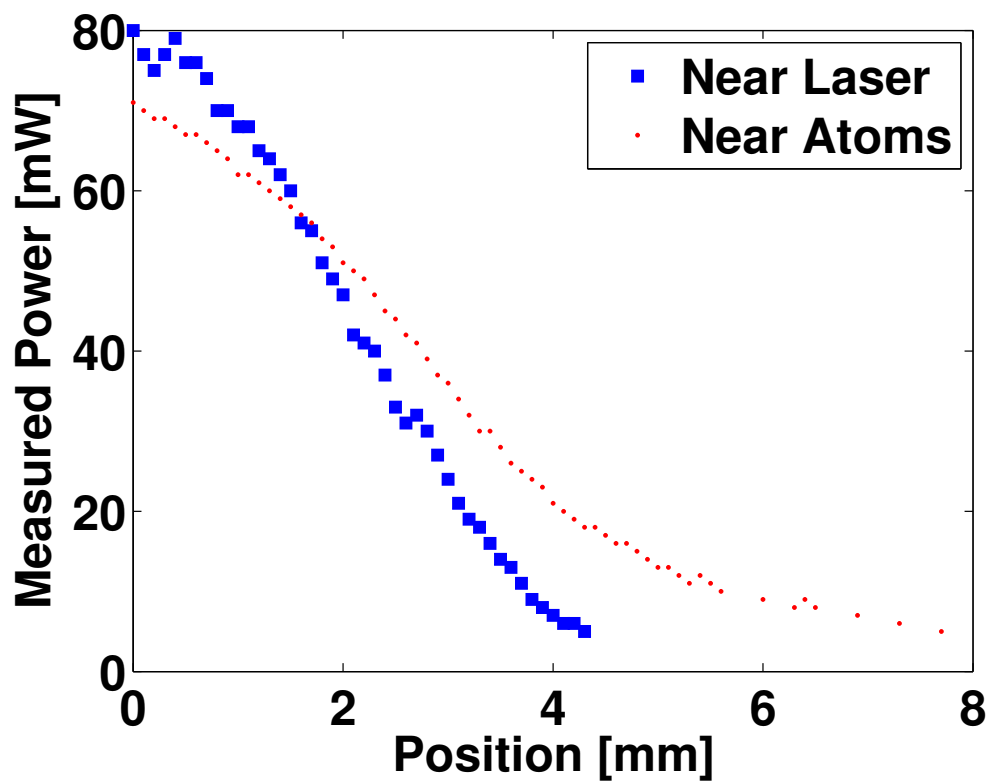


Figure C.1 : Knife edge measurement of intensity profile of OPO laser at $3 \mu\text{m}$. The measurement is made in two places to show the divergence of the beam: the first is near the output of the laser, and the second is near the chamber before the beam is incident upon the atoms. The $1/e^2$ radius is the point at which the power has dropped by half.

this point A . The distance from the peak of the gaussian distribution to the position where we measure 13.5% of the “half power” is position B , which corresponds to the $1/e^2$ radius. Table C.1 lists the $1/e^2$ radius for each measurement.

Table C.1 : Measurements of the size of the 3 μm laser beam.

Measurement Location	Position A	Position B	$1/e^2$ Radius (B-A)
Near Laser	2.3 mm	3.7 mm	1.4 mm
Near Atoms	3.0 mm	5.7 mm	2.7 mm

The intensity, of course, is the incident power divided by the area of the beam (πr^2). The maximum power during experiments was 60 mW. Therefore, the peak intensity of the beam near the atoms ($1/e^2 = 2.7$ mm) is ~ 260 mW/cm².

C.2 Wavemeter Calibration

We perform absorption spectroscopy of ammonia [75] at room temperature and a pressure of ~ 1 Torr to calibrate the wavemeter absolutely [76]. Figure C.2 shows the spectrum of the ammonia for a particular frequency range. We create a model spectrum from the line values and intensities from the HITRAN database and fit it to the data. The pressure shifts expected for these conditions (~ 1 MHz; [97]) are negligible, and Doppler broadening is thought to be the dominant contribution to the linewidth. The approximate error in the measurement is 0.0025 cm⁻¹, and the estimated systematic error in reading the wavemeter is 0.004 cm⁻¹. What this systematic shift means is that when we are on-resonance with the ^{88}Sr ($5s5p$)³P₂ –

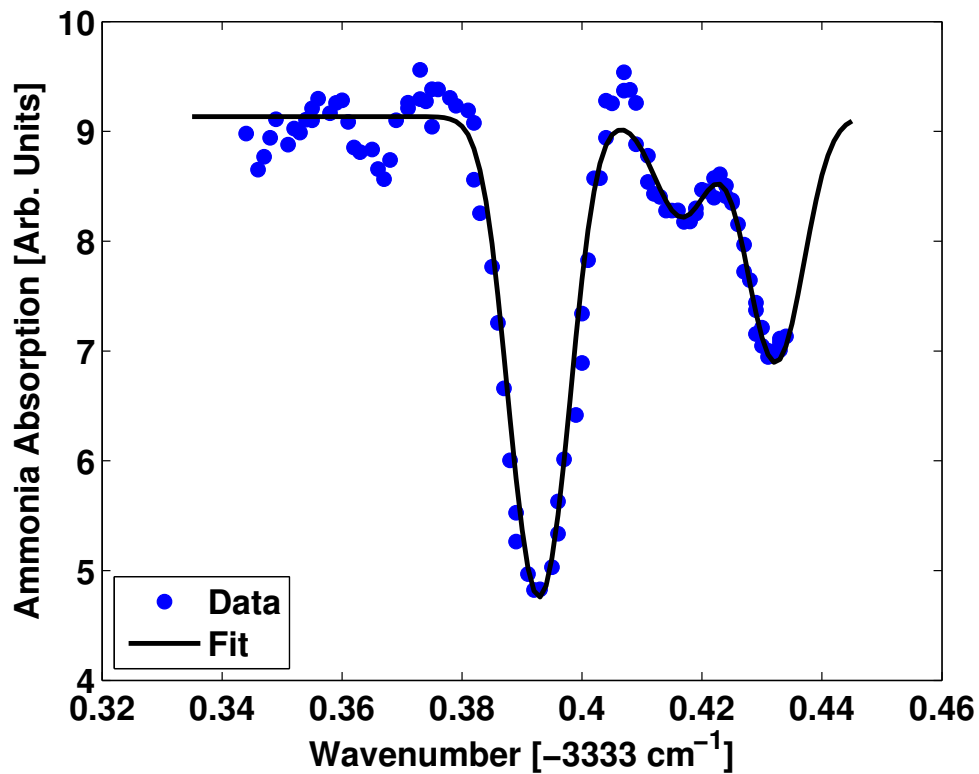


Figure C.2 : Absorption spectroscopy of ammonia for wavemeter calibration. We fit the peaks using a multiple Gaussian line shape and compare the center frequency of the strongest line to data from [75] to determine the systematic error of our wavemeter readings. The uncertainty of our fit to these frequencies is about 0.0015 cm^{-1} .

$(5s4d)^3D_2$ transition, we read a value of 3320.222 cm^{-1} from the wavemeter, while the absolute correct frequency is actually 3320.226 cm^{-1} .

Appendix D

Zeeman Splitting of Lineshapes

The spectrum shown in Fig. 3.6(B) has two peaks. In the text, we presume that these should be assigned to the two transitions which come out of the $^3\text{P}_2$, $M_J = 2$ sub-level (level structure shown in Fig. 3.7). This appendix calculates the Zeeman splitting of the levels under the magnetic field gradient of the MOT coils and estimates what the observed frequencies of the transitions should be from the $^3\text{P}_2$, $M_J = 2$ sub-level.

D.1 Energies of the $^3\text{P}_2$ and $^3\text{D}_2$ States

Experimentally, we know the magnetic field gradient, but not the absolute field. Therefore, we need to estimate the absolute field that the typical atom sees. The gradient determines the confining potential, a linear magnetic trap, but the temperature of the atoms determines how far up the gradient atoms are typically “found”. A higher temperature means the atoms experiences a higher magnetic field gradient. Here, we assume a Boltzmann distribution of atoms (k_bT), equate it to the energy at some characteristic distance, r , along the gradient ($\mu_b \nabla B r = k_bT$), and solve for r as a function of the atom temperature.

This estimate becomes a question of how well we know the temperature in the magnetic trap. In the Killian Lab magnetic trapping paper [50], the inset to Figure 5

shows the $^3\text{P}_2$ atom temperature as about 1 mK for a magnetic trap depth of 15 mK. In that paper, 15 mK is obtained with a 115 G/cm magnetic field gradient. Since we have a lower gradient than this (52.5 G/cm for 35 amps; we run less current through our coils than did the older experiment), we would expect colder temperatures, but it turns out that using 1.5 mK gives the best fit to the data we observe with the repumping laser on; perhaps there are heating processes such as background gas collisions in play.

Rearranging the equation above for the characteristic distance, r , we get:

$$r(T) = \frac{k_b T}{\mu_b \nabla B}. \quad (\text{D.1})$$

The magnetic field experienced by $T_0 = 1.5$ mK atoms is then $\nabla B \cdot r[T_0] = 22$ Gauss.

The Zeeman splitting is

$$E[m_j, \ell] = \mu_b B m_j \left(g_\ell \frac{j(j+1) + \ell(\ell+1) - s(s+1)}{2j(j+1)} + g_u \frac{j(j+1) - \ell(\ell+1) + s(s+1)}{2j(j+1)} \right), \quad (\text{D.2})$$

where j is the total electronic angular momentum, ℓ is the electronic angular momentum, and s is the electronic spin. μ_b is the Bohr magneton and m_j is the magnetic quantum number good for L-S coupling. Finally, g_ℓ and g_u are the g factors of the upper and lower states ($^3\text{P}_2$ and $^3\text{D}_2$), respectively.

The energies of the levels in the $^3\text{P}_2$ manifold are, expressed in frequency units (MHz): $E[2, 1] = 2 \Rightarrow 93.8$ MHz, $E[1, 1] = 1 \Rightarrow 46.9$ MHz, $E[0, 1] = 0 \Rightarrow 0$ MHz, $E[-1, 1] = -1 \Rightarrow -46.9$ MHz, and $E[-2, 1] = -2 \Rightarrow -93.8$ MHz. Similarly, the energies of the levels in the $^3\text{D}_2$ manifold are, expressed in frequency units (MHz),

$E[2, 2] = 2 \Rightarrow 72.9$ MHz, $E[1, 2] = 1 \Rightarrow 36.5$ MHz, $E[0, 2] = 0 \Rightarrow 0$ MHz, $E[-1, 2] = -1 \Rightarrow -36.5$ MHz, and $E[-2, 2] = -2 \Rightarrow -72.9$ MHz.

D.2 Transition Energies Between the 3P_2 and 3D_2 States

The difference in the energies of the sub-levels in the 3P_2 and 3D_2 manifolds yields the transition energies (again in frequency units, MHz) for :

- $E[\pm 2, 2] - E[\pm 2, 1] = \mp 21$ MHz;
- $E[\pm 1, 2] - E[\pm 2, 1] = \mp 57$ MHz;
- $E[\pm 2, 2] - E[\pm 1, 1] = \pm 26$ MHz;
- $E[\pm 1, 2] - E[\pm 1, 1] = \mp 10$ MHz;
- $E[0, 2] - E[\pm 1, 1] = \mp 47$ MHz;
- $E[\pm 1, 2] - E[0, 1] = \pm 36$ MHz;
- $E[\pm 1, 2] - E[0, 1] = 0$ MHz;

The data in Fig. 3.6(B) shows transitions at about -20 and -55 MHz, numbers which are consistent with the ${}^3P_2, m_j = 2 \rightarrow {}^3D_2, m_j = 2$ and ${}^3P_2, m_j = 2 \rightarrow {}^3D_2, m_j = 1$ transitions, respectively. As mentioned in the text of the thesis, we hypothesize that the other transitions are not observed because atoms in energy levels that are not $m_j = 2$ are not trapped strongly by the magnetic trap. Therefore, it is through this

calculation that we set the “zero” of the 3P_2 and 3D_2 transition from the spectrum in Fig. 3.6(B).

Bibliography

- [1] P. G. Mickelson, Y. N. M. de Escobar, P. Anzel, B. J. DeSalvo, S. B. Nagel, A. J. Traverso, M. Yan, and T. C. Killian, *J. Phys. B* **42**, 235001 (Nov. 2009).
- [2] P. Mickelson, Y. N. M. de Escobar, M. Yan, B. DeSalvo, and T. Killian, *Phys. Rev. A* (in press).
- [3] M. H. Anderson, J. R. Ensher, M. R. Matthews, C. E. Wieman, and E. A. Cornell, *Science* **269**, 198 (Jul. 1995).
- [4] C. C. Bradley, C. A. Sackett, J. J. Tollett, and R. G. Hulet, *Phys. Rev. Lett.* **75**, 1687 (Aug. 1995).
- [5] K. B. Davis, M. O. Mewes, M. R. Andrews, N. J. van Druten, D. S. Durfee, D. M. Kurn, and W. Ketterle, *Phys. Rev. Lett.* **75**, 3969 (Nov. 1995).
- [6] B. DeMarco and D. S. Jin, *Science* **285**, 1703 (Sep. 1999).
- [7] A. G. Truscott, K. E. Strecker, W. I. McAlexander, G. B. Partridge, and R. G. Hulet, *Science* **291**, 2570 (Mar. 2001).
- [8] H. F. Hess, *Phys. Rev. B* **34**, 3476 (Sep. 1986).
- [9] C. J. Myatt, E. A. Burt, R. W. Ghrist, E. A. Cornell, and C. E. Wieman, *Phys. Rev. Lett.* **78**, 586 (Jan. 1997).
- [10] W. Süptitz, G. Wokurka, F. Strauch, P. Kohns, and W. Ertmer, *Opt. Lett.* **19**, 1571 (Oct. 1994).
- [11] M. S. Santos, P. Nussenzeig, L. G. Marcassa, K. Helmerson, J. Flemming, S. C. Zilio, and V. S. Bagnato, *Phys. Rev. A* **52**, R4340 (Dec. 1995).
- [12] M. Machholm, P. S. Julienne, and K.-A. Suominen, *Phys. Rev. A* **64**, 033425 (Aug. 2001).
- [13] J. Ye, H. J. Kimble, and H. Katori, *Science* **320**, 1734 (Jun. 2008).
- [14] H. Katori, T. Ido, Y. Isoya, and M. Kuwata-Gonokami, *Phys. Rev. Lett.* **82**, 1116 (Feb. 1999).
- [15] T. Ido, Y. Isoya, and H. Katori, *Phys. Rev. A* **61**, 061403 (May 2000).

- [16] T. Mukaiyama, H. Katori, T. Ido, Y. Li, and M. Kuwata-Gonokami, *Phys. Rev. Lett.* **90**, 113002 (Mar. 2003).
- [17] A. J. Daley, M. M. Boyd, J. Ye, and P. Zoller, *Phys. Rev. Lett.* **101**, 170504 (Oct. 2008).
- [18] A. V. Gorshkov, A. M. Rey, A. J. Daley, M. M. Boyd, J. Ye, P. Zoller, and M. D. Lukin, *Phys. Rev. Lett.* **102**, 110503 (Mar. 2009).
- [19] I. Reichenbach, P. S. Julienne, and I. H. Deutsch, *Phys. Rev. A* **80**, 020701 (Aug. 2009).
- [20] M. Hermele, V. Gurarie, and A. M. Rey, *Phys. Rev. Lett.* **103**, 135301 (Sep. 2009).
- [21] A. V. Gorshkov, M. Hermele, V. Gurarie, C. Xu, P. S. Julienne, J. Ye, P. Zoller, E. Demler, M. D. Lukin, and A. M. Rey, *Nat. Phys.* **6**, 289 (Feb. 2010).
- [22] T. Binnewies, G. Wilpers, U. Sterr, F. Riehle, J. Helmcke, T. E. Mehlstäubler, E. M. Rasel, and W. Ertmer, *Phys. Rev. Lett.* **87**, 123002 (Aug. 2001).
- [23] J. Grünert and A. Hemmerich, *Phys. Rev. A* **65**, 041401 (Mar. 2002).
- [24] J. R. Guest, N. D. Scielzo, I. Ahmad, K. Bailey, J. P. Greene, R. J. Holt, Z.-T. Lu, T. P. O'Connor, and D. H. Potterveld, *Phys. Rev. Lett.* **98**, 093001 (Feb. 2007).
- [25] T. Kuwamoto, K. Honda, Y. Takahashi, and T. Yabuzaki, *Phys. Rev. A* **60**, R745 (Aug. 1999).
- [26] Y. Takasu, K. Maki, K. Komori, T. Takano, K. Honda, M. Kumakura, T. Yabuzaki, and Y. Takahashi, *Phys. Rev. Lett.* **91**, 040404 (Jul. 2003).
- [27] T. Fukuhara, Y. Takasu, M. Kumakura, and Y. Takahashi, *Phys. Rev. Lett.* **98**, 030401 (Jan. 2007).
- [28] S. Kraft, F. Vogt, O. Appel, F. Riehle, and U. Sterr, *Phys. Rev. Lett.* **103**, 130401 (Sep. 2009).
- [29] T. H. Loftus, T. Ido, A. D. Ludlow, M. M. Boyd, and J. Ye, *Phys. Rev. Lett.* **93**, 073003 (Aug. 2004).
- [30] S. Nagel, P. Mickelson, A. Saenz, Y. Martinez, Y. Chen, T. Killian, P. Pellegrini, and R. Côté, *Phys. Rev. Lett.* **94**, 083004 (Mar. 2005).
- [31] N. Poli, R. E. Drullinger, G. Ferrari, J. Leonard, F. Sorrentino, and G. M. Tino, *Phys. Rev. A* **71**, 061403 (Jun. 2005).

- [32] T. Chanelière, L. He, R. Kaiser, and D. Wilkowski, *Eur. Phys. J. D* **46**, 507 (Mar. 2008).
- [33] R. Ciurylo, E. Tiesinga, and P. Julienne, *Phys. Rev. A* **71**, 030701 (Mar. 2005).
- [34] I. Reichenbach and I. H. Deutsch, *Phys. Rev. Lett.* **99**, 123001 (Sep. 2007).
- [35] T. Akatsuka, M. Takamoto, and H. Katori, *Nat. Phys.* **4**, 954 (Dec. 2008).
- [36] S. Stellmer, M. K. Tey, B. Huang, R. Grimm, and F. Schreck, *Phys. Rev. Lett.* **103**, 200401 (Nov. 2009).
- [37] Y. N. M. de Escobar, P. G. Mickelson, M. Yan, B. J. DeSalvo, S. B. Nagel, and T. C. Killian, *Phys. Rev. Lett.* **103**, 200402 (Nov. 2009).
- [38] G. Ferrari, R. E. Drullinger, N. Poli, F. Sorrentino, and G. M. Tino, *Phys. Rev. A* **73**, 023408 (Feb. 2006).
- [39] P. Mickelson, Y. Martinez, A. Saenz, S. Nagel, Y. C. Chen, T. Killian, P. Pellegrini, and R. Coté, *Phys. Rev. Lett.* **95**, 223002 (Nov. 2005).
- [40] M. Yusada, T. Kishimoto, M. Takamoto, and H. Katori, *Phys. Rev. A* **73**, 011403(R) (Jan. 2006).
- [41] Y. N. M. de Escobar, P. G. Mickelson, P. Pellegrini, S. B. Nagel, A. Traverso, M. Yan, R. Côté, and T. C. Killian, *Phys. Rev. A* **78**, 062708 (Dec. 2008).
- [42] A. Stein, H. Knockel, and E. Tiemann, *Phys. Rev. A* **78**, 042508 (Oct. 2008).
- [43] G. Ferrari, N. Poli, F. Sorrentino, and G. M. Tino, *Phys. Rev. Lett.* **97**, 060402 (Aug. 2006).
- [44] C. Lisdat, J. S. R. V. Winfred, T. Middelmann, F. Riehle, and U. Sterr, *Phys. Rev. Lett.* **103**, 090801 (Aug. 2009).
- [45] K. Enomoto, K. Kasa, M. Kitagawa, and Y. Takahashi, *Phys. Rev. Lett.* **101**, 203201 (Nov. 2008).
- [46] W. D. Phillips and H. J. Metcalf, *Phys. Rev. Lett.* **48**, 596 (Mar. 1982).
- [47] J. Prodan, A. Migdall, W. D. Phillips, I. So, H. J. Metcalf, and J. Dalibard, *Phys. Rev. Lett.* **54**, 992 (Mar. 1985).
- [48] E. Raab, M. Prentiss, A. Cable, S. Chu, and D. Pritchard, *Phys. Rev. Lett.* **59**, 2631 (Dec. 1987).
- [49] T. Loftus, J. R. Bochinski, and T. W. Mossberg, *Phys. Rev. A* **66**, 013411 (Jul. 2002).

- [50] S. B. Nagel, C. E. Simien, S. Laha, P. Gupta, V. S. Ashoka, and T. C. Killian, *Phys. Rev. A* **67**, 011401 (Jan. 2003).
- [51] A. Traverso, R. Chakraborty, Y. N. M. de Escobar, P. G. Mickelson, S. B. Nagel, M. Yan, and T. C. Killian, *Phys. Rev. A* **79**, 060702 (Jun. 2009).
- [52] W. Demtröder, *Laser Spectroscopy*, 3rd ed. (Springer-Verlag, Berlin Heidelberg New York, 2003).
- [53] Y. N. M. de Escobar, *Bose-Einstein Condensation of ^{84}Sr* , Ph.D. thesis, Rice University (Apr. 2010).
- [54] B. A. Bushaw and W. Nörtershäuser, *Spectrochim. Acta, Part B* **55**, 1679 (Jul. 2000).
- [55] M. Yasuda and H. Katori, *Phys. Rev. Lett.* **92**, 153004 (Apr. 2004).
- [56] A. L. Migdall, J. V. Prodan, W. D. Phillips, T. H. Bergeman, and H. J. Metcalf, *Phys. Rev. Lett.* **54**, 2596 (Jun. 1985).
- [57] X. Xu, T. H. Loftus, J. L. Hall, A. Gallagher, and J. Ye, *Journal of the Optical Society of America B* **20**, 968 (May 2003).
- [58] H. J. Metcalf and P. van der Straten, *Laser Cooling and Trapping*, Graduate Texts in Contemporary Physics (Springer, New York, 1999).
- [59] A. D. Ludlow, *The Strontium Optical Lattice Clock: Optical Spectroscopy with Sub-Hertz Accuracy*, Ph.D. thesis, University of Colorado (2008).
- [60] P. Bouyer, P. Lemonde, M. B. Dahan, A. Michaud, C. Salomon, and J. Dalibard, *Europhys. Lett.* **27**, 569 (Sep. 1994).
- [61] S. B. Nagel, *Ultracold Collisions in Atomic Strontium*, Ph.D. thesis, Rice University (Feb. 2008).
- [62] S. B. Nagel, *A Narrow Linewidth Diode Laser System for Strontium Laser Cooling Applications*, M.S. thesis, Rice University (Apr. 2004).
- [63] R. Grimm, M. Weidemüller, and Y. B. Ovchinnikov, arXiv:physics/9902072v1 (Feb. 1999).
- [64] R. Grimm, M. Weidemüller, and Y. Ovchinnokov, *Adv. Atom. Mol. Opt. Phys.* **42**, 95 (2000).
- [65] A. Derevianko, *Phys. Rev. Lett.* **87**, 023002 (Jun. 2001).
- [66] T. P. Dinneen, K. R. Vogel, E. Arimondo, J. L. Hall, and A. Gallagher, *Phys. Rev. A* **59**, 1216 (Feb. 1999).

- [67] A. Bruschi, R. L. Targat, X. Baillard, M. Fouche, and P. Lemonde, Phys. Rev. Lett. **96**, 103003 (Mar. 2006).
- [68] A. Dunn, *A Novel Extended-Cavity Diode Laser in Red Wavelengths*, Undergraduate thesis, Rice University (Apr. 2008).
- [69] L. R. Hunter, W. A. Walker, and D. S. Weiss, Phys. Rev. Lett. **56**, 823 (Feb. 1986).
- [70] B. A. Bushaw, H. J. Kluge, J. Lantzsch, R. Schwalbach, J. Stenner, H. Stevens, K. Wendt, and K. Zimmer, Z. Phys. D: At. Mol. Clusters **28**, 275 (Dec. 1993).
- [71] S. M. Heider and G. O. Brink, Phys. Rev. A **16**, 1371 (Oct. 1977).
- [72] W. H. King, J. Opt. Soc. Am. **53**, 638 (Oct. 1963).
- [73] U. Dammalapati, S. De, K. Jungmann, and L. Willmann, Eur. Phys. J. D **53**, 1 (May 2009).
- [74] B. A. Bushaw and B. D. Cannon, Spectrochim. Acta, Part B **52**, 1839 (Apr. 1997).
- [75] G. Guelachvili, A. H. Abdullah, N. Tu, K. N. Rao, S. Urban, and D. Papousek, J. Mol. Spectrosc. **133**, 345 (Jul. 1989).
- [76] P. Anzel, *Calibrating our Wavemeter for Spectroscopy of the $^3P_2 - ^3D_2^{88}\text{Sr}$ Transition*, Undergraduate thesis, Rice University (Apr. 2009).
- [77] J. E. Sansonetti and W. C. Martin, J. Phys. Chem. Ref. Data **34**, 1559 (Sep. 2005).
- [78] A. Stein, H. Knöckel, and E. Tiemann, Eur. Phys. J. D **57**, 171 (Apr. 2010).
- [79] M. Yan, R. Chakraborty, P. G. Mickelson, Y. N. M. de Escobar, and T. C. Killian, arXiv:0905.2223v1 (May 2009).
- [80] D. Comparat, A. Fioretti, G. Stern, E. Dimova, B. L. Tolra, and P. Pillet, Phys. Rev. A **73**, 043410 (Apr. 2006).
- [81] C. R. Monroe, E. A. Cornell, C. A. Sackett, C. J. Myatt, and C. E. Wieman, Phys. Rev. Lett. **70**, 414 (Jan. 1993).
- [82] O. J. Luiten, M. W. Reynolds, and J. T. M. Walraven, Phys. Rev. A **53**, 381 (Jan. 1996).
- [83] C. S. Adams, H. J. Lee, N. Davidson, M. Kasevich, and S. Chu, Phys. Rev. Lett. **74**, 3577 (May 1995).

- [84] K. M. O'Hara, M. E. Gehm, S. R. Granade, and J. E. Thomas, *Phys. Rev. A* **64**, 051403 (Oct. 2001).
- [85] W. Ketterle, D. Durfee, and D. Stamper-Kurn, in *Proc. Int. School of Physics - Enrico Fermi*, edited by M. I. et al. (IOS Press, Amsterdam, 1999).
- [86] F. Dalfovo, S. Giorgini, L. P. Pitaevskii, and S. Stringari, *Rev. Mod. Phys.* **71**, 463 (Apr. 1999).
- [87] P. A. Ruprecht, M. J. Holland, K. Burnett, and M. Edwards, *Phys. Rev. A* **51**, 4704 (Jun. 1995).
- [88] C. C. Bradley, C. A. Sackett, and R. G. Hulet, *Phys. Rev. Lett.* **78**, 985 (Feb. 1997).
- [89] C. A. Sackett and R. G. Hulet, *J. Opt. B* **3**, R1 (Feb. 2001).
- [90] P. Fedichev, Y. Kagan, G. Shlyapnikov, and J. Walraven, *Phys. Rev. Lett.* **77**, 2913 (Sep. 1996).
- [91] M. Theis, G. Thalhammer, K. Winkler, M. Hellwig, G. Ruff, R. Grimm, and J. H. Denschlag, *Phys. Rev. Lett.* **93**, 123001 (Sep. 2004).
- [92] G. D. Montesinos, V. M. Pérez-García, and P. J. Torres, *Physica D* **191**, 193 (Jan. 2004).
- [93] W. Parkinson, E. Reeves, and F. Tomkins, *J. Phys. B* **9**, 157 (Sep. 1976).
- [94] H. G. C. Werij, C. H. Greene, C. E. Theodosiou, and A. Gallagher, *Phys. Rev. A* **46**, 1248 (Aug. 1992).
- [95] H. Katori, T. Ido, and M. Kuwata-Gonokami, *J. Phys. Soc. Jap.* **68**, 2479 (Aug. 1999).
- [96] A. Henderson and R. Stafford, *Opt. Express* **14**, 767 (Jan. 2006).
- [97] P. Bernath, *Spectra of Atoms and Molecules*, 1st ed. (Oxford University Press, New York, 1995).